New metal-organic frameworks and coordination polymers constructed from bifunctional linkers with carboxylate, pyrazolate and phosphonate

Kumulative Dissertation

zur Erlangung des Doktorgrades der Mathematisch-
Naturwissenschaftlichen Fakultät der Heinrich-Heine-Universität
Düsseldorf
vorgelegt von

Christian Heering
aus Magdeburg

Düsseldorf, Juni 2016

aus dem Institut für Anorganische Chemie und Strukturchemie der Heinrich-Heine Universität Düsseldorf

Gedruckt mit der Genehmigung der Mathematisch-Naturwissen-schaftlichen Fakultät der Heinrich-Heine-Universität Düsseldorf

Referent: Prof. Dr. Christoph Janiak

Korreferent: Prof. Dr. Christian Ganter

Tag der mündlichen Prüfung: 07.07.2016

Meiner lieben Familie

Ich danke meinem verehrten Lehrer

Herrn Prof. Dr. Christoph Janiak

für die Förderung dieser Arbeit sowie das von ihm entgegengebrachte Interesse.

Herrn Prof. Dr. Christian Ganter,

für die Zweitbegutachtung dieser Arbeit, möchte ich ebenfalls danken.

Sonja, Frieda und Pola

gebührt größter Dank.

Eidesstattliche Erklärung

Ich versichere an Eides statt, dass die vorliegende Dissertation von mir selbstständig, ohne unzulässige fremde Hilfe unter der Beachtung der „Grundsätze zur Sicherung guter wissenschaftlicher Praxis" an der Heinrich-Heine Universität Düsseldorf erstellt worden ist. Die aus fremden Quellen direkt oder indirekt übernommenen Gedanken sowie Ergebnisse sind als solche kenntlich gemacht. Die Arbeit wurde bisher weder im Inland noch im Ausland in gleicher oder ähnlicher Form einer anderen Prüfungsbehörde vorgelegt. Es wurden keine früheren erfolglosen Promotionsversuche unternommen.

_____

Ort, Datum

_____

Unterschrift

The completion of this work spans the period from August 2012 to June 2016, in which the author was PhD student in the group of Prof. Dr. Christoph Janiak at the Heinrich-Heine-Universität Düsseldorf.

Publication list

<u>Christian Heering</u>, Ishtvan Boldog, Vera Vasylyeva, Joaquín Sanchiz, Christoph Janiak: „Bifunctional pyrazolate–carboxylate ligands for isoreticular cobalt and zinc MOF-5 analogs with magnetic analysis of the {$Co_4(\mu_4$-O)} node" *CrystEngComm*, **2013**,*15*, 9757-9768. DOI: 10.1039/C3CE41426D

Ishtvan Boldog, Konstantin Domasevitch, Jana K. Maclaren, <u>Christian Heering</u>, Gamall Makhloufi and Christoph Janiak: A fluorite isoreticular series of porous framework complexes with tetrahedral ligands: new opportunities for azolate PCPs *CrystEngComm*, **2014**,*16*, 148-151. DOI: 10.1039/C3CE42162G

Sladjana B. Novaković, Goran A. Bogdanović, <u>Christian Heering</u>, Gamall Makhloufi, Djordje Francuski and Christoph Janiak: Charge-Density Distribution and Electrostatic Flexibility of ZIF-8 Based on High-Resolution X-ray Diffraction Data and Periodic Calculations *Inorg. Chem.*, **2015**, *54* (6), 2660–2670. DOI: 10.1021/ic5028256

Biju Francis, <u>Christian Heering</u>, Ricardo O. Freire, M. L. P. Reddy and Christoph Janiak: Achieving visible light excitation in carbazole-based Eu^{3+}–β-diketonate complexes *via* molecular engineering *RSC Adv.*, **2015**, *5*, 90720-90730. DOI: 10.1039/C5RA18819A

<u>Christian Heering</u>, Bahareh Nateghi, Christoph Janiak: „Charge-Assisted Hydrogen-Bonded Networks of NH_4^+ and $[Co(NH_3)_6]^{3+}$ with the New Linker Anion of 4-Phosphono-Biphenyl-4′-Carboxylic Acid" *Crystals,* **2016**, *6*(3), 22, 1-14. DOI:10.3390/cryst6030022

Christian Heering, Biju Francis, Bahareh Nateghi, Gamall Makhloufi, Steffen Lüdeke and Christoph Janiak: „Syntheses, structures and properties of group 12 element (Zn, Cd, Hg) coordination polymers with a mixed-functional phosphonate-biphenyl-carboxylate linker" *CrystEngComm*, **2016** DOI: 10.1039/C6CE00587J

Anas Tahli, Anne-Christine Chamayou, Ümit Köc, Robin Brückner, Reda F.M. Elshaarawy, Christian Heering, Christoph Janiak: Homochiral zinc benzene-1,3,5-tricarboxylate coordination networks with a chiral nitrogen ligand or template: spontawneous resolution of a twofold interpenetrated 2D sql (4,4) network and formation of enantiopure 3D sra (SrAl$_2$) networks *Inorg. Chim.* Acta, **2016** DOI: 10.1016/j.ica.2016.05.042

Kurzfassung

In der vorliegenden Arbeit werden bifunktionelle Liganden sowie deren Komplexe mit Metallionen vorgestellt, welche einen Beitrag zu den Metall-organischen Gerüstverbindungen (engl. MOFs, Metal-organic frameworks) leisten. Jene MOFs, welche aus Metallionen (-zentren) als Verknüpfungspunkte bestehen, die durch polyfunktionelle, verbrückende Liganden dreidimensionale Netzwerke ausbilden, haben aufgrund Ihrer Struktur vielfältige interessante Eigenschaften. Eine intrinsische Porosität, hervorgerufen durch Poren und Kanäle innerhalb der MOFs, führt zu teilweise hoher spezifischer Oberfläche, wodurch MOFs für viele potentielle Anwendungen in Frage kommen, zu denen Katalyse, Gasspeicherung und –trennung und weitere gehören. Durch die Einbringung von Funktionen wie Pyrazol- als auch Phosphonsäuregruppen in Liganden konnten in der vorliegenden Arbeit Metallkomplexe synthetisiert werden, welche über hohe thermische sowie hydrolytische Stabilität verfügen. Mit dem Liganden 3,5-Dimethylpyrazol-4-carbonsäure sowie 3,5-Dimethyl-(pyrazol-4-yl)-benzoesäure konnten mit Co, Cu und Zn MOFs hergestellt werden. Diese besitzen Oberflächen (BET), welche von 100-1500 m^2/g variieren. Des weiteren wurden mit der 4-Phosphono-biphenyl-4'-carbonsäure Koordinationspolymere und Wasserstoffbrücken-verbundene Netzwerke mit $[Co(NH_3)_6]^{3+}$, NH_4^+, Zn, Cd, Hg und Co erhalten. Die vorgestellten Metallkomplexe sowie die organischen Liganden werden eingehend charakterisiert und deren Erscheinen als Publikationen in wissenschaftlichen Journalen vorgestellt.

Abstract

In this work bifunctional ligands and their complexes with metals are presented that contribute to the area of Metal-organic frameworks (MOFs). MOFs, which consist of metal centres or nodes that are connected by bridging, polyfunctional ligands to form three-dimensional networks, have certain properties of interest related to their structure. An intrinsic porosity, caused by channels and voids inside the MOF, leads to a high specific surface area, allowing the use of MOFs in several potential applications, like catalysis, gas storage and separation and others. By incorporation of pyrazole or phosphonic acid groups in the ligand, new metal complexes were synthesized, which are thermally and hydrolytically stable. With the ligands 3,5-dimethylpyrazol-4-carboxylic acid and 3,5-dimethyl-(pyrazol-4-yl)-benzoic acid MOFs were synthesized with Co, Cu und Zn MOF. Those have surface areas (BET) ranging from 100-1500 m^2/g. With 4-phosphono-biphenyl-4'-carboxylic acid as ligand new coordination polymers and hydrogen-bonded networks with $[Co(NH_3)_6]^{3+}$, NH_4^+, Zn, Cd, Hg and Co were obtained, which have luminescent properties. The herein introduced new metal complexes and organic ligands are characterized in detail and their properties and appearance as publications in scientific journals is presented.

List abbreviations

MOF	*Metal-organic framework*
CP	*Coordination polymer*
BET	*Brunauer-Emmett-Teller*
ZIF	*Zeolithic Imidazolate framework*
SBU	*Secondary building unit*
bdc	*benzene dicarboxylic acid*
btc	*benzene tricarboxylic acid*
PCP	*porous coordination polymer*
MIL	*Matériaux de l'institute Lavoisier*
UiO	*Universitetet i Oslo*
***H*pz**	*1H-pyrazole*
pz⁻	*pyrazolate*
H₂L	*3,5-dimethyl-4-(pyrazol-4-yl)benzoic acid*
H₃BPPA	*4-phosphono-biphenyl-4'-carboxylic acid*
IR	*Infrared spectroscopy*
MS	*Mass spectroscopy*
CHN	*Elemental analysis*
TGA	*Thermogravimetric analysis*
XRD	*X-ray diffraction*
SCXRD	*Single crystal X-ray diffraction*
PXRD	*Powder X-ray diffraction*
DMF	*N,N'-dimethyl formamide*
DEF	*N,N'-diethyl formamide*
EtOH	*Ethanol*
MeOH	*Methanol*
DI	*Deionized*

Table of contents

1 Introduction

In chemistry and related disciplines the design of and search for so-called 'functional' or 'advanced' materials became a steadily rising and important task in recent years.[1] Those materials may combine several properties of interest, which are catalytic activity,[2] porosity,[3] sensing,[4,5] luminescence,[6] magnetism[7] and others.[8,9,10] To challenge actual and future demands on functional materials for industrial use or to cope with environmental issues, it is a common aim to combine desired functions and properties and introduce them into new molecules or compounds.[11] This quest led to intense research in different areas, in inorganic chemistry it is especially in the area of Metal-Organic Frameworks (MOFs) and coordination polymers (CPs).[12,13,14] In the year 1990 Hoskins and Robson published a new polymeric, three-dimensional framework,[15] and later, in 1999, Yaghi defined the term MOF,[16] publishing the structure of the now well known and intensively investigated MOF-5, a zinc terephthalate complex, that has an estimated surface area (BET) of 2,900 m^2g^{-1}. The number of MOF structures listed in crystal structure databases grew almost exponentially since then. The imminent property of a MOF is its porosity due to cavities, pores or channels within a three-dimensional network, resulting in a significantly higher surface area than observed in other highly porous materials. Zeolites, well porous materials, show surface areas up to 1,000 m^2g^{-1}.[17] They have been used in gas separation, catalysis and molecular storage applications for decades already. Activated carbons and silica gels also exhibit high surface areas, which range from 600 m^2g^{-1} for silica gels to 3,000 m^2g^{-1} for activated carbons, respectively. Those materials have already been proven to be very useful in industrial applications, for medicinal purposes and life science in general, as those could be used for drug delivery as well.[18]

Zeolitic imidazolate frameworks (ZIFs) are porous materials, in which the linker is imidazole or imidazolate, respectively, which bridges metal ions to form networks. ZIFs have a higher stability than common, carboxylate based MOFs due to the stronger binding of N donor ligands towards metal ions. ZIF-8, a zinc methyl-imidazolate, is one example of a very well investigated compound of this class.[19,20,21]

The design of new MOFs, with even higher surface areas and improved stability, could be better understood due to knowledge of rational design concepts

and reticular synthesis. A broad spectrum of organic linkers and building units, metal centres or nodes, is known so far.[22] Typical coordination behaviour of metal ions in different oxidation states, bond strengths and binding modes of different functional groups give rise to a widespread pool of possible coordination polymers.[23,24] The synthesis of new organic or mixed inorganic-organic ligands, which might act as linkers, is therefore imminent for accomplishing that aim. With surface areas progressively increasing in MOFs, the possible applications, in which MOFs could be used, are rising. The efforts, which are made to synthesize new MOFs demonstrate and underline the importance that those metal-organic hybrids have.

1.1 Reticular Synthesis

Reticular synthesis, creation of netlike structures, allows certain predictions about structures by incorporating known design motives and applying them in syntheses of metal complexes. It is therefore possible to increase the pore size in a 3D network by elongating a linker and by keeping its rigidity. That has been shown before, when the group of Yaghi successfully synthesized several MOF-5 analogues by isoreticular synthesis.[25] The aforementioned MOF-5, which consists of Zn_4O clusters or secondary building units (SBUs), wherein two Zn atoms are bridged by one carboxylate group of a terephthalate and each of them surrounded by four oxygen atoms, is the prototypical MOF. Its surface area of 2,900 m^2g^{-1} has been further increased in a series of *iso*-reticular MOFs by enlargement of the *bdc* as linker by elongation with additional phenyl rings or other rigid groups as spacers to give extended structures with larger voids successively.

Rigidity of the linkers is important to maintain certain surface characteristics. If flexible linkers are used, it is often observed, that surface areas are low and networks collapse upon activation. The term of crystal engineering has to be mentioned here, a discipline that allows topologically predictions and syntheses over rational design.[26] It is a powerful tool in the MOF area to deliver highly crystalline materials with predictable and tuneable void size and porosity.

In general, the knowledge of SBUs and coordination motives generates a catalogue with which properties can be tailored and structures being adjusted to certain applicational demands.[27] With linker size increased, new possibilities for modification of the molecule arise. Other functions or groups can added, to name -

2

OH, -NH$_2$, -OCH$_3$, to achieve a change or creation of a certain characteristic in the MOF, which could be a change in polarity and others.

1.2 Breathing structures

Breathing structures or breathing MOFs have gained interest over the last years.[28,29,30,31] Those are structures, which adapt structural changes, 'breathe', by changing cell parameters upon guest removal or exchange and upon external stimuli such as pressure or electric field. The investigation on crystal transitions or transformations is useful for understanding the processes that take place when adsorption appears in MOFs or other porous structures.

The definition of breathing structures refers to the fact that a variety of crystal structures have a certain flexibility,[32,33] which allows the structure to deform in terms of changing cell dimensions and angles upon stimuli. Those stimuli can be external, like pressure induced, temperature induced or the breathing can be triggered by an internal stimulus like solvent removal or substitution.

The effect of breathing in a MOF might find use in applications like sensing, storage and others. Flexible structures might also show less damage caused by mechanical force to the material.

1.3 Coordination polymers based on carboxylates, pyrazolates or phosphonates as linker

1.3.1 Carboxylates

Coordination polymers with linkers bearing at least two carboxylic acid functions are well investigated and there are many structures published of carboxylate complexes that show permanent porosity and high surface areas.[12,34] Some basic di- and tricarboxylic acids, which have been applied in MOF synthesis are shown in the following scheme (Scheme 1).
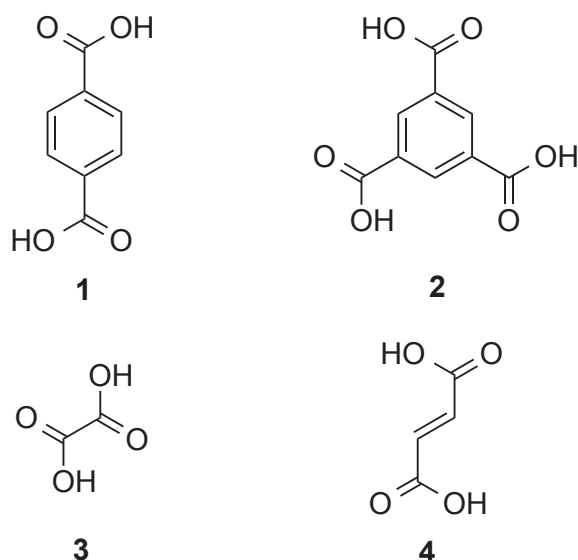
Scheme 1 A selection of carboxylic acid bearing ligands, which have been used for construction of various CPs and MOFs: terephthalic acid (bdc, 1), trimesic acid (btc, 2), oxalic acid (3) and fumaric acid (4).

The basically facile synthesis and availability of carboxylate linkers and good crystallization of most metal ions with carboxylates are reasons for their wide applicability. The MOF compounds MOF-210 and NU-100 have surface areas (BET) that reach up to 6,000 m^2g^{-1}.[35,36] The carboxylate, derived from deprotonated carboxylic acid function, as coordinating group has basically three modes of coordination towards metal ions amongst other, rare examples. Bridging, chelating and monodentate modes are observed, to be found in complexes and depending on metal ion size and charge.[37] The aforementioned terephthalic acid (BDC) as simple aromatic bifunctional carboxylate has been employed in syntheses with a large number of metal ions to form a pool of porous coordination polymers (PCPs) of different stabilities and surface areas.[38] As carboxylate PCPs show a, in general, high thermal stability and robustness they are used in multiple applications. The several complexes of the MOF, MIL (Matériaux de l'institute Lavoisier) and UiO (Universitetet i Oslo) family are well known for their exceptional high surface areas. The MOF series contains several PCPs derived from poly-functional carboxylates with different linker sizes and conformations.

The largest pore aperture reported for a carboxylate based MOF has an estimated size of 32 Å.[39] As ligand size and nucleation influence the surface areas by enlargement of the voids, the charge and size of metal ions determine the overall

stability significantly. The MIL series, wherein three-valent metal ions like Fe^{3+} and Cr^{3+} and Al^{3+} are incorporated, shows thermal stabilities up to 275 °C and surface areas up to 5,900 m^2g^{-1}.[40] Their stability in air, moisture and water is far beyond the stabilities reported for the zinc and copper based MOF analogues with carboxylic acids.[41]

The term 'waterproof', as used by Férey,[42] is one aspect that plays an important role when MOFs are considered as materials for applications.[43] As MOF-5 undergoes rapid hydrolysis in aqueous environment already,[44] zirconium terephthalate complexes can be regarded as highly waterproof. The reason for that difference can be explained with an increasing strength in coordination, starting with zinc as +2 cation, *via* +3 cations, Al^{3+} and Cr^{3+}, to +4 cations Zr^{4+} and Ti^{4+}. The higher the charge that is located on the metal ion, the less energy is stored in the bonds and therefore the complexes with +4 cations and carboxylic acids are significantly more stable. UiO-66, ($[Zr_6O_4(\mu_3\text{-}OH)_4(bdc)_6]$), could be seen as one of the most stable MOFs, with decomposition at 400 °C and stability even in boiling water and alkaline solutions. Linkers, that bear more than two $-COO^-$ functions, tend to give even more stable complexes, taking into account that linking of more than two SBUs by one linker forms a denser, more rigid network. The HKUST-1 is one example for that behaviour,[45] noting that *btc* is the used ligand whereas bdc and Cu^{2+} does not give a compound with comparable stability and properties.

With fumaric acid, an aluminium based MOF, Al-fumarate A520, has been synthesized and its structure published recently.[46] This compound exhibits a very high stability and has a surface area (BET) of 1000 m^2g^{-1}.

1.3.2 Pyrazoles and pyrazolates

The 1*H*-pyrazole (*H*pz, Scheme 2) is one molecule in the group of five-membered nitrogen containing heterocycles,[47] which are belongs to the azoles. Trofimenko *et al.* first introduced it as a ligand in coordination chemistry in 1972.[48] They are important ligands and building blocks in medicine, biology and coordination chemistry.[49] More important than the 1*H*-pyrazole, which coordinates *via* the N2 nitrogen in monohapto- mode, is the pyrazolate (pz⁻), wherein the 1*H*-pyrazole is deprotonated at the N1. Its affinity towards metal ions is much stronger than that of carboxylate, explained by its higher basicity.
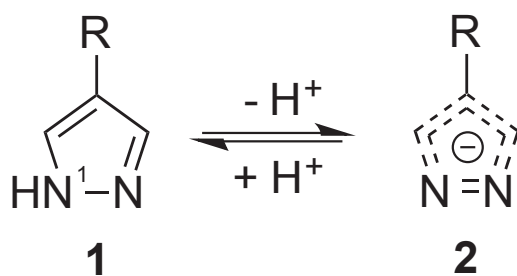
Scheme 2 The 1*H*-pyrazole (R = H, 1) and the pyrazolate anion (2). The group -R in 4-position can be any rest for suitable poly-functional ligands.

The coordination modes of pyrazolates range from bridging *via* N1 and N2 to chelating. It has therefore the ability to mimic the carboxylate, when coordinating to metal ions, which is very similar to coordination modes of 1,2,3-triazole and 1*H*-tetrazole.[50] Because of stronger bonds between pyrazolate and metal ion, in general, the derived complexes are more stable than their carboxylate analogues, concerning thermal stability and water stability. A variety of pyrazolate based PCPs has been published so far, that all exhibit interesting features and the aforementioned stability features.

Knowing the main coordination modes, pyrazolate ligand design can be adjusted to obtain PCPs with desired properties. From +1 coin metal ions chainlike structures or trigonal SBUs are predicted and observed.[51] Several structures include 3d transition metals, with which porous systems were synthesized.[52,53,54] Tetrahedral environment with MN_4 moieties is dominant in those 3D networks. The imitation of the -COO$^-$ function by the -pz$^-$ is of importance here, allowing rational design concepts for pyrazolate metal complexes, which has been demonstrated by the author.[55]

As 3-D coordination compounds are derived from pyrazolate ligands, like the [Co(bpz)] network, their enhanced stability combined with high porosity is an important feature for applications.

It has been shown, that crystallinity of pyrazolate complexes is harder to achieve, when ligands are elongated following the isoreticular approach. Furthermore, the chance of interpenetration of networks rises.[56][57] Nonetheless, pyrazolates embody very important linkers in MOF chemistry because of the strong coordination behaviour.

The design of highly stable compounds with MOFs consisting of pyrazolate linkers is possible and leads to complexes, which are even suitable for water

sorption.[58] A naphthalenediimide based pyrazolate functionalized linker by Dinca *et al.* has to be mentioned here, with which a Zn-MOF was synthesized that showed exceptional water uptake for a pyrazolate-based MOF.[59]

1.3.3 Phosphonates

The phosphonate group, $-PO(O)_2^{2-}$ (Scheme 3), derived from the phosphonic acid which has been twice deprotonated, allows a variety of coordination modes with several metal ions when embedded in ligands or linkers .[60] One of the first examples of metal phosphonates came from Alberti *et al.* in 1978,[61] when a zirconium phosphonate was presented, which has been synthesized by reaction of Zr^{4+} source with phosphonic acid. Since then, a variety of phosphonate complexes with other metal ions and also phosphonate MOFs were published.[62] Basically, because of the three oxygens that can coordinate towards a metal centre, many different chelating and bridging modes are known.[63] The higher acidity of the phosphonic acid (pKs_1 ~ 2.0, pKs_2 ~ 6.5) compared to 1*H*-pyrazole (pKs ~ 2.5) and carboxylic acid (aromatic, pKs ~ 4.0) leads to strong bonds in its complexes, stronger than those in pyrazolates or carboxylates. Together with the enhanced stability due to chelating, metal phosphonates are, in general, more stable than their carboxylate or pyrazolate analogues. Therefore, increased water stability, often a complete resistance to hydrolysis, and high thermal stability are observed in phosphonate complexes.[64]
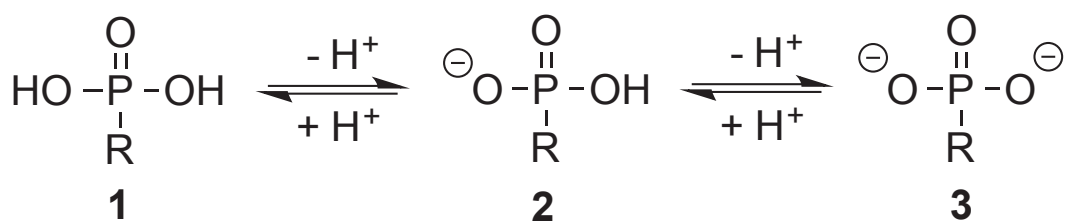
Scheme 3 The organic phosphonate function (H2Phos, 1), wherein –R is a rest, the mono-deprotonated form (2) and the phosphonate group (3).

The derived porous complexes feature interesting and novel properties related to the phosphonate linkers. A barium monoester-phosphonate PCP, CALF-25 , shows a moderate surface area of 385 m^2g^{-1},[65] and does not show any structural change even after 24 h at 90% relative humidity and elevated temperature of 353 K.[66]

From the group of Clearfield a biphenyl bisphosphonate has been used in order to synthesize a series of aluminium complexes with the ability to adsorb hydrogen in quantities up to 1.8 wt%.[67] Small amounts of H_3PO_3 were incorporated within the complexes to enhance the H_2 adsorption by the factor two.

With 1,3,5-benzene triphosphonic acid very stable complexes with titanium (IV) were realised, having a surface areas (BET) of up to 250 m^2g^{-1} and are thermally stable > 200 °C.[68] Pramanik *et al.* were the authors of that work from 2013, in which a structure could not be determined due to the microcrystallinity of the titanium compound.

The incorporation of phosphonates into ligand or linker design is a proper tool to enhance the complex stability. As mentioned in many related publications, there are difficulties to obtain porous compounds with phosphonate linkers or to have quality crystals for structure determination.

It has to be mentioned that the main structural motif of phosphonate complexes is a layered form, therefore two-dimensional structures are often obtained.[69] Rather uncommon are three-dimensional networks that would, together with the high stability, be of great interest in terms of possible applications. In general, research on porous phosphonate based complexes is rather few and the area only poorly investigated.

Not representing a polymeric structure, but important because of the coordination of phosphonate groups toward copper (II), is the complex $Cu(C_6H_{10}(OH)PO_3)(H_2O)_2$ by Yao ,[70] in which copper ions are coordinated by phosphonates and water molecules. The compound, which consists of layers, is stable up to 200 °C and shows interesting magnetic behaviour.

The combination of pyrazolate and carboxylate as functions in a linker is used to increase stability of the derived complexes while maintaining high crystallinity and surface areas. Bi- or polyfunctional linker design has the advantage of incorporation of both functions in a complex, whereas the synthesis with two different linkers, one having carboxylate and the other pyrazolate function, does not necessarily lead to compounds with enhanced stability. Examples for mixed-functional complexes have been studied and are part of the authors' own work as well.[55] Gao *et al.* have demonstrated recently that an isophthal-pyrazolate based complex with copper (II) did not only show significant stability in water, but also a high surface area of 2,100 m^2g^{-1}.[71] The complex, which has **rht** topology, is porous and shows a significant

CO_2 uptake over methane. A trigonal Cu_3 cluster is formed by Cu^{2+} and bridging pyrazoles, and the copper ions coordinated in a square-planar mode by two water molecules.

With the smallest bifunctional pyrazolate-carboxylate, the 3,5-dimethyl pyrazole 4-carboxylic acid, the group of Navarro have published a zinc complex in 2010,[72] which was used to capture toxic gases. It was demonstrated, that porosity is given and could be used to separate harmful gases from air.

Mixed carboxylate-phosphonate ligands in coordination polymers allow to enhance the overall stability of those because of their aforementioned properties . The disadvantage is mainly the poor crystallization of complexes with pure phosphonate ligands. To avoid that problematic the use of bifunctional mixed carboxylate-phosphonate ligands is one solution to improve crystal growth and quality. The possible applications of CPs constructed from carboxy-phosphonates range from gas separation, recognition, proton conduction, luminescence, magnetism and others.[73]

The zinc carboxyphosphonate framework, $\{[Zn_3(pbdc)_2]\ 2H_3O\}n$ (H_4pbdc = 5-phosphonobenzene-1,3-dicarboxylic acid) shows high CO_2 adsorption and a remarkable CO_2 selection over N_2 at the same time.[74] Although the surface area detected by N_2 sorption was not significantly high, CO_2 could be adsorbed nonetheless.

It is a common observation in the area of porous metal phosphonates and carboxy-phosphonates, that surface areas are rather low compared to the corresponding carboxylates.[75]

With a piperidine based carboxylate-phosphonate linker, $H_2O_3PCH_2(NC_5H_9)COOH$, Zhang presented a cadmium (II) based 3D-network in 2009.[76] The complex has an open-framework structure and a thermal stability up to 320 °C.

Rueff *et al.* published a europium complex with luminescence properties and high thermal stability in 2009.[77] The prototypical carboxylate-phosphonate linker, the rigid 4-phosphono benzoic acid, was used by the group to synthesize the rare-earth metal complex. An ultra-high stability of 510 °C was established, which cannot be competed by carboxylate or pyrazolate linkers alone. The group proved, that a mixed-functional carboxylate-phosphonate linker allows to obtain a very stable complex, that has interesting properties, which was luminescence in that example.

An often observed phenomenon is that metal phosphonates crystallize as layered structures, which also occurs with bifunctional carboxylate-phosphonate linkers. In 2002 Clearfield *et al.* presented two structures with N-(phosphonomethyl)iminodiacetic acid as linkers, with which layered structures with cobalt and zinc were formed.[78] Because of the flexibility of this linker, it might not be possible to allow general predictions for other mixed carboxylate-phosphonate linkers. The two networks show strong intermolecular hydrogen-bond interactions. Hydrogen-bonded networks are a common motif for carboxylate-phosphonate and phosphinates, which was demonstrated by other groups in the past.[7980]

With presentation of this thesis no bifunctional phosphonate-pyrazolate linker, complex or molecule, that incorporates both functions, has been synthesized yet. How such a linker could look like is presented in the following scheme (Scheme 4).
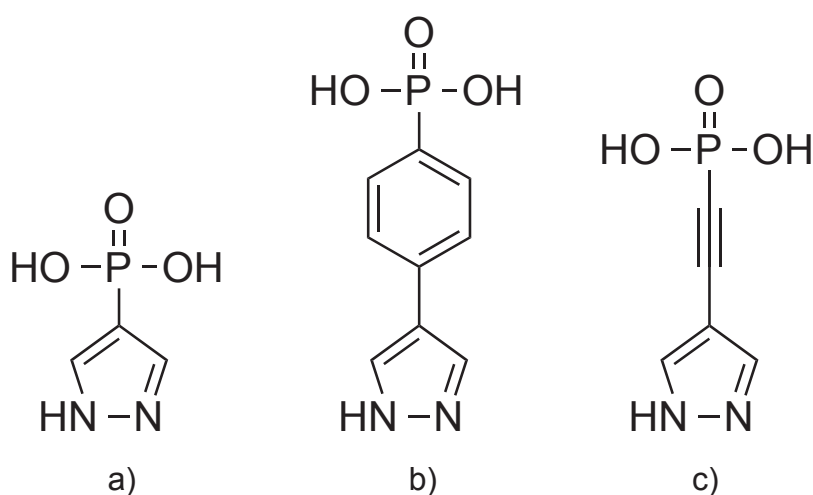
Scheme 4 Rigid pyrazole and phosphonic acid containing linkers, which incorporate both functions in 180° orientation: 1*H*-pyrazole-4-phosphonic acid (a), 4-(4'phosphonophenyl)-1*H*-pyrazole (b) and 4-posphonoethinyl-1*H*-pyrazole.

Complexes with both, pyrazole and phosphonate ligands are known, but rare. One example was published by Sheikh *et al.* in 2013,[81] an octadecanuclear copper (II) complex with bridging pyrazoles and phosphonate and pyridine ligands. A bifunctional ligand, which combines both groups, would give the chance to synthesize metal complexes that could be extremely stable, while being potentially porous due to rigid linker design.

With triazole and phosphonate, a bifunctional ligand has been published by Zhei *et al.* also in 2013,[82] which has shown a high stability in a complex with nickel in boiling water and furthermore at pH = 1 for seven days. It was also demonstrated, that CO_2 could be adsorbed in a significant amounts. The surface area was determined to be 430 m^2g^{-1} (BET).

While 1,2,4-triazole is a neutral group, the pyrazolate function as anionic donor is stronger in its coordination towards metals and together with the phosphonate function, having a charge of -3, would possibly allow to obtain three-dimensional complexes. The expected stability of such a complex is expected to be higher than the one of the triazole-phosphonate. Therefore, the combination of pz and -$PO(OH)_2$ in one linker could be the next step in design of ultra-stable MOFs.

1.3.4 Hydrogen bonded networks and Inclusion complexes

The formation of three-dimensional networks, in which hydrogen bonds are the dominating intermolecular interactions instead of covalent or coordinative bonds, has been investigated in recent studies.[83][84] Several properties are of interest, when hydrogen bonded networks are discussed, like proton conduction, sensors and catalysis. Also porous compounds are available, which has been demonstrated by Wuest and co-workers in 1997.[85] In 1996 Yaghi *et al.* synthesized metal-carboxylates from hydrogen-bonded metal complexes of btc.[86] The weaker H-bonds, compared to coordinative bonds, allow a somewhat simpler approach for the construction of metal-organic polymers, as the H-bond formation is reversible and to obtain at lower temperatures.

A variety of mixed salts and inclusion complexes with hexamine cobalt, $[Co(NH_3)_6]^{3+}$, are published so far, sharing the Co(III) centred, octahedrally ammonia coordinated cation with different, mostly aromatic anions, which bear preferably sulfonate and carboxylate groups.[87] Most of those complexes are insoluble, thermally stable compounds in which solvent or guest molecules are embedded between layers alternating charge. Because of the high charges of +3 for the Co cation complex and -3 for the anions, those complexes can be seen metal salts in which weak Coulomb interactions exist. The dominant force behind the formation of a three-dimensional motif is existence of hydrogen bonds. Published by Sevov *et al.* in 2007,[88] a series of inclusion complexes with different guest molecules has been synthesized with 4,4'-biphenyldisulfonate as anion. They

are similar to the guanidinium sulfonate complex, in which hydrogen bonds play an important role for stability.[89] Those pillar-layered structures could possibly be tailored to obtain flexible hydrogen-bonded complexes for certain applications.

Reddy has also demonstrated the potential of $[Co(NH_3)_6]^{3+}$ based sulfonate complexes as supramolecular host compounds, which do not only exhibit porosity, but are suitable for guest embedment or guest exchange as well.[90]

Nickel (II) complexes with inclusion properties are under investigation because of hydrogen-bonded coordination networks, wherein guest molecules can also be incorporated withn the cavities of such a structure. Published by Sekiya and Nishikiori in 2011, [91] nickel (II) hydrogen-bonded networks of the formula $[Ni(SCN)_2(pppeH)_2]_x$(guest) were synthesized, sharing different linkers and guest molecules . The authors could show that the guest molecule itself has a cavity size determining role, therefore being a templating agent. The three-dimensional network is built by hydrogen bonding between the acid functions of the ligands.

It can be assumed that not only MOF structures, but also hydrogen-bonded networks could find use as porous compounds in potential applications in the same way as it is expected for MOFs.

1.4   Scope of this work

The construction of new highly stable CPs and MOFs is the aim and scope of this work. Therefore strongly coordinating ligands, which combine carboxylate and pyrazolate or carboxylate and phosphonate as functional groups, shall be used to synthesize metal-organic compounds, which have certain desired properties, like an enhanced thermal stability, resistance against hydrolysis and which also have a high porosity for possible applications, which were listed in the introduction. The new compounds shall then be characterized in detail with standard and latest techniques and investigated with focus on their potential in applications.

2   Published work

This chapter contains the authors' publications as first author in chronological order, starting with the first publication of the author. The publications are presented as they appeared in the scientific, peer-reviewed journal, as full publications with their own reference lists and order for each. Figures, schemes and tables do not follow the numbering of the main text, but the numbering of the publication itself. Each publication is introduced by a short profile that contains the name of the journal, its impact factor, the authors' contribution to the work (%) and that of co-authors and an abstract.

The yet unpublished results are presented in chapter 3, unpublished work.

2.1 Bifunctional pyrazolate-carboxylate ligands for isoreticular cobalt and zinc MOF-5 analogs with magnetic analysis of the {Co$_4$(µ$_4$-O)} node

Christian Heering, Ishtvan Boldog, Vera Vasylyeva, Joaquín Sanchiz and Christoph Janiak

Abstract:

The ditopic ligands 3,5-dimethyl-pyrazolate-4-carboxylate, $^-$Me$_2$pzCO$^-$, and 4-(3,5-dimethyl-1H-pyrazol-4-yl)benzoate, $^-$Me$_2$pzC$_6$H$_4$CO$^-$, combine a pyrazolate and carboxylate functionality in axial orientation and lead to porous cobalt or zinc azolate–carboxylate frameworks that have the same cubic pcu-a topology and {M$_4$(µ$_4$-O)} nodes (M = Co, Zn) as MOF-5 and other IRMOFs. The microporous networks [M$_4$(µ$_4$-O)(Me$_2$pzCO$_2$)$_3$] (M = Co, Zn) with the short linker exhibit a solvent-induced gate effect, evidenced by gas desorption hysteresis due to small pore apertures of 2.8 Å diameter together with small amounts of high-boiling solvent remaining in the activated samples. For [Co$_4$(µ$_4$-O)(Me$_2$pzCO$_2$)$_3$], the low-pressure H$_2$ storage capacity (1.7 wt%, 1 bar , 77 K) is higher than for MOF-5, and the CO$_2$ uptake of 20.8 wt% puts it among the top MOFs for low-pressure CO$_2$ sorption even though the BET surface is less than 1000 m^{2}g^{-1}. The analysis of the magnetic properties of [Co$_4$(µ$_4$-O)(Me$_2$pzCO$_2$)$_3$] takes into account the distribution of tetrahedra resulting from the disorder of the pyrazolate–carboxylate linker. An antiferromagnetic coupling observed for [Co$_4$(µ$_4$-O)(Me$_2$pzCO$_2$)$_3$] arises from the interactions of the cobalt(II) ions through the combined µ$_4$-O + *syn–syn* carboxylate and µ$_4$-O + pyrazolate bridges.

Bifunctional pyrazolate–carboxylate ligands for isoreticular cobalt and zinc MOF-5 analogs with magnetic analysis of the {Co$_4$(μ$_4$-O)} node†‡

Christian Heering,[a] Ishtvan Boldog,[a] Vera Vasylyeva,[a] Joaquín Sanchiz[*b] and Christoph Janiak[*a]

The ditopic ligands 3,5-dimethyl-pyrazolate-4-carboxylate, $^-$Me$_2$pzCO$_2$$^-$, and 4-(3,5-dimethyl-1*H*-pyrazol-4-yl)benzoate, $^-$Me$_2$pzC$_6$H$_4$CO$_2$$^-$, combine a pyrazolate and carboxylate functionality in axial orientation and lead to porous cobalt or zinc azolate–carboxylate frameworks that have the same cubic *pcu-a* topology and {M$_4$(μ$_4$-O)} nodes (M = Co, Zn) as MOF-5 and other IRMOFs. The microporous networks [M$_4$(μ$_4$-O)(Me$_2$pzCO$_2$)$_3$] (M = Co, Zn) with the short linker exhibit a solvent-induced gate effect, evidenced by gas desorption hysteresis due to small pore apertures of 2.8 Å diameter together with small amounts of high-boiling solvent remaining in the activated samples. For [Co$_4$(μ$_4$-O)(Me$_2$pzCO$_2$)$_3$], the low-pressure H$_2$ storage capacity (1.7 wt%, 1 bar , 77 K) is higher than for MOF-5, and the CO$_2$ uptake of 20.8 wt% puts it among the top MOFs for low-pressure CO$_2$ sorption even though the BET surface is less than 1000 m^2 g^{-1}. The analysis of the magnetic properties of [Co$_4$(μ$_4$-O)(Me$_2$pzCO$_2$)$_3$] takes into account the distribution of tetrahedra resulting from the disorder of the pyrazolate–carboxylate linker. An antiferromagnetic coupling observed for [Co$_4$(μ$_4$-O)(Me$_2$pzCO$_2$)$_3$] arises from the interactions of the cobalt(II) ions through the combined μ$_4$-O + *syn–syn* carboxylate and μ$_4$-O + pyrazolate bridges.

Introduction

Metal–organic frameworks (MOFs) receive continuous attention[1,2] due to their high porosity that promises applications such as gas storage,[3,4] gas[5,6] and liquid[7] separation processes, drug delivery,[8] heterogeneous catalysis,[9] heat transformation,[10] *etc.*

Isoreticular (IR) MOFs with linear dicarboxylate linkers ($^-$O$_2$C–R–CO$_2$$^-$) and the {Zn$_4$O(O$_2$CR)$_6$} secondary building unit are attractive in their predictable design of the same *pcu-a* primitive cubic network featuring high surface areas and wide 3-D channel porosity.[12,13] MOF-5, [Zn$_4$O(BDC)$_3$] (BDC = benzene-1,4-dicarboxylate, terephthalate), is one of the best known MOFs,[14] has a high surface area (3000 m^2 g^{-1}) and has high thermal stability (up to 400 °C)[12] but low water stability.[15,16] Many MOFs cannot withstand prolonged contact with water or moisture at room temperature.[16] This is due to the

a Institut für Anorganische Chemie und Strukturchemie, Heinrich-Heine Universität Düsseldorf, Universitätsstraße 1, D-40225 Düsseldorf, Germany. E-mail: janiak@uni-duesseldorf.de
b Departamento de Quimica Inorgánica, Facultad de Quimica, C/ Astrofísico Francisco Sánchez s/n, La Laguna 38206, Tenerife, Spain. E-mail: jsanchiz@ull.es
† Electronic supplementary information (ESI) available: Details of syntheses and spectroscopic analysis, thermogravimetric and sorption studies. CCDC 937761–937763. For ESI and crystallographic data in CIF or other electronic format see DOI: 10.1039/c3ce41426d
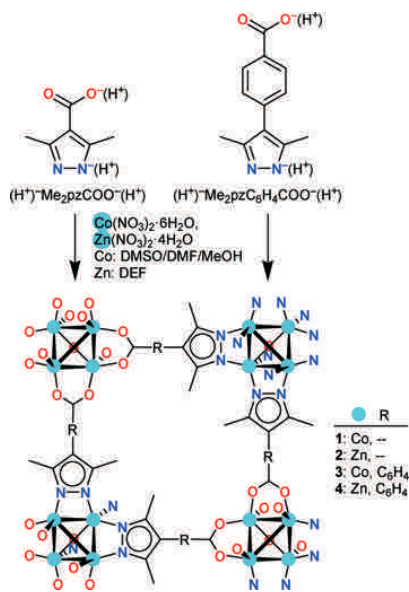‡ Dedicated to Prof. Dr. Bernt Krebs on the occasion of his 75th birthday.

hydrolysis of coordination bonds and often limits the practical use of these materials. Only a few MOFs have had their moisture/water stability proven with retention of porosity.[10,17,18] The development of hydrolytically stable MOFs is one important goal to advance MOFs to the application stage.[5,17] One of the most hydrolytically stable MOFs is ZIF-8, [Zn(2-methylimidazolate)$_2$],[16,19] which is stable in boiling water over a broad pH range, excluding only strongly alkaline conditions, and exceeds MIL-101[20] and UiO-66.[21] The hydrolytic stability of ZIF-8 can be associated with the greater basicity of the imidazolate linker, leading to higher covalency of the metal-to-azolate bonds[22] compared to carboxylates and with higher hydrophobicity of the ZIF-8 framework. Recent advances in pyrazolate MOFs[23] by Masciocchi, Navarro, Bordiga,[24] Long,[22] and Volkmer (MFU-1,2)[25] prove the high hydrolytic stability of novel hydrophobic bis-pyrazolate MOFs.[26]

There are few but pro mising reports on the utilization of bifunctional pyrazolate–carboxylate linkers. The 4-pyrazolate–carboxylate linker $^-$pzCO$_2$$^-$ has been employed in the synthesis of MOF-325 with {Cu$_2$(O$_2$C)$_4$} paddle wheel and trinuclear pyramidal {Cu$_3$(μ$_3$-O)(pz)$_3$} units as nodes.[27] A related 4-triazolate–carboxylate linker $^-$tzCO$_2$$^-$ gave the double-walled metal triazolate framework, MTAF-1, material with pentanuclear zinc clusters {Zn$_5$(μ$_3$-O)(tz)$_5$(O$_2$C)$_5$}.[28] A porous metal azolate framework MAF-X8 has been reported with the 4-(3,5-dimethyl-pyrazolate)benzoate linker with one-dimensional

channels and $Zn(\mu-O_2C)(\mu-pz)$ chains.[29] The 1,2,4-triazol-4-yl-isophthalate linker contains a neutral azole but also yields multinuclear copper and cobalt nodes in microporous MOFs.[30] A MOF-5 analog has been reported with the 3,5-dimethyl-pyrazolate-4-carboxylate linker $^-Me_2pzCO_2^-$ (Scheme 1) crystal and shown to exhibit remarkable hydrolytic, thermal, mechanical, and chemical stability.[31,32] The hydrolytic stability of the $[Zn_4(\mu_4-O)(Me_2pzCO_2)_3]$ framework was traced to its hydrophobic nature. The ligands $^-pzCO_2^-$ and $^-pzC_6H_4CO_2^-$ (cf. the ligands in Scheme 1 without the methyl groups) yielded isoreticular $[Ni_8(OH)_4(H_2O)_2(L)_6]$ frameworks.[26]

Here we utilize the two rigid linear ligands $^-Me_2pzCO_2^-$ and $^-Me_2pzC_6H_4CO_2^-$ with combined but differently spaced azolate and carboxylate functionality to assess the isoreticular principle for the synthesis of microporous Metal–Azolate–Carboxylate (MAC) frameworks with cobalt and zinc (Scheme 1).

Results and discussion

Solvothermal reaction of cobalt or zinc nitrate with 3,5-dimethyl-1H-pyrazole-4-carboxylic acid (HMe_2pzCO_2H) or 4-(3,5-dimethyl-1H-pyrazol-4-yl)benzoic acid ($HMe_2pzC_6H_4CO_2H$) yields small blue-violet (Co) or yellowish (Zn) crystals of cubic shape (Scheme 1, Fig. 1) (see ESI† for full syntheses details). Previously, $[Zn_4(\mu_4-O)(Me_2pzCO_2)_3]$ (2) was prepared in a basic ethanol medium as a microcrystalline material

Fig. 1 Scanning electron micrographs of (a) **1**, (b) **2**, (c) **3** and (d) **4**. The cubic morphology of **1** and **2** (cubic space group $F\bar{4}3m$) is identical to MOF-5 (cubic space group $Fm\bar{3}m$).[11] For color photographs of crystals and additional SEM pictures, see ESI†.

from which the structure was obtained by Rietveld refinement.[31] Here we used a solvent mixture (DMSO, DMF, and MeOH) for the Co analog **1** or DEF alone for **2** to obtain $[M_4(\mu_4-O)(Me_2pzCO_2)_3]$ (M = Co, Zn) as single crystals, which were also susceptible to single-crystal X-ray diffraction analysis.

Solid-state structural studies

Compounds of Co (**1**) and Zn (**2**) with the short pyrazolate–carboxylate linker are isostructural (cf. Table 2) and of the same cubic topology and have the same tetrahedral $\{M_4(\mu_4-O)(pz/O_2C)_3\}$ node (M = Co, Zn) as in MOF-5 (Fig. 2, Fig. S23 in ESI†). The previous Rietveld refinement of compound **2** gave the cubic space group $Fm\bar{3}m$.[31] The six edges of the oxido-metal tetrahedron $\{M_4(\mu_4-O)\}$ are bridged by either the carboxylate or the pyrazolate group of the ligand. Each 3,5-dimethyl-pyrazolate-4-carboxylate ligand bridges between two $\{M_4(\mu_4-O)\}$ clusters, just like the terephthalate ligand in MOF-5.

The pyrazolate–carboxylate ligand is disordered (Fig. 2a), and each $\{M_4(\mu_4-O)\}$ cluster has a mixed pyrazolate/carboxylate coordination environment (cf. Fig. 9). The fixed alternating canting of the dimethylpyrazolate ring plane (Fig. 2a) leads to alternating small (van der Waals diameter, Ø ~6 Å) and large pores (Ø ~11 Å) connected by small channels or pore apertures (Ø ~2.8 Å) (Fig. 2c).

Frameworks of Co (**3**) and Zn (**4**) with the long pyrazolate–benzoate ligand are also isostructural to each other (by X-ray powder diffraction, cf. Fig. S26†) and again of near cubic topology and with the tetrahedral $\{M_4(\mu_4-O)(pz/O_2C)_3\}$ node (M = Co, Zn) as in carboxylate IRMOFs[12] (Fig. 3). Thus, elongation of rigid bifunctional pyrazolate–carboxylate linkers appears to follow the isoreticular priniciple.[12]

Scheme 1 Bifunctional pyrazolate–carboxylate ligands and derived cubic metal–azolate–carboxylate frameworks (extension into the third dimension is not shown for clarity, cf. Fig. 1). Note that the edges of the tetrahedral $\{M_4(\mu_4-O)\}$ nodes will be statistically bridged by both carboxylate or pyrazolate groups as indicated in the lower half of the sketched framework (cf. Fig. 9).
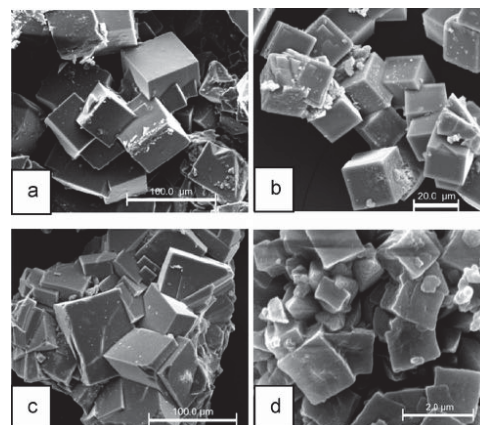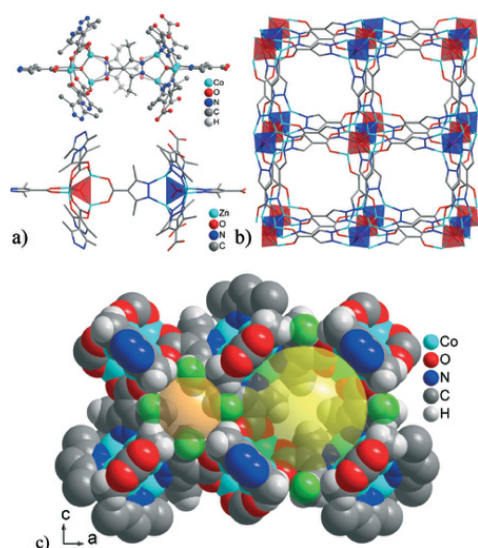
16

Fig. 2 Building unit (a) and framework (b) in [M$_4$(μ$_4$-O)(Me$_2$pzCOO)$_3$] (M = Co, **1**; Zn, **2**) as MOF-5-analogs with the pyrazolate–carboxylate ligand (*cf.* Scheme 1). The central ligand in (a) illustrates the ligand disorder. For graphic simplicity, an idealized pyrazolate-only and carboxylate-only coordination for alternating {M$_4$O} clusters in the framework (b) is depicted with all-oxygen coordination as red and all-nitrogen coordination as blue tetrahedra; methyl groups and hydrogen atoms are not shown in (b). A space-filling plot in (c) shows the alternating small (transparent orange sphere, diameter, Ø = 6 Å) and large (yellow sphere, Ø = 11 Å) cavities due to the alternating pyrazolate plane orientation with pore apertures (green spheres, Ø = 2.8 Å) in between.

We note that numerous crystallization experiments to obtain single crystals of **3** of suitable large size gave at best crystals of about 0.01 × 0.01 × 0.01 mm, which were at the manageable limit for an X-ray diffractometer even when equipped with a microfocus source. Still, a representative X-ray data set could be obtained for **3**, even though the small crystal size and high absorption coefficient of Co atoms limited the 2θ angle to 80° for Cu-Kα radiation and the data set quality.

Porosity and gas sorption

According to the X-ray structure (*cf.* Fig. 2, Fig. S24†), the pore openings in the isostructural compounds **1** and **2** are very narrow. Thus, the traditional solvent exchange procedure, through soaking in a low-boiling solvent (like MeOH, CH$_2$Cl$_2$), was regarded ineffective. Hence, activation of **1** and **2** was carried out by direct high-temperature degassing. The thermogravimetric (TG) analyses of **1** and **2** (Fig. S13 and S16,† respectively) revealed that complete loss of solvent guest molecules should be finished at temperatures of ~300–350 °C at atmospheric pressure. Samples of **1** were degassed at different temperatures in ~10^{-6} bar vacuum, and H$_2$ adsorption was measured in order to determine the optimum degassing conditions for both **1** and
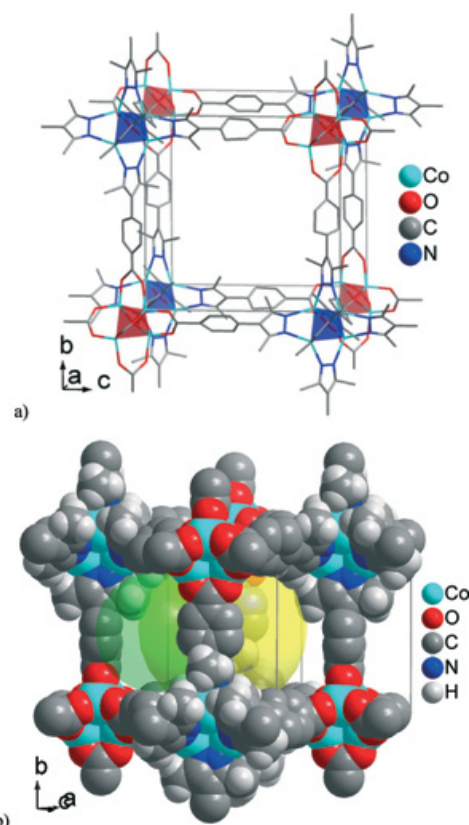

Fig. 3 (a) Framework in [M$_4$(μ$_4$-O)(Me$_2$pzC$_6$H$_4$CO$_2$)$_3$] (M = Co, **3**; Zn, **4**) as IRMOF analogs with the pyrazolate–benzoate ligand (*cf.* Scheme 1). The ligands are crystallographically disordered by a C$_2$ symmetry operation, which is detailed in Fig. S25.† An idealized pyrazolate-only (blue) and carboxylate-only (red tetrahedra) coordination for {M$_4$O} clusters is depicted. (b) Space-filling plot for **3** showing the large cavity (yellow transparent sphere, Ø = 14 Å) and one of the pore apertures (green transparent sphere, Ø = 10 Å).

2. For **1** degassed at 190 °C, an H$_2$ adsorption of 145 cm^3 g^{-1} at STP (standard temperature and pressure) was found; at 220 °C, an H$_2$ adsorption of 188 cm^3 g^{-1} was observed; and at 250 °C, an H$_2$ adsorption of 193 cm^3 g^{-1} was obtained (*cf.* Fig. 5). TG analysis of a sample degassed at a temperature of 250 °C confirmed the complete removal of guest molecules, and this degassing condition was used for subsequent gas sorption measurements for both **1** and **2**. Still, N$_2$ is not adsorbed even on these optimally degassed samples of **1** and **2** at 77 K. This is presumably due to activated diffusion effects associated with the low thermal energy of N$_2$ relative to the high barrier for diffusion through the small 2.8 Å diameter pore apertures (*cf.* Fig. 2c). In other words, at slow thermal motion at 77 K, the N$_2$ molecule will statistically only seldom approach the small

17

pore aperture with the correct orientation for penetration, that is, at right angle with its molecule axis. It is a frequently encountered phenomenon of kinetic hindrance of small pores or pore aperture windows (cf. Fig. S24†) that N_2 adsorption (kinetic diameter, 3.64 Å) at 77 K does not occur, while H_2 at 77 K or CO_2 at 273 K is adsorbed (see below).[33] Therefore, argon sorption experiments at 87 K were carried out for an experimental surface area determination of **1** (Ar diameter, 3.4 Å) (Fig. 4). The start of the argon adsorption branch for **1** is very steep and follows a type I isotherm with most of the argon adsorbed below 0.05 P/P_0 (Fig. 4a). The adsorption at higher relative pressure is irreversible due to small pore openings, which gives rise to an open-loop hysteresis because of a gate effect (see below). BET and Langmuir surface areas were found to be 760 and 840 m^2 g^{-1}, respectively (from $0.02 < P/P_0 < 0.1$), with 0.32 cm^3 g^{-1} pore volume (at $P/P_0 = 0.95$). A DFT calculation gave a narrow pore diameter distribution with the maximum at ~12 Å (Fig. 4b) in good agreement with the cavity diameter of ~11 Å from the structural data (Fig. S24†).

For the microcrystalline zinc compound **2**, which was previously synthesized in basic ethanol, a BET surface area of 840 m^2 g^{-1} together with a micropore volume of 0.45 cm^3 per cm^3 of **2** had been reported from an N_2 adsorption isotherm
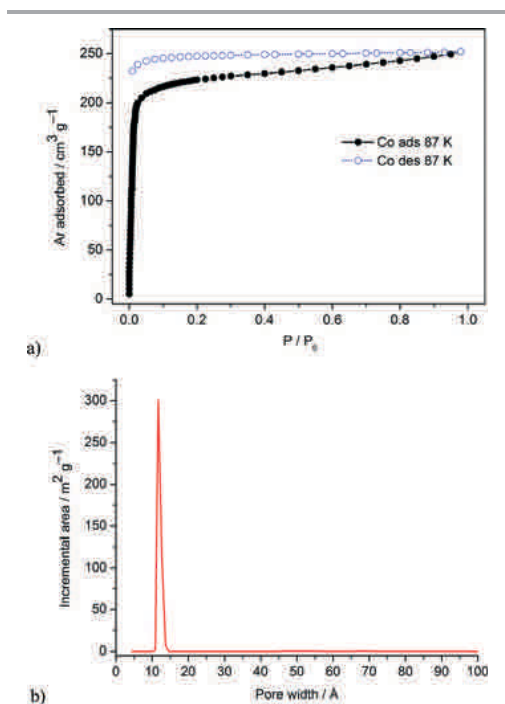

Fig. 4 (a) Argon sorption isotherms and (b) pore size distribution curve from DFT calculation (Ar on carbon, slit based model) based on argon adsorption isotherm for **1**.
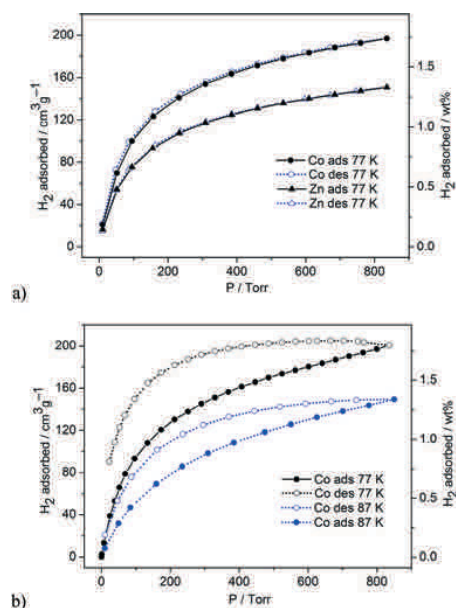

Fig. 5 (a) Hydrogen sorption isotherms for **1** (Co) and **2** (Zn) at 77 K. The samples were degassed at 250 °C for 10 h (Co) and 220 °C for 15 h (Zn) until the pressure rise rate was approximately 3 μTorr min^{-1}. No significant additional weight loss was registered. (b) Hydrogen sorption isotherms for **1** at 77 K and 87 K. Note the hysteresis due to hindered desorption. A similar type of broad desorption hysteresis was observed in NOTT-200.[36] The maximum amount of adsorbed H_2 at ~1.1 bar of 200 cm^3 g^{-1} corresponds to 1.75 wt%.

at 77 K.[31] The similar surface area for **1** and **2** suggests an optimal degassing of **1**. We considered a different N_2 adsorption behavior at 77 K for the larger crystallite size of **1** and **2** from the solvothermal synthesis conditions of our samples. In the larger crystals, the thermodynamic adsorption equilibrium may take a longer time to be reached because of the small pore apertures (Ø = 2.8 Å, cf. Fig. 2). We note that the sorption isotherms can deviate from ideal equilibrium experiments as pronounced kinetic effects occur because of the small channel size. Such effects were even seen in the case of H_2 sorption (kinetic diameter, 2.9 Å), depending on the sample preparation. We already stated that sorption studies with H_2 indicated that a larger amount of gas was adsorbed as degassing temperatures were increased, and therefore, a larger pore volume became accessible for guest molecules. Furthermore, samples used for H_2 sorption after long (10–15 h) degassing time did not display a hysteresis (Fig. 5a), while samples with shorter degassing time (2 h) featured a desorption hysteresis (Fig. 5b) even though the maximum amount of adsorbed H_2 at ~1.1 bar is identical (200 cm^3 g^{-1} or 1.75 wt%). We trace this to channel blocking by residual solvent molecules as a solvent guest-induced gate effect. Normally, a gate effect is associated with structural flexibility in a MOF, with the guest

18

Table 1 H_2, CO_2 and CH_4 uptake of **1** and **2** at 1 bar

Compd	$H_2{}^a$ / wt%	$CO_2{}^b$ cm³ g⁻¹/mmol g⁻¹	g g⁻¹/wt%	$CH_4{}^b$ cm³ g⁻¹/mmol g⁻¹	g g⁻¹/wt%
1	1.70	134.4/5.5	0.26/20.8	41.1/1.8	0.03/2.9
2	1.35	84.4/3.46	0.16/14.3	26.0/1.1	0.02/1.9

^{a} H_2 uptake at 77 K. ^{b} Gas uptake at 273 K.

causing the closed–open structural transformation.[34] Also, flexible side groups on the linker can act as molecular gates for guest molecules in MOFs.[35]

The gravimetric H_2 storage capacity of 1.7 wt% in **1** and 1.35 wt% in **2** at 1 bar (Table 1) is higher than or equal to values in many reports for MOF-5 (1.15–1.35 wt% at 1 bar, 77 K, BET surface area of 2885–3362 m² g⁻¹) and other higher surface area MOFs.[3b] From two adsorption isotherms acquired at different temperatures (Fig. 5b), the differential heat of adsorption $\Delta H_{ads,diff}$ in **1** is determined to be 5–6 kJ mol⁻¹ (see ESI†). $\Delta H_{ads,diff}$ for H_2 in **1** is higher than for MOF-5 (3.8–4.8 kJ mol⁻¹) and ZIF-8 (4.5 kJ mol⁻¹),[3b] which is traced to the small pore and channel size in **1**. While N_2 is not adsorbed at 77 K, CO_2 and CH_4 are adsorbed at 273 K (Table 1, Fig. S30†). The CO_2 adsorption capacity of 20.8 wt% puts **1** among the top MOFs for low pressure CO_2 sorption, exceeding the values for most Zn–carboxylate MOFs.[5a,37]

We suggest that the passage of CO_2 and CH_4 guest molecules (kinetic diameters, 3.3 and 3.8 Å, respectively) in and out of the cavities through the pore apertures of ~2.8 Å diameter proceeds by a temporary expansion of the window size.[38,39] The selectivity for CO_2 over CH_4 (Table S2†) can be ascribed to the combined effects of the size of the pore apertures and the strong quadrupolar interactions of CO_2 with nitrogen atoms present on the pore surface. The quadrupole moment of CO_2 (CO_2: 14.3 × 10⁻⁴⁰ cm², N_2: 4.65 × 10⁻⁴⁰ cm², CH_4: none)[40] leads to a stronger electrostatic interaction with the framework and can have a distinct effect on framework flexibility in that it induces a dynamic window-widening process through a concerted ligand tilt to allow gas molecules to pass.[3,5] The cobalt framework **1** consistently exhibits a higher gas uptake than the zinc framework **2** (Table 1, Fig. 5, and Fig. S30†). Both frameworks are isostructural with essentially identical estimated pore volumes and apertures from the X-ray structure. We have to assign the higher sorption capacity of **1** to its easier and better activation in line with the thermogravimetic analyses (see Fig. S13 and S16 in ESI†).

The MAC frameworks **3** and **4** with the longer pyrazolate–benzoate were able to adsorb N_2 at 77 K with a type I isotherm for microporous materials (Fig. 6, Fig. S31†). From these, the BET surfaces were calculated to be 1072 m² g⁻¹ for the cobalt compound **3** and 980 m² g⁻¹ for the zinc compound **4** (Table S1†).

Water stability

Water and chemical stability of compound **2** was investigated in the work by Montoro *et al.* because of the sought practical applications.[31] Stabilities were tested by suspending **2** in water at room temperature and in boiling benzene or MeOH for 24 h. No changes were noticed when comparing the powder X-ray diffractograms to the as-synthesized sample of **2**. Also, thermodiffractometric measurements in air indicated thermal robustness of **2**, with decomposition beginning only at 773 K.[31] Montoro *et al.* also found that H_2O adsorption in **2** at 298 K takes place only at very high relative pressures ($P/P_0 >$ 0.7), which is indicative of a highly hydrophobic nature of the material to which they assign the overall water stability.[31]

Cychosz and Matzger argued convincingly that it is important to assess water stability in the liquid phase explicitly.[17] Previous studies on MOF water stability have focused on exposure to water in the gas phase. Yet, it has been shown in the literature that gas phase adsorption is not a good predictor for liquid phase behavior.[7,41] Cychosz and Matzger tested the effect of water concentration for a series of MOFs. Powder X-ray diffraction (PXRD) was used to determine if the structure remains untransformed with increasing water concentration or at what water concentration the structure began to change. In a typical experiment, the as-synthesized MCP was placed in fresh DMF and defined aliquots of deionized water were added to the solution sequentially. Between aliquots, the mixture was agitated at room temperature on a shaker for 1 h.[17] We decided to follow this protocol to test the water stability of **1–4** (Fig. 7).

A water stability test[17] of the zinc complexes **2** and **4** in comparison to MOF-5 revealed a higher stability for the pyrazolate–carboxylate frameworks. Immersing crystals in a different mixture of water–DMF for 1 h did not show any structural changes by powder X-ray diffraction (Fig. 7), while for MOF-5, a
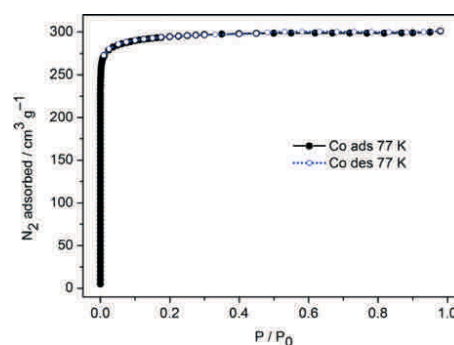

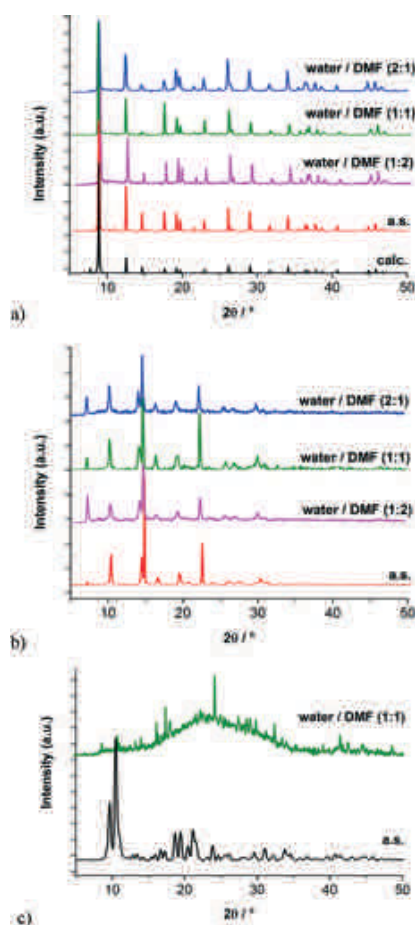**Fig. 6** N_2 sorption isotherms for **3**.

19

Fig. 7 Water stability tests by comparison of powder X-ray diffraction patterns of (a) **2**, (b) **4** and (c) MOF-5 (calc = calculated from single-crystal data, a.s. = as synthesized and after 1 hour treatment with water/DMF at different v : v ratios).

Magnetic properties of 1

The magnetic properties of MOFs and coordination polymers are of continuous interest.[2,42–44] The ground state of Co(II) ions (d^7) in a tetrahedral environment is $^4A_2$, for which the orbital angular momentum contribution is a second-order effect, and so, the spin-only model can be used to describe the magnetic behaviour of compound **1**.[45] Fig. 8 shows the temperature dependence of the $\chi_M T$ product for **1**. At room temperature, the $\chi_M T$ product has a value of almost 5.0 cm^3 mol^{-1} K, which is lower than expected for four isolated spin quartets, and it continuously decreases on lowering temperature, reaching a value of 0.50 cm^3 mol^{-1} K at 2.0 K (the value expected at room temperature in the spin-only model for four cobalt(II) ions is $4 \times (N\beta^2 g^2/3kT)S(S + 1) = 9.075$ cm^3 mol^{-1} K with $g = 2.2$ and $S = 3/2$). The behavior shown is indicative of a dominant antiferromagnetic interaction in compound **1**.

According to the tetrahedral structure of the $\{Co_4(\mu_4\text{-O})\}$ clusters, as a first approach, the magnetic properties are investigated by means of an isotropic Heisenberg–Dirac–Van Vleck Hamiltonian formalism, in which J is the exchange coupling constant and $\hat{S}_i$ the spin operator of the centre i (eqn (1)).

$$\widehat{H}_{HDVV} = -J(\hat{S}_1\hat{S}_2 + \hat{S}_1\hat{S}_3 + \hat{S}_1\hat{S}_4 + \hat{S}_2\hat{S}_3 + \hat{S}_2\hat{S}_4 + \hat{S}_3\hat{S}_4) \qquad (1)$$

In this model, all the tetrahedra are considered to be equivalents, and so the coupling through the pyrazolate and through the *syn–syn* carboxylate groups is assumed to be identical (which is a rough approximation). The Eigenvalues for such a system can be obtained with the following coupling scheme in which $S_A = S_1 + S_2$, $S_B = S_3 + S_4$, $S = S_A + S_B$ and $S_1 = S_2 = S_3 = S_4 = 3/2$ (eqn (2)).

$$E = -\frac{J}{2}\left[S(S+1) - \sum_{i=1}^{4} S_i(S_i +1) \right] \qquad (2)$$

The splitting of the energy levels, the degeneracy and the corresponding spin are shown in Fig. 8b, and the equation (eqn (3)) for the susceptibility is then

$$x = \left(N\beta^2 g^2/(3kT)\right)\left[\frac{54e^{J/kT} + 330e^{3J/kT} + 840e^{6J/kT} + 1080e^{10J/kT} + 990e^{15J/kT} + 546e^{21J/kT}}{4 + 27e^{J/kT} + 55e^{3J/kT} + 70e^{6J/kT} + 54e^{10J/kT} + 33e^{15J/kT} + 13e^{21J/kT}}\right] \qquad (3)$$

ratio of 1 : <4 (water–DMF) already induced hydrolysis (Fig. 7c).[17] In comparison, the same hydrophobic network with cobalt in compound **1** showed pronounced decomposition after 1 h in a 1 : 1 water–DMF mixture (Fig. S27 in ESI†). This indicates that the hydrophobic nature of the framework alone will not prevent hydrolysis if the metal–ligand bonds are sufficiently labile. Thermogravimetric analysis shows that framework decomposition starts only above 350–400 °C (Fig. S13, S16, S19 and S22 in ESI†).

The best-fit parameters to this model are $J = -14.70$ cm^{-1}, $g = 1.84$, and $R = 1.22 \times 10^{-2}$, and it can be seen that the theoretical plot does not match very well with the experimental values, and the value of g is lower than expected.[46] The reason for the deviation is evidently the fact that the pyrazolate and *syn–syn* carboxylate bridges mediate, in a different way, the magnetic interaction in addition to the μ_4-oxo group, and so the model is oversimplified. Moreover, for this model, it can be observed that the ground state in
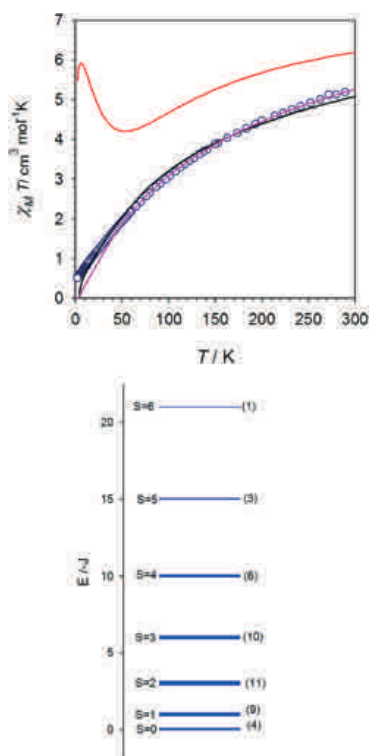
20

Fig. 8 Temperature dependence of the $\chi_M T$ product for complex **1**, blue circles. The black solid line is the theoretical plot for a tetrahedron with one magnetic coupling constant. The pink solid line is the theoretical plot considering two tetrahedra each with a different magnetic coupling constant. The red line corresponds to the theoretical model for a single tetrahedron with two different magnetic coupling constants. (b) Energy diagram for the spin states of the regular tetrahedron of spin quartets.

the case of antiferromagnetic interactions is $S = 0$, which exhibits a four-fold degeneracy. This means that on lowering the temperature, the magnetic moments of the cobalt(II) ions would cancel each other and the $\chi_M T$ product should tend to zero. But the experimental magnetic susceptibility values do not tend to zero on lowering temperature, which is an additional deviation of the model.

A better approximation to the problem would consider magnetic interactions through the carboxylate and pyrazolate bridges, but without disorder in the pyrazolate–carboxylate linker. Therefore, 50% of the tetrahedra would be $\{M_4(\mu_4\text{-O})(pz)_6\}$, and the other 50% would be $\{M_4(\mu_4\text{-O})(O_2C)_6\}$. This way, we would have two different kinds of tetrahedra, each with a different magnetic coupling constant J_1 and J_2. The expression for the magnetic susceptibility can be easily derived from eqn (3). The best-fit parameters for this model are $J_1 = -13.29$ cm^{-1} and $J_2 = -71.24$ cm^{-1}, $g = 2.18$ and $R = 1.2 \times 10^{-4}$.

This model gives a much better match for the theoretical plot, and the values of g and J_1 and J_2 seem reasonable. However, the theoretical curve deviates again at low temperatures since for this model, the ground state, and the only one populated at low temperatures, is again $S = 0$.

There are many magneto-structural studies which involve separately μ-oxo, *syn–syn* carboxylate and pyrazolate bridges.[45,47] When they occur separately, *syn–syn* carboxylate and pyrazolate bridges mediate moderate antiferromagnetic coupling, and the μ-oxo bridges also mediate antiferromagnetic interactions for angles larger than 97° (we have 109.6° in **1**).[48] However, there is a lack of magneto-structural studies in combined μ$_4$-oxo + *syn–syn* carboxylate and μ$_4$-oxo + pyrazolate bridges with Co(II) ions in tetrahedral surroundings, and just a few studies can be found for other cations such as Cu(II),[49,50] Ni(II)[51] or Co(II)[52] in octahedral surrounding. In those studies, antiferromagnetic interactions are found for large M–O–M angles,[49,51] which is the case of compound **1**. (Although ferromagnetic coupling is found for octahedral Co(II) ions with μ$_2$-oxo + *syn–syn* carboxylate, the environment of the Co(II) ion is critical since the ground term for an octahedron is $^4T_{1g}$ and that of a tetrahedron is $^4A_2$. This implies a different location of the unpaired electrons and very different orbital angular momentum contribution.)[52–54] Moreover, antiferromagnetic interactions have been observed in other Co(II) compounds with very similar μ$_4$-oxo + *syn–syn* carboxylate bridges, so antiferromagnetic interactions are expected.[55,56] However, we cannot assign unambiguously the values of J_1 and J_2 to any of the bridges.

The definitive model to study the magnetic properties of compound **1** should consider the disorder in the pyrazolate–carboxylate linker. This disorder causes the six edges of the metal tetrahedron to be randomly bridged by either the carboxylate or the pyrazolate groups, which leads to the occurrence of tetrahedra having, from six to zero and from zero to six, *syn–syn* carboxylate and pyrazolate bridges, respectively. The probability of each kind of tetrahedron is shown in Fig. 9. Of course, such a study is not feasible: we would need to solve separately the Hamiltonian (by diagonalizing the 256×256 matrix) for each tetrahedron (15 in total), calculate the numerical expression for the susceptibility for each one and include them with their correct weight in a full expression to calculate J_1 and J_2 simultaneously. This full study is beyond our purpose, and probably, there are other compounds more simple to investigate the magnetic properties of cobalt(II) ions bridged by combined μ$_4$-O and *syn–syn* carboxylate and pyrazolate bridges. Nevertheless, this analysis of the topology of the tetrahedra will allow us to understand why the $\chi_M T$ product does not tend to zero at low temperatures, and we will explain it focusing on one of the $\{Co_4(\mu_4\text{-O})(pz)_3(O_2C)_3\}$ tetrahedra.

One of those $\{Co_4(\mu_4\text{-O})(pz)_3(O_2C)_3\}$ tetrahedra has one cobalt(II) ion with three *syn–syn* carboxylate bridges connecting this cobalt(II) ion with its three nearest neighbors (encircled in Fig. 9a). Let us assume that the coupling through this *syn–syn* carboxylate bridge is the strongest one with $J_1 = -71.24$ cm^{-1}.
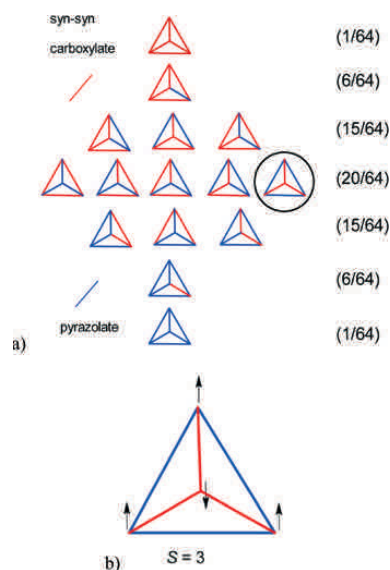
21

Fig. 9 Statistic distribution of the randomly bridged {Co$_4$(μ_4-O)(pz/O$_2$C)$_6$} tetrahedra. Blue edges correspond to pyrazolate bridges and red ones to *syn–syn* carboxylate. (b) The ground state S = 3 is expected for the selected tetrahedron on the basis of the stronger antiferromagnetic coupling through the *syn–syn* carboxylate with respect to the pyrazolate bridge (which is frustrated). Other tetrahedra may also exhibit S ≠ 0 ground states or at least S ≠ 0 populated states at low temperatures.

As the coupling through this bridge is stronger than the coupling through the pyrazolate bridge, the former predominates, whereas the latter is frustrated, and the resulting situation leads to a $S = 3$ ground state. As we have four vertices in a tetrahedron, 4/64 of the total of tetrahedra will have this arrangement, and so at least 6.25% of the clusters will not have a $S = 0$ as ground state, and therefore, at low temperatures, the experimental $\chi_M T$ product would not tend to zero. We can simulate the $\chi_M T$ product for other tetrahedra, and we can see that only the two with all six magnetic coupling identical have a $\chi_M T$ product which tends to zero; all the rest tend to positive values, so the positive value of the $\chi_M T$ product at low temperatures is a consequence of the disorder in the linker. On the other hand, compounds with similar structure and with just one kind of bridge have experimental $\chi_M T$ plots which tend to zero.[54]

Conclusions

In summary, we have presented here four isoreticular Metal–Azolate–Carboxylate (MAC) frameworks based on {M$_4$(μ_4-O)} nodes (M = Co, Zn) with ligands combining a pyrazolate and carboxylate functionality at two different lengths. The four MACs feature the cubic *pcu-a* topology as in MOF-5 and

analogous IRMOFs. The Zn frameworks are stable in water–DMF mixtures for at least one hour. Small pore apertures and inner BET surface areas <1000 m^2 g^{-1} in the MACs with the short 3,5-dimethyl-pyrazolate-4-carboxylate ligand still yield a H$_2$ and CO$_2$ uptake, higher than MOF-5 with three times BET surface area. The compounds are thermally stable up to 350–400 °C. The antiferromagnetic coupling observed for **1** arises from the interactions of the cobalt(II) ions through the combined μ_4-O + *syn–syn* carboxylate and μ_4-O + pyrazolate bridges.

Experimental section

Synthesis and spectroscopic analysis details of the ligands and compounds **1**–**4** are given in the ESI.†

Powder X-ray diffraction (PXRD) measurements

Powder X-ray diffraction (PXRD) measurements were carried out on samples at ambient temperature with a Bruker D2 Phaser using a flat silicon, low background sample holder and Cu-K$_\alpha$ radiation (λ = 1.54184 Å) at 30 kV and 0.04° s^{-1}. Simulated PXRD patterns were calculated from single-crystal data using the MERCURY 3.0.1 software suite from CCDC.

Gas sorption measurements

Sorption isotherms were measured using a Micromeritics ASAP 2020 automatic gas sorption analyzer equipped with oil-free vacuum pumps (ultimate vacuum <10^{-8} mbar) and valves, which guaranteed contamination-free measurements.

For the sorption measurements, 30 to 100 mg of freshly synthesized samples were subjected to a solvent-removal procedure and were processed immediately afterwards. After filtration and washing with small amounts of the same solvent as used for synthesis, the samples were pre-dried at a vacuum of 10^{-3} Torr and stored under nitrogen.

The dried samples were transferred to nitrogen-filled and pre-weighed sample tubes capped with a septum. The tube was immediately purged with nitrogen after the transfer and the solvent removed with a syringe and through drying in vacuum (~10 Torr), which was followed by a control weighing. Then the sample was connected to the preparation port of the sorption analyzer and degassed under vacuum until the outgassing rate, *i.e.*, the rate of pressure rise in the temporarily closed manifold with the connected sample tube was less than 2 μTorr min^{-1} at the specified temperature (70–250 °C). Typically, the samples were degassed for over 24 h in a vacuum of 10^{-5} to 10^{-6} bar and 200 °C. No solvent exchange process was carried out before degassing (see below). After their synthesis, the samples were only washed with DMF or DEF.

According to the X-ray structural data (*cf.* Fig. 2), the pore openings in the isostructural compounds **1** and **2** are very narrow. Therefore, the traditional solvent exchange procedure, through soaking in a low-boiling solvent (like MeOH, CH$_2$Cl$_2$), was regarded ineffective. Hence, activation of **1** and **2** was carried out by direct high-temperature degassing (see

22

above). Thermogravimetric analyses of **1** and **2** (Fig. S13 and S16,† respectively) revealed that complete loss of solvent guest molecules should be finished at temperatures of ~300–350°C at atmospheric pressure. Samples of **1** were degassed at different temperatures in ~10^{-6} bar vacuum, and the H_2 adsorption was measured in order to determine the optimum degassing conditions for both **1** and **2**. For **1** degassed at 190 °C, an adsorption of 145 cm^3 H_2 at STP (standard temperature and pressure) was found, at 220 °C, an H_2 adsorption of 188 cm^3 and at 250 °C of 193 cm^3 was obtained. TG analysis of a sample degassed at a temperature of 250 °C confirmed the complete removal of guest molecules, and this degassing condition was used for subsequent gas sorption measurements for both **1** and **2**.

After weighing, the sample tube was then transferred to the analysis port of the sorption analyzer. All used gases (H_2, Ar, N_2, CO_2, CH_4) were of ultra high purity (UHP, grade 5.0, 99.999%), and the STP volumes are given according to the NIST standards (293.15 K, 101.325 kPa). Helium gas was used for the determination of the cold and warm free space of the sample tubes. H_2 and N_2 sorption isotherms were measured at 77 K (liquid nitrogen bath), whereas CO_2 and CH_4 sorption isotherms were measured at 293 ± 1 K (passive thermostating) and 273.15 K (ice/deionized water bath). The determination of the heat of adsorption values using the Clausius–Clapeyron equation and the DFT calculations ('N_2 DFT slit pore' model) were done using the ASAP 2020 v3.05 software.

Some of the secondary measurements, specified in the description, were performed using a Quantachrome iQ MP or NOVA automatic sorption analyzer. The DFT calculations, *e.g.*, for the pore size distribution curves were carried out using the native ASiQWin 1.2 software employing the N_2 at 77 K on carbon, slit pore, NLDFT equilibrium model.[57–59]

Water stability tests

The water stability test performed here followed the procedure by Cychosz and Matzger.[17] Sample preparation was done using the same parameters and equipment as used in the literature procedure. For direct comparison, MOF-5 was synthesized by us[14] to assess its water stability in direct comparison. In the literature, the PXRD patterns of MOF-5 already indicate decomposition at a (v:v) water–DMF ratio of 1:2.[17]

X-ray crystallography

Suitable single crystals were carefully selected under a polarizing microscope.

Data collection. Compound **1** and **2**: Super Nova A from Agilent Technologies with microfocus tube, Cu-Kα radiation (λ = 1.54178 Å), 293 ± 2 K; ω-scans, mirror system. Data collection, cell refinement and data reduction with CrysAlisPro, experimental absorption correction using spherical harmonics, implemented in SCALE3 ABSPACK scaling algorithm.[60] Compound **3**: Bruker Kappa APEX2 CCD diffractometer with

Table 2 Crystal data and structure refinement

Compound	1	2	3
Empirical formula	$C_{18}H_{18}Co_4N_6O_7{}^a$	$C_{18}H_{18}N_6O_7Zn_4{}^b$	$C_{36}H_{30}Co_4N_6O_7{}^c$
M/g mol^{-1}	666.11	691.87	884.30
Crystal size/mm	0.13 × 0.11 × 0.11	0.12 × 0.12 × 0.12	0.01 × 0.01 × 0.01
2θ range/°	8.8–132.72	8.82–132.52	6.18–80.16
h; k; l range	−8,23; −4,16; −23,21	−15,11; −15,23; −21,16	±11, ±11, −10,11
Crystal system	Cubic	Cubic	Orthorhombic
Space group	$F\bar{4}3m$ (no. 216)	$F\bar{4}3m$ (no. 216)	$P222$ (no. 16)
a/Å	20.1090(7)	20.071(3)	14.242(3)
b/Å	20.1090(7)	20.071(3)	14.278(3)
c/Å	20.1090(7)	20.071(3)	14.2332(4)
V/Å^3	8131.5(5)	8085.4(18)	2914.5(12)
Z	8	8	1
D_{calc}/g cm^{-3}	1.088	1.137	0.504
F (000)	2656	2752	442
μ/mm^{-1}	12.829	2.964	4.529
Max/min transmission	0.307/0.196	1.000/0.816	0.748/0.458
Reflection collected (R_{int})	1559 (0.0354)	1275 (0.0425)	6548 (0.0890)
Data completeness/%	99.0	99.3	95.3
Independent reflections	641	604	1690
Parameters refined	54	54	130
Max/min $\Delta\rho^d$ /e Å^{-3}	1.341/−0.668	0.47/−0.50	0.230/−0.159
R_1/wR_2 [$I > 2\sigma(I)$]^e	0.0723/0.2078	0.0376/0.0937	0.0691/0.1453
R_1/wR_2 (all reflections)^e	0.0814/0.2203	0.0491/0.0998	0.1120/0.1574
Goodness-of-fit on $F^2{}^f$	1.157	1.001	0.923
Weighting scheme w, a/b^g	0.1464/0.0000	0.0450/0.0000	0.0914/0.000

^{a} For **1**, a total of 860 electrons per 3100 Å^3 was squeezed, which corresponds to ~107 electrons per $C_{18}H_{18}Co_4N_6O_7$ formula unit (Z = 8). PLATON^{64} calculates a total potential solvent area volume of 3182 Å^3 per unit cell volume of 8131.5 Å^3 (39.1%). ^{b} For **2**, a total of 812 electrons per 3688 Å^3 was squeezed, which corresponds to ~101 electrons per $C_{18}H_{18}N_6O_7Zn_4$ formula unit (Z = 8). PLATON^{64} calculates a total potential solvent area volume of 3736.8 Å^3 per unit cell volume of 8085.0 Å^3 (46.2%). ^{c} For **3**, total of 749 electrons per 2107 Å^3 and formula unit (Z = 1) was squeezed. PLATON^{64} calculates a total potential solvent area volume of 2088.6 Å^3 per unit cell volume of 2914.5 Å^3 (71.7%). ^{d} Largest difference peak and hole. ^{e} $R_1 = [\Sigma(||F_0|-|F_c||)/\Sigma|F_0|]$; $wR_2 = [\Sigma[w(F_0{}^2-F_c{}^2)^2]/\Sigma[w(F_0{}^2)^2]]^{1/2}$. ^{f} Goodness-of-fit = $[\Sigma[w(F_0{}^2-F_c{}^2)^2]/(n-p)]^{1/2}$. ^{g} $w = 1/[\sigma^2(F_0{}^2) + (aP)^2 + bP]$, where $P = (\max(F_0{}^2$ or 0$) + 2F_c{}^2)/3$.

23

microfocus tube. Cu-Kα radiation (λ = 1.54178 Å), 95 ± 2 K, multi-layer mirror system, ω- and θ-scan. Data collection with APEX2,[61] cell refinement and data reduction with SAINT,[61] experimental absorption correction with SADABS.[62] Several crystallization experiments were performed both at room and low temperature to obtain single crystals of **3** of suitable large size. However, from these numerous attempts, only small-size crystals of about 0.01 × 0.01 × 0.01 mm could be obtained. Because of this small size of about 0.01 × 0.01 × 0.01 mm and the high absorption coefficient of Co atoms, the crystals did not diffract over a 2θ angle of 75°. For this reason, the 2θ angle was limited to 80° for the given measurement, which however caused Alert level A (value of sine(theta_max)/wavelength is less than 0.550; maximum shift/error of 0.27) and Alert level B (low theta full of 0.953). The low diffracting power originates from the crystal size, guest molecules in the MOF cavities and disorder in the crystal. Generally, a combination of weak high-angle data and pores in the crystal is the reason for low X-ray data quality in MOF structures.

Structure analysis and refinement. Using Olex2[63] for **1** and **2**, all three structures were solved by direct methods using SHELXS-97; refinement was done by full-matrix least squares on F^2 using the SHELXL-97 program suite.[64] The crystal solvent in the voids of **1–3** was found to be highly disordered and could not be properly defined. Hence, the option SQUEEZE in PLATON for Windows[65] was used to refine the framework structure without the disordered electron density in the voids. All non-hydrogen positions in **1** and **2** were refined with anisotropic displacement parameters. Hydrogen atoms for CH– or CH$_3$ were positioned geometrically (C–H = 1.00 Å for aliphatic CH, C–H = 0.99 Å for CH$_2$, C–H = 0.98 Å for CH$_3$) and refined using riding models (AFIX 83 for OH, AFIX 43 for NH, AFIX 13 for aliphatic CH, AFIX 23 for CH$_2$, AFIX 33 or 137 for CH$_3$) with U_{iso}(H) = 1.2 U_{eq}(CH, CH$_2$) and U_{iso}(H) = 1.5 U_{eq}(CH$_3$).

For **3**, only cobalt, oxygen and one of the nitrogen atoms (N1) were refined with anisotropic displacement parameters. Carbon atoms and nitrogen atoms N2 and N3 remained isotropic. One aromatic hydrogen atom CH– and all hydrogen atoms of the CH$_3$–groups were positioned geometrically and refined using a riding model with the same prerequisites as above.

All three crystal structures were found to be disordered on several positions. Disordered atoms were refined using the PART command.

Structures **1** and **3** were refined as near racemic twins with batch scale factors (BASF) of 0.42(7) for **1** and 0.459(6) for **3**.

Graphics were obtained with DIAMOND.[66] Crystal data and details on the structure refinement are given in Table 2. The structural data have been deposited with the Cambridge Crystallographic Data Center (CCDC numbers 937761–937763).

Magnetic measurements. Magnetic susceptibility measurements on polycrystalline samples were carried out in the temperature range 1.9–300 K by means of a Quantum Design SQUID magnetometer operating at 10 000 Oe. Diamagnetic corrections

of the constituent atoms were estimated from Pascal's constants. Experimental susceptibilities were also corrected for the magnetization of the sample holder.

Notes and references

1 Introductions to special MOF issues: J. R. Long and O. M. Yaghi, *Chem. Soc. Rev.*, 2009, **38**, 1213–1214; H.-C. Zhou, J. R. Long and O. M. Yaghi, *Chem. Rev.*, 2012, **112**, 673–674.

2 C. Janiak and J. K. Vieth, *New J. Chem.*, 2010, **34**, 2366–2388; S.-H. Jhung, N. A. Khan and Z. Hasan, *CrystEngComm*, 2012, **14**, 7099–7109.

3 (*a*) J.-R. Li, R. J. Kuppler and H.-C. Zhou, *Chem. Soc. Rev.*, 2009, **38**, 1477–1504; (*b*) M. Paik Suh, H. J. Park, T. K. Prasad and D.-W. Lim, *Chem. Rev.*, 2012, **112**, 782–835.

4 H. Wu, Q. Gong, D. H. Olson and J. Li, *Chem. Rev.*, 2012, **112**, 836–868; L. J. Murray, M. Dincă and J. R. Long, *Chem. Soc. Rev.*, 2009, **38**, 1294–1314.

5 (*a*) Z. Zhang, Y. Zhao, Q. Gong, Z. Li and J. Li, *Chem. Commun.*, 2013, **49**, 653–661; (*b*) H. B. Tanh Jeazet, C. Staudt and C. Janiak, *Dalton Trans.*, 2012, **41**, 14003–14027; (*c*) J.-R. Li, J. Sculley and H.-C. Zhou, *Chem. Rev.*, 2012, **112**, 869–932; (*d*) G. Férey, C. Serre, T. Devic, G. Maurin, H. Jobic, P. L. Llewellyn, G. De Weireld, A. Vimont, M. Daturif and J.-S. Chang, *Chem. Soc. Rev.*, 2011, **40**, 550–562; (*e*) J.-R. Li, Y. Ma, M. C. McCarthy, J. Sculley, J. Yu, H.-K. Jeong, P. B. Balbuena and H.-C. Zhou, *Coord. Chem. Rev.*, 2011, **255**, 1791–1823.

6 B. Zheng, H. Liu, Z. Wang, X. Yu, P. Yi and J. Bai, *CrystEngComm*, 2013, **15**, 3517–3520; Z.-M. Zhang, T.-Z. Zhang, Y. Lu, F. Hai and E.-B. Wang, *CrystEngComm*, 2013, **15**, 459–462; C. Hou, Q. Liu, T.-a. Okamura, P. Wang and W.-Y. Sun, *CrystEngComm*, 2012, **14**, 8569–8576; W.-Y. Gao, Y. Niu, Y. Chen, L. Wojtas, J. Cai, Y.-S. Chen and S. Ma, *CrystEngComm*, 2012, **14**, 6115–6117; C. Li, W. Qiu, W. Shi, H. Song, G. Bai, H. He, J. Li and M. J. Zaworotko, *CrystEngComm*, 2012, **14**, 1929–1932; M. Kim and S. M. Cohen, *CrystEngComm*, 2012, **14**, 4096–4104.

7 K. A. Cychosz, R. Ahmad and A. J. Matzger, *Chem. Sci.*, 2010, **1**, 293–302.

8 P. Horcajada, R. Gref, T. Baati, P. K. Allan, G. Maurin, P. Couvreur, G. Férey, R. E. Morris and C. Serre, *Chem. Rev.*, 2012, **112**, 1232–1268.

9 J.-Y. Lee, O. K. Farha, J. Roberts, K. A. Scheidt, S. T. Nguyen and J. T. Hupp, *Chem. Soc. Rev.*, 2009, **38**, 1450–1459; M. Yoon, R. Srirambalaji and K. Kim, *Chem. Rev.*, 2012, **112**, 1196–1231; J. Guo, J. Yang, Y.-Y. Liu and J.-F. Ma, *CrystEngComm*, 2012, **14**, 6609–6617; B. J. Burnett, P. M. Barron and W. Choe, *CrystEngComm*, 2012, **14**,

24

3839–3846; H.-j. Pang, H.-y Ma, J. Peng, C.-j. Zhang, P.-p. Zhang and Z.-m. Su, *CrystEngComm*, 2011, **13**, 7079–7085.

10 F. Jeremias, V. Lozan, S. Henninger and C. Janiak, *Dalton Trans.*, 2013, DOI: 10.1039/c3dt51471d; C. Janiak and S. K. Henninger, *Chimia*, 2013, **67**, 419–424; C. Janiak and S. K. Henninger, *Nachr. Chem.*, 2013, **61**, 520–523; A. Khutia, H. U. Rammelberg, T. Schmidt, S. Henninger and C. Janiak, *Chem. Mater.*, 2013, **25**, 790–798; F. Jeremias, A. Khutia, S. K. Henninger and C. Janiak, *Eur. J. Inorg. Chem.*, 2012, 2625–2634; F. Jeremias, A. Khutia, S. K. Henninger and C. Janiak, *J. Mater. Chem.*, 2012, **22**, 10148–10151; J. Ehrenmann, S. K. Henninger and C. Janiak, *J. Mater. Chem.*, 2011, 471–474.

11 A. U. Czaja, N. Trukhan and U. Müller, *Chem. Soc. Rev.*, 2009, **38**, 1284–1293; G. Férey, *Dalton Trans.*, 2009, 4400–4415; M. J. Prakash and M. S. Lah, *Chem. Commun.*, 2009, 3326–3341.

12 M. Eddaoudi, J. Kim, N. Rosi, D. Vodak, J. Wachter, M. O'Keeffe and O. M. Yaghi, *Science*, 2002, **295**, 469–472.

13 I. Boldog, L. Xing, A. Schulz and C. Janiak, *C. R. Chim.*, 2012, **15**, 866–877; E. V. Alexandrov, V. A. Blatov, A. V. Kochetkov and D. M. Proserpio, *CrystEngComm*, 2011, **13**, 3947–3958.

14 S. S. Kaye, A. Dailly, O. M. Yaghi and J. R. Long, *J. Am. Chem. Soc.*, 2007, **129**, 14176–14177; H. Li, M. Eddaoudi, M. O'Keeffe and O. M. Yaghi, *Nature*, 1999, **402**, 276–279.

15 S. S. Han, S.-H. Choi and A. C. T. van Duin, *Chem. Commun.*, 2010, **46**, 5713–5715.

16 J. J. Low, A. I. Benin, P. Jakubczak, J. F. Abrahamian, S. A. Faheem and R. R. Willis, *J. Am. Chem. Soc.*, 2009, **131**, 15834–15842.

17 K. A. Cychosz and A. J. Matzger, *Langmuir*, 2010, **26**, 17198–17202.

18 V. Guillerm, F. Ragon, M. Dan-Hardi, T. Devic, M. Vishnuvarthan, B. Campo, A. Vimont, G. Clet, Q. Yang, G. Maurin, G. Ferey, A. Vittadini, S. Gross and C. Serre, *Angew. Chem., Int. Ed.*, 2012, **51**, 9267–9271.

19 X.-C. Huang, Y.-Y. Lin, J.-P. Zhang and X.-M. Chen, *Angew. Chem., Int. Ed.*, 2006, **45**, 1557–1559; K. S. Park, Z. Ni, A. P. Côté, J. Y. Choi, R. Huang, F. J. Uribe-Romo, H. K. Chae, M. O'Keeffe and O. M. Yaghi, *Proc. Natl. Acad. Sci. U. S. A.*, 2006, **103**, 10186–10191.

20 G. Férey, C. Mellot-Draznieks, C. Serre, F. Millange, J. Dutour, S. Surble and I. Margiolaki, *Science*, 2005, **309**, 2040–2042.

21 J. H. Cavka, S. Jakobsen, U. Olsbye, N. Guillou, C. Lamberti, S. Bordiga and K. P. Lillerud, *J. Am. Chem. Soc.*, 2008, **130**, 13850–13851.

22 I. Boldog, K.V. Domasevitch, I. A. Baburin, H. Ott, B. Gil-Hernández, J. Sanchiz and C. Janiak, *CrystEngComm*, 2013, **15**, 1235–1243; H. J. Choi, M. Dincă, A. Dailly and J. R. Long, *Energy Environ. Sci.*, 2010, **3**, 117–123.

23 J.-P. Zhang, Y.-B. Zhang, J.-B. Lin and X.-M. Chen, *Chem. Rev.*, 2012, **112**, 1001–1033; M. A. Halcrow, *Dalton Trans.*, 2009, 2059–2073.

24 V. Colombo, C. Montoro, A. Maspero, G. Palmisano, N. Masciocchi, S. Galli, E. Barea and J. A. R. Navarro, *J. Am. Chem. Soc.*, 2012, **134**, 12830–12843; N. Masciocchi, S. Galli, V. Colombo, A. Maspero, G. Palmisano, B. Seyyedi,

C. Lamberti and S. Bordiga, *J. Am. Chem. Soc.*, 2010, **132**, 7902–7904.

25 M. Tonigold, Y. Lu, A. Mavrandonakis, S. Puls, R. Staudt, J. Maellmer, J. Sauer and D. Volkmer, *Chem.–Eur. J.*, 2011, **17**, 8671–8695.

26 N. M. Padial, E. Quartapelle Procopio, C. Montoro, E. López, J. E. Oltra, V. Colombo, Maspero, N. Masciocchi, S. Galli, I. Senkovska, S. Kaskel, E. Barea and J. A. R. Navarro, *Angew. Chem.*, 2013, **125**, 8448–8452.

27 D. J. Tranchemontagne, K. S. Park, H. Furukawa, J. Eckert, C. B. Knobler and O. M. Yaghi, *J. Phys. Chem. C*, 2012, **116**, 13143–13151.

28 W.-Y. Gao, W. Yan, R. Cai, L. Meng, A. Salas, X.-S. Wang, L. Wojtas, X. Shi and S. Ma, *Inorg. Chem.*, 2012, **51**, 4423–4425.

29 C.-T. He, J.-Y. Tian, S.-Y. Liu, G. Ouyang, J.-P. Zhang and X.-M. Chen, *Chem. Sci.*, 2013, **4**, 351–356.

30 J. Lincke, D. Lässig, M. Kobalz, J. Bergmann, M. Handke, J. Möllmer, M. Lange, C. Roth, A. Möller, R. Staudt and H. Krautscheid, *Inorg. Chem.*, 2012, **51**, 7579–7586.

31 C. Montoro, F. Linares, E. Quartapelle Procopio, I. Senkovska, S. Kaskel, S. Galli, N. Masciocchi, E. Barea and J. A. R. Navarro, *J. Am. Chem. Soc.*, 2011, **133**, 11888–11891.

32 A. Bétard, S. Wannapaiboon and R. A. Fischer, *Chem. Commun.*, 2012, **48**, 10493–10495.

33 A. Bhunia, V. Vasylyeva and C. Janiak, *Chem. Commun.*, 2013, **49**, 3961–3963.

34 S. Henke and R. A. Fischer, *J. Am. Chem. Soc.*, 2011, **133**, 2064–2067.

35 S. S. Mondal, A. Bhunia, I. A. Baburin, C. Jäger, A. Kelling, U. Schilde, G. Seifert, C. Janiak and H.-J. Holdt, *Chem. Commun.*, 2013, **49**, 7567–7570.

36 S. Yang, X. Lin, A. J. Blake, G. S. Walker, P. Hubberstey, N. R. Champness and M. Schröder, *Nat. Chem.*, 2009, **1**, 487–493.

37 K. Sumida, D. L. Rogow, J. A. Mason, T. M. McDonald, E. D. Bloch, Z. R. Herm, T.-H. Bae and J. R. Long, *Chem. Rev.*, 2012, **112**, 724–781.

38 A. J. Fletcher, E. J. Cussen, T. J. Prior, M. J. Rosseinsky, C. J. Kepert and K. M. Thomas, *J. Am. Chem. Soc.*, 2001, **123**, 10001–10011; E. J. Cussen, J. B. Claridge, M. J. Rosseinsky and C. J. Kepert, *J. Am. Chem. Soc.*, 2002, **124**, 9574–9581.

39 S.-i. Noro, S. Kitagawa, T. Akutagawa and T. Nakamura, *Prog. Polym. Sci.*, 2009, **34**, 240–279; S. Kitagawa and R. Matsuda, *Coord. Chem. Rev.*, 2007, **251**, 2490–2509.

40 C. Graham, D. A. Imrie and R. E. Raab, *Mol. Phys.*, 1998, **93**, 49–56.

41 K. A. Cychosz, A. G. Wong-Foy and A. J. Matzger, *J. Am. Chem. Soc.*, 2008, **130**, 6938–6939.

42 M. Kurmoo, *Chem. Soc. Rev.*, 2009, **38**, 1353–1379; D. Maspoch, D. Ruiz-Molina and J. Veciana, *Chem. Soc. Rev.*, 2007, **36**, 770–818; D. Maspoch, D. Ruiz-Molina and J. Veciana, *J. Mater. Chem.*, 2004, **14**, 2713–2723; S. R. Batten and K. S. Murray, *Coord. Chem. Rev.*, 2003, **246**, 103–130; C. Janiak, *Dalton Trans.*, 2003, 2781–2804.

43 J. K. Maclaren, J. Sanchiz, P. Gili and C. Janiak, *New J. Chem.*, 2012, **36**, 1596–1609; B. Gil-Hernández, J. K. Maclaren,

25

H. A. Höppe, J. Pasan, J. Sanchiz and C. Janiak, *CrystEngComm*, 2012, **14**, 2635–2644; B. Gil-Hernández, H. Höppe, J. K. Vieth, J. Sanchiz and C. Janiak, *Chem. Commun.*, 2010, **46**, 8270–8272; B. Gil-Hernández, P. Gili, J. K. Vieth, C. Janiak and J. Sanchiz, *Inorg. Chem.*, 2010, **49**, 7478–7490; H. A. Habib, J. Sanchiz and C. Janiak, *Inorg. Chim. Acta*, 2009, **362**, 2452–2460; H. A. Habib, J. Sanchiz and C. Janiak, *Dalton Trans.*, 2008, 4877–4884; H. A. Habib, J. Sanchiz and C. Janiak, *Dalton Trans.*, 2008, 1734–1744.

44 T. Gao, X.-Z. Wang, H.-X. Gu, Y. Xu, X. Shen and D.-R. Zhu, *CrystEngComm*, 2012, **14**, 5905–5913; S.-Q. Guo, D. Tian, X. Zheng and H. Zhang, *CrystEngComm*, 2012, **14**, 3177–3182; J.-Q. Liu, Y.-Y. Wang, T. Wu and J. Wu, *CrystEngComm*, 2012, **14**, 2906–2913.

45 O. Kahn, *Molecular Magnetism*, VCH, New York, 1993.

46 D. Nelson and W. Haar, *Inorg. Chem.*, 1993, **32**, 182–188.

47 J. Olguín, M. Kalisz, R. Clérac and S. Brooker, *Inorg. Chem.*, 2012, **51**, 5058–5069.

48 V. H. Crawford, H. W. Richardson, J. R. Wasson, D. J. Hodgson and W. E. Hatfield, *Inorg. Chem.*, 1976, **15**, 2107–2110.

49 S. Ferrer, F. Lloret, I. Bertomeu, G. Alzuet, J. Borrás, S. García-Granada, M. Liu-González and J. G. Haasnoot, *Inorg. Chem.*, 2002, **41**, 5821–5830.

50 S. Ferrer, F. Lloret, E. Pardo, J. M. Clemente-Juan, M. Liu-González and S. García-Granda, *Inorg. Chem.*, 2012, **51**, 985–1001.

51 J. Ruiz, A. J. Mota, A. Rodríguez-Diéguez, I. Oyarzabal, J. M. Seco and E. Colacio, *Dalton Trans.*, 2012, **41**, 14265–14273.

52 H. Arora, S. K. Barman, F. Lloret and M. Mukherjee, *Inorg. Chem.*, 2012, **51**, 5539–5553.

53 S. M. Ostrovsky, K. Falk, J. Pelikan, D. A. Brown, Z. Tomkowicz and W. Haase, *Inorg. Chem.*, 2006, **45**, 688–694.

54 F. Lloret, J. Julve, J. Cano, R. Ruiz-García and E. Pardo, *Inorg. Chim. Acta*, 2008, **361**, 3432–3445.

55 P. Jaitner, J. Veciana, C. Sporer, H. Kopacka, K. Wurst and D. Ruiz-Molina, *Organometallics*, 2001, **20**, 568–571.

56 A. B. Blake, *Chem. Commun.*, 1966, 569.

57 L. D. Gelb, K. E. Gubbins, R. Radhakrsihan and M. Sliwinska-Bartowiak, *Rep. Prog. Phys.*, 1999, **62**, 1573–1659.

58 N. A. Sedron, J. P. R. B. Walton and N. Quirke, *Carbon*, 1989, **27**, 853–861.

59 A. Vishnyakov, P. Ravikovitch and A. V. Neimark, *Langmuir*, 2000, **16**, 2311–2320.

60 CrysAlisPro, Agilent Technologies, Version 1.171.36.2 (release 08-11-2011 CrysAlis171.NET).

61 Apex2, Data Collection Program for the CCD Area-Detector System; SAINT, Data Reduction and Frame Integration Program for the CCD Area-Detector System., Bruker Analytical X-ray Systems, Madison, Wisconsin, USA, 1997–2006.

62 G. Sheldrick, Program SADABS: Area-detector absorption correction, University of Göttingen, Germany, 1996.

63 OLEX2: a complete structure solution, refinement and analysis programO. V. Dolomanov, L. J. Bourhis, R. J. Gildea, J. A. K. Howard and H. Puschmann, *J. Appl. Crystallogr.*, 2009, **42**, 339–341.

64 G. M. Sheldrick, *Acta Crystallogr. A*, 2008, **64**, 112–122.

65 A. L. Spek, *J. Appl. Crystallogr.*, 2003, **36**, 7–13; PLATON – A Multipurpose Crystallographic Tool, Utrecht University, Utrecht, The Netherlands, A. L. Spek, 2008; Windows implementation: L. J. Farrugia, University of Glasgow, Scotland, Version 40608, 2008.

66 K. Brandenburg, Diamond (Version 3.2), crystal and molecular structure visualization, Crystal Impact. K. Brandenburg & H. Putz Gbr, Bonn, Germany, 2007–2012.

26

Bifunctional pyrazolate-carboxylate ligands for isoreticular cobalt and zinc MOF-5 analogs with magnetic analysis of the {Co$_4$(μ$_4$-O)} node

Christian Heering,[a] Ishtvan Boldog,[a] Vera Vasylyeva,[a] Joaquín Sanchiz,*[b] Christoph Janiak*[a]

[a] Institut für Anorganische Chemie und Strukturchemie, Universität Düsseldorf, D-40204 Düsseldorf, Germany. Fax: +49 211 8112287;
E-mail: christian.heering@uni-duesseldorf.de
E-mail: ishtvan.boldog@uni-duesseldorf.de
E-mail: vira.vasylyeva@uni-duesseldorf.de
E-mail: janiak@uni-duesseldorf.de

[b] Departamento de Química Inorgánica, Universidad de La Laguna, La Laguna 38206, Tenerife, Spain
E-mail: jsanchiz@ull.es

Experimental Section

Materials

1*H*-Pyrazole-4-carboxylic acid was purchased in 97 % grade from Carbolution.
Solvents were p.a. grade.

Methods

Melting point measurement was performed in an open capillary using a Büchi-B450 apparatus. FT-IR measurements were carried out on a Bruker TENSOR 37 IR spectrometer at ambient temperature in the range of 4000 to 500 cm^{-1} either in a KBr pellett or with an ATR unit (Platinum ATR-QL, Diamond). ^{1}H and ^{13}C spectra were recorded on Bruker Avance DRX-200 Bruker Avance DRX-500 instruments respectively. High resolution mass spectra (ESI) were collected with a UHR-QTOF maXis 4G from Bruker Daltonics. Elemental (CHN) analyses were carried out on a Perkin Elmer CHN 2400.

Thermogravimetric analysis (TGA) was performed on a Netzsch TG 209 F3 at 10 °C/min heating rate using corundum sample holders and nitrogen as carrier gas.

Synthesis of ligands

3,5-Dimethyl-1*H*-pyrazole-4-carboxylic acid (HMe₂pzCO₂H)

This compound has been synthesized according to literature procedures, following those of Knorr and Rosenberg (Fig. S1).[1] Diacetyl ethylcacetate (**I**) was obtained in 45% yield in a first step by the method of Spassow.[2] Intermediate **I** with hydrazine monohydrate gave the ethyl ester of HMe₂pzCO₂H, **II** in 80% yield in water. As the final step the ester was hydrolyzed to give the product in 90% yield. FTIR (ATR): 3007, 2919, 1700, 1542, 1505, 1477, 1420, 1391, 1368, 1309, 1171, 997, 950, 816, 803, 745, 712, 671, 617 cm^{-1} (Fig. S2)

^{1}H-NMR (CDCl₃, 500 MHz): δ/ppm = 1.88 (s, 6H, CH_3), 12.8 (s, COOH) (Fig. S3).

^{13}C-NMR (CDCl₃, 500 MHz): δ/ppm = 40.0 (s, CH_3), 129.0 135.5 143.5 (pyrazole C's) 167.8 (s, $COOH$) (Fig. S4).
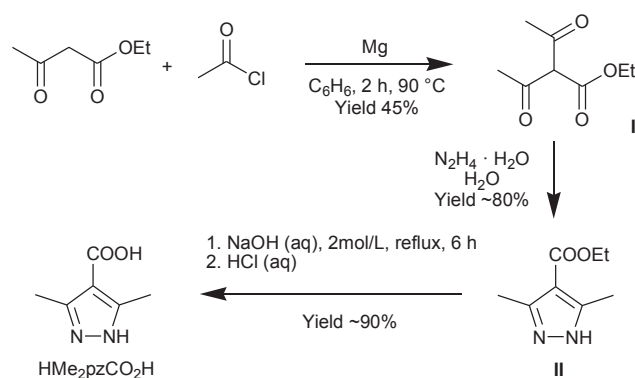
Fig. S1. Synthesis for 3,5-dimethyl-1*H*-pyrazole-4-carboxylic acid (HMe₂pzCO₂H).

[1] G. D. Rosengarten, *Justus Liebigs Annalen der Chemie* **1894**, *279*, 237–243.
[2] A. Spassow, *Organic Syntheses* **1955**, *3*, 390.
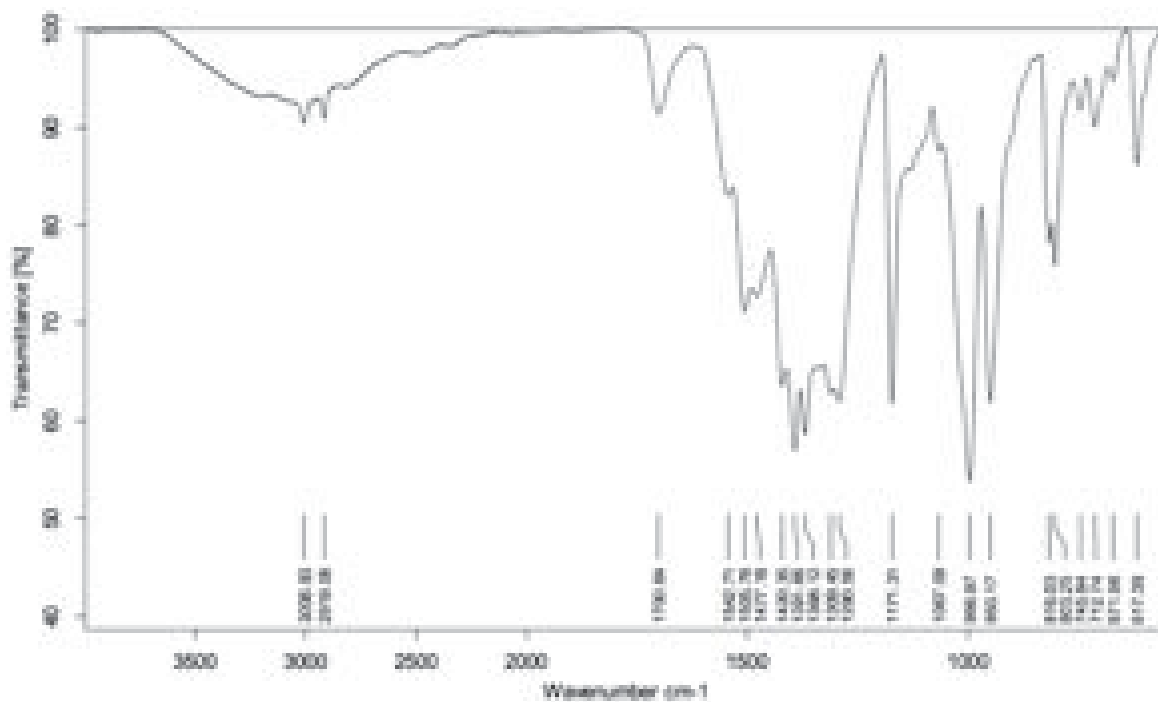
Fig. S2. FTIR (ATR) of 3,5-dimethyl-1*H*-pyrazole-4-carboxylic acid (HMe$_2$pzCO$_2$H).
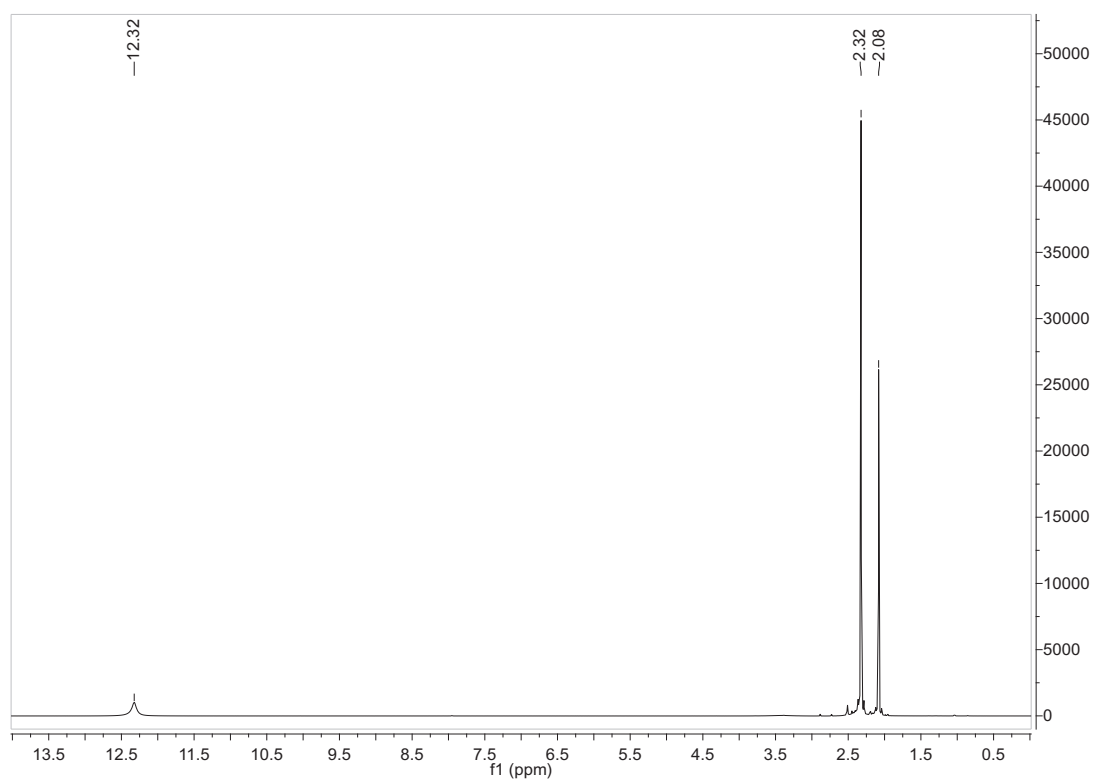
Fig. S3. ^{1}H NMR (in CDCl$_3$) of 3,5-dimethyl-1*H*-pyrazole-4-carboxylic acid (HMe$_2$pzCO$_2$H).
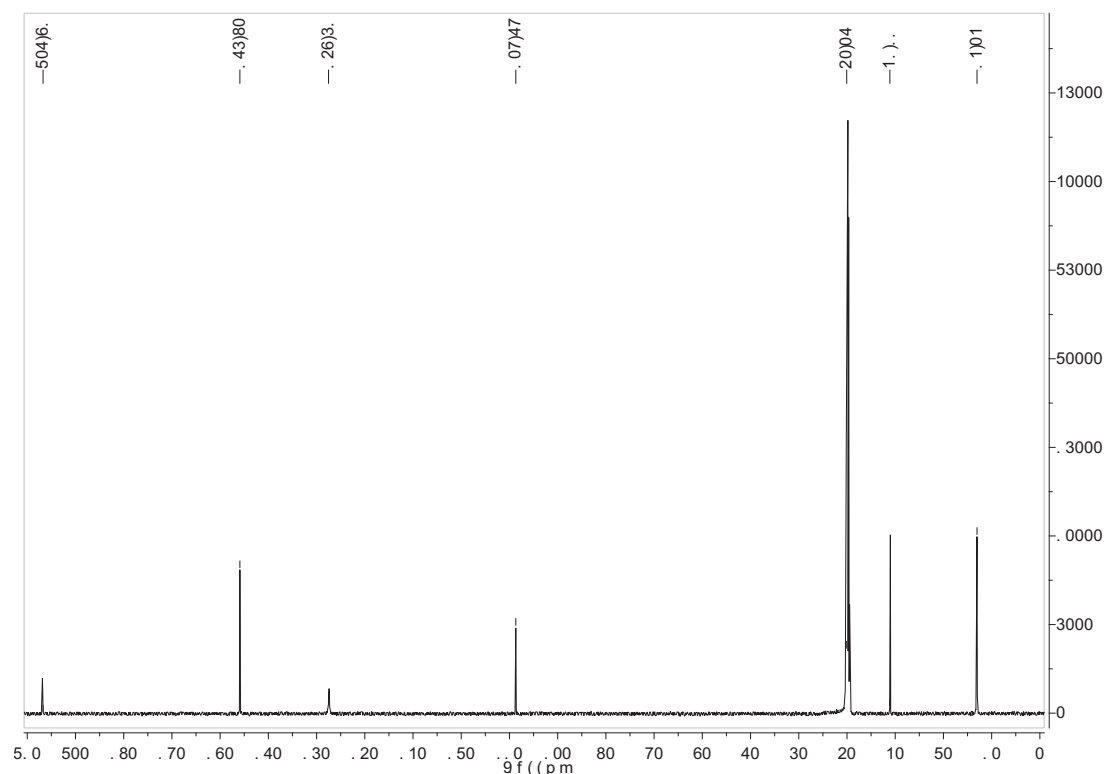
Fig. S4. ^{13}C NMR (in CDCl$_3$) of 3,5-dimethyl-1*H*-pyrazole-4-carboxylic acid (HMe$_2$pzCO$_2$H).

3,5-Dimethyl-4-(4-carboxyphenyl)-1*H*-pyrazole, 4-(3,5-dimethyl-1H-pyrazol-4-yl)benzoic acid (HMe$_2$pzC$_6$H$_4$CO$_2$H) (see Fig. S5)

a) 3-(4-Carboxyphenyl)-2,4-pentanedione

In a first step 3-(4-carboxyphenyl)-2,4-pentanedione (**III**) was synthesized in a copper-catalyzed reaction with L-proline.[3] In a 0.5 L round-bottom flask 12 g (48 mmol) of 4-iodobenzoic acid and 14 g (threefold excess, 144 mmol) of 2,4 pentanedione were dissolved in 250 mL of dimethylsulfoxide (DMSO). After addition of 1.8 g (9.5 mmol) CuI and 2.2 g (19 mmol) L-proline the solution turned from yellow to bluish-green and 32.2 g (0.24 mol) of K$_2$CO$_3$ was added as a base. Under constant stirring under nitrogen atmosphere the reaction mixture was heated to 90 °C and kept at this temperature for 24 h. After cooling down to room temperature the dark solution was poured into 250 mL water and acidified with aqueous 12 mol/L HCl to pH 3. The solution became yellow again and was then extracted three times by 25 mL portions of ethyl acetate. The separated organic phase was treated with 15 mL of brine (saturated solution), separated again and dried over Na$_2$SO$_4$. After evaporation of the solvent the brown and oilish residue was poured into water,

---

[3] Y. Jiang, N. Wu, H. Wu, M. He, *ChemInform* **2006**, 37.

yielding 4.2 g of a brown solid compound (40 % based on 4-iodobenzoic acid).

mp = 95 °C (lit. value unknown)

FTIR (ATR): 2832, 2724, 2667, 2547, 1928, 1803, 1672, 1582, 1482, 1422, 1391, 1317, 1292, 1271, 1178, 1124, 1107, 1052, 1003, 929, 847, 807, 750, 682, 655, 625, 563 cm^{-1} (Fig. S6)

^{1}H-NMR (DMSO-d_6, 500 MHz): δ/ppm = 1.88 (s, 6H, CH$_3$CO), 5.5 (s, 1H, acidic H -CO-CH-CO-), 7.43, 7.98 (2xd, 4H, C$_6$H$_4$), 13.0 (s, COOH) (Fig. S7).

^{13}C-NMR (DMSO-d_6, 500 MHz): δ/ppm = 40.0 (s, CH$_3$), 101.6 (s, -CO-CH-CO-), 130-137 (aromatic C's), 167.3 (C=O).
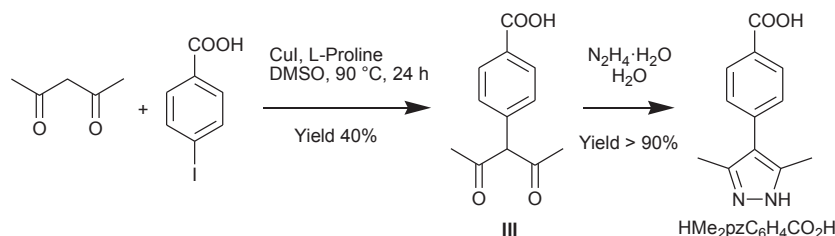
Fig. S5. Synthesis of 3,5-dimethyl-4-(4-carboxyphenyl)-1H-pyrazole, 4-(3,5-dimethyl-1H-pyrazol-4-yl)benzoic acid (HMe$_2$pzC$_6$H$_4$CO$_2$H).
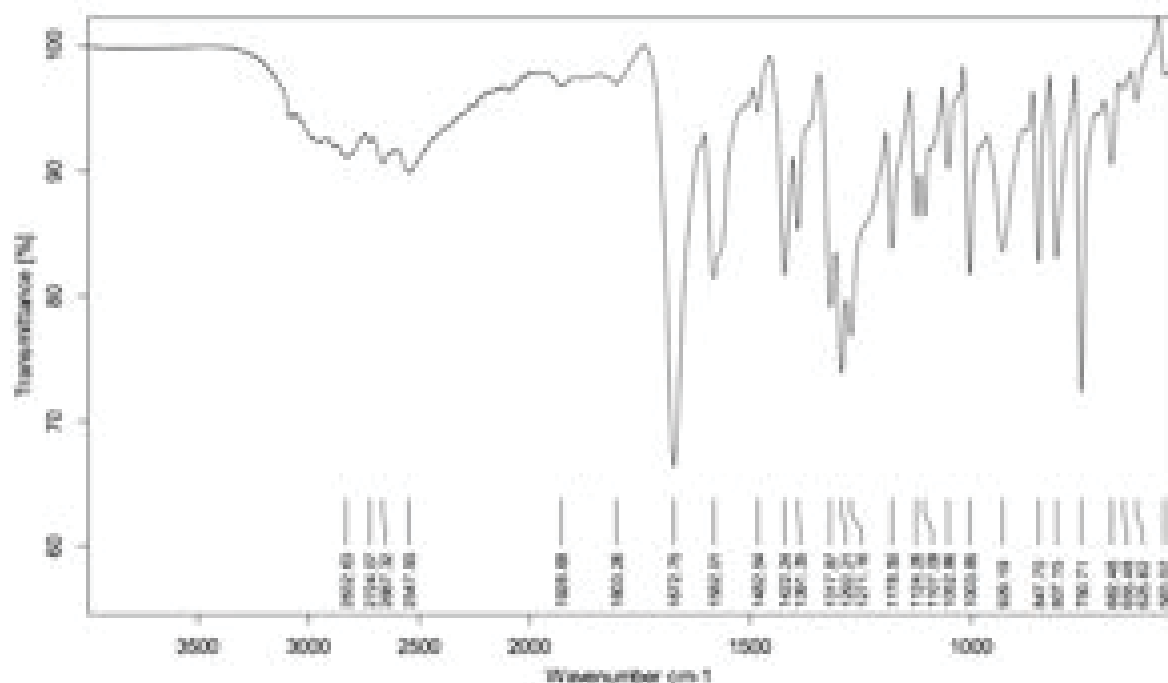
Fig. S6. FTIR (ATR) of 3-(4-carboxyphenyl)-2,4-pentanedione (**III**).
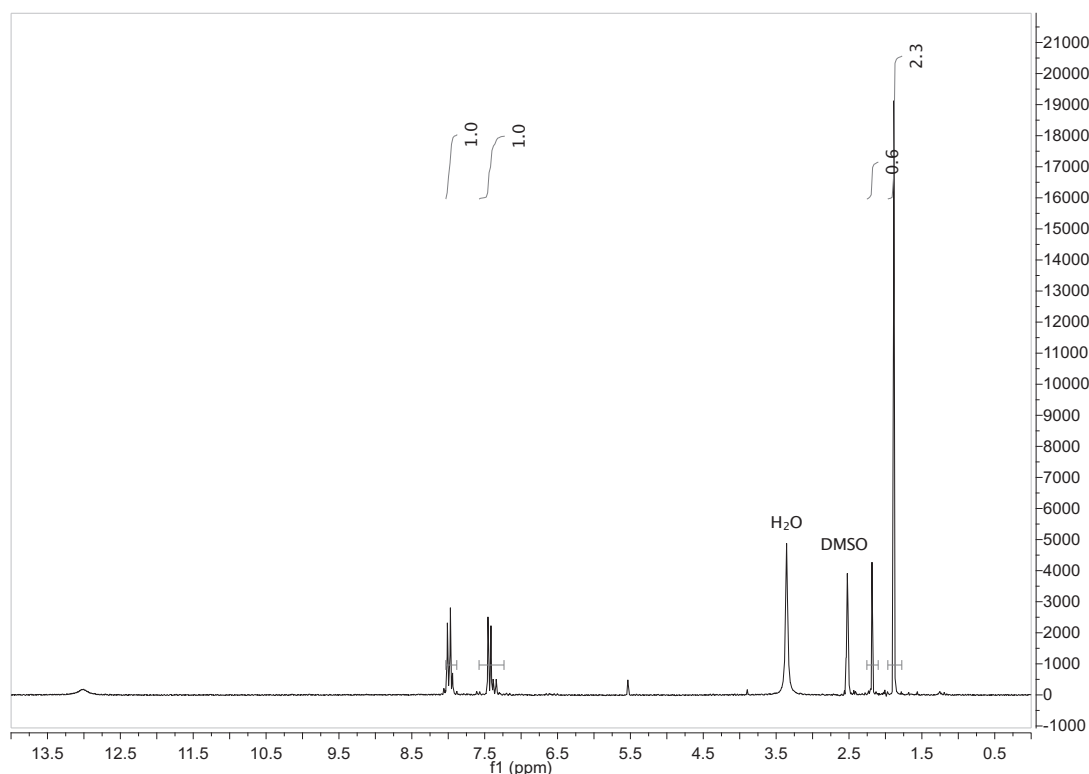
Fig. S7. ^{1}H NMR (in DMSO-d_6) of 3-(4-carboxyphenyl)-2,4-pentanedione (**III**).

b) 3,5-Dimethyl-4-(4-carboxyphenyl)-1H-pyrazole, 4-(3,5-dimethyl-1H-pyrazol-4-yl)benzoic acid (HMe$_2$pzC$_6$H$_4$CO$_2$H)

The pentanedione **III** was suspended in 20 mL of water in a 50 mL round-bottom flask. Under constant stirring 75 mg (1.5 mmol) of hydrazine monohydrate dissolved in 5 mL of water was added dropwise to the flask. After one hour the clear solution was treated with concentrated HCl (12 mol/L) to bring the mixture to a pH value of 3. The white precipitate was separated by filtration, dried under vacuum and washed with 15 mL of aceton to give 0.28 g of pure product (> 90 % based on **III**).

mp > 295 °C (decomp.). Calcd. for C$_{12}$H$_{12}$N$_2$O$_2$ (216.24 g/mol) C 66.65, H 5.59, N 12.96; found C 65.91, H 5.71, N 12.64%.

FTIR (ATR): 3276, 2988, 2933, 2438, 1942, 1677, 1607, 1412, 1254, 1174 cm^{-1} (see Fig. S8).

^{1}H-NMR (DMSO-d_6, 500 MHz): δ/ppm = 2.25 (s, 6H, CH$_3$), 7.42 (d, 2H), 7.98 (d, 2H), 13 (s, br, COOH) (Fig. S9).

^{13}C-NMR (DMSO-d_6, 500 MHz): δ/ppm = 11.87 (s, CH$_3$), 124-130 (aromatic C's), 139.27 (s, C-N), 167.85 (s, COOH) (Fig. S10).

ESI-MS (neg.) 215.08234 [M-H$^+$]$^-$, calcd. ^{12}C$_{12}$H$_{11}$N$_2$O$_2$: 215.08260 (100%).
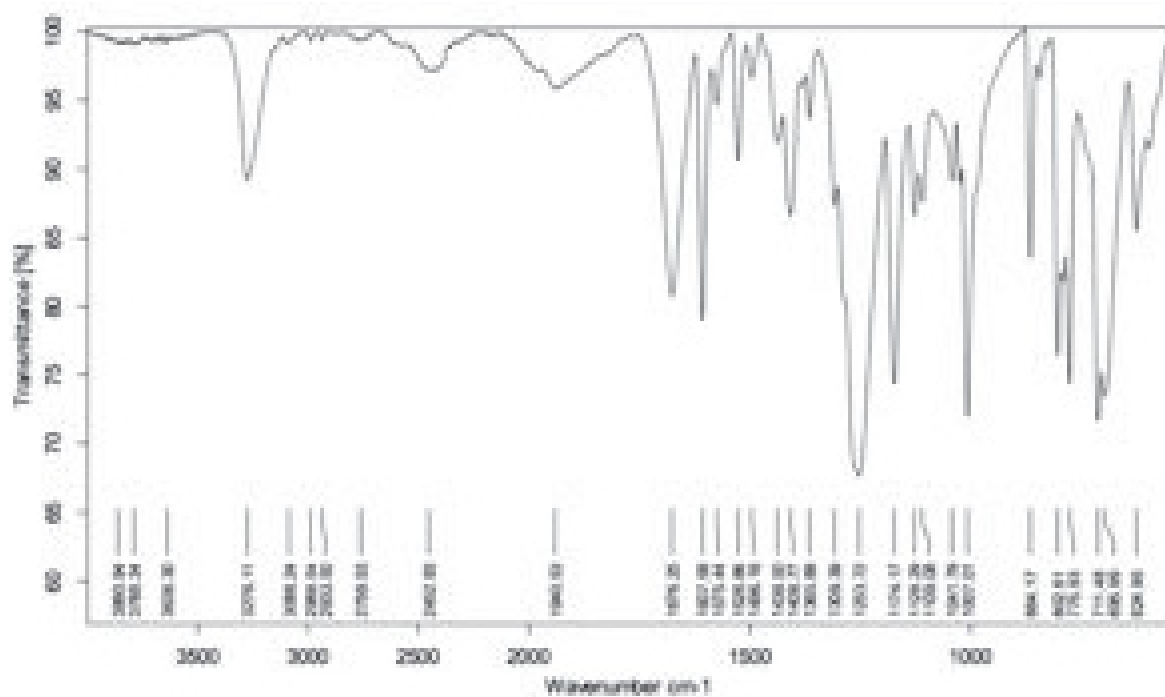
Fig. S8. FTIR (ATR) of 4-(3,5-dimethyl-1H-pyrazol-4-yl)benzoic acid $HMe_2pzC_6H_4CO_2H$.
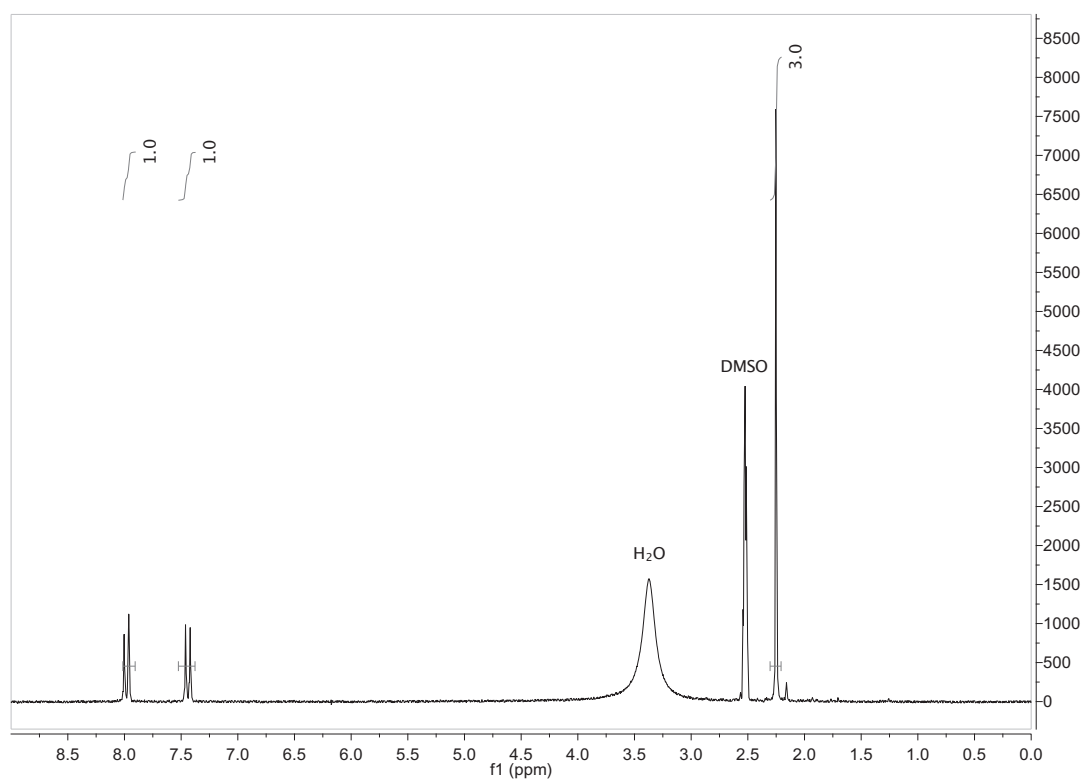
Fig. S9. ^{1}H-NMR (DMSO-d_6) of 4-(3,5-dimethyl-1H-pyrazol-4-yl)benzoic acid $HMe_2pzC_6H_4CO_2H$.
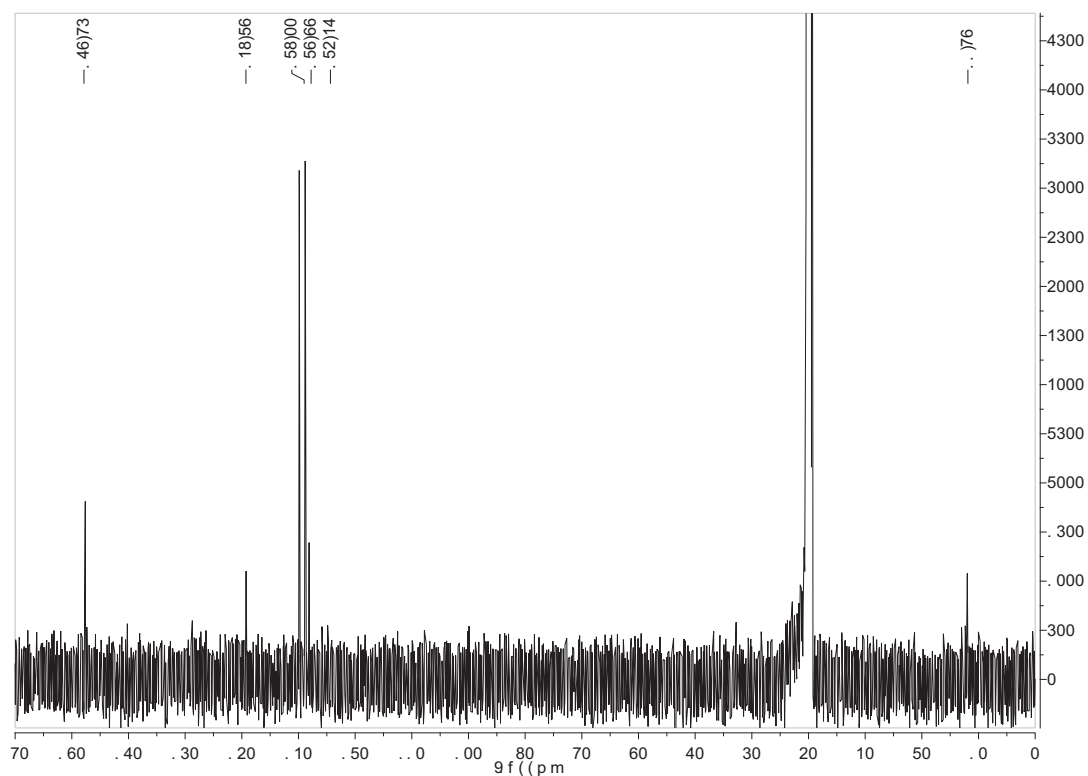
Fig. S10. ^{13}C-NMR (DMSO-d_6) of 4-(3,5-dimethyl-1H-pyrazol-4-yl)benzoic acid HMe$_2$pzC$_6$H$_4$CO$_2$H.

35

Synthesis of complexes

$\{[Co_4(\mu_4\text{-}O)(Me_2pzCO_2)_3]\cdot\text{~}3\ DMSO\}_n$ (1)

In a screw-capped Pyrex tube 20.6 mg ($7.0\cdot10^{-2}$ mmol) of $Co(NO_3)_2\cdot6\ H_2O$ and 10.0 mg ($7.0\cdot10^{-2}$ mmol) of HMe_2pzCO_2H were dissolved in 1.5 mL of a mixture of DMSO/DMF/MeOH (10:4:1). The solution was heated to 110 °C and then up to 120 °C within three days. The clear, deep-violet cubic crystals (Fig. S11) were filtered and washed three times with 10 mL of DMF. They were dried under a vacuum of 10^{-2} Torr and stored under inert atmosphere.

Yield: 40 mg (60 % based on ligand)

FTIR (ATR): 3216, 3010, 2920, 2340, 1706, 1543, 1507, 1477, 1421, 1393, 1369, 1289, 1172, 1107, 1069, 997, 950, 815, 803, 745, 712, 670, 617 cm^{-1} (see Fig. S12).

We note that meaningful elemental analyses of MOFs are difficult to obtain due to solvent loss and different sample states (different states of dryness vs. not dried).

A total of 860 electrons per 3100 $Å^3$ (compare with total potential solvent area volume of 3182 $Å^3$ calcd. by PLATON VOID) was squeezed by PLATON in the structure refinement of **1** which corresponds to ~107 electrons per $C_{18}H_{18}Co_4N_6O_7$ formula unit ($Z = 8$). One DMSO molecule provides 42 electrons.

In TG/DTA (see Fig. S13) the dried compound shows a first weight loss of 27.7% in a temperature range from 200 °C to 300 °C. This weight loss can be assiged to the loss of about 3 DMSO solvent molecules (theor. 26%). In the range from ~450 °C to 500 °C a second weight loss of ~39% takes place which is due to decomposition of the ligand.

For the cobalt complex a removal of solvent is easier than for the zinc complex with the same ligand because of the smaller DMSO molecule in $\{[Co_4(\mu_4\text{-}O)(Me_2pzCO_2)_3]\cdot\text{~}3\ DMSO\}_n$ compared with the diethylformamide, DEF molecule in $\{[Zn_4(\mu_4\text{-}O)(Me_2pzCO_2)_3]\cdot\text{~}2\ DEF\}_n$ (see. Fig. S16).
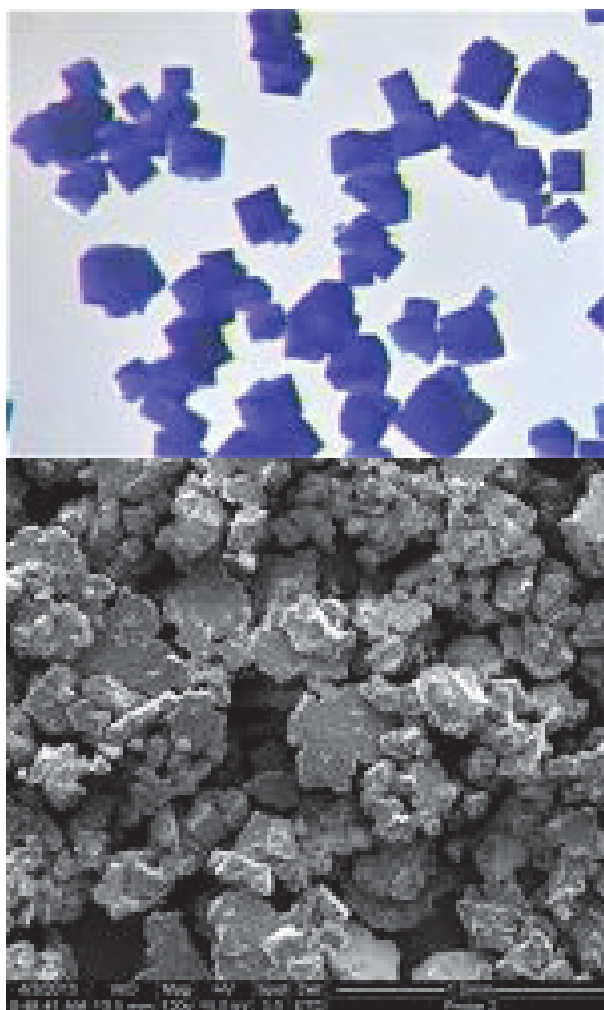
Fig. S11. Crystals of $\{[Co_4(\mu_4\text{-}O)(Me_2pzCO_2)_3] \cdot 3\ DMSO\}_n$ (**1**) by optical photography and scanning electron microscopy. The cubic shape of the crystals already hints at the cubic crystal system with space group F-43m.
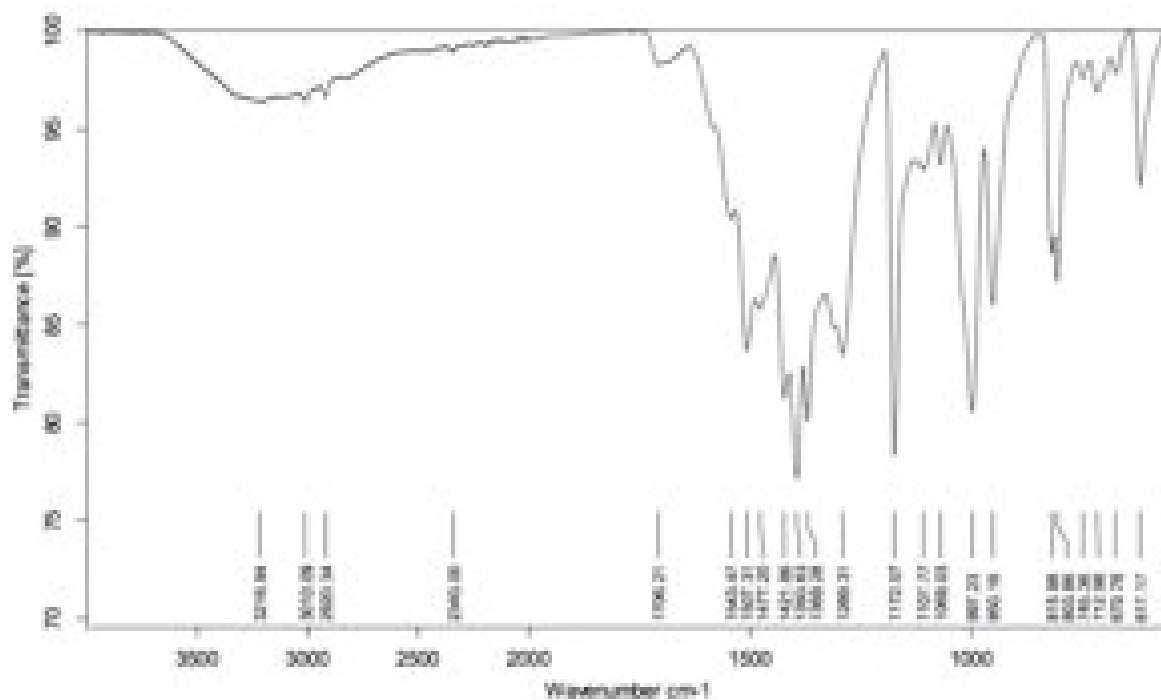
Fig. S12. FTIR (ATR) of compound $\{[Co_4(\mu_4\text{-}O)(Me_2pzCO_2)_3] \cdot \sim 3\ DMSO\}_n$ **1**.

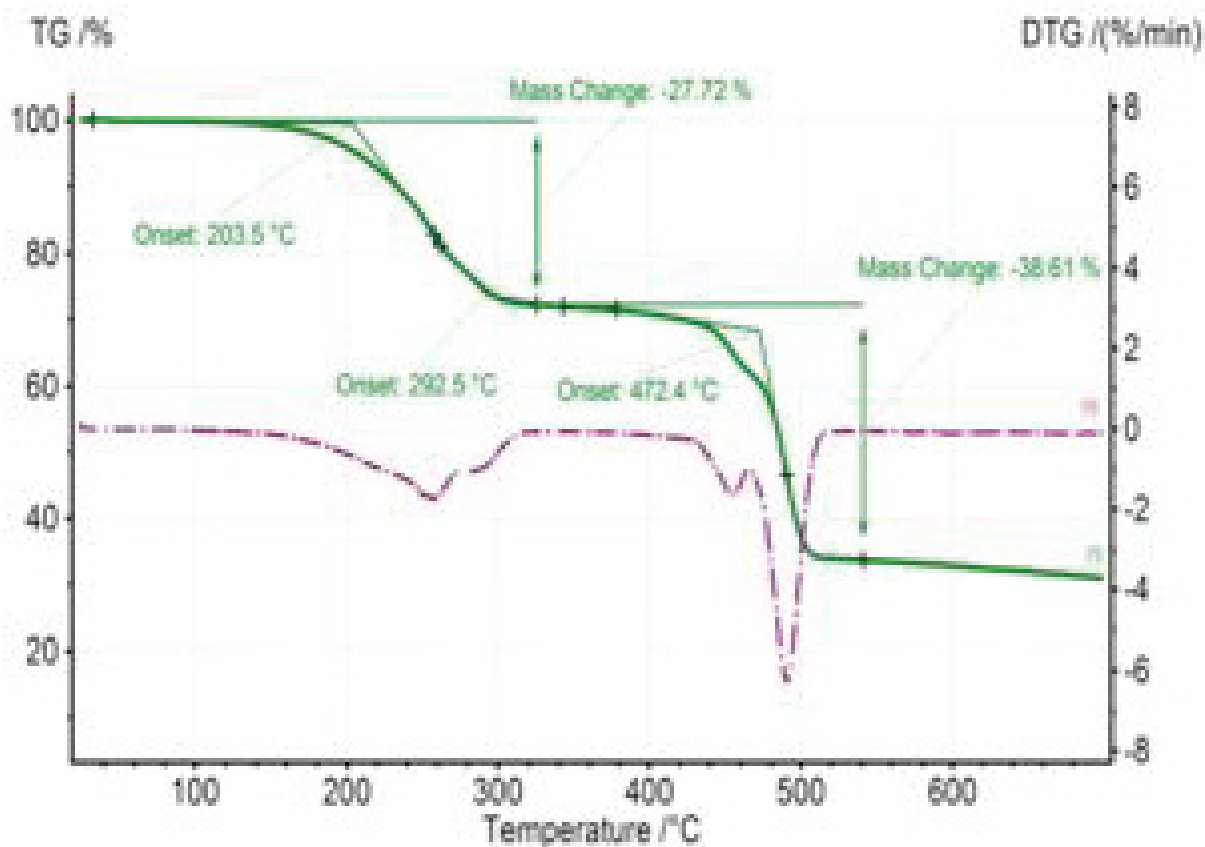**Fig. S13.** TG/DTG of $\{[Co_4(\mu_4\text{-}O)(Me_2pzCO_2)_3] \cdot \sim 3\ DMSO\}_n$ (**1**)

{[Zn$_4$(μ_4-O)(Me$_2$pzCO$_2$)$_3$] ·~2 DEF}$_n$ (2)

In a screw-capped Pyrex tube 1.13 g (0.28 mmol) of Zn(NO$_3$)$_2$ · 4 H$_2$O and 0.3 g (0.14 mmol) of HMe$_2$pzCO$_2$H were dissolved in 30 mL of DEF. The clear solution was heated to 140 °C within two days and kept for another two days at this temperature. The clear yellowish cubic crystals (Fig. S14) were decanted and seperated from impurities by density difference using a mixture of bromoforme and methanol. After centrifugation the product was washed three times with 10 mL of DEF, dried under a vacuum of 10^{-2} Torr and stored under inert atmosphere.

Yield: 310 mg (22 % based on ligand)

FTIR (ATR): 2971, 2927, 1675, 1567, 1516, 1490, 1428, 1405, 1377, 1307, 1259, 1216, 1182, 1106, 1071, 1041, 994, 941, 820, 803, 667, 642, 620 cm^{-1} cm^{-1} (see Fig. S15).

We note that meaningful elemental analyses of MOFs are difficult to obtain due to solvent loss and different sample states (different states of dryness vs. not dried).

A total of 812 electrons per 3688 Å^3 (compare to total potential solvent area volume of 3737 Å^3 calcd. by PLATON VOID) was squeezed by PLATON in the structure refinement of **2** which corresponds to ~101 electrons per C$_{18}$H$_{18}$N$_6$O$_7$Zn$_4$ formula unit (Z = 8). One DEF molecule provides 56 electrons.

In TG/DTA (see Fig. S16) the dried compound shows a small and continuous weight loss starting at 200 °C and which becomes more visible at 300 °C. This weight loss is assigned to high-boiling/low-volatile DEF crystal solvent molecules which have to escape through the narrow pores. The solvent weight loss continues into the ligand decomposition between 400 and 500 °C (cf. Fig. S13 for the ligand decomposition at the Co compound **1**).
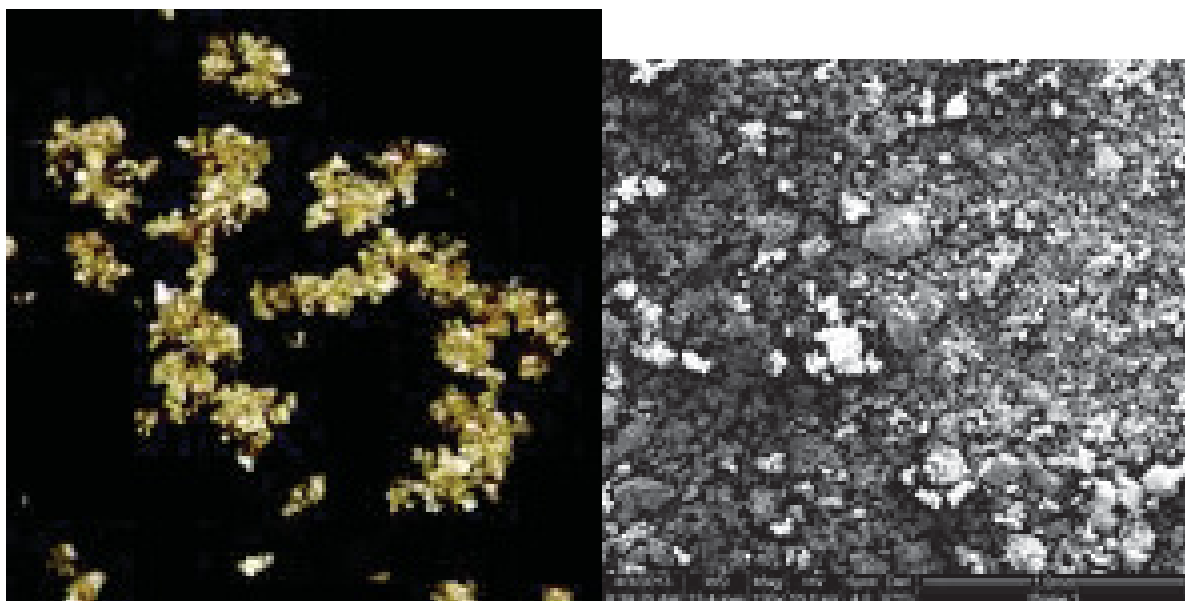
Fig. S14. Crystals of $\{[Zn_4(\mu_4\text{-}O)(Me_2pzCO_2)_3] \cdot{\sim}2\ DEF\}_n$ **(2)** by optical photography and scanning electron microscopy. The cubic shape of the crystals already hints at the cubic crystal system with space group F-43m.
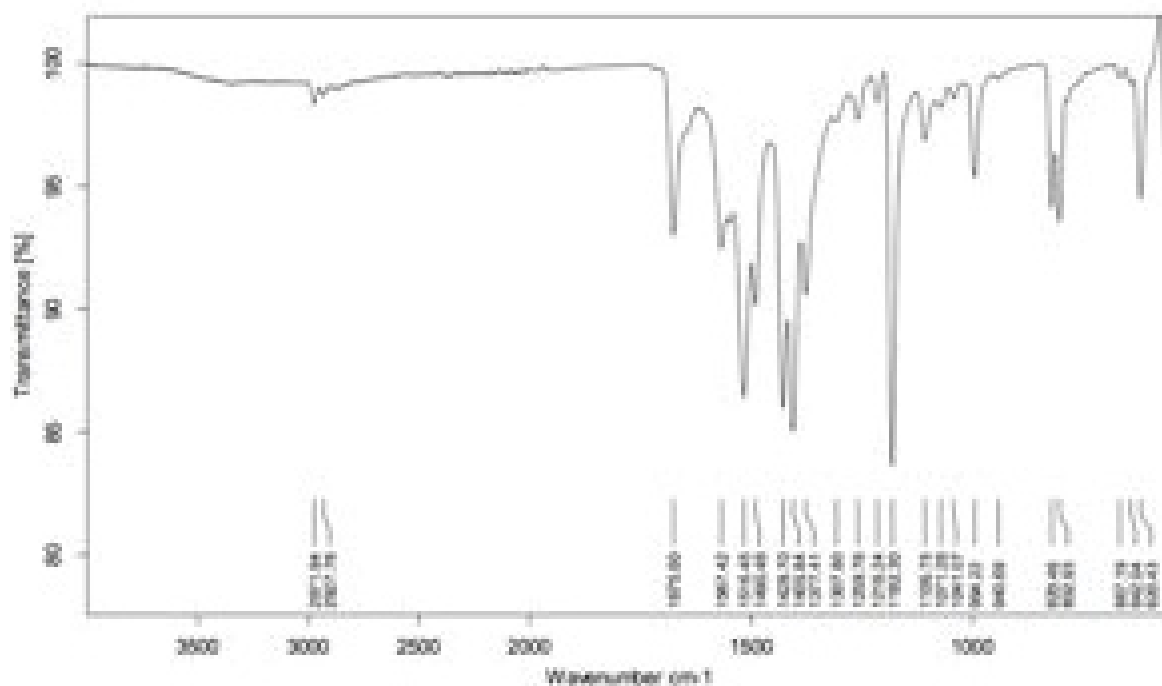
Fig. S15. FTIR (ATR) of compound $\{[Zn_4(\mu_4\text{-}O)(Me_2pzCO_2)_3] \cdot{\sim}2\ DEF\}_n$ **(2)**.
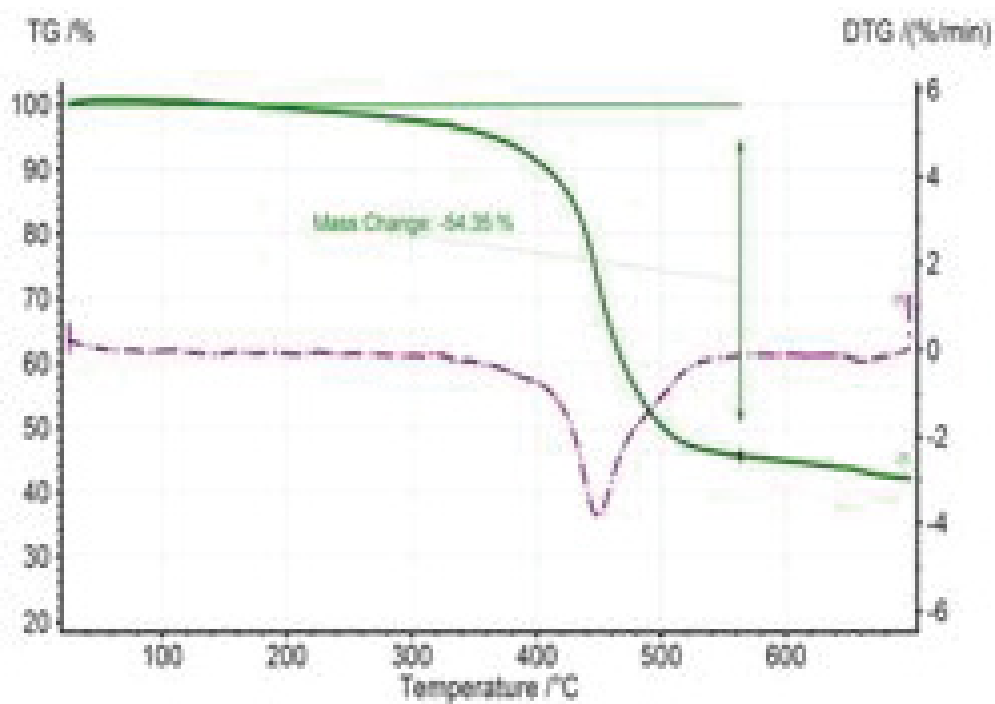
Fig. S16. TG/DTG of {[$Zn_4(\mu_4$-O)(Me_2pzCO_2)$_3$] ·~2 DEF}$_n$ (**2**).

{[Co$_4$(μ$_4$-O)(Me$_2$pzC$_6$H$_4$CO$_2$)$_3$] ·~6 DMSO ·~6 H$_2$O ·~2 DMF}$_n$ (3)

In a screw-capped Pyrex tube 20.2 mg (0.07 mmol) of Co(NO$_3$)$_2$· 6 H$_2$O and 10.0 mg (0.046 mmol) of 3,5-dimethyl-4-(4-carboxyphenyl)-1H-pyrazole (HMe$_2$pzC$_6$H$_4$CO$_2$H) were dissolved in 1.5 mL of a mixture of DMSO/DMF/MeOH (10:4:1). The solution was then heated from 115 °C to 130 within three days and kept for another two day at this temperature. Deep-violet cubic crystals (Fig. S17) were formed which were filtered and washed three times with 5 mL portions of DMF. They were dried under a vacuum of 10^{-2} Torr and stored under inert atmosphere.

Yield: 50 mg (70 % based on ligand).

FTIR (ATR): 3326, 2933, 2829, 1586, 1545, 1400, 1303, 1178, 1103, 1030, 1015, 867, 789, 716, 665, 634, 607 cm^{-1} (see Fig. S18).

We note that meaningful elemental analyses of MOFs are difficult to obtain due to solvent loss and different sample states (different states of dryness vs. not dried).

A total of 749 electrons per 2107 Å^3 was squeezed by PLATON in the structure refinement of **3** which corresponds to an appropriate number of solvent molecules per unit cell ($Z = 1$). There is one formula unit [Co$_4$(μ$_4$-O)(Me$_2$pzC$_6$H$_4$CO$_2$)$_3$], C$_{36}$H$_{30}$Co$_4$N$_6$O$_7$ per unit cell ($Z = 1$). The possible solvent molecules provide the following number of electrons:

molecule	number of electrons
DMSO, (CH$_3$)$_2$SO	42
H$_2$O	10
DMF, (CH$_3$)$_2$NCHO	40
MeOH, CH$_3$OH	18

TG/DTA (see Fig. S19) shows two weight losses of 9.32 and 12.0 wt% up to 300 °C.
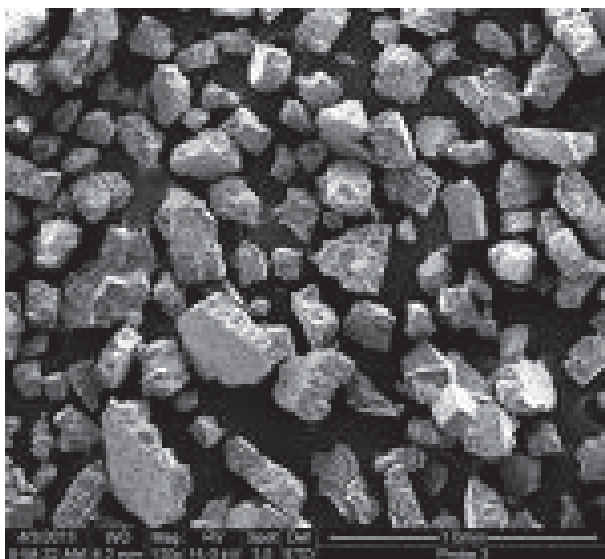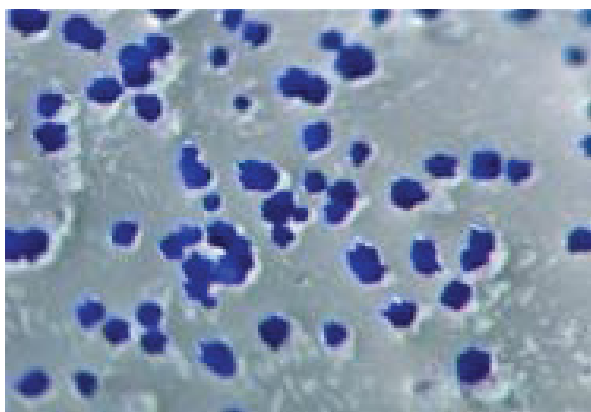
Fig. S17. Crystals of $\{[Co_4(\mu_4\text{-}O)(Me_2pzC_6H_4CO_2)_3] \cdot solvent\}_n$ (**3**) by optical photography and scanning electron microscopy. The cubic shape of the crystals already hints at a near cubic crystal system with the orthorhombic space group P222 and nearly identical cell constants a = 14.242(3), b = 14.278(3), c = 14.332(4) Å (see Table 2).
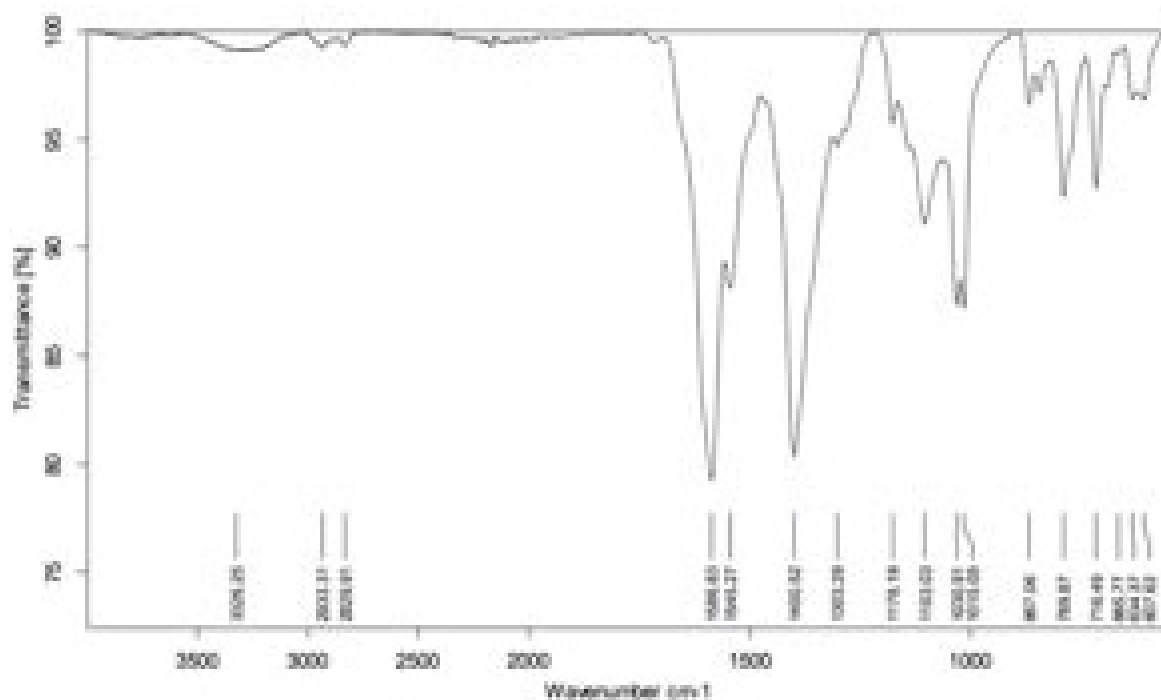
43

Fig. S18. FTIR (ATR) of compound {[Co$_4$(μ_4-O)(Me$_2$pzC$_6$H$_4$CO$_2$)$_3$] ·solvent}$_n$ (**3**).

A TGA of the dried compound shows a series of steady weight losses from the very beginning and up to over 500 °C with only narrow plateaus in between (Fig. S19). The first immediate mass loss of ~9% ends at ~100 °C where the second mass loss of ~12% starts which continous to about 300 °C or perhaps even 400 °C. These two differentiated weight loss ranges can be assigned to at least two different types of crystal solvent because of the three (four) different solvents DMSO, DMF, MeOH (and water) present in the crystallization process. Up to 100 °C methanol and water molecules may leave the compound. The weight loss from over 100 °C to ~400 °C indicates the removal of higher boiling/less volatile DMSO and DMF molecules.

Around 400 °C a steeper mass loss of ~14% starts, immediately followed by another steep mass loss of ~19.5%. These two mass losses are attributed to ligand decomposition (Fig. S19).

44
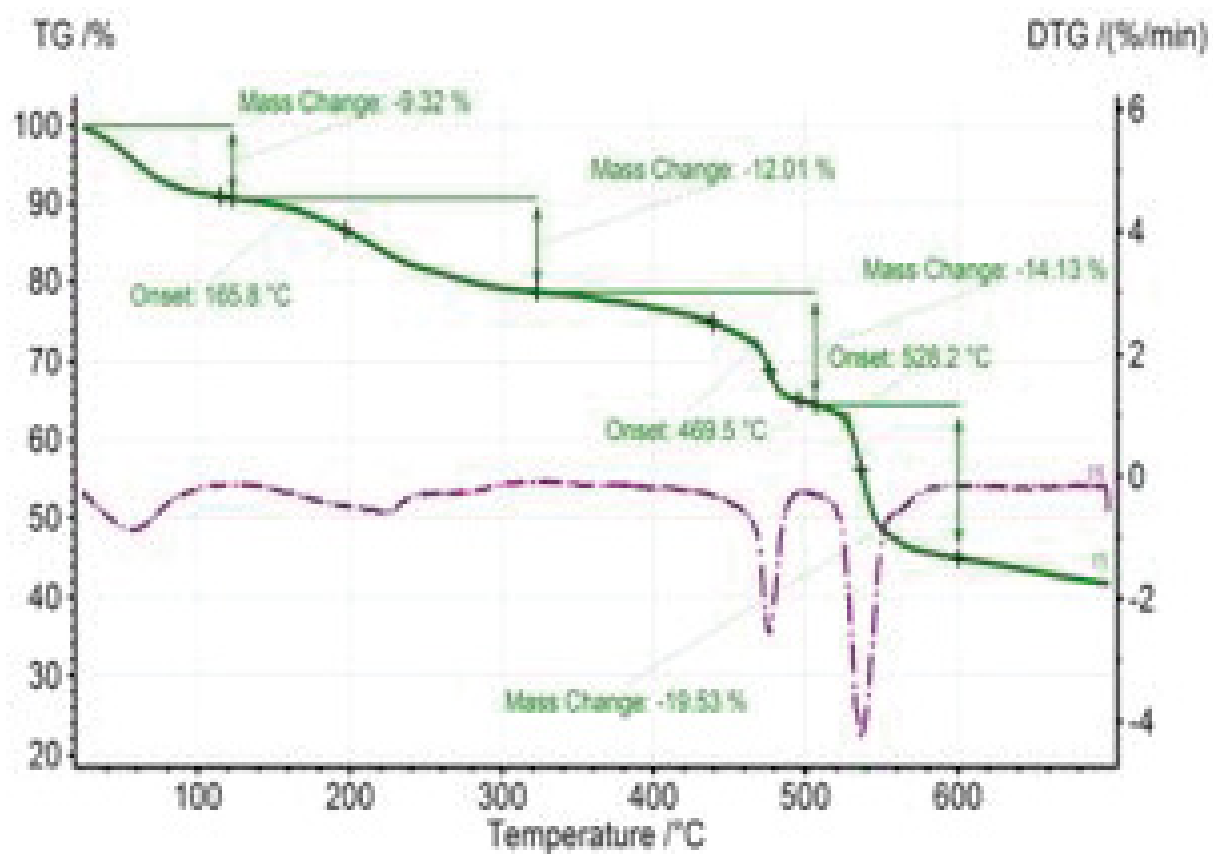
Fig. S19. TG/DTG of {[Co$_4$(μ_4-O)(Me$_2$pzC$_6$H$_4$CO$_2$)$_3$] ·solvent}$_n$ (**3**)

{[Zn$_4$(μ_4-O)(Me$_2$pzC$_6$H$_4$CO$_2$)$_3$] ·~3 DEF}$_n$ (4)

In a screw-capped Pyrex tube 18.0 mg (0.07 mmol) Zn(NO$_3$)$_2$ · 4 H$_2$O and 10.0 mg (0.046 mmol) 3,5-dimethyl-4-(4-carboxyphenyl)-1*H*-pyrazole (HMe$_2$pzC$_6$H$_4$CO$_2$H) were dissolved in 1.5 mL DEF. The solution was then heated to 140 °C within three days and kept for another two day at this temperature. Clear cubic crystals (Fig. S20) were formed which were filtered and washed three times with 5 mL portions of DEF. They were dried under a vacuum of 10^{-2} Torr and stored under inert atmosphere.Yield: 11.7 mg (60 % based on ligand).

FTIR (ATR): 2972, 2931, 2869, 1671, 1608, 1583, 1534, 1491, 1410, 1335, 1307, 1286, 1261, 1216, 1183, 1107, 1030, 1013, 941, 870, 850, 806, 784, 717, 699, 664, 637, 606, 588, 560 cm^{-1} (see Fig. S21).

We note that meaningful elemental analyses of MOFs are difficult to obtain due to solvent loss and different sample states (different states of dryness vs. not dried).
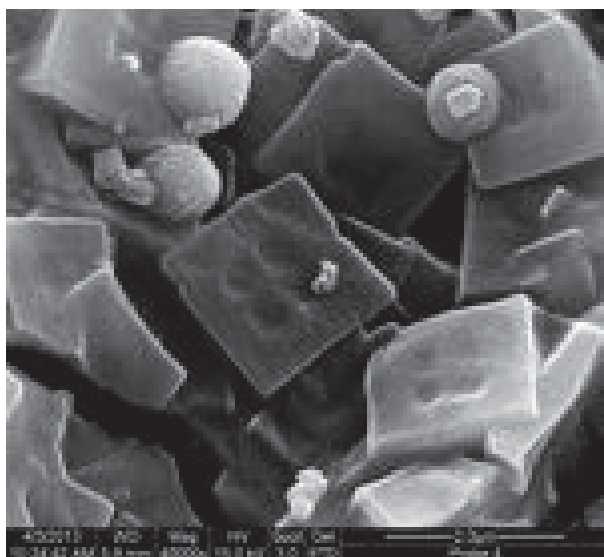
Fig. S20. Crystals of {[Zn$_4$(μ_4-O)(Me$_2$pzC$_6$H$_4$CO$_2$)$_3$] ·~3 DEF}$_n$ (**4**) by optical photography and scanning electron microscopy. The cubic shape of the crystals already hints at a near cubic crystal system most likely with the same orthorhombic space group P222 and nearly identical cell constants as for **3**.
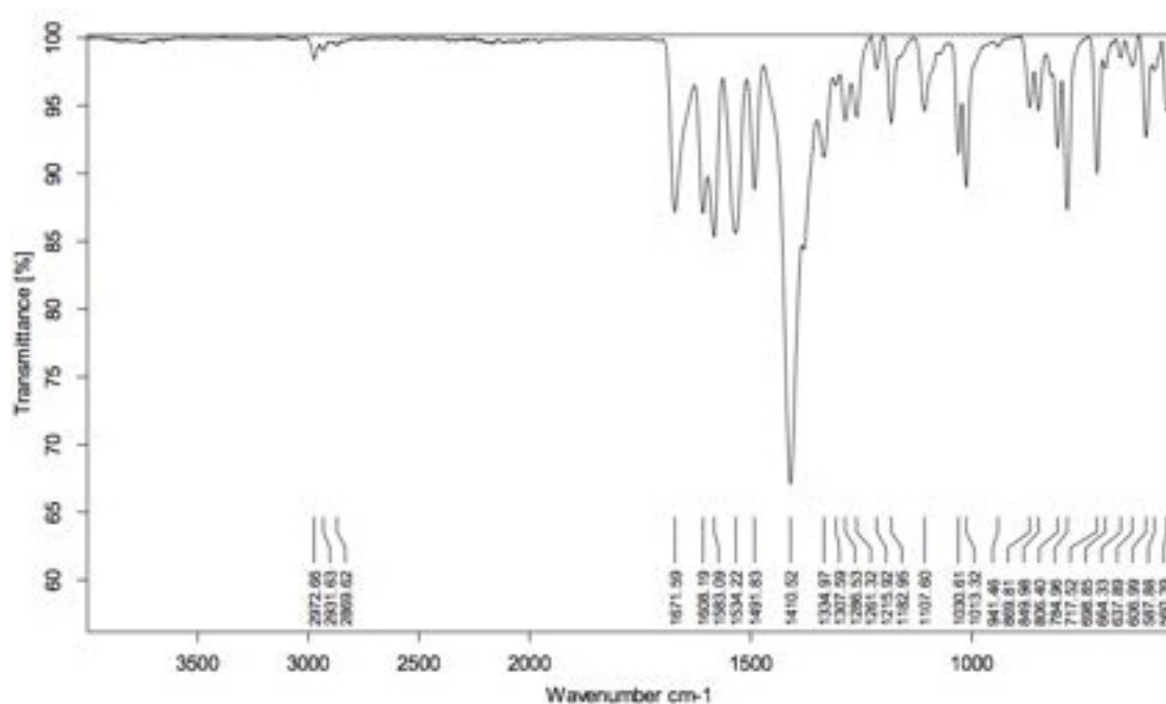

Fig. S21. FTIR (ATR) of compound {[Zn$_4$(μ_4-O)(Me$_2$pzC$_6$H$_4$CO$_2$)$_3$] ·~3 DEF}$_n$ (**4**).

A TGA of the complex shows a weight loss of ~28% from the very beginning up to 200 °C (Fig. S22). This immediate weight loss can be correlated to about three DEF molecules (theor. 25%). From 200 °C to ~450 °C the framework appears thermally stable. Over 450 °C the ligand decomposes with a weight loss of ~40%.
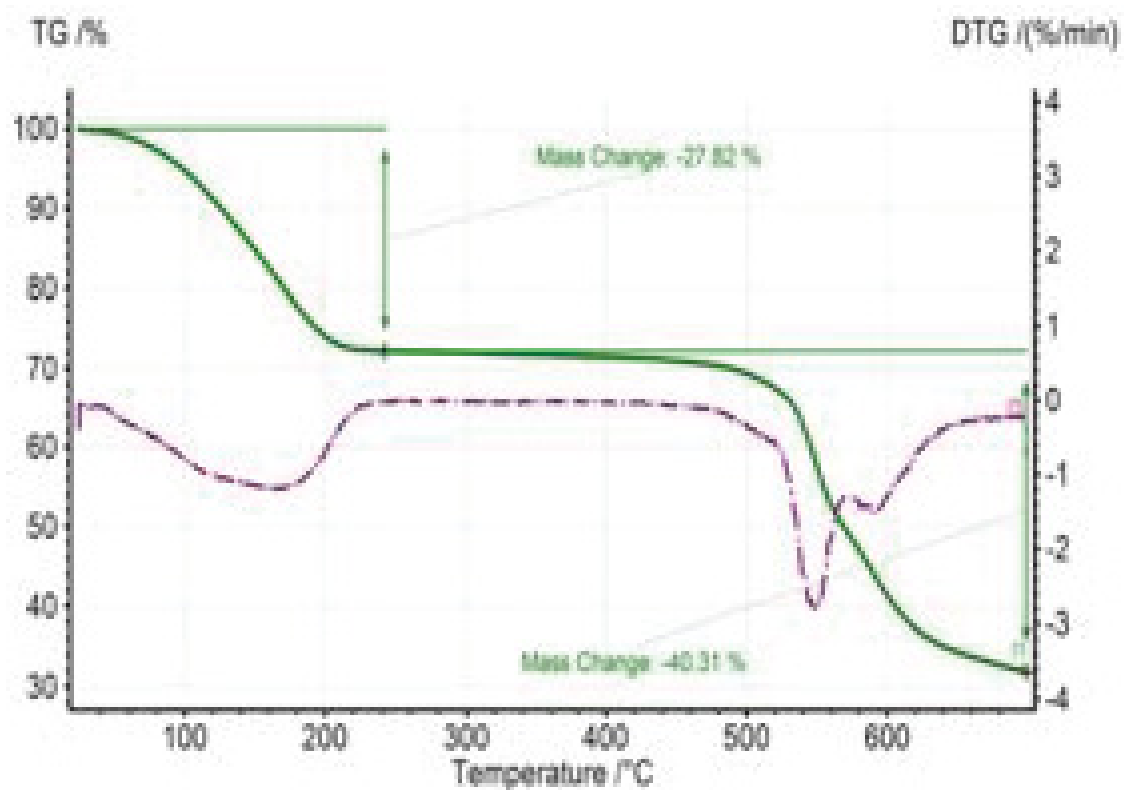
Fig. S22. TG/DTG of $\{[Zn_4(\mu_4\text{-}O)(Me_2pzC_6H_4CO_2)_3] \cdot \sim 3\ DEF\}_n$ (**4**).

Additional figures of building blocks and packing diagrams

[Zn$_4$(µ$_4$-O)(O$_2$C-C$_6$H$_4$-CO$_2$)$_3$], MOF-5:

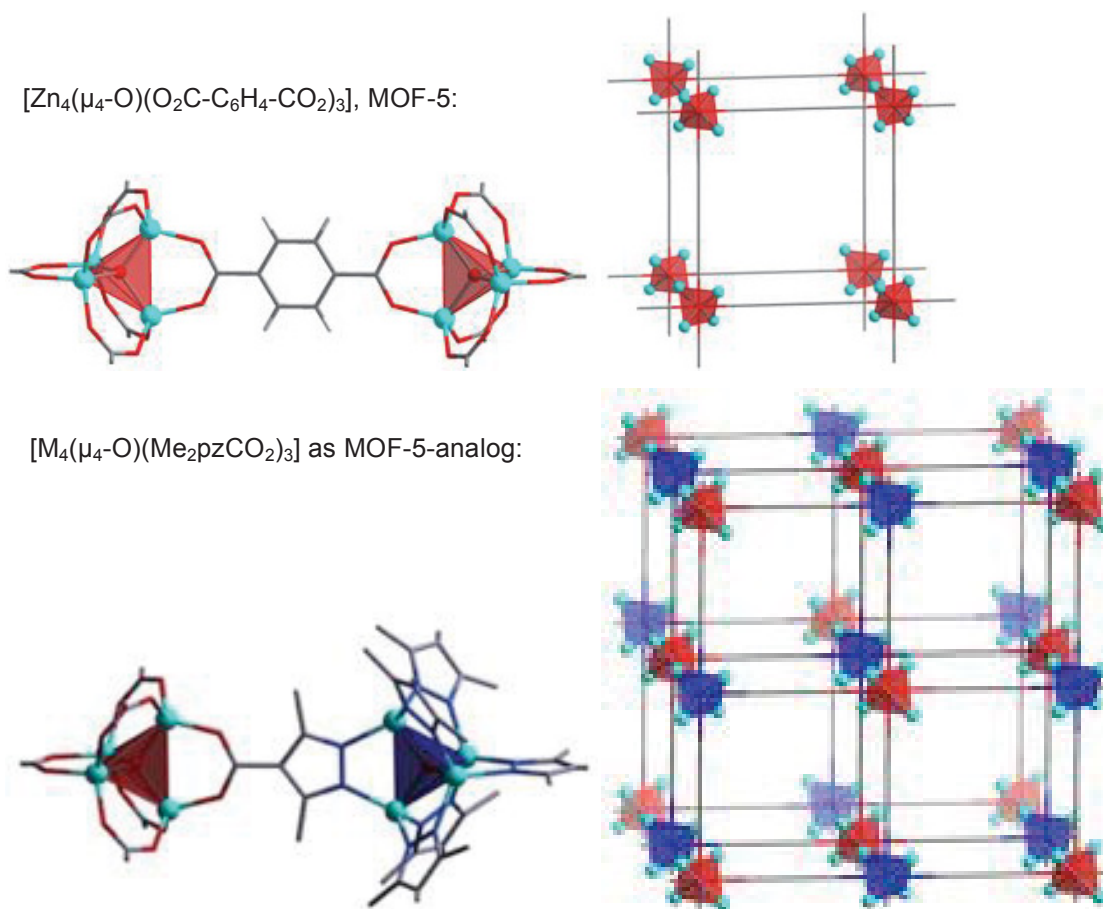[M$_4$(µ$_4$-O)(Me$_2$pzCO$_2$)$_3$] as MOF-5-analog:

Fig. S23. Building blocks and cubic *pcu-a* frameworks in MOF-5 and **1** (M = Co) or **2** (M = Zn) to illustrate the analogy. Colors: oxygen atoms red, nitrogen atoms blue, metal atoms cyan, carbon atoms grey, hydrogen atoms (in MOF-5) light grey.

The fixed alternating canting of the dimethylpyrazolate ring plane (cf. Fig. S24a) leads to alternating small (van der Waals diameter, Ø ~6 Å) and large pores (Ø ~11 Å) connected by small channels or pore apertures (Ø ~2.8 Å) (Fig. 24b). Failure of N$_2$ adsorption in **1** and **2** is presumably due to activated diffusion effects associated with the low thermal energy of N$_2$ relative to the high barrier for diffusion through the small 2.8-diameter pore apertures (cf. Fig. S24b). In other words, at slow thermal motion at 77 K the N$_2$ molecule will statistically only seldom approach the small pore aperture with the correct orientation for penetration, that is, at right angle with its molecule axis.
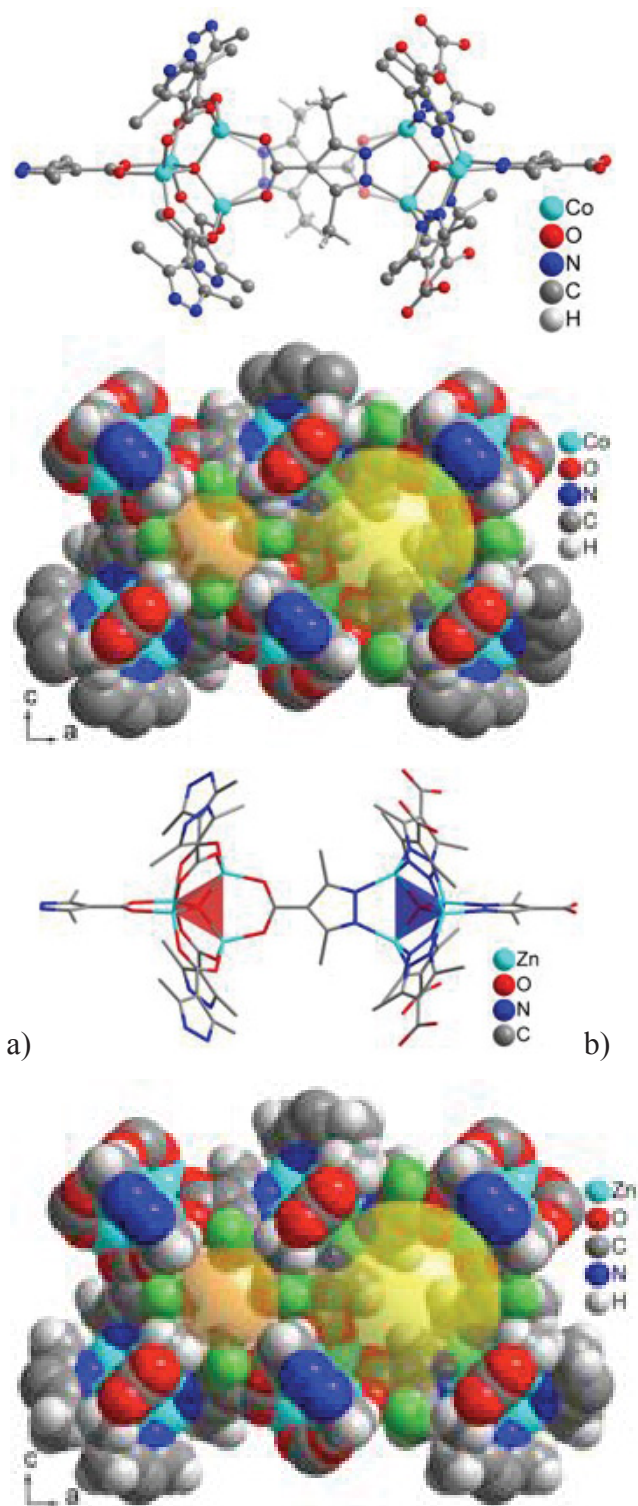
Fig. S24. Building units (a) in $[M_4(\mu_4\text{-}O)(Me_2pzCO_2)_3]$ (M = Co, **1**; Zn, **2**). Space-filling plots for M = Co and Zn in (b) show the alternating small (transparent orange sphere, diameter, $\emptyset = 6$ Å) and large (yellow sphere, $\emptyset = 11$ Å) cavities due to the alternating pyrazolate plane orientation with pore apertures (green spheres, $\emptyset = 2.8$ Å) in between.
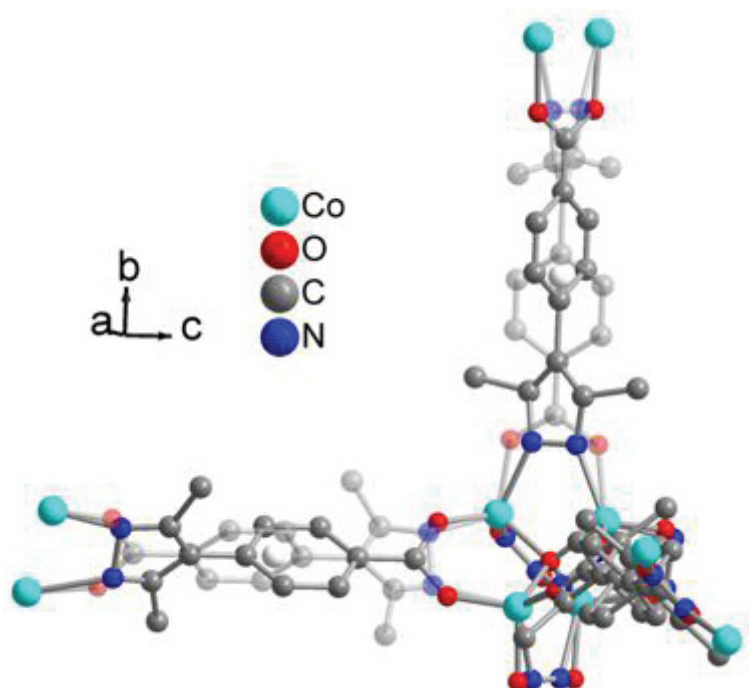
Fig. S25. Schematic presentation of the idealized crystallographically induced ligand disorder in **3** by showing two of the three symmetry-independent pyrazolate-benzoate ligands. As a visual aid one of the symmetry-related disordered orientations is shown transparent. The crystallographically-induced disorder is due to C2-axes passing through the white atom at the ligand center and running parallel to the unit-cell axes. Hydrogen atoms are not shown.
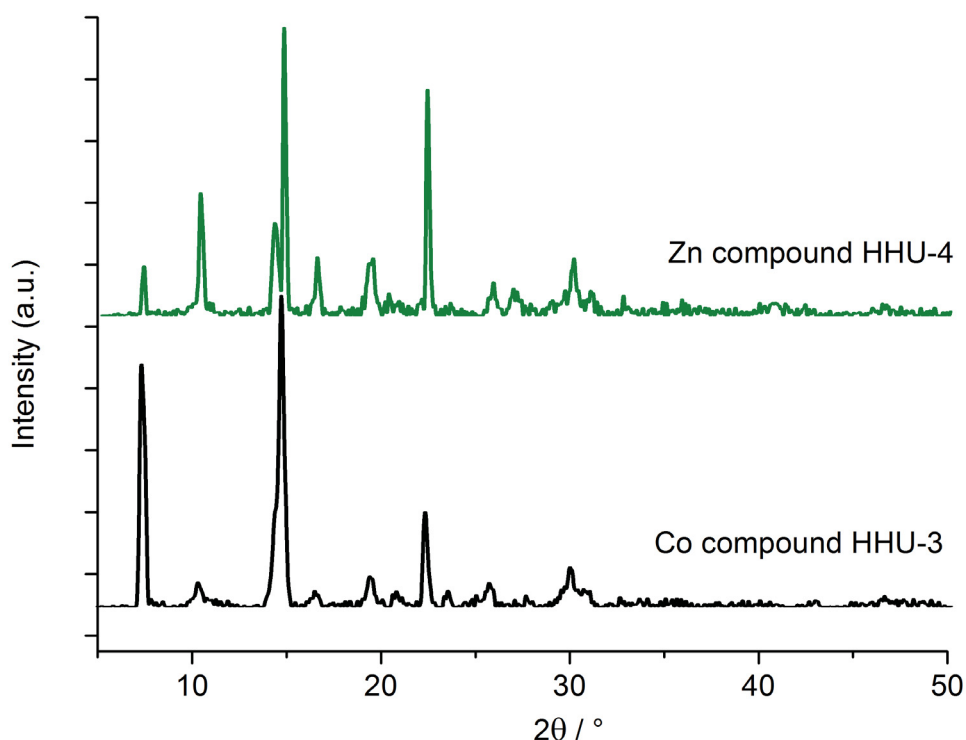

Fig. S26. Powder X-ray diffractograms of $[M_4(\mu_4\text{-}O)(Me_2pzC_6H_4CO_2)_3]$ (M = Co, **3**; Zn, **4**). Diffractograms were obtained on flat layer sample holders where at low angle the beam spot is strongly broadened so that only a fraction of the reflected radiation reaches the detector which leads to the low relative intensities measured at $2\theta < 10°$.
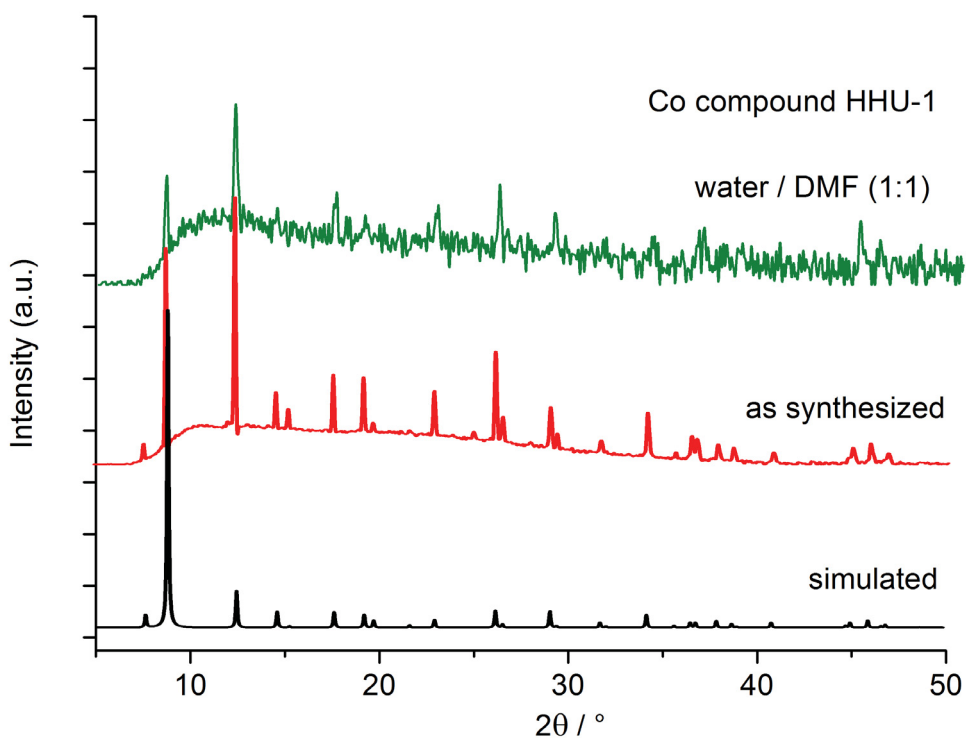
51

Fig. S27. Powder X-ray diffractograms of $[Co_4(\mu_4\text{-}O)(Me_2pzCO_2)_3]$ (**1**) before (as synthesized) and after the water stability test in water/DMF (1:1 volumetric mixture). The simulated diffractogram is based on the X-ray data refinement.

Diffractograms were obtained on flat layer sample holders where at low angle the beam spot is strongly broadened so that only a fraction of the reflected radiation reaches the detector which leads to the low relative intensities measured at $2\theta < 10°$. Diffractograms for Co compounds often have a high background because of Co-based X-ray fluorescence (see Daugherty, K. E.; Robinson, R. J.; Mueller, J. I. *Analytical Chemistry* **1964**, 36, 1869–1870.)
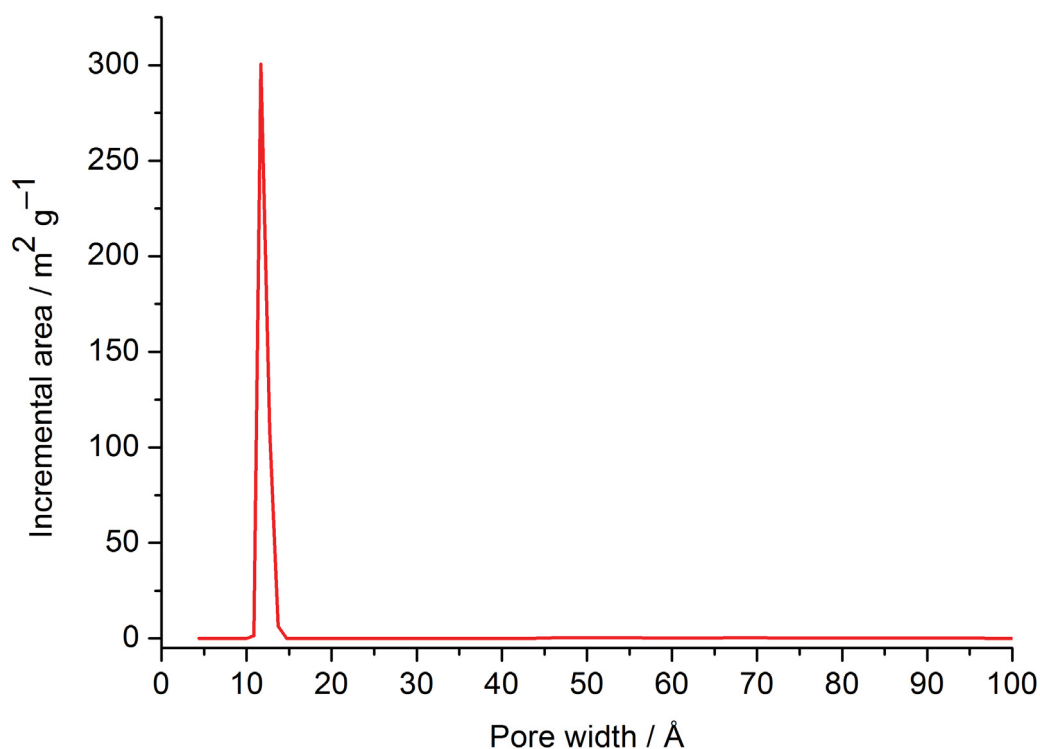
Fig. S28a. Pore size distribution curve of $\{[Co_4(\mu_4\text{-}O)(Me_2pzCO_2)_3]\}_n$ (activated **1**) from DFT calculation (Ar on carbon, slit based model) based on argon adorption isotherm (cf. Fig. 4).
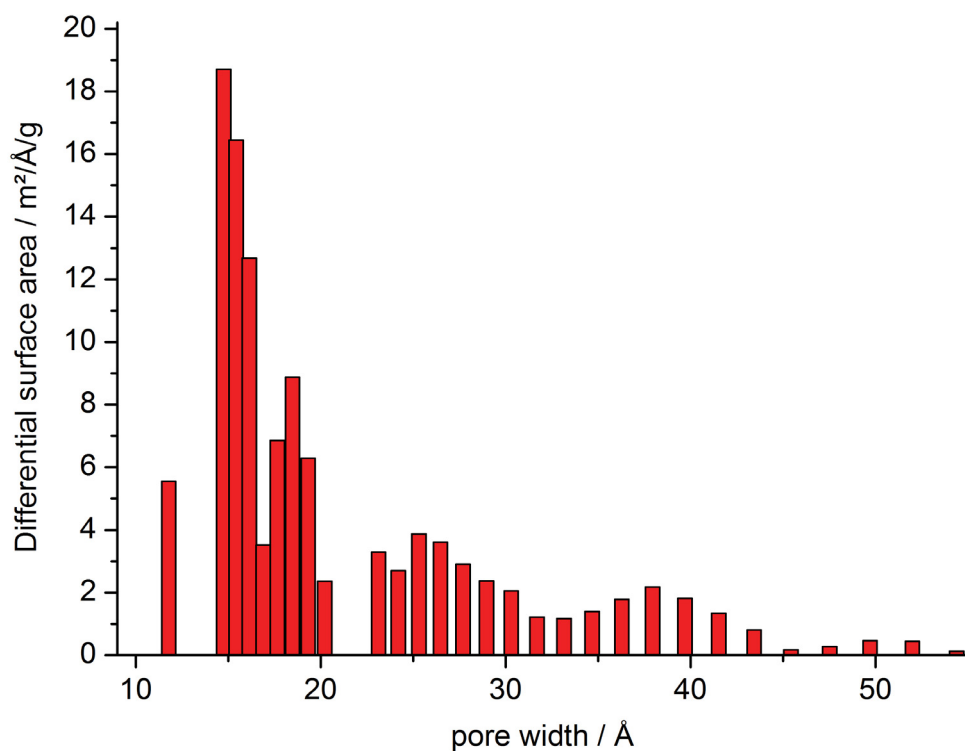

Fig. S28b. Differential surface area curve of $\{[Co_4(\mu_4\text{-}O)(Me_2pzC_6H_4CO_2)_3]\}_n$ (activated **3**) from DFT calculation (N_2 at 77 K on carbon, slit pore, NLDFT equilibrium model) based on N_2 adorption isotherm (cf. Fig. 6).

Hydrogen, carbon dioxide and methane gas sorption studies

From two adsorption isotherms acquired at different temperatures T_1 and T_2 (Fig. 5b), the differential heat of adsorption $\Delta H_{ads,diff}$ can be calculated for any amount of adsorbed substance after determining the required relative pressures p_1 and p_2. A modified form of the Clausius-Clapeyron equation is used (eq (1)).[4] $\Delta H_{ads,diff}$ was calculated over the whole adsorption range from the 77 K and 87 K isotherms for H_2 in **1** (Fig. 5b).

$$\Delta H_{ads,diff} = -R ln\left(\frac{p_2}{p_1}\right)\frac{T_1 T_2}{T_2 - T_1} \qquad (1)$$

The heat of adsorption for H_2 in **1** is determined to 5-6 kJ/mol. The increase with coverage is explained by the sequential filling of the large cavities, small cavities and eventually the channel volume with increasing adsorbate–surface interactions.
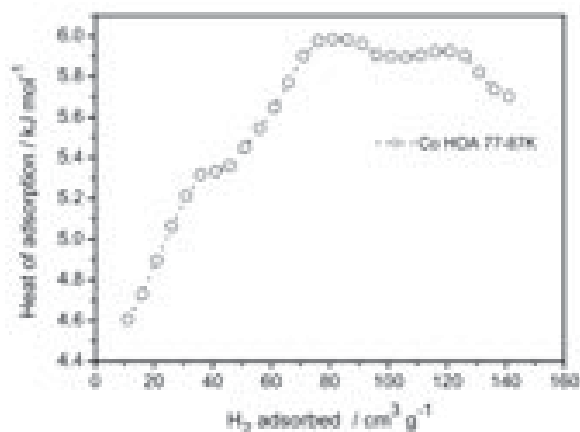

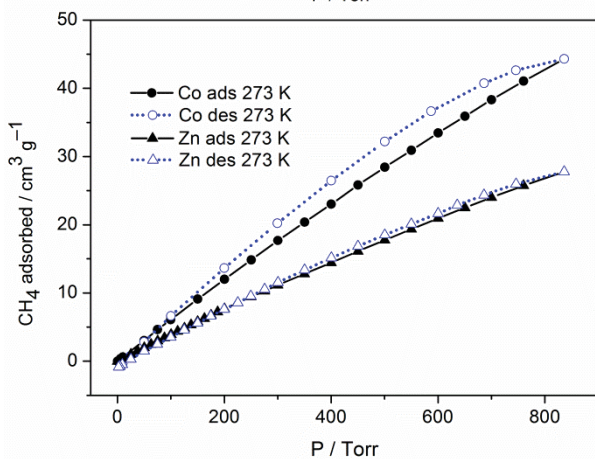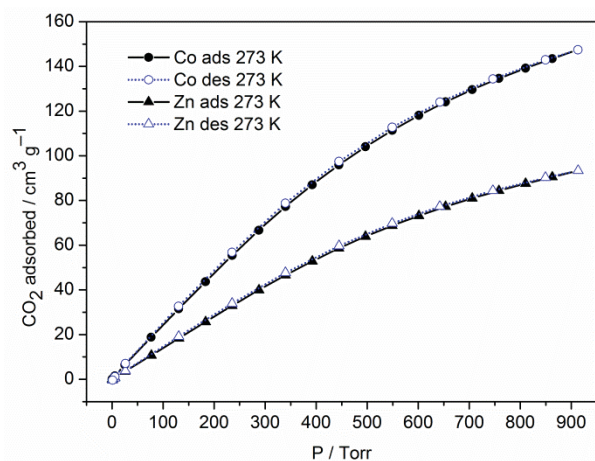**Fig. S29.** Heat of adsorption for H_2 in **1** at 77-87 K.

[4] F. Rouquerol, J. Rouquerol and K. Sing, *Adsorption by powders and porous solids*, (F. Rouquerol, J. Rouquerol, K. Sing, Eds.), Academic Press, San Diego, 1999, vol. 11.

Fig. S30. (a) CO_2 and (b) CH_4 sorption isotherms for **1** (Co) and **2** (Zn).
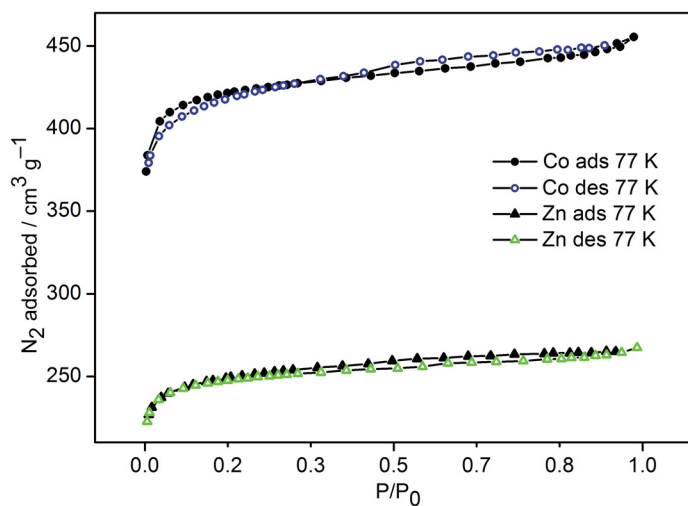
Fig. S31. N_2 sorption isotherms for **3** (Co) and **4** (Zn).
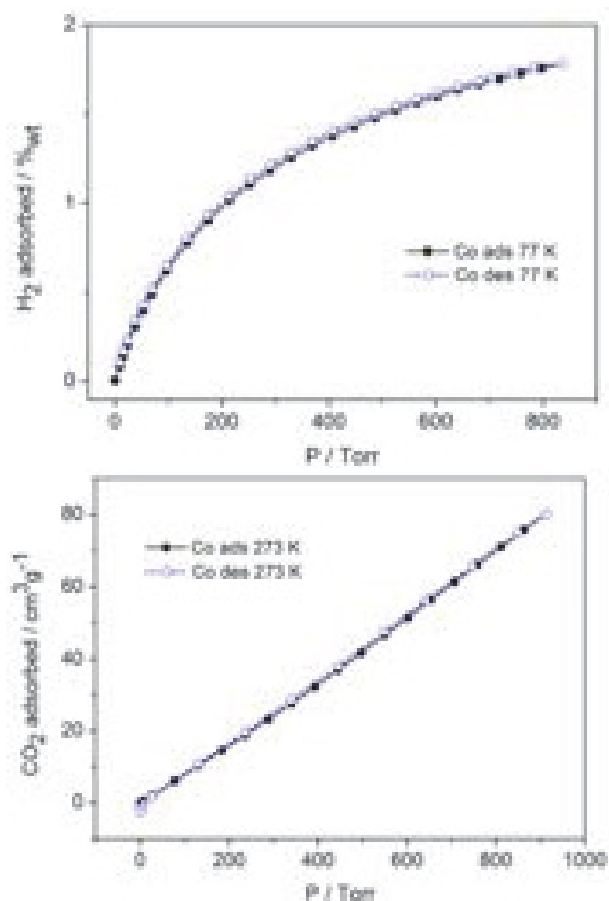
(a)   (b)

Fig. S32. (a) H_2 and (b) CO_2 sorption isotherms for **3** (Co).

Table S1 Porosity data for **3** and **4** from N_2 isotherms at 77 K.

Compd	S_{BET} [a]	S_{Lang}	V_{tot} [b]
	(m^2/g)	(m^2/g)	(cm^3/g)
3	1072	1195	0.44
4	980	1063	0.41

[a] Calculated BET surface area over the pressure range 0.01-0.05 P/P_0; [b] total pore volume at $P/P_0 = 0.95$.

Gas selectivity

The ratio of the initial slopes in the Henry region of the adsorption isotherms (Fig. S33, Fig. S34)[5,6] determines the selectivities exhibited by **1** and **2** for adsorption of CO_2 over CH_4. **1** shows a selectivity ratio for $CO_2:CH_4$ of 4:1 at 273 K. The selectivity does not only depend on the size of the gas components (kinetic diameter: CO_2 3.3 Å, CH_4 3.8) but also on the polarizability of the surface and of the gas components.

Selectivities were estimated from the ratio of the initial slopes in the Henry region of the adsorption isotherms (Table S2).

Table S2 Initial slopes of adsorption isotherms and selectivities for $CO_2:N_2$ and $CO_2:CH_4$ at 273.

Compounds	initial slopes for gas adsorption isotherms	
	CO_2	CH_4
1 (Co)	0.2465	0.06146
2 (Zn)	0.1398	0.03913
	gas selectivities	
	$CO_2:CH_4$ selectivity at 273 K	
1 (Co)	~4:1	
2 (Zn)	~3.5:1	

[5] V. Abetz, T. Brinkmann, M. Dijkstra, K. Ebert, D. Fritsch, K. Ohlrogge, D. Paul, K. V. Peinemann, S. Pereira-Nunes, N. Scharnagl and M. Schossig, *AIChE J.*, **2006**, *8*, 328-358.

[6] Y.-S. Bae, O. K. Farha, A. M. Spokoyny, C. A. Mirkin, J. T. Hupp and R. Q. Snurr, *Chem. Commun.*, **2008**, 4135-4137.
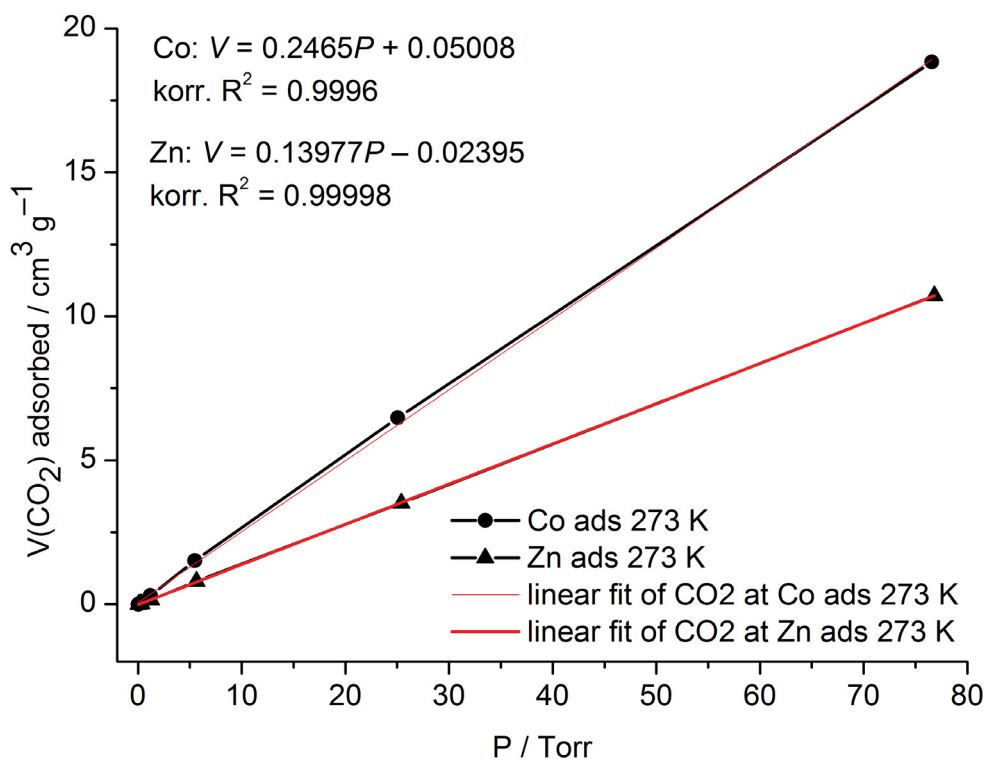
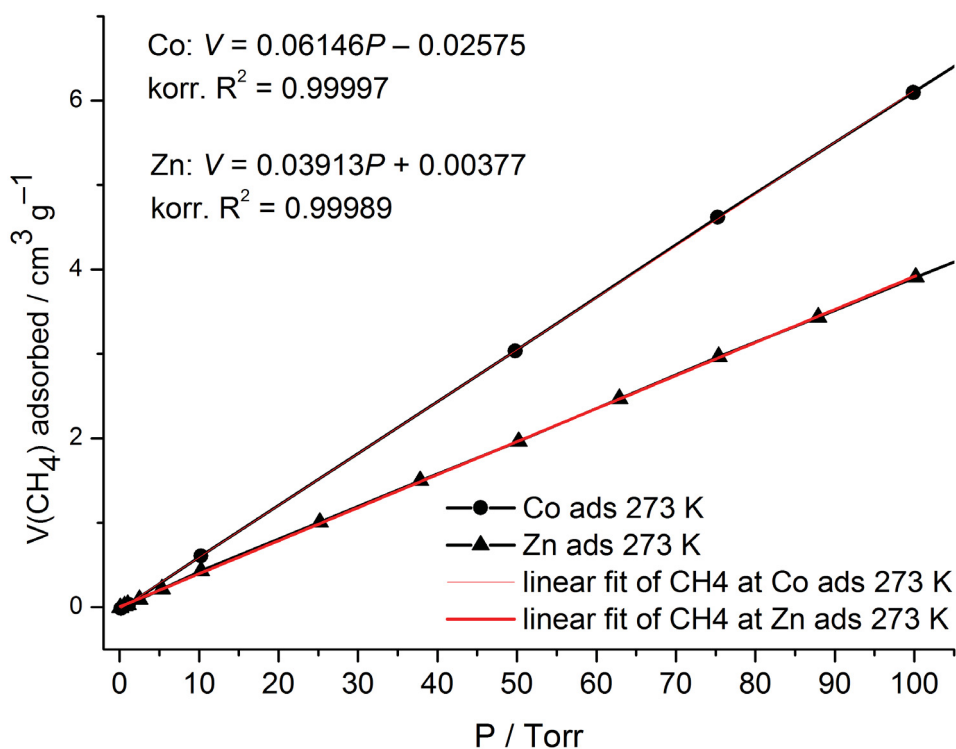**Fig. S33.** The initial slope in the Henry region of the adsorption isotherms of CO_2 of **1** and **2** at 273 K.

Fig. S34. The initial slope in the Henry region of the sorption isotherms of CH_4 of **1** and **2** at 273 K.

59

2.2 Charge-Assisted Hydrogen-Bonded Networks of NH_4^+ and $[Co(NH)_6)]^{3+}$ with the New Linker Anion of 4-Phosphono-Biphenyl-4'-Carboxylic Acid

Christian Heering, Bahareh Nateghi and Christoph Janiak

Abstract:

The new linker molecule 4-phosphono-biphenyl-4'-carboxylic acid ($H_2O_3P\text{-}(C_6H_4)_2\text{-}COOH$, H_3BPPA) has been structurally elucidated in hydrogen-bonded networks with the ammonium cation $NH_4(H_2BPPA)(H_3BPPA)$ (**1**) and the hexaamminecobalt(III) cation $[Co(NH_3)_6](BPPA) \cdot 4H_2O$ (**2**). The protic O-H and N-H hydrogen atoms were found and refined in the low-temperature single-crystal X-ray structures. The hydrogen bonds in both structures are so-called charge-assisted; that is, the H-bond donor and/or acceptor carry positive and/or negative ionic charges, respectively. The H-bonded network in **1** consists of one formally mono-deprotonated 4-phosphonato-biphenyl-4'-carboxylic acid group; that is, a H_2BPPA^- anion and a neutral H_3BPPA molecule, which together form a 3D hydrogen-bonded network. However, an almost symmetric resonance-assisted hydrogen bond (RAHB) bond [$O\cdots H$ = 1.17(3) and 1.26(3) Å, $O\cdots H\cdots O$ = 180(3)°] signals charge delocalization between the formal H_2BPPA^- anion and the formally neutral H_3BPPA molecule. Hence, the anion in **1** is better formulated as $[H_2BPPA\cdots H\cdots H_2BPPA]^-$. In the H-bonded network of **2** the 4-phosphonato-biphenyl-4'-carboxylic acid is triply deprotonated, $BPPA^{3-}$. The $[Co(NH_3)_6]^{3+}$ cation is embedded between H-bond acceptor groups, $-COO^-$ and $-PO_3^{2-}$ and H_2O molecules. The incorporation of sixteen H_2O molecules per unit cell makes **2** an analogue of the well-studied guanidinium sulfonate frameworks.

Article

Charge-Assisted Hydrogen-Bonded Networks of NH₄⁺ and [Co(NH₃)₆]³⁺ with the New Linker Anion of 4-Phosphono-Biphenyl-4′-Carboxylic Acid

Christian Heering, Bahareh Nateghi and Christoph Janiak *

Institut für Anorganische Chemie und Strukturchemie, Universitätsstra*ße* 1, 40225 Düsseldorf, Germany;
christian.heering@hhu.de (C.H.); bahareh.nateghi@hhu.de (B.N.)
* Correspondence: janiak@hhu.de; Tel.: +49-211-81-12286

Abstract: The new linker molecule 4-phosphono-biphenyl-4′-carboxylic acid (H_2O_3P-$(C_6H_4)_2$-COOH, H_3BPPA) has been structurally elucidated in hydrogen-bonded networks with the ammonium cation $NH_4(H_2BPPA)(H_3BPPA)$ (**1**) and the hexaamminecobalt(III) cation $[Co(NH_3)_6](BPPA)\cdot 4H_2O$ (**2**). The protic O-H and N-H hydrogen atoms were found and refined in the low-temperature single-crystal X-ray structures. The hydrogen bonds in both structures are so-called charge-assisted; that is, the H-bond donor and/or acceptor carry positive and/or negative ionic charges, respectively. The H-bonded network in **1** consists of one formally mono-deprotonated 4-phosphonato-biphenyl-4′-carboxylic acid group; that is, a H_2BPPA^- anion and a neutral H_3BPPA molecule, which together form a 3D hydrogen-bonded network. However, an almost symmetric resonance-assisted hydrogen bond (RAHB) bond [O···H = 1.17 (3) and 1.26 (3) Å, O···H···O = 180 (3)°] signals charge delocalization between the formal H_2BPPA^- anion and the formally neutral H_3BPPA molecule. Hence, the anion in **1** is better formulated as $[H_2BPPA···H···H_2BPPA]^-$. In the H-bonded network of **2** the 4-phosphonato-biphenyl-4′-carboxylic acid is triply deprotonated, $BPPA^{3-}$. The $[Co(NH_3)_6]^{3+}$ cation is embedded between H-bond acceptor groups, $-COO^-$ and $-PO_3^-$ and H_2O molecules. The incorporation of sixteen H_2O molecules per unit cell makes **2** an analogue of the well-studied guanidinium sulfonate frameworks.

Keywords: hydrogen-bonded network; phosphonate-carboxylate; symmetric hydrogen bond; crystal engineering; charge-assisted H-bonds

1. Introduction

The organophosphonic acid function, which has a pK_{a1} of 2.0 for the first and a pK_{a2} of 6.59 for the second proton, is capable of forming strong metal-to-ligand coordinative bonds in thermodynamically stable complexes with high stability constants [1]. Metal organophosphonate compounds are multifunctional organic-inorganic hybrid materials and as open frameworks can be regarded in between zeolite-like [1,2] and metal-organic framework materials [3,4], whereas phosphonate metal-organic frameworks (MOFs) are considerably rarer than MOFs with carboxylate linkers, with phosphonates forming stronger bonds to metals than carboxylate groups [3]. Metal organophosphonates are stable in water or aqueous environment [5]. The use of metal phosphonates in catalysis, luminescence [6], ion or proton exchange or conductivity [7,8] and in separation is discussed and investigated [9]. Further, cobalt and iron organophosphonates are investigated for their magnetic properties [10–13]. Metal phosphonates are also promising porous materials [14,15], and can be reversibly hydrated and dehydrated [16].

Organophosphonates can contain additional functional groups such as carboxylate, hydroxyl or amino in the organo-moiety which presents a tunable functionality with a wide variety of structural motifs and properties [1,3,17]. Carboxy-phosphonates (Scheme 1) can be seen as intermediates between pure carboxylates and pure phosphonates, sharing synergies of both ligand classes. Carboxy-phosphonates can form porous or 3D metal-ligand networks [18–20]. Weng *et al.* described a 3D zinc carboxy-phosphonate, ZnPC-2, as a material for CO_2 adsorption [21].
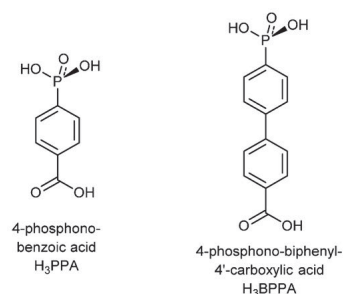
Scheme 1. Examples of phosphono-carboxylic acids.

Various metal complexes have been synthesized with a ligand from deprotonated 4-phosphono-benzoic acid, including the metals barium [22], cobalt [23], copper [23], europium [24], lead [20], lithium [25], silver [26], strontium [27], thorium [28], titanium [29], uranium [28] and zinc [30,31]. However, the extended biphenyl-based variant 4-phosphono-biphenyl-4'-carboxylic acid (H_3BPPA) was unknown so far (Scheme 1).

Herein, we present the new linker 4-phosphono-biphenyl-4'-carboxylic acid, H_3BPPA, and its deprotonated structure in hydrogen-bonded networks with NH_4^+ and $[Co(NH_3)_6]^{3+}$ cations.

2. Results and Discussion

4-Phosphono-biphenyl-4'-carboxylic acid H_3BPPA has been synthesized, following a known procedure by Merkushev *et al.* from 4-biphenyl carboxylic acid through the intermediates 4'-iodo-biphenyl-4-carboxylic acid [32] and its methyl ester, followed by the nickel(II)-catalyzed conversion to a phosphonate ester, which after hydrolysis gave H_3BPPA (Scheme 2).
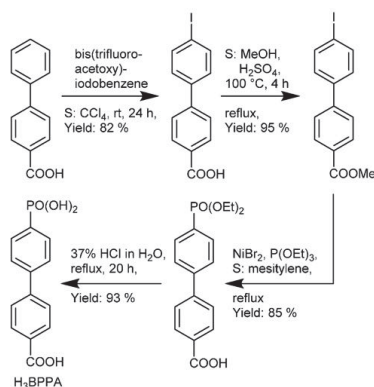
Scheme 2. Reaction sequence for the synthesis of H_3BPPA from 4-biphenyl carboxylic acid.

Neutralization of H_3BPPA with one equivalent of ammonium acetate yielded colorless crystals of formula $NH_4(HO_3P\text{-}(C_6H_4)_2\text{-}COOH)(H_2O_3P\text{-}C_6H_4\text{-}C_6H_4\text{-}COOH)$ (**1**). The ammonium monohydrogenphosphonato-biphenyl-carboxylic acid crystallized with one molecule of the free H_3BPPA acid. The best results were obtained using a 1:1 ratio, though less ammonium acetate also led to product formation of lower quality. When the neutralization of H_3BPPA was carried out with excess conc. aqueous NH_3 instead of stoichiometric ammonium acetate, the same product, **1**, was formed, albeit of lower purity. Importantly, no complete or even twofold deprotonation of H_3BPPA was achieved in that way.

The asymmetric unit of **1** consists of the ammonium-cation, and formally a H_2BPPA$^-$ anion and a neutral H_3BPPA molecule (see below) (Figure 1a). The H_2BPPA$^-$ anion is derived by mono-deprotonation of the phosphonic acid group. The protic O–H and N–H hydrogen atoms were found and refined with $U_{eq} = 1.5\ U_{eq}(O,N)$. The three building blocks form a three-dimensional (3D) hydrogen bonded network.

The carboxylic acid groups are oriented towards each other with the typical tail-to-tail arrangement, also known as $R_2^2(8)$-motif in the Etter-notation (Figure 1b) [33].

The biphenyl systems of the BPPA molecules are in nearly planar geometry with 0.31 (14) and 2.79 (14)° for the dihedral angles between the aryl ring planes, and 1.7 (2)° and 3.3 (2)° for the dihedral angle between −COOH and its aryl ring in the P1 and P2 molecule, respectively. The shape of the thermal ellipsoids of the carboxyl oxygen atoms O1, O2, O6, and O7 is indicative of some rotational movement (vibration) around the (carboxyl)C–C(aryl) bond (yet, no split refinement was suggested by SHELX from the principal mean square atomic displacements). Despite the presence of the biphenyl π-systems in **1**, there are no π-π interactions [34] and only few intermolecular C–H···π [35] are evident. The angle is 57° for the plane formed by one biphenyl system to its neighbor.

The ammonium cation engages all of its four (found and refined) N–H bonds in the hydrogen network to four different phosphono groups. The ammonium cations and phosphono groups form hydrogen-bonded layers parallel to the *ab*-plane, separated by the biphenyl-carboxylic acid parts (Figure 1c). Ammonium benzenephosphonate, $NH_4(HO_3PC_6H_5)$ [36], consists of a layered structure due to hydrogen bonds, with a similar motif to that of **1**.
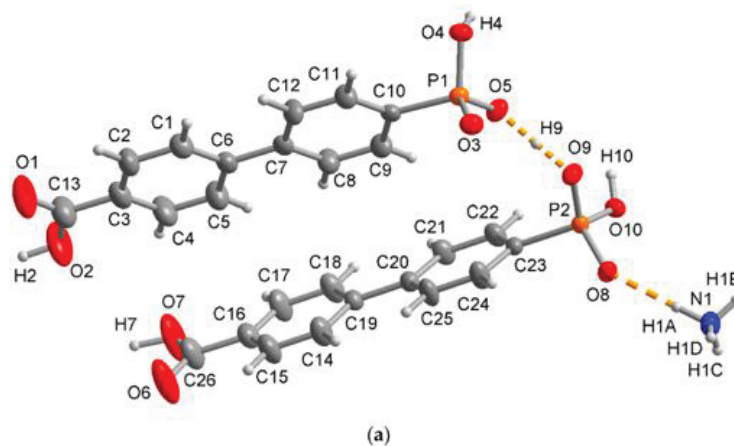

(a)

Figure 1. *Cont*.

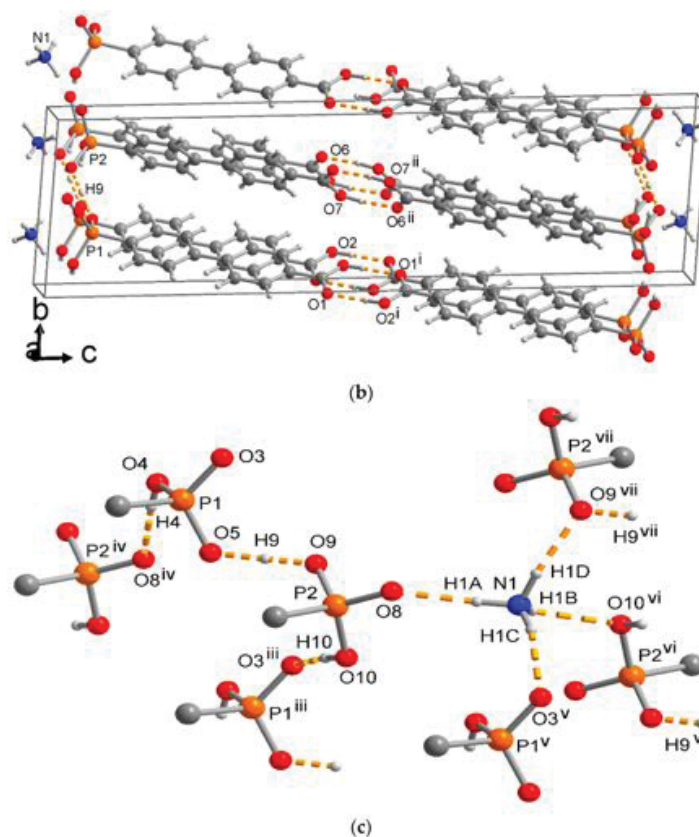**Figure 1.** (**a**) Asymmetric unit of **1** (50% thermal ellipsoids); (**b**) unit-cell packing diagram with tail-to-tail arrangement of the carboxylic acid groups (showing only the carboxyl and the O9-H-O5 H bonds for clarity); and (**c**) full hydrogen-bonding arrangement around the NH_4^+ cation and the phosphonate and phosphonic acid groups. Details of the H-bonding interactions (orange dashed lines) are given in Table 1, selected non-hydrogen bonds and angles in Table 2. Symmetry transformations: i = −1 − x, −y, 1 − z; ii = −x, 1 − y, 1 − z; iii = 1 + x, y, z; iv = x, −1 + y, z; v = 1 + x, 1 + y, z; vi = 2 − x, 2 − y, −z; vii = 1 − x, 2 − y, −z.

Table 1. Details of the hydrogen bonding interactions in **1** [a].

| D–H···A	D–H [Å]	H···A [Å]	D···A [Å]	D–H···A [°]	Symmetry Transformations
N1–H1A···O8	0.94 (3)	1.90 (3)	2.840 (3)	177 (3)	
N1–H1B···O10 vi	0.86 (3)	2.25 (3)	2.945 (3)	138 (3)	vi = 2 − x, 2 − y, −z
N1–H1C···O3 v	0.84 (3)	2.00 (3)	2.817 (3)	165 (3)	v = 1 + x, 1 + y, z
N1–H1D···O9 vii	0.95 (3)	1.92 (3)	2.845 (3)	164 (2)	vii = 1 − x, 2−y, −z
O2–H2···O1 i	0.94 (5)	1.71 (5)	2.623 (3)	164 (4)	i = −1 − x, −y, 1 − z
O4–H4···O8 iv	0.78 (3)	1.78 (3)	2.563 (2)	175 (3)	iv = x, −1 + y, z
O7–H7···O6 ii	0.99 (5)	1.66 (5)	2.642 (3)	172 (4)	ii = −x, 1 − y, 1 − z
O9–H9···O5	1.17 (3)	1.26 (3)	2.428 (2)	180 (3)	
O10–H10···O3 iii	0.83 (3)	1.72 (3)	2.537 (2)	170 (3)	iii = 1 + x, y, z

Notes: [a] D = donor, A = acceptor.

Table 2. Selected bond lengths [Å] and angles [°] in **1**.

P1–O3	1.4975 (18)	P2–O8	1.5045 (18)
P1–O5	1.5174 (18)	P2–O9	1.5190 (18)
P1–O4	1.5583 (19)	P2–O10	1.5553 (19)
P1–C10	1.787 (3)	P2–C23	1.796 (3)
C13–O1	1.235 (4)	C26–O6	1.230 (4)
C13–O2	1.283 (4)	C26–O7	1.275 (4)
O3–P1–O5	115.63 (11)	O8–P2–O9	112.38 (11)
O3–P1–O4	107.83 (10)	O8–P2–O10	109.16 (10)
O5–P1–O4	108.78 (11)	O9–P2–O10	110.04 (10)
O3–P1–C10	109.35 (11)	O8–P2–C23	109.32 (11)
O5–P1–C10	107.54 (11)	O9–P2–C23	108.76 (11)
O4–P1–C10	107.44 (11)	O10–P2–C23	107.04 (11)

Noteworthy, the H-bond O9–H9···O5 refined to an almost symmetric O9···H9···O5 hydrogen bridge with very similar distances of the H atom to both oxygen neighbors (1.17 (3) and 1.26 (3) Å) and a 180 (3)° O–H···O bond angle. This symmetric resonance-assisted hydrogen bond (RAHB) [37–41] O···H···O signals charge delocalization between the formal H_2BPPA^- anion (of P2) and the formally neutral H_3BPPA molecule (of P1). Hence, the anion is better formulated as $[H_2BPPA···H···H_2BPPA]^-$.

The interpretation of delocalized anion charge over the two phosphono groups is in agreement with the P–O bond lengths (Scheme 2). In each phosphonato group, there is a longer P–O bond of ~1.56 Å and two shorter P–O bonds between 1.50–1.52 Å. The P–O(H) bonds are 1.5583 (19) Å and 1.5553 (19) Å. One cannot clearly distinguish between a formally P=O double bond and a formally deprotonated P–O$^-$ bond. The P–O bond lengths of the symmetric O9···H9···O5 hydrogen bridge are only slightly longer (~1.52 Å) then what should be P=O double bonds (~1.50 Å). The negative charge is delocalized over the P–O$^-$ and P=O bonds, giving both of them a partial double bond character with P–O bond lengths between 1.50–1.52 Å (Scheme 3).
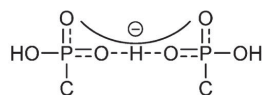
Scheme 3. Lewis valence structure for the bond order and charge-delocalization in the phosphonate groups in **1**.

Thermogravimetric analysis (TGA) of **1** shows a first a mass loss of ~4% up to 240 °C (Figure 2), which can be assigned to one molecule of ammonia (~3%), which is in agreement with literature values [42]. In a second step decarboxylation of one mol CO_2 (44 g/mol) leads to a mass loss of ~8%. With a third step of ~24% rapid dephosphonation of one mol $PO(OH)_2$ and final decarboxylation of another mol CO_2 takes place, which is followed by steady decomposition up to 700 °C.

The hydrated salt $[Co(NH_3)_6](O_3P\text{-}(C_6H_4)_2\text{-}COO)\cdot 4H_2O$, **2** could be crystallized from an aqueous ammonia solution 4-phosphono-biphenyl-4′-carboxylic acid. In a similar approach, 4-phosphono benzoic acid was crystallized with hexaaquacobalt(II) [43], and sulfonate ligands were crystallized with $[Co(NH_3)_6]^{3+}$ cations, resulting in hydrogen-bonded networks [44].

In the asymmetric unit of **2** there is one trivalent hexaamminecobalt cation, one completely deprotonated $BPPA^{3-}$ trianion and four water molecules (Figure 3a). The coordination sphere of Co^{3+} with six crystallographically different ammine ligands results in the well-known $[Co(NH_3)_6]^{3+}$ octahedron [45]. Despite its high symmetry, the $Co(NH_3)_6^{3+}$ octahedron does not reside on a special

position. The Co-N distances (Table 3) are comparable with that of $[Co(NH_3)_6]^{3+}$ in related complexes (Co-N = 1.951 (2) $-$ 1.976 (2) Å, av. 1.956 (2) Å) [43,44,46].
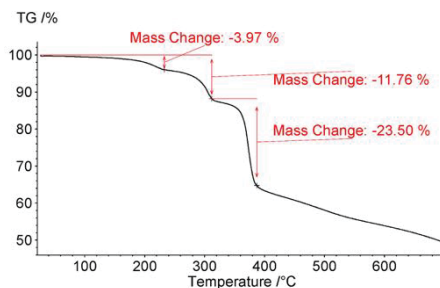

Figure 2. Thermogravimetric analysis (TGA) of **1** in the temperature range 20–700 °C.

Again, the hydrophilic groups, $[Co(NH_3)_6]^{3+}$, $-COO^-$, and $-PO_3^{2-}$, and the crystal water molecules are arranged in slabs (parallel to the *ac* plane) with slabs of the hydrophobic biphenyl part in-between (Figure 3b,c). Such a separation of hydrophilic and hydrophobic parts of molecules is a common packing motif [47–49]. Here the hydrophilic region is organized by hydrogen bonding, the biphenyl rings are arranged by singular N–H$\cdots\pi$, O–H$\cdots\pi$, C–H$\cdots\pi$ or van-der-Waals interactions (see Supplementary Information). The dihedral angles within the biphenyl-carboxylate are 26.8 (4)° (ring to ring) and 42.0 (4)° ($-CCOO^-$ to aryl ring).
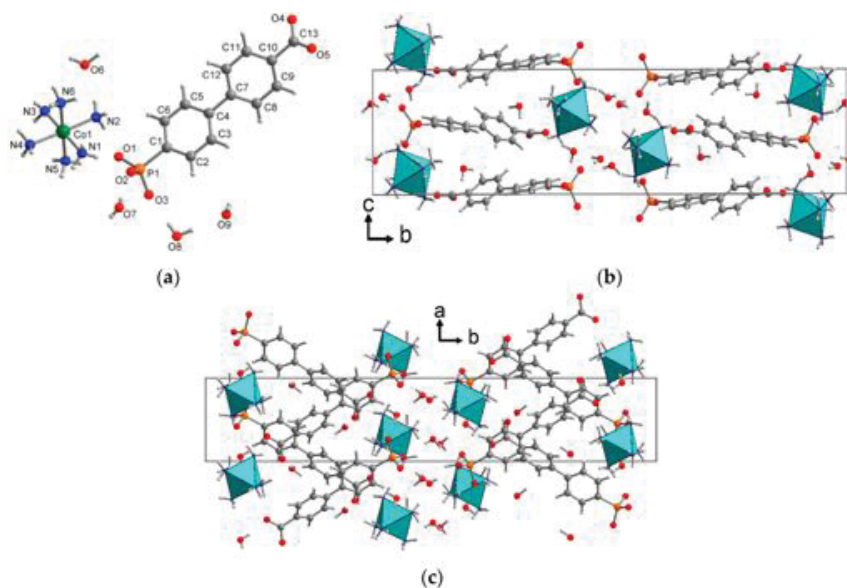

Figure 3. (**a**) Asymmetric unit of **2**; and (**b**,**c**) projections of the unit-cell packing on different planes. The $[Co(NH_3)_6]^{3+}$ cations are illustrated as octahedra; hydrogen bonds are not shown in (**a**–**c**) for clarity. Selected bond distances and angles are given in Table 3.

Table 3. Selected bond lengths and angles (Å, °) in **2**.

Co1–N1	1.957 (2)	P1–O1	1.5235 (18)
Co1–N2	1.965 (2)	P1–O2	1.5283 (18)
Co1–N3	1.951 (2)	P1–O3	1.5247 (18)
Co1–N4	1.959 (2)	P1–C1	1.820 (2)
Co1–N5	1.976 (2)		
Co1–N6	1.961 (2)		
N5–Co1–N1	87.17 (9)	N3–Co1–N4	89.51 (9)
N4–Co1–N1	91.46 (9)	N3–Co1–N2	90.46 (9)
N4–Co1–N5	90.01 (9)	N6–Co1–N1	91.82 (9)
N2–Co1–N1	88.66 (9)	N6–Co1–N5	178.81 (9)
N2–Co1–N5	92.53 (9)	N6–Co1–N2	88.07 (9)
N2–Co1–N4	177.47 (9)	N6–Co1–N3	90.31 (9)
N3–Co1–N1	177.66 (9)	N6–Co1–N4	89.40 (9)
N3–Co1–N5	90.71 (9)		

The BPPA^{3-} anions and the [Co(NH$_3$)$_6$] octahedra are connected to each other by hydrogen bonding (Table 4, Figure 4). The fully deprotonated phosphonate-carboxylate is solely an H-acceptor for the N–H and water O–H bonds. The carboxylate group is acceptor to O–H from water molecules. The four water molecules are held by hydrogen bonding from N–H and O–H-donors and –COO$^-$ and –P(O)$_2$O^{2-} acceptors.

Table 4. Details of the hydrogen bonding interactions in **2** [a].

D–H···A	D–H [Å]	H···A [Å]	D···A [Å]	D–H···A [°]	Symmetry Transformations
N1–H1A···O8 [i]	0.84 (5)	2.71 (4)	3.327 (3)	132 (4)	i = x, y, z − 1
N1–H1B···O2	0.84 (4)	2.14 (4)	2.976 (3)	173 (3)	
N1–H1C···O8 [ii]	0.87 (4)	2.15 (4)	2.971 (3)	156 (3)	ii = −x + 1, −y, −z + 1
N2–H2A···O4 [vi]	0.86 (4)	2.28 (4)	3.086 (3)	157 (3)	vi = x + 1/2, −y + 1/2, z − 1/2
N2–H2B···O6	0.86 (4)	2.07 (4)	2.909 (4)	163 (3)	
N2–H2C···O1	0.89 (3)	2.00 (3)	2.864 (3)	165 (3)	
N3–H3A···O6	0.82 (5)	2.60 (5)	3.177 (4)	129 (4)	
N3–H3B···O2 [iii]	0.90 (4)	1.90 (4)	2.791 (3)	174 (3)	iii = x + 1, y, z
N3–H3C···O5 [viii]	0.69 (5)	2.56 (4)	3.048 (3)	130 (4)	viii = x + 3/2, −y + 1/2, z − 1/2
N3–H3C···O4 [viii]	0.69 (5)	2.56 (4)	3.180 (3)	152 (4)	
N4–H4A···O9 [iv]	0.90 (4)	2.05 (4)	2.937 (3)	171 (3)	iv = x + 1, y, z − 1
N4–H4B···O7 [v]	0.83 (4)	2.77 (3)	3.270 (4)	120 (3)	v = −x + 1, −y, −z
N4–H4C···O7 [iii]	0.86 (4)	2.00 (4)	2.852 (3)	171 (3)	iii = x + 1, y, z
N5–H5A···O8 [ii]	0.90 (4)	2.19 (4)	3.035 (3)	157 (3)	ii = −x + 1, −y, −z + 1
N5–H5B···O2 [iii]	0.88 (4)	2.63 (4)	3.437 (3)	153 (3)	iii = x + 1, y, z
N5–H5C···O1	0.83 (4)	2.13 (4)	2.939 (3)	162 (3)	
N6–H6A···O3 [i]	0.82 (4)	2.09 (4)	2.904 (3)	175 (3)	i = x, y, z − 1
N6–H6B···O5 [viii]	0.93 (4)	2.26 (4)	3.170 (3)	167 (3)	viii = x + 3/2, −y + 1/2
N6–H6C···O4 [vi]	0.85 (4)	2.13 (4)	2.948 (3)	160 (3)	vi = x + 1/2, −y + 1/2, z − 1/2
O6–H6E···O5 [viii]	0.87	1.82 (1)	2.657 (4)	161 (4)	viii = x + 3/2, −y + 1/2, z − 1/2
O7–H7A···O3 [ii]	0.62 (5)	2.12 (5)	2.740 (3)	171 (6)	ii = −x + 1, −y, −z + 1
O7–H7B···O2	0.85 (4)	1.89 (5)	2.690 (3)	156 (4)	
O8–H8A···O9	0.82 (5)	1.99 (5)	2.802 (3)	175 (4)	
O8–H8B···O3	0.73 (5)	1.97 (5)	2.693 (3)	175 (5)	
O9–H9A···O1 [vii]	0.74 (4)	1.96 (4)	2.704 (3)	176 (4)	vii = x − 1, y, z
O9–H9B···O4 [ix]	0.78 (4)	1.95 (4)	2.728 (3)	173 (4)	ix = x + 1/2, −y + 1/2, z + 1/2

Notes: [a] D = donor, A = acceptor.

Finally, we note that in both structures, **1** and **2**, the H-bonds to the phosphonato groups are so-called charge-assisted hydrogen bonds. The hydrogen bond donor and/or acceptor carry positive and negative ionic charges, respectively, hence are usually stronger and shorter than neutral H-bonds [12,46,47,50–54]. In **1** these are bonds NH$_4^{(+)}$···$^{(-)}$O-P and NH$_4^{(+)}$···(H)O-P, -P-OH···$^{(-)}$O-P (Figure 1c). In **2** these are bonds Co-NH$_3^{(+)}$···$^{(-)}$O-P and HOH···$^{(-)}$O-P (Figure 4).
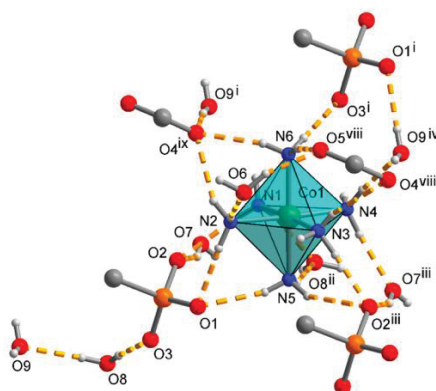
Figure 4. Most relevant H-bonding interactions (orange dashed lines) around a $[Co(NH_3)_6]^{3+}$ cation in the structure of **2**. Details of the H-bond distances and angles are listed in Table 4. Symmetry transformations: i = x, y, z − 1; ii = −x + 1, −y, −z + 1; iii = x + 1, y, z; iv = x + 1, y, z − 1; v = −x + 1, −y, −z; vi = x + 1/2, −y + 1/2, z − 1/2; vii = x − 1, y, z; viii = x + 3/2, −y + 1/2, z − 1/2; ix = x + 1/2, −y + 1/2, z + 1/2.

The large number of hydrogen-bonds in **2** results in a thermal stability that is higher than that of other supramolecular complexes of $[Co(NH_3)_6]^{3+}$ [55,56]. The thermal stability of $BPPA^{3-}$ is reflected by the TGA measurement (Figure 5). The mass loss in **2** up to (~17%) is due to the evaporation of the four water molecules together with one ammine ligand (17.5%). The next five ammine ligands are removed along with decarboxylation of BPPA in the range from 220 °C to 500 °C, followed by decomposition of the biphenyl system (~42% in total). The remaining mass of ~40% can be assigned to cobalt phosphonate species (~35%). It has been observed that metal phosphonates are stable up to 650 °C and higher [57].
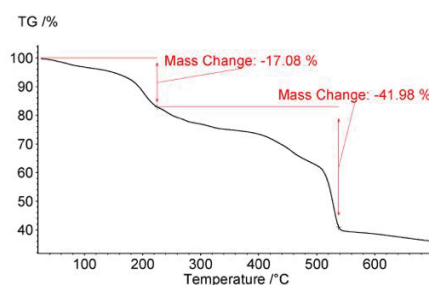

Figure 5. TGA of **2** in the temperature range 20–700 °C.

Comparison of the experimental powder X-ray diffractogram for **2** with the simulation from the single-crystal X-ray dataset (Figure 6) shows that the investigated single crystal was representative of the bulk amount when one takes into account the preferential orientation of the column- or rod-shaped crystals of **2** (Figure S1 in Supplementary Material) on the flat sample holder. Due to the preferred orientation of the rod-shaped crystals on the flat sample holder during the powder X-ray diffraction (PXRD) measurement, and their small quantity, some reflections were not present in the experimental diffraction pattern or their intensity was strongly changed. Such a behavior is discussed in detail in the literature [58–60].
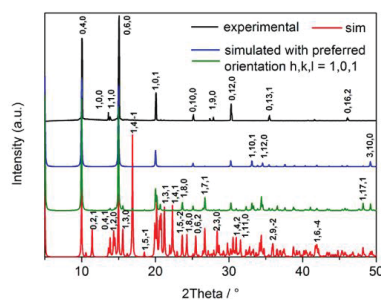
Figure 6. Comparison of the experimental PXRD pattern of **2** (**black**) with the unconstrained simulated pattern from the X-ray data (**red**) and simulated patterns with the preferred orientation of *h*, *k*, *l* = 1, 0, 1 and March–Dollase parameter = 4 (**green**) and = 10 (**blue**). The latter simulations try to take into account the rod-shaped crystal morphology of **2** with their non-random orientation on the flat sample holder. The Miller indices have been assigned to the reflections. Simulations were carried out with *Mercury* [61].

3. Materials and Methods

The chemicals used were obtained from commercial sources. No further purification has been carried out. The ligand has been synthesized starting from 4-biphenyl carboxylic acid in a four-step-synthesis. CHN analysis was performed with a Perkin Elmer CHN 2400. IR-spectra were recorded on a Bruker Tensor 37 IR spectrometer with ATR unit. Thermogravimetric analysis (TGA) was done with a Netzsch TG 209 F3 Tarsus in the range from 20 to 700 °C, equipped with Al-crucible and applying a heating rate of 10 K·min^{-1}. The melting point was determined using a Büchi Melting Point apparatus B540. For powder X-ray diffraction patterns (PXRD), a Bruker D2 Phaser powder diffractometer was used with a flat silicon, low background sample holder, at 30 kV, 10 mA for Cu-Kα radiation (λ = 1.5418 Å), with a scan speed of 0.2 s/step and a step size of 0.02° (2θ). Diffractograms were obtained on flat layer sample holders with a beam scattering protection blade installed, which led to the low relative intensities measured at 2θ < 7°. Details of the synthesis of 4-phosphono-biphenyl-4'-carboxylic acid (H_2O_3P-(C_6H_4)$_2$-COOH, H_3BPPA) will be given elsewhere [62].

NH$_4$(HO$_3$P-(C$_6$H$_4$)$_2$-COOH)(H$_2$O$_3$P-(C$_6$H$_4$)$_2$-COOH): In a Teflon-lined stainless steel reactor 30 mg (0.108 mmol) of H_3BPPA and 8.3 mg (0.108 mmol) of ammonium acetate, NH_4(CH$_3$COO), were suspended in 2 mL of doubly de-ionized water. Heating at 180 °C for 24 h and cooling to room temperature within 12 h led to formation of colorless crystals (Figure S1a in Supplementary Information). Yield: 29 mg (91% based on BPPA). Mp > 350 °C. Calc. for $C_{26}H_{25}NO_{10}P_2$ (573.43 g·mol^{-1}): C, 54.46; H, 4.39; N, 2.44%. Found: C, 53.93; H, 4.36; N, 2.02%. FT-IR (ATR) ν/cm^{-1} = 3810 (w), 3196 (w, b) 2999 (w, b), 2859 (w, b), 1672 (m), 1605 (m), 1569 (w), 1446 (m), 1248 (m), 1126 (vs), 1029 (vs), 921 (vs), 824 (vs), 763 (vs), 704 (m), 576 (s), 560 (s) (Figure S2 in Supplementary Material).

[Co(NH$_3$)$_6$](O$_3$P-(C$_6$H$_4$)$_2$-COO)·4H$_2$O: In a glass vial 9.6 mg (0.036 mmol) of [Co(NH$_3$)$_6$]Cl$_3$ and 10 mg (0.036 mmol) of 4-phosphono-biphenyl-4'-carboxylic acid were dissolved in 1.5 mL of 25% aqueous ammonia. The vial was sealed and the crystals were allowed to grow for a period of days at room temperature. After several days deep orange column-shaped crystals had grown (Figure S1b in Supplementary Material). Yield: 17 mg (91%). Mp > 350 °C. Calc. for $C_{13}H_{33}CoN_6O_9P$ (507.34 g·mol^{-1}): C, 30.78; H, 6.56; N, 16.57%. Found: C, 30.92; H, 6.33; N, 17.12%. FT-IR (ATR) ν/cm^{-1} = 3466 (w, b), 3132 (m, b), 3051 (m, b), 2852 (w, b), 1586 (m), 1554 (m), 1528 (m), 1388 (s), 1228 (w), 1138 (m), 1100 (s), 873 (vs), 835 (m), 786 (m), 701 (m), 579 (vs) (Figure S3 in Supplementary Material).

Single Crystal X-ray Structures

Suitable crystals were carefully selected under a polarizing microscope, covered in protective oil and mounted on a 0.05 mm cryo loop. *Data collection.* Bruker Kappa APEX2 CCD X-ray diffractometer with microfocus tube, Mo-Kα radiation (λ = 0.71073 Å), multi-layer mirror system, ω- and θ-scans; data collection with APEX2, cell refinement and data reduction with SAINT [63], experimental absorption correction with SADABS [64]. *Structure analysis and refinement:* All structures were solved by direct methods using SHELXL2014; refinement of **1** was done by full-matrix least squares on F^2 using the SHELX-97 program suite [65], of **2** with OLEX 2 [66,67]. Non-hydrogen atoms were refined with anisotropic displacement parameters. Hydrogen atoms were positioned geometrically (C–H = 0.95 Å) and refined using riding models (AFIX 43 for aromatic CH with C–H = 0.93 Å and U_{iso}(H) = 1.2U_{eq}(C). In **1** the protic hydrogen atoms (O–H, N–H) were found and freely refined with U_{iso}(H) = 1.5U_{eq} (NH and OH).

In **2**, NH$_3$ hydrogen atoms were found and freely refined. Water hydrogen atoms were also found and refined, except for O6, where they were positioned geometrically (O–H = 0.870 Å) and refined using a riding model (AFIX 6) with U_{iso}(H) = 1.5U_{eq}(O).

Crystal data and details on the structure refinement are given in Table 5. Graphics were drawn with DIAMOND [68]. Analyses on the supramolecular C–H$\cdots$O, C–H$\cdots\pi$ and π-π-stacking interactions were done with *PLATON* for Windows [69]. CCDC 1450889 and 1450890 contain the supplementary crystallographic data for this paper. These data can be obtained free of charge via http://www.ccdc.cam.ac.uk/conts/retrieving.html.

Table 5. Crystal data and refinement details.

	1	**2**
Chemical formula	$C_{26}H_{21}O_{10}P_2 \cdot H_4N$	$C_{13}H_8O_5P \cdot CoH_{18}N_6 \cdot 4(H_2O)$
Mr	573.41	508.36
Crystal system, space group	Triclinic, P$\bar{1}$	Monoclinic, P2$_1$/n
Temperature (K)	150	173
a (Å)	5.9358(5)	7.0193(5)
b (Å)	7.5309(5)	35.454(3)
c (Å)	27.781(2)	9.2797(7)
α (°)	95.413(4)	90
β (°)	90.768(5)	111.921(4)
γ (°)	92.816(5)	90
V (Å^3)	1234.65(16)	2142.4 (3)
Z	2	4
μ (mm^{-1})	0.24	0.93
Crystal size (mm)	0.20 × 0.15 × 0.01	0.33 × 0.3 × 0.15
Absorption correction	Multi-scan, wR2(int) was 0.0937 before and 0.0571 after correction. The Ratio of minimum to maximum transmission is 0.9165. The 1/2 correction factor is 0.0000.	Multi-scan, wR2(int) was 0.1520 before and 0.0844 after correction. The Ratio of minimum to maximum transmission is 0.6784. The 1/2 correction factor is 0.0015.
T_{min}, T_{max}	0.683, 0.746	0.507, 0.748
No. of measured, independent and observed reflections	20157, 4937, 3104 [I > 2σ(I)]	89006, 4214, 4150 [I > 2σ(I)]
R_{int}	0.066	0.073
(sin θ/λ)max (Å^{-1})	0.617	0.617
R[F^2 > 2σ (F^2)], wR(F^2), S	0.049, 0.121, 1.02	0.038, 0.100, 1.04
No. of reflections	4937	4214
No. of parameters	379	374
$\Delta\rho_{max}$, $\Delta\rho_{min}$ (e$\cdot$Å^{-3})	0.30, –0.34	1.10, –0.85

4. Conclusions

We investigated the hydrogen-bonding potential of the new organo-phosphonate linker, H_3BPPA, in its (partially) deprotonated forms H_2BPPA^- and $BPPA^{3-}$. As expected, the protonated phosphonic acid and deprotonated phosphonate group enters into H-bonds with all of its P–O–H donors and P–O$^-$ acceptors. Remarkably and unexpectedly, an almost symmetric resonance-assisted hydrogen bond (RAHB) bond was found between the formal H_2BPPA^- anion and the formally neutral H_3BPPA molecule in **1** to give the overall anion $[H_2BPPA\cdots H\cdots H_2BPPA]^-$.

References

1. Clearfield, A.; Demadis, K. *Metal Phosphonate Chemistry: From Synthesis to Applications*; Royal Society of Chemistry: Oxford, UK, 2012; pp. 45–128.

2. Deng, M.; Liu, X.; Zheng, Q.; Chen, Z.; Fang, C.; Yue, B.; He, H. Controllable preparation and structures of two zinc phosphonocarboxylate frameworks with MER and RHO zeolitic topologies. *CrystEngComm* **2013**, *15*, 7056–7061. [CrossRef]

3. Gagnon, K.J.; Perry, H.P.; Clearfield, A. Conventional and unconventional metal-organic frameworks based on phosphonate ligands: MOFs and UMOFs. *Chem. Rev.* **2012**, *112*, 1034–1054. [CrossRef] [PubMed]

4. Janiak, C. Engineering coordination polymers towards applications. *Dalton Trans.* **2003**, 2781–2804. [CrossRef]

5. Taylor, J.M.; Vaidhyanathan, R.; Iremonger, S.S.; Shimizu, G.K.H. Enhancing water stability of metal-organic frameworks via phosphonate monoester linkers. *J. Am. Chem. Soc.* **2012**, *134*, 14338–14340. [CrossRef] [PubMed]

6. Patterson, A.R.; Schmitt, W.; Evans, R.C. Lighting-Up Two-dimensional lanthanide phosphonates: Tunable structure-property relationships towards visible and near-infrared emitters. *J. Phys. Chem. C* **2014**, *118*, 10291–10301. [CrossRef]

7. Jiménez-García, L.; Kaltbeitzel, A.; Pisula, W.; Gutmann, J.S.; Klapper, M.; Müllen, K. Phosphonated hexaphenylbenzene: A crystalline proton conductor. *Angew. Chem. Int. Ed.* **2009**, *48*, 9951–9953. [CrossRef] [PubMed]

8. Corma, A.; García, H.; Llabrés i Xamena, F.X. Engineering metal organic frameworks for heterogeneous catalysis. *Chem. Rev.* **2010**, *110*, 4606–4655. [CrossRef] [PubMed]

9. Shimizu, G.K.H.; Vaidhyanathan, R.; Taylor, J.M. Phosphonate and sulfonate metal organic frameworks. *Chem. Soc. Rev.* **2009**, *38*, 1430–1449. [CrossRef] [PubMed]

10. Rojo, T.; Mesa, J.L.; Lago, J.; Bazan, B.; Pizarro, J.L.; Arriortua, M.I. Organically templated open-framework phosphite. *J. Mater. Chem.* **2009**, *19*, 3793–3818. [CrossRef]

11. Hou, S.-Z.; Cao, D.-K.; Liu, X.-G.; Li, Y.-Z.; Zheng, L.-M. Metal phosphonates based on (4-carboxypiperidyl)-*N*-methylene-phosphonate: *In situ* ligand cleavage and metamagnetism in $Co_3(O_3PCH_2\text{-}NHC_5H_9\text{-}COO)_2(O_3PCH_2\text{-}NC_5H_{10})(H_2O)$. *Dalton Trans.* **2009**, *15*, 2746–2750. [CrossRef] [PubMed]

12. Habib, H.A.; Gil-Hernández, B.; Abu-Shandi, K.; Sanchiz, J.; Janiak, C. Iron, copper and zinc ammonium-1-hydroxyalkylidene-diphosphonates with zero-, one- and two-dimensional covalent

metal-ligand structures extended into three-dimensional supramolecular networks by charge-assisted hydrogen-bonding. *Polyhedron* **2010**, *29*, 2537–2545. [CrossRef]

13. Abu-Shandi, K.; Winkler, H.; Janiak, C. Structure and mössbauer study of the first mixed-valence iron diphosphonate. *Z. Anorg. Allg. Chem.* **2006**, *632*, 629–633. [CrossRef]

14. Zhao, X.; Bell, J.G.; Tang, S.-F.; Li, L.; Thomas, K.M. Kinetic molecular sieving, thermodynamic and structural aspects of gas/vapor sorption on metal organic framework [$Ni_{1.5}$(4,4′-bipyridine)$_{1.5}$(H_3L)-(H_2O)$_3$][H_2O]$_7$ where H_6L = 2,4,6-trimethylbenzene-1,3,5-triyl tris(methylene)triphosphonic acid. *J. Mater. Chem. A* **2016**, *4*, 1353–1365. [CrossRef]

15. Zhai, F.; Zheng, Q.; Chen, Z.; Ling, Y.; Liu, X.; Weng, L.; Zhou, Y. Crystal transformation synthesis of a highly stable phosphonate MOF for selective adsorption of CO_2. *CrystEngComm* **2013**, *15*, 2040–2043. [CrossRef]

16. Kinnibrugh, T.L.; Ayi, A.A.; Bakhmutov, V.I.; Zon, J.; Clearfield, A. Reversible dehydration behavior reveals coordinatively unsaturated metal sites in microporous aluminum phosphonates. *Cryst. Growth Des.* **2013**, *13*, 2973–2981. [CrossRef]

17. Menelaou, M.; Dakanali, M.; Raptopoulou, C.P.; Drouza, C.; Lalioti, N.; Salifoglou, A. pH-Specific synthetic chemistry, and spectroscopic, structural, electrochemical and magnetic susceptibility studies in binary Ni(II)-(carboxy)phosphonate systems. *Polyhedron* **2009**, *28*, 3331–3339. [CrossRef]

18. Ling, Y.; Deng, M.; Chen, Z.; Xia, B.; Liu, X.; Yang, Y.; Zhou, Y.; Weng, L. Enhancing CO_2 adsorption of a Zn-phosphonocarboxylate framework by pore space partitions. *Chem. Commun.* **2013**, *49*, 78–80. [CrossRef] [PubMed]

19. Breeze, B.A.; Shanmugam, M.; Tuna, F.; Winpenny, R.E.P. A series of nickel phosphonate-carboxylate cages. *Chem. Commun.* **2007**, *48*, 5185–5187. [CrossRef] [PubMed]

20. Rueff, J.-M.; Perez, O.; Leclaire, A.; Couthon-Gourvès, H.; Jaffrès, P.-A. Lead(II) Hybrid Materials from 3- or 4-Phosphonobenzoic Acid. *Eur. J. Inorg. Chem.* **2009**, 4870–4876. [CrossRef]

21. Liao, T.-B.; Ling, Y.; Chen, Z.-X.; Zhou, Y.-M.; Weng, L.-H. A rutile-type porous zinc(II)-phosphonocarboxylate framework: Local proton transfer and size-selected catalysis. *Chem. Commun.* **2010**, *46*, 1100–1102. [CrossRef] [PubMed]

22. Svoboda, J.; Zima, V.; Beneš, L.; Melánová, K.; Trchová, M.; Vlček, M. New barium 4-carboxyphenylphosphonates: Synthesis, characterization and interconversions. *Solid State Sci.* **2008**, *10*, 1533–1542. [CrossRef]

23. Pütz, A.-M.; Carrella, L.M.; Rentschler, E. A distorted honeycomb motive in divalent transition metal compounds based on 4-Phosphonbenzoic acid and exchange coupled Co(II) and Cu(II): Synthesis, structural description and magnetic properties. *Dalton Trans.* **2013**, *42*, 16194–16199. [CrossRef] [PubMed]

24. Rueff, J.-M.; Barrier, N.; Boudin, S.; Dorcet, V.; Caignaert, V.; Boullay, P.; Hix, G.B.; Jaffrès, P.-A. Remarkable thermal stability of Eu(4-phosphonobenzoate): Structure investigations and luminescence properties. *Dalton Trans.* **2009**, *47*, 10614–10620. [CrossRef] [PubMed]

25. Li, J.-T.; Guo, L.-R.; Shen, Y.; Zheng, L.-M. LiF-assisted crystallization of zinc 4-carboxyphenylphosphonates with pillared layered structures. *CrystEngComm* **2009**, *11*, 1674–1678. [CrossRef]

26. Rueff, J.-M.; Perez, O.; Caignaert, V.; Hix, G.; Berchel, M.; Quentel, F.; Jaffrès, P.-A. Silver-based hybrid materials from meta- or para-phosphonobenzoic acid: Influence of the topology on silver release in water. *Inorg. Chem.* **2015**, *54*, 2152–2159. [CrossRef] [PubMed]

27. Zima, V.; Svoboda, J.; Beneš, L.; Melánová, K.; Trchová, M.; Dybal, J. Synthesis and characterization of new strontium 4-carboxyphenylphosphonates. *J. Solid State Chem.* **2007**, *180*, 929–939. [CrossRef]

28. Adelani, P.O.; Albrecht-Schmitt, T.E. Comparison of thorium (IV) and uranium (VI) carboxyphosphonates. *Inorg. Chem.* **2010**, *49*, 5701–5705. [CrossRef] [PubMed]

29. Melánová, K.; Klevcov, J.; Beneš, L.; Svoboda, J.; Zima, V. New layered functionalized titanium (IV) phenylphosphonates. *J. Phys. Chem. Solids* **2012**, *73*, 1452–1455. [CrossRef]

30. Li, J.-T.; Cao, D.-K.; Akutagawa, T.; Zheng, L.M. Zn_3(4-$OOCC_6H_4PO_3$)$_2$: A polar metal phosphonate with pillared layered structure showing SHG-activity and large dielectric anisotropy. *Dalton Trans.* **2010**, *39*, 8606–8608. [CrossRef] [PubMed]

31. Chen, Z.; Zhou, Y.; Weng, L.; Zhao, D. Mixed-solvothermal syntheses and structures of six new zinc phosphonocarboxylates with zeolite-type and pillar-layered frameworks. *Cryst. Growth Des.* **2008**, *8*, 4045–4053. [CrossRef]

32. Merkushev, E.B.; Shvartzberg, M.S. *Organoiodine Compounds and Syntheses Based on Them*; Tomsk Gos. Pedagogicheskii Institut: Tomsk, Soviet Union, 1982; pp. 2598–2601.

33. Etter, M.C. Encoding and decoding hydrogen-bond patterns of organic compounds. *Acc. Chem. Res.* **1990**, *23*, 120–126. [CrossRef]

34. Janiak, C. A critical account on π–π stacking in metal complexes with aromatic nitrogen-containing ligands. *J. Chem. Soc. Dalton Trans.* **2000**, *21*, 3885–3896. [CrossRef]

35. Nishio, M. CH/π hydrogen bonds in crystals. *CrystEngComm* **2004**, *6*, 130–158. [CrossRef]

36. Lin, Z.; Lei, X.-Q.; Bai, S.-D.; Ng, S.W. Ammonium benzenephosphonate. *Acta Crystallogr. Sect. E.—Struct Rep. Online* **2008**, *64*, o1607. [CrossRef] [PubMed]

37. Gilli, G.; Gilli, P. *On Noncovalent Interactions in Crystals: Supramolecular Chemistry: From Molecules to Nanomaterials*; Steed, J., Gale, P.A., Eds.; Wiley: Chichester, UK, 2012; Volume 6, pp. 2829–2868.

38. Góra, R.W.; Maj, M.; Grabowski, S.J. Resonance-assisted hydrogen bonds revisited. Resonance stabilization *vs.* charge delocalization. *Phys. Chem. Chem. Phys.* **2013**, *15*, 2514–2522. [CrossRef] [PubMed]

39. Sanz, P.; Mó, O.; Yáñez, M.; Elguero, J. Resonance-assisted hydrogen bonds: A critical examination. structure and stability of the enols of β-diketones and β-enaminones. *J. Phys. Chem. A* **2007**, *111*, 3585–3591. [CrossRef] [PubMed]

40. Gilli, P.; Bertolasi, V.; Pretto, L.; Ferretti, V.; Gilli, G. Covalent *versus* electrostatic nature of the strong hydrogen bond: Discrimination among single, double, and asymmetric single-well hydrogen bonds by variable-temperature X-ray crystallographic methods in β-diketone enol RAHB systems. *J. Am. Chem. Soc.* **2004**, *126*, 3845–3855. [CrossRef] [PubMed]

41. Gilli, P.; Bertolasi, V.; Ferretti, V.; Gilli, G. Evidence for intramolecular N–H···O resonance-assisted hydrogen bonding in enaminones and related heterodienes. A combined crystal-structural, IR and NMR spectroscopic, and quantum-mechanical investigation. *J. Am. Chem. Soc.* **2000**, *122*, 10405–10417. [CrossRef]

42. Feng, C.; Liang, M.; Jiang, J.; Huang, J.; Liu, H. Synergistic effect of a Novel triazine Charring Agent and ammonium polyphosphate on the flame retardant properties of Halogen-Free Flame Retardant Polypropylene composites. *Thermochim. Acta* **2016**. [CrossRef]

43. Wilk, M.; Janczak, J.; Videnova-Adrabinska, V. Hexaaquacobalt(II) bis[hydrogen bis(4-carboxyphenyl-phosphonate)] dihydrate. *Acta Crystallogr. Sect. C—Cryst. Struct. Commun.* **2011**, *67*, 9–12. [CrossRef] [PubMed]

44. Wang, X.-Y.; Justice, R.; Sevov, S.C. Hydrogen-bonded metal-complex sulfonate (MCS) inclusion compounds: Effect of the guest molecule on the host framework. *Inorg. Chem.* **2007**, *46*, 4626–4631. [CrossRef] [PubMed]

45. Morral, F.R. Alfred werner and cobalt complexes. *Adv. Chem.* **2009**, *6*, 70–77.

46. Reddy, D.S.; Duncan, S.; Shimizu, G.K.H. A Family of supramolecular inclusion solids based upon second-sphere interactions. *Angew. Chem. Int. Ed.* **2003**, *42*, 1360–1364. [CrossRef] [PubMed]

47. Dorn, T.; Chamayou, A.-C.; Janiak, C. Hydrophilic interior between hydrophobic regions in inverse bilayer structures of cation–1,1′-binaphthalene- 2,2′-diyl phosphate salts. *New J. Chem.* **2006**, *30*, 156–167. [CrossRef]

48. Maclaren, J.K.; Sanchiz, J.; Gili, P.; Janiak, C. Hydrophobic-exterior layer structures and magnetic properties of trinuclear copper complexes with chiral amino alcoholate ligands. *New J. Chem.* **2012**, *36*, 1596–1609. [CrossRef]

49. Enamullah, M.; Vasylyeva, V.; Janiak, C. Chirality at metal and helical ligand folding in optical isomers of chiral bis(naphthaldiminato)nickel(II) complexes. *Inorg. Chim. Acta* **2013**, *408*, 109–119. [CrossRef]

50. Ward, M.D. Design of crystalline molecular networks with charge-assisted hydrogen bonds. *Chem. Commun.* **2005**, *47*, 5838–5842. [CrossRef] [PubMed]

51. Gil-Hernández, B.; Maclaren, J.K.; Höppe, H.A.; Pasan, J.; Sanchiz, J.; Janiak, C. Homochiral lanthanoid(III) mesoxalate metal-organic frameworks: Synthesis, crystal growth, chirality, magnetic and luminescent properties. *CrystEngComm* **2012**, *14*, 2635–2644. [CrossRef]

52. Maclaren, J.K.; Janiak, C. Amino-acid based coordination polymers. *Inorg. Chim. Acta* **2012**, *389*, 183–190.

53. Chamayou, A.-C.; Neelakantan, M.A.; Thalamuthu, S.; Janiak, C. The first vitamin B6 zinc complex, pyridoxinato-zinc acetate: A 1D coordination polymer with polar packing through strong inter-chain hydrogen bonding. *Inorg. Chim. Acta* **2011**, *365*, 447–450. [CrossRef]

54. Drašković, B.M.; Bogdanović, G.A.; Neelakantan, M.A.; Chamayou, A.-C.; Thalamuthu, S.; Avadhut, Y.S.; Schmedt auf der Günne, J.; Banerjee, S.; Janiak, C. *N-o*-Vanillylidene-L-histidine: Experimental charge density

analysis of a double zwitterionic amino acid Schiff-base compound. *Cryst. Growth Des.* **2010**, *10*, 1665–1676. [CrossRef]

55. Collins, L.W.; Wendlandt, W.W.; Gibson, E.K. The thermal dissociation of the $[Co(NH_3)_5Cl]Cl_2$ and $[Co(NH_3)_5Br]Br_2$ complexes in vacuo. *Thermochim. Acta* **1974**, *8*, 303–306. [CrossRef]

56. Saito, A. Thermal decomposition of the complexes $[Co(NH_3)_6][Nd(SO_4)_3] \cdot nH_2O$. *Thermochim. Acta* **1986**, *102*, 373–386. [CrossRef]

57. Dines, M.B.; DiGiacomo, P.M. Derivatized lamellar phosphates and phosphonates of M(IV) ions. *Inorg. Chem.* **1981**, *20*, 92–97. [CrossRef]

58. Mittemeijer, E.J.; Welzel, U. *Modern Diffraction Methods*; Wiley: Weinheim, Germany, 2013.

59. Pecharsky, V.; Zavalij, P. *Fundamentals of Powder Diffraction and Structural Characterization of Materials*, 2nd ed.; Springer: New York, NY, USA, 2008.

60. Dollase, W.A. Correction of intensities for preferred orientation in powder diffractometry: Application of the March model. *J. Appl. Cryst.* **1986**, *19*, 267–272. [CrossRef]

61. Macrae, C.F.; Edgington, P.R.; McCabe, P.; Pidcock, E.; Shields, G.P.; Taylor, R.; Towler, M.; van de Streek, J. Mercury: Visualization and analysis of crystal structures. *J. Appl. Cryst.* **2006**, *39*, 453–457. [CrossRef]

62. Heering, C.; Francis, B.; Nateghi, B.; Makhloufi, G.; Janiak, C. Syntheses, structures and properties of group 12 element (Zn, Cd, Hg) coordination polymers with a phosphonate-biphenyl-carboxylate linker. *CrystEngComm* **2016**. (to be submitted).

63. APEX2. *SAINT, Data Reduction and Frame Integration Program for the CCD Area-Detector System, Bruker Analytical X-ray Systems*; Data Collection program for the CCD Area-Detector System: Madison, WI, USA, 1997–2006.

64. Sheldrick, G. *SADABS: Area-Detector Absorption Correction*; University of Göttingen: Göttingen, Germany, 1996.

65. Hübschle, C.B.; Sheldrick, G.M.; Dittrich, B. ShelXle: A graphical user interface for SHELXL. *J. Appl. Cryst.* **2011**, *44*, 1281–1284. [CrossRef] [PubMed]

66. Bourhis, L.J.; Dolomanov, O.V.; Gildea, R.J.; Howard, J.A.K.; Puschmann, H. The anatomy of a comprehensive constrained, restrained refinement program for the modern computing environment—*Olex2* dissected. *Acta Crystallogr. Sect. A* **2015**, *71*, 59–75. [CrossRef] [PubMed]

67. Dolomanov, O.V.; Bourhis, L.J.; Gildea, R.J.; Howard, J.A.K.; Puschmann, H. *OLEX2*: A complete structure solution, refinement and analysis program. *J. Appl. Cryst.* **2009**, *42*, 339–341. [CrossRef]

68. Brandenburg, K. *DIAMOND*; version 3.2; Crystal and Molecular Structure Visualization; Crystal Impact—K. Brandenburg & H. Putz Gbr: Bonn, Germany, 2009.

69. Spek, A.L. Structure validation in chemical crystallography. *Acta Crystallogr. Sect. D—Biol. Crystallogr.* **2009**, *65*, 148–155. [CrossRef] [PubMed]

Supplementary Materials: Charge-assisted hydrogen-bonded networks of NH₄⁺ and [Co(NH₃)₆]³⁺ with the new linker anion of 4-phosphono-biphenyl-4'-carboxylic acid

Christian Heering, Bahareh Nateghi and Christoph Janiak
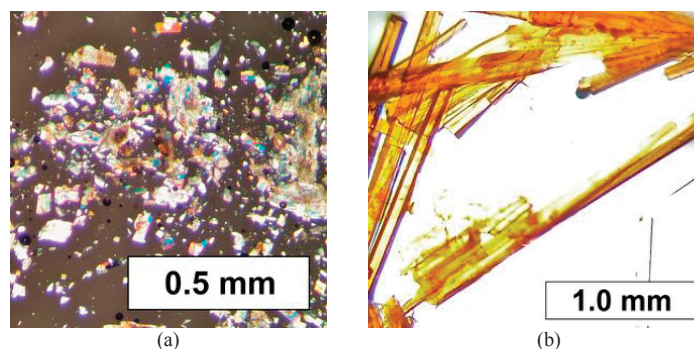
Figure S1. Photographs of crystals of (**a**) NH₄(HO₃P-(C₆H₄)₂-COOH)(H₂O₃P-(C₆H₄)₂-COOH), **1** and (**b**) [Co(NH₃)₆](O₃P-(C₆H₄)₂-COO)·4H₂O, **2** taken with a light microscope.
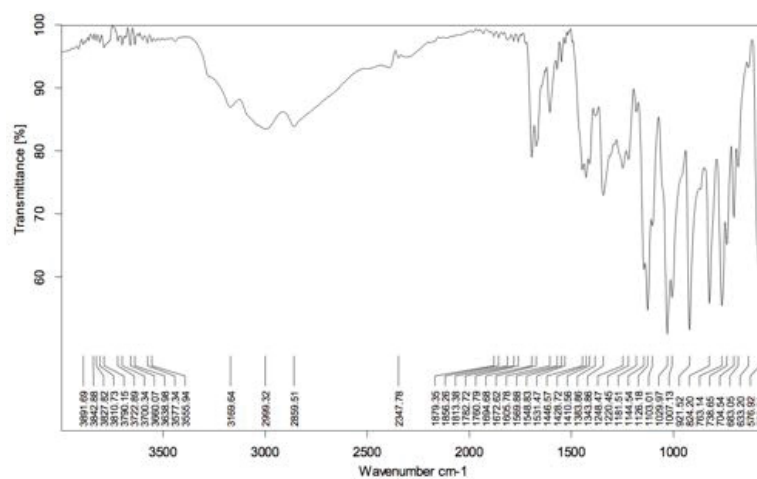
Figure S2. FT-IR (ATR) spectrum of NH₄(HO₃P-(C₆H₄)₂-COOH)(H₂O₃P-(C₆H₄)₂-COOH), **1**.

75
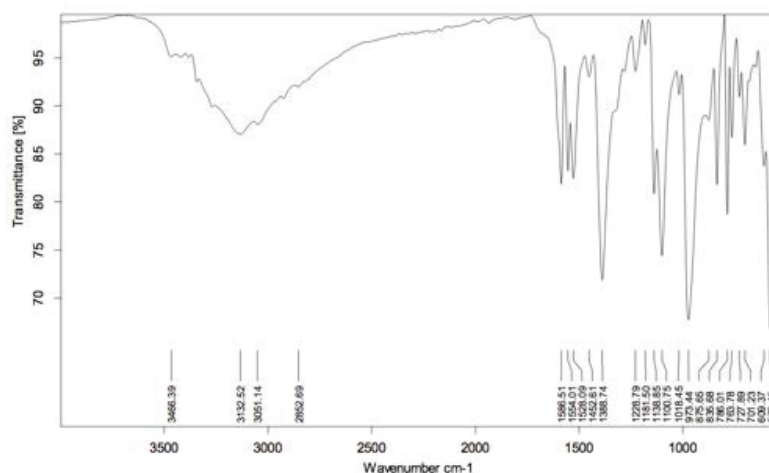
Figure S3. FT-IR (ATR) spectrum of [Co(NH₃)₆](O₃P-(C₆H₄)₂-COO)·4H₂O, **2**.
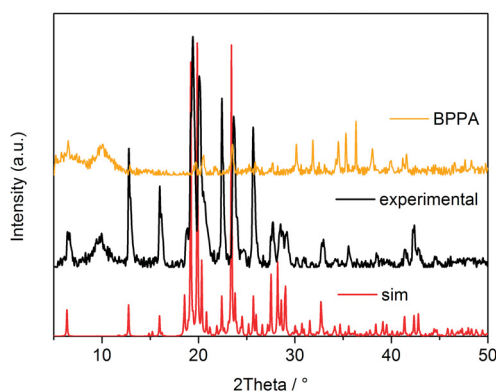
Figure S4. Comparison of the experimental PXRD pattern of **1** (black) with the simulated pattern from the X-ray data (red). An additional comparison of the experimental powder pattern with the experimental pattern of the linker 4-phosphono-biphenyl-4'-carboxylic acid, BPPA shows, that there is a contribution of the linker in the measured pattern.

Packing Analyses

Packing Analysis by PLATON ((a) A. Spek, *Acta Crystallographica Section D*, **2009**, *65*, 148–155; (b) A.L. Spek *PLATON—A multipurpose crystallographic tool*, Utrecht University: Utrecht, The Netherlands, 2005.)

Despite the presence of biphenyl π-systems in compounds **1** and **2**, there are no π–π interactions [1] and only few intermolecular C–H···π [2–5] evident.

The supramolecular packing analyses of the biphenyl rings are tabulated below (Tables S1 and S2).

The listed "Analysis of Short Ring-Interactions" for possible π-stacking interactions yielded rather rather long centroid-centroid distances (>4.0 Å) together with non-parallel ring planes (alpha >> 0°) and large slip angles (β, γ > 30°).

In comparison, significant π-stackings show rather short centroid-centroid contacts (<3.8 Å), near parallel ring planes (alpha < 10° to ~0° or even exactly 0° by symmetry), small slip angles

(β, γ < 25°) and vertical displacements (slippage < 1.5 Å) which translate into a sizable overlap of the aryl-plane areas [1,6–11].

Significant intermolecular C–H···π contacts start around 2.7 Å for the (C–)H···ring centroid distances with H-perp also starting at 2.6–2.7 Å and C–H··Cg > 145° [2–5,12–16].
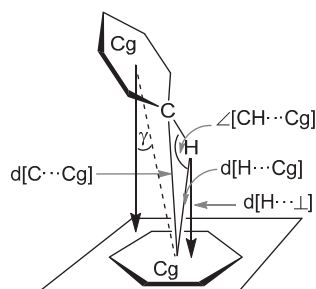
Scheme S1. Graphical presentation of the parameters used for the description of CH-π interactions.

Packing Analysis for compound $NH_4(HO_3P–(C_6H_4)_2–COOH)(H_2O_3P–(C_6H_4)_2–COOH)$, **1** for possible **CH–π interactions** (see Scheme S1 for explanation)**:**

==

Analysis of X-H..Cg(π-Ring) Interactions (H..Cg < 3.0 Ang. - Gamma < 30.0 Deg)

==

-Cg(J) = Center of gravity of ring J (Plane number above)

-H-Perp = Perpendicular distance of H to ring plane J

-Gamma = Angle between Cg-H vector and ring J normal

-X-H..Cg = X-H-Cg angle (degrees)

-X..Cg = Distance of X to Cg (Angstrom)

-X-H, π = Angle of the X-H bond with the π-plane (*i.e.*, Perpendicular = 90 degrees, Parallel = 0 degrees)

X--H(I)	Res(I)	Cg(J)	[ARU(J)]	H..Cg	H-Perp	Gamma	C-H..Cg	C..Cg	X-H,π
C(2)-H(2A)	[1]	->Cg(5)	[1445.01]	2.94	2.91	7.42	137	3.684(3)	50
C(9)-H(9A)	[1]	->Cg(6)	[1555.01]	2.91	−2.88	7.85	135	3.638(3)	48
C(15)-H(15)	[1]	->Cg(3)	[1565.01]	2.91	−2.83	13.23	126	3.551(3)	49
			Min or Max	2.910	−2.880	7.42	137.00	3.551	50

[1445] = −1 + X, −1 + Y, Z

[1555] = X, Y, Z

[1565] = X, 1 + Y, Z

The Cg(I) refer to the Ring Centre-of-Gravity numbers given in

Ring 3: C1-C2-C3-C4-C5-C6

Ring 5: C14-C15-C16-C17-C18-C19

Ring 6: C20-C21-C22-C23-C24-C25

Packing Analysis for compound $[Co(NH_3)_6](O_3P–(C_6H_4)_2–COO)·4H_2O$, **2** for possible **N–H···π, O–H···π, CH–π interactions** (see Scheme S1 for explanation)**:**

==

Analysis of X-H...Cg(Pi-Ring) Interactions (H..Cg < 3.0 Ang. - Gamma < 30.0 Deg)

==

-Cg(J) = Center of gravity of ring J (Plane number above)

-H-Perp = Perpendicular distance of H to ring plane J

-Gamma = Angle between Cg-H vector and ring J normal

-X-H..Cg = X-H-Cg angle (degrees)

-X..Cg = Distance of X to Cg (Angstrom)

-X-H, π = Angle of the X-H bond with the π-plane (*i.e.*, Perpendicular = 90 degrees, Parallel = 0 degrees)

X--H(I)	Res(I)	Cg(J)	[ARU(J)]	H..Cg	H-Perp	Gamma	C-H..Cg	C..Cg	X-H,π
N(3)-H(3A)	[2]	->Cg(1)	[1655.01]	2.94(5)	−2.78	18.99	151(4)	3.672(3)	44
O(6)-H(6D)	[3]	->Cg(2)	[4554.01]	2.69(5)	2.51	20.96	139(4)	3.395(4)	43
C(11)-H(11)	[1]	-> Cg(1)	[4454.01]	2.766(3)	2.73	9.36	137.5(3)	3.525(3)	38
			Min or Max	2.690	−2.780	9.36	151.00	3.395	44

[1655] = 1 + X, Y, Z

[4554] = 1/2 + X,1/2 − Y,−1/2 + Z

[4454] = −1/2 + X,1/2 − Y,−1/2 + Z

The Cg(I) refer to the Ring Centre-of-Gravity numbers given in

Ring 1: C1-C2-C3-C4-C5-C6

Ring 2: C7-C8-C9-C10-C11-C12

References

1   Janiak, C. A critical account on π–π stacking in metal complexes with aromatic nitrogen-containing ligands. *J. Chem. Soc. Dalton Trans.* **2000**, *21*, 3885–3896.
2   Nishio, M. CH/π hydrogen bonds in crystals. *CrystEngComm* **2004**, *6*, 130–158.
3   Nishio, M.; Umezawa, M.H.Y. *The CH/π Interaction: Evidence, Nature and consequences*; Wiley: Weinheim, Germany, 1998.
4   Umezawa, Y.; Tsuboyama, S.; Honda, K.; Uzawa, J.; Nishio, M. CH/π Interaction in the crystal structure of organic compounds. A database study. *Bull. Chem. Soc. Jpn.* **1998**, *71*, 1207–1213.
5   Janiak, C.; Temizdemir, S.; Dechert, S.; Deck, W.; Girgsdies, F.; Heinze, J.; Kolm, M. J.; Scharmann, T.G.; Zipffel, O.M. Binary [Hydrotris(indazol-1-yl)borato] metal Complexes, M(Tp⁴ᴮᵒ)₂[1] with M = Fe, Co, Ni, Cu, Zn: Electronic Properties and Solvent Dependent Framework Structures through C–H···π Interactions. *Eur. J. Inorg. Chem.* **2000**, *11*, 1229–1241.
6   Lozan, V.; Lassahn, P.-G.; Zhang, C.; Wu, B.; Janiak, C.; Rheinwald, G.; Lang, H. Dinuclear nickel (II) and palladium (II) complexes in combination with different co-catalysts as highly active catalysts for the vinyl/addition polymerization of norbornene. *Z. Naturforsch. B* **2003**, *58*, 1152–1164.
7   Zhang, C.; Janiak, C. Synthesis and crystal structure of manganese(II) bipyridine carboxylato complexes: [(bipy)₂Mn(II)(μ-C₂H₅CO₂)Mn(II)(bipy)₂](ClO₄)₂ and [Mn(II)(ClCH₂CO₂)(H₂O)(bipy)₂]ClO₄·H₂O (bipy = 2,2'-bipyridine). *Z. Anorg. Allg. Chem*. **2001**, *627*, 1972–1975.
8   Zhang, C.; Janiak, C. Six-coordinated zinc complexes: [Zn(II)(H₂O)₄(phen)](NO₃)₂·H₂O and [Zn(II)NO₃(H₂O)(bipy)(Him)]NO₃ (phen = 1,10-phenanthroline, bipy = 2,2'-bipyridine and Him = imidazole). *J. Chem. Crystallogr.* **2001**, *31*, 29–35.
9   Wu, H.-P.; Janiak, C.; Rheinwald, G.; Lang, H. 5,5'-Dicyano-2,2'-bipyridine silver complexes: Discrete units or co-ordination polymers through a chelating and/or bridging metal–ligand interaction. *J. Chem. Soc. Dalton Trans.* **1999**, *2*, 183–190.
10   Janiak, C.; Uehlin, L.; Wu, H.-P.; Klüfers, P.; Piotrowski, H.; Scharmann, T.G. Cordination engineering: When can one speak of an "understanding"? Case study of the multidentate ligand 2,2'-dimethyl-4,4'-bipyrimidine. *J. Chem. Soc. Dalton Trans.* **1999**, 3121–3131.
11   Wu, H.-P.; Janiak, C.; Uehlin, L.; Klüfers, P.; Mayer, P. 2,2'-Bi-1,6-naphthyridine metal complexes: A new ligand and a novel 2 × 2 inclined interpenetration of (4,4) nets or formation of helicoidal chains. *Chem. Commun.* **1998**, *23*, 2637–2638.

12 Yang, X.-J.; Drepper, F.; Wu, B.; Sun, W.-H.; Haehnel, W.; Janiak, C. From model compounds to protein binding: Syntheses, characterizations and fluorescence studies of [Ru^{II}(bipy)(terpy)L]$^{2+}$ complexes (bipy = 2,2′-bipyridine; terpy = 2,2′:6′,2″-terpyridine; L = imidazole, pyrazole and derivatives, cytochrome *c*). *Dalton Trans.* **2005**, *2*, 256–267.

13 Madhavi, N.N.L.; Katz, A.K.; Carrell, H.L.; Nangia, A.; Desiraju, G.R. Evidence for the characterisation of the C–H···π interaction as a weak hydrogen bond: Toluene and chlorobenzene solvates of 2,3,7,8-tetraphenyl-1,9,10-anthyridine. *Chem. Commun.* **1997**, *20*, 1953–1954.

14 Weiss, H.-C.; Bläser, D.; Boese, R.; Doughan, B.M.; Haley, M.M. C–H···π interactions in ethynylbenzenes: The crystal structures of ethynylbenzene and 1,3,5-triethynylbenzene, and a redetermination of the structure of 1,4-diethynylbenzene. *Chem. Commun.* **1997**, *18*, 1703–1704.

15 Steiner, T.; Tamm, M.; Lutz, B.; van der Maas, J. First example of cooperative O–H···C[triple bond, length as m-dash]C–H···Ph hydrogen bonding: crystalline 7-ethynyl-6,8-diphenyl-7H-benzocyclohepten-7-ol. *Chem. Commun.* **1996**, *10*, 1127–1128.

16 Anelli, P.L.; Ashton, P.R.; Ballardini, R.; Balzani, V.; Delgado, M.; Gandolfi, M.T.; Goodnow, T.T.; Kaifer, A.E.; Philp, D.; Pietraszkiewicz, M.; Prodi, L.; Reddington, M.V.; Slawin, A.M.Z.; Spencer, N.; Stoddart, J.F.; Vicent, C.; Williams, D.J. Molecular meccano. 1. [2]Rotaxanes and a [2]catenane made to order. *J. Am. Chem. Soc.* **1992**, *114*, 193–218.

2.3 Syntheses, structures and properties of group 12 element (Zn, Cd, Hg) coordination polymers with a mixed-functional phosphonate-biphenyl-carboxylate linker

Christian Heering, Biju Francis, Bahareh Nateghi, Gamall Makhloufi, Steffen Lüdeke and Christoph Janiak

Abstract:

The new phosphonate-carboxylate ligand from 4-phosphono-biphenyl-4′-carboxylic acid ($H_2O_3P–(C_6H_4)_2–CO_2H$, H_3BPPA) is based on the rigid biphenyl system and is studied toward the coordination behavior of group 12 elements zinc, cadmium and mercury. The crystalline products from hydrothermal syntheses highlight the versatile and different coordination modes with the (partially) deprotonated H_3BPPA ligand to give coordination polymeric 3D-$[Zn_5(\mu_3\text{-OH})_4(\mu_4\text{-}O_3P–(C_6H_4)_2–CO_2\text{-}\mu_2)_2]_n$ (5), 2D-$[Zn(\mu_6\text{-}O_3P–(C_6H_4)_2–CO_2H)]_n$ (6), 3D-$[Cd_3(\mu_5\text{-}O_3P–(C_6H_4)_2–CO_2\text{-}\mu_2)(\mu_6\text{-}O_2P–(C_6H_4)_2–CO_2\text{-}\mu_3)]_n$ (7) and 2D-$[Hg(\mu_3\text{-}HO_3P–(C_6H_4)_2–CO_2H)]_n$ (8). The cobalt complex, 2D-$[Co(\mu_4\text{-}O_3P–(C_6H_4)_2–CO_2H)]_n$ (9) is isostructural to 6. Through additional classic strong carbonyl O–H⋯O hydrogen bonding the dimensionality of the 2D coordination networks increases to 3D supramolecular frameworks. The carboxy-phosphonate ligand shows five differ- ent coordination modes which can be described as $\mu_4\text{-}O_3P–CO_2\text{-}\mu_2$ (5), $\mu_6\text{-}O_3P–$ (6), $\mu_5\text{-}O_3P–CO_2\text{-}\mu_2$, $\mu_5\text{-}O_3P–CO_2\text{-}\mu_3$ (7), and $\mu_3\text{-}O_3P–$ (8), that is, the ligand bridges altogether between 3 to 8 metal atoms with the phosphonate group alone connecting already 3 to 6 metal atoms. Layers of metal–oxygen polyhedra are interconnected *via* the biphenyl linker, which either coordinates metal atoms with both donor groups or the –COOH end forms tail-to-tail hydrogen bonds to create 3D or 2D coordination networks, respec- tively. In the flat {MO_x} layers in 6 and 7 the Zn and Cd metal nodes represent a honeycomb and an mcm net, respectively. The coordination polyhedra of the Cd atoms in compound 7 were analyzed towards a trigonal-prismatic coordination environment. The

complexes are hydrolytically very stable due to their hy- drothermal preparation from aqueous solution at 180–200 °C. The compounds could be stored in water or air for months without apparent decomposition. Compounds 5 and 7, where the ligand is fully deprotonated, start to decompose at ~400 °C. The fluorescence emission spectrum of the ligand, 4, shows an intense peak at 365 nm (λ_{ex} = 316 nm). The fluorescence emission of the metal complexes 5, 7 and 9 is shifted towards larger wavelengths with values of 417 nm, 415 nm and 410 nm, respectively (λ_{ex} = 354 nm for 5, λ_{ex} = 350 nm for 7, λ_{ex} = 400 nm for 8, λ_{ex} = 360 nm for 9). In addition, the crystal structures of the H3BPPA ligand precursors 4-iodo-4′-biphenylcarboxylic acid methyl ester, and 4-diethylphosphono-4'-biphenylcarboxylic acid methyl ester are described here for the first time.

Syntheses, structures and properties of group 12 element (Zn, Cd, Hg) coordination polymers with a mixed-functional phosphonate-biphenyl-carboxylate linker†

Christian Heering,[a] Biju Francis,‡[a] Bahareh Nateghi,[a] Gamall Makhloufi,[a] Steffen Lüdeke[b] and Christoph Janiak*[a]

The new phosphonate-carboxylate ligand from 4-phosphono-biphenyl-4′-carboxylic acid (H_2O_3P–(C_6H_4)$_2$–CO_2H, H_3BPPA) is based on the rigid biphenyl system and is studied toward the coordination behavior of group 12 elements zinc, cadmium and mercury. The crystalline products from hydrothermal syntheses highlight the versatile and different coordination modes with the (partially) deprotonated H_3BPPA ligand to give coordination polymeric 3D-[Zn_5(μ_3-OH)$_4$(μ_4-O_3P–(C_6H_4)$_2$–CO_2-μ_2)$_2$]$_n$ (**5**), 2D-[Zn(μ_6-O_3P–(C_6H_4)$_2$–CO_2H)]$_n$ (**6**), 3D-[Cd_3(μ_5-O_3P–(C_6H_4)$_2$–CO_2-μ_2)(μ_6-O_3P–(C_6H_4)$_2$–CO_2-μ_3)]$_n$ (**7**) and 2D-[Hg(μ_3-HO_3P–(C_6H_4)$_2$–CO_2H)]$_n$ (**8**). The cobalt complex, 2D-[Co(μ_4-O_3P–(C_6H_4)$_2$–CO_2H)]$_n$ (**9**) is isostructural to **6**. Through additional classic strong carbonyl O–H···O hydrogen bonding the dimensionality of the 2D coordination networks increases to 3D supramolecular frameworks. The carboxy-phosphonate ligand shows five different coordination modes which can be described as μ_4-O_3P–CO_2-μ_2 (**5**), μ_6-O_3P– (**6**), μ_5-O_3P–CO_2-μ_2, μ_5-O_3P–CO_2-μ_3 (**7**), and μ_3-O_3P– (**8**), that is, the ligand bridges altogether between 3 to 8 metal atoms with the phosphonate group alone connecting already 3 to 6 metal atoms. Layers of metal–oxygen polyhedra are interconnected *via* the biphenyl linker, which either coordinates metal atoms with both donor groups or the –COOH end forms tail-to-tail hydrogen bonds to create 3D or 2D coordination networks, respectively. In the flat {MO_x} layers in **6** and **7** the Zn and Cd metal nodes represent a honeycomb and an **mcm** net, respectively. The coordination polyhedra of the Cd atoms in compound **7** were analyzed towards a trigonal-prismatic coordination environment. The complexes are hydrolytically very stable due to their hydrothermal preparation from aqueous solution at 180–200 °C. The compounds could be stored in water or air for months without apparent decomposition. Compounds **5** and **7**, where the ligand is fully deprotonated, start to decompose at ~400 °C. The fluorescence emission spectrum of the ligand, **4**, shows an intense peak at 365 nm (λ_{ex} = 316 nm). The fluorescence emission of the metal complexes **5**, **7** and **9** is shifted towards larger wavelengths with values of 417 nm, 415 nm and 410 nm, respectively (λ_{ex} = 354 nm for **5**, λ_{ex} = 350 nm for **7**, λ_{ex} = 400 nm for **8**, λ_{ex} = 360 nm for **9**). In addition, the crystal structures of the H_3BPPA ligand precursors 4-iodo-4′-biphenylcarboxylic acid methyl ester, and 4-diethylphosphono-4′-biphenylcarboxylic acid methyl ester are described here for the first time.

[a] *Institut für Anorganische Chemie und Strukturchemie, Universität Düsseldorf, Universitätsstr. 1, 40225 Düsseldorf, Germany. E-mail: janiak@hhu.de*
[b] *Institut für Pharmazeutische Wissenschaften, Universität Freiburg, Albertstr. 25, 79104 Freiburg, Germany*

‡ Permanent address: CSIR-Network of Inst. for Solar Energy, National Institute for Interdisciplinary Science & Technology (NIIST), Thiruvananthapuram-695 019, India.

Introduction

Metal–organic frameworks, MOFs, and coordination polymers became a rapidly growing research area in recent years, because of possible applications,[1,2] for example in catalysis,[3] sensing by fluorescence changes,[4,5] gas storage[6,7] and separation.[8,9] However, the water or moisture stability of such networks is often low.[10]

One approach to increase hydrothermal stability is the use of three- or four-valent, highly charged metal ions such as Cr^{3+}, Al^{3+}, Fe^{3+}, Ti^{4+} or Zr^{4+} in MIL-MOF compounds[11–14] (MIL = Materials of Institute Lavoisier) or UiO-MOFs[15] (UiO

University of Oslo).[16–18] Carboxylate linkers were also replaced by azolates with improved stability of analogous or isoreticular compounds.[19,20] Yet, the focus has seldom been set on very strongly coordinating (organo)phosphonate groups,[21,22] which could significantly raise the stability of such metal–ligand coordination compounds.
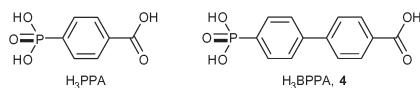
Organophosphonic acids, which have a pK_{a1} of 2.0 for the first and a pK_{a2} of 6.59 for the second proton, are more acidic ligands than pyrazoles ($pK_a = 2.49$). Organophosphonates generate strong metal–ligand coordinative bonds in thermodynamically stable complexes with high stability constants. Metal organophosphonate compounds are organic–inorganic hybrid materials,[23] can be porous networks,[24–27] and as such be placed in between zeolite-like[28,29] and metal–organic framework materials.[30] Metal organophosphonates are stable in water or aqueous environment[31] and can be reversibly hydrated and dehydrated.[27,32–36] The use of metal phosphonates in catalysis, luminescence,[37] ion or proton exchange or conductivity[38,39] and in separation is discussed and investigated.[40] Cobalt and iron organophosphonates exhibit magnetic properties.[41–48]

Organophosphonates can contain additional functional groups such as carboxylate, hydroxyl or amino in the organomoiety which presents a tunable functionality with a wide variety of structural motifs and properties.[49]

The controlled growth of crystalline metal–organophosphonate complexes is not a straightforward procedure.[28] This is probably due to the strong metal–ligand bond, which is formed with little reversibility to correct for crystal defects. Therefore, we started to investigate carboxyl-phosphonate ligands,[50] which can be seen as intermediates between pure carboxylates and pure phosphonates, and share synergies of both ligand classes. Metal complexes with mixed-functional 4-phosphono-benzoic acid (H₃PPA) (Scheme 1 and S1 in ESI†) with barium,[51] cobalt,[52] copper,[52] europium,[53] lead,[54] lithium,[55] silver,[56] strontium,[57] thorium,[58] titanium,[59] uranium[58] and zinc[55,60,61] are known. Carboxy-phosphonates can form porous or 3D metal–ligand networks.[62–64] Weng *et al.* described a 3D zinc carboxy-phosphonate, ZnPC-2, as a material for CO_2 adsorption.[65] As in MOFs, di- or tri-substituted rigid phosphonato-aryl-carboxylate linkers are a rational choice for rigid networks.

Here we present the synthesis of the new mixed-functional linker 4-phosphono-4′-biphenylcarboxylic acid, H₃BPPA (**4**) (Schemes 1 and 2) and four crystal structures of coordination networks with the group 12 metal ions zinc, cadmium and mercury.

The concept of a mixed-functional rigid linker with carboxylate and phosphonate coordinating groups was used to

obtain hydrothermally stable coordination networks. Up to now, no carboxy-phosphonate complexes with mercury have been known or published to the best of our knowledge.

Results and discussion

Linker synthesis

The linker H₃BPPA has been synthesized for the first time here (Scheme 2), following a known procedure by Merkushev *et al.* to synthesize 4′-iodo-biphenyl-4-carboxylic acid (**1**) through the iodination of 4-biphenyl carboxylic acid.[66] Compound **1** was transformed into the carboxy methyl ester **2**, followed by the nickel(II) catalyzed conversion to a phosphonate ester (**3**), which after hydrolysis gave H₃BPPA (**4**).

Crystals of the 4-iodo-4′-biphenylcarboxylic acid methyl ester (**2**) were obtained by slow evaporation of a chloroform solution. The crystal structure of compound **2** shows a nearly in-plane conformation of both aryl rings and the carboxy methyl ester group (Fig. 1a). The dihedral angle between both aryl rings is 1.4(3)° and between the plane of the –COOMe
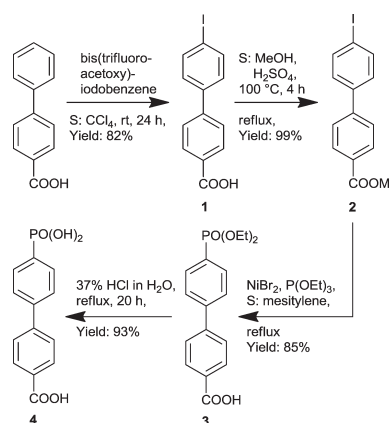
Scheme 2 Reaction sequence for the synthesis of H₃BPPA (**4**) from 4-biphenyl carboxylic acid.

Fig. 1 (a) Asymmetric unit (50% thermal ellipsoids) and (b) projection of the unit cell packing of **2**. Selected distances (Å) and angles (°): C1–I1 2.082(9), C13–O1 1.202(13), C13–O2 1.303(12), O1–C13–C10 123.4(9), O1–C13–O2 123.6(10).

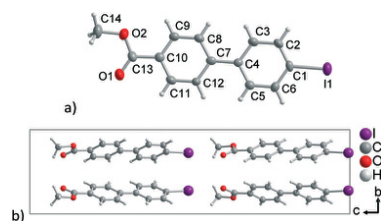**Scheme 1** 4-Phosphono-benzoic acid (H₃PPA) and 4-phosphono-4′-biphenylcarboxylic acid (H₃BPPA, **4**).

group and its aryl ring it is 8.1(6)°. In 4-biphenyl carboxylic acid the dihedral angle between the –COOH group and the aryl ring is 29.05° and the dihedral angle between both aryl rings is 2.89°.[67] This implies a better π-conjugation in the 4-iodo-derivative 2. Compound 2 crystallizes in the non-centrosymmetric orthorhombic space group $Pca2_1$. The non-centrosymmetric packing (Flack parameter 0.080(17))[68] originates from the identical orientation of the iodo or carboxyl groups, respectively, along the crystallographic c axis at an angle of ±21.7(8)° (Fig. 1b).

Crystals of 4-diethylphosphono-4′-biphenylcarboxylic acid methyl ester (3) were derived from mesitylene solution. In the crystal structure of compound 3 (Fig. 2) the carboxy methyl ester and aryl ring form a dihedral angle of 13.7(2)°, the two aryl rings a dihedral angle of 35.8(2)°.

The thermal stability of the phosphono-carboxylic acid 4 (mp > 350 °C, decomp. > 400 °C, see TGA in Fig. S18 in ESI†) is higher than that of biphenyl-4,4′-dicarboxylic acid, which has a melting point of 310 °C.[69]

Metal compound syntheses and structures

Due to poor solubility of the phosphono-carboxylic acid in most common solvents, the reactions between ligand and metal salts were carried out under hydrothermal conditions at high temperatures (up to 180 °C) in water. All five metal complexes 5–9 share the common coordination motif of layers of metal ions, bridged by either carboxylate and phosphonate or the phosphonate group only (Scheme 3).

The zinc compound $[Zn_5(\mu_3\text{-OH})_4(\mu_4\text{-}O_3P\text{–}(C_6H_4)_2\text{–}CO_2\text{-}\mu_2)_2]$ (5) was obtained from a 3:2 molar ratio of $Zn(OAc)_2$ and H_3BPPA in water in the presence of oxalic acid. Oxalic acid was added as a buffer to give stable pH values. There was little effect on the yield or product composition when the reactant stoichiometry was adjusted to the ratio found in the X-ray structure in subsequent repeated reactions.
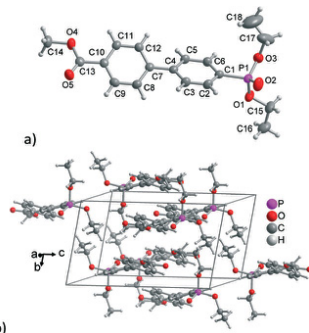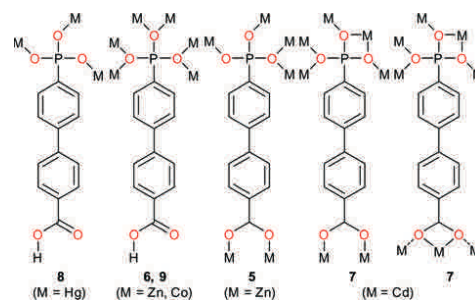

Fig. 2 (a) Asymmetric unit (50% thermal ellipsoids) and (b) crystal packing in 3. Selected distances (Å) and angles (°): P1–O1 1.560(2), P1–O2 1.462(2), P1–O3 1.567(2), C13–O5 1.195(3), C13–O4 1.341(3), O1–P1–O2 116.11(13), O2–P1–O3 113.98(13), O1–P1–O3 102.44(13).

Scheme 3 Coordination modes of the BPPA ligand in the structures of 5–9. The metal atom (M) can be Zn, Cd, Hg or Co.

The structure of 5 consists of Zn(II) ions that are coordinated by hydroxide ions and either carboxylate (–COO⁻) or phosphonate groups (–PO$_3$²⁻). The asymmetric unit contains three crystallographically different zinc atoms (one of them, Zn3 is half occupied on the special position of a C_2 rotation axis, bisecting the O1–Zn–O1^{vi} angle, Fig. 3a), two triply bridging (μ_3) hydroxide ligands and one fully deprotonated BPPA³⁻ ligand. Thereby, a {Zn2O$_4$} tetrahedron, a {Zn1O$_5$} trigonal bipyramid and a {Zn3O$_6$} octahedron are formed (Fig. 3 and Fig. S27 in ESI†). For the five-coordinated Zn1 atom the difference between the two largest angles yields τ = (172.9 − 128.6)°/60° = 0.74, which is closer to the value for a trigonal bipyramid (τ = 1) than for a square pyramid (τ = 0).[70] The two oxygens from the –COO⁻ group bridge two Zn ions and the –PO$_3$²⁻ group is coordinated to four Zn ions (Fig. 3a). Overall the BPPA³⁻ ligand bridges between six Zn atoms. The {ZnO$_x$} polyhedra are edge- and corner-sharing (Fig. 3c and S28 in ESI†). The {ZnO$_x$} (x = 4–6) polyhedra with their bridging μ_3-OH⁻, μ_4-PO$_3$²⁻ and μ_2-COO⁻ groups are arranged in layers (parallel to the bc plane) (Fig. 3b and c) and these layers are connected by the biphenyl part of the ligand to a 3D network (Fig. 3d).

The phosphorus atom in 5 has four different substituents, thus, is asymmetric and R-configured in the investigated single crystal. Only P atoms of the same handedness are assembled in the layers of 5 giving the non-centrosymmetric point group C_2 (Flack parameter 0.030(3)).[68] Circular dichroism (CD) spectra of 5 performed with KBr pellets (0.05 wt% of 5 according to a previously published protocol for solid state CD)[71] (Fig. S33 in ESI†) do not contain any significant spectral features that would indicate enantiomeric excess of either one of the two possible enantiomers of 5. Therefore, as previously observed for other cases of spontaneous resolution,[72,73] the overall crystal ensemble is racemic.

Zn compounds with 4-phosphonate-biphenyl-3′,5′-dicarboxylate as a linker and templating amine bases are known[74] but do not show the same layer motif. A zinc complex with the shorter 4-phosphonate-benzoate ligand PPA³⁻ has a zeolite-like structure, in which zigzag chains exist and {Zn$_4$O} tetrahedra are coordinated by PPA³⁻.[75]
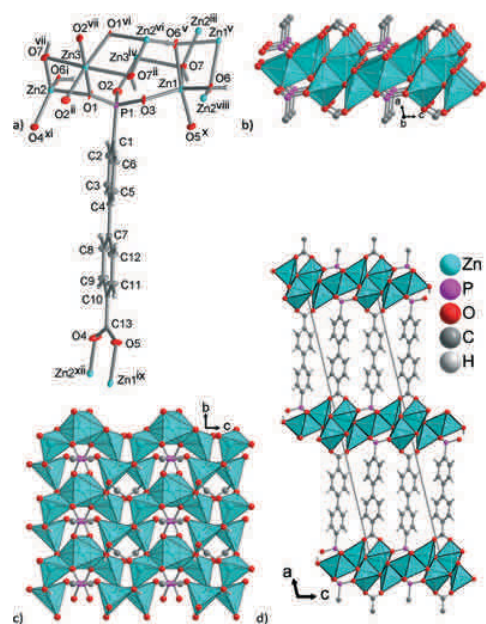
Fig. 3 (a) Expanded asymmetric unit of **5** (70% thermal ellipsoids, except for C with 50% and H with arbitrary radii) and (b, c) layers of zinc ions, bridged by hydroxido, carboxylate and phosphonate groups, $\{Zn_5(\mu_3\text{-OH})_4(\mu_4\text{-}O_3PC\text{-})_2(\text{-}CO_2\text{-}\mu_2)_2\}$ with the $\{ZnO_x\}$ polyhedra presented as such. (d) Projection of the three-dimensional packing on the ac plane. Symmetry transformations: i = x, y, 1 + z; ii = x, 1 + y, z; iii = x, y, −1 + z; iv = x, −1 + y, z; v = −x, y, −z; vi = −x, y, 1 − z; vii = −x, 1 + y, 1 − z; viii = −x, −1 + y, 1 − z; ix = 1/2 − x, 1/2 + y, 1 − z; x = 1/2 − x, −1/2 + y, 1 − z; xi = 1/2 − x, 1/2 + y, 2 − z; xii = 1/2 − x, −1/2 + y, 2 − z. Further figures also showing the O–H···O H-bonds are given in ESI† as Fig. S27–S29. Selected distances and angles are given in Table 1.
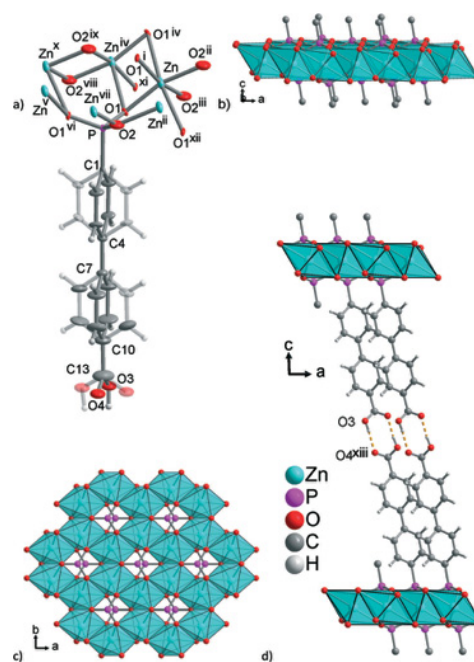
Fig. 4 (a) Expanded asymmetric unit of the zinc compound **6** (isostructural with the cobalt compound **9**) (50% thermal ellipsoids) and (b, c) layers of zinc ions, bridged by phosphonate groups, $\{Zn(\mu_6\text{-}O_3PC\text{-})\}$ with the $\{ZnO_6\}$ octahedra shown as polyhedra. (d) Section of the three-dimensional supramolecular packing through the tail-to-tail hydrogen-bonding arrangement (orange dashed lines) of the carboxylic acid groups. Symmetry transformations: i = −x + 1, y, −z + 1; ii = −x + 3/2, −y + 3/2, −z + 1; iii = x − 1/2, y + 1/2, z; iv = −x + 1/2, −y + 3/2, −z + 1; v = −x + 1, −y + 1, −z + 1; vi = x, −y + 1, z; vii = x + 1/2, y − 1/2, z; viii = −1 + x, y, z; ix = 1 − x, y, 1 − z; x = −1/2 + x, −1/2 + y, z; xi = −1/2 + x, 3/2 − y, z; xii = 1/2 + x, 3/2 − y, z; xiii = 2 − x, 1 − y, −z. Selected distances and angles are given in Table 2.

The zinc compound $[Zn(\mu_6\text{-}O_3P\text{-}(C_6H_4)_2\text{-}CO_2H)]$ (**6**) was obtained from a 1:1 molar ratio of $Zn(NO_3)_2\cdot4H_2O$ and H_3BPPA in water without any modifier. No deprotonating or buffer agent was added. The structure of **6** consists of Zn(II) ions that are coordinated by the $HBPPA^{2-}$ ligand with only the phosphono group deprotonated ($-PO_3^{2-}$) and the carboxyl group still protonated ($-COOH$). The asymmetric unit contains a unique zinc atom and the ligand $HBPPA^{2-}$ on special positions with half-occupancy. This leads to a crystallographically induced disorder of the ligand over two split-positions (Fig. 4a).

In the cobalt structure with the shorter 4-phosphono benzoic acid ligand,[52] which is analogous to compound **9** (see below), the same disorder of the phenyl ring and of the –COOH was observed. The Zn atom is coordinated by six oxygen atoms in a distorted octahedron with four shorter bonds in the equatorial plane and two longer axial bonds. The oxygen atoms of $\mu_6\text{-}PO_3^{2-}$ coordinate to six zinc ions with each O atom bridging two zinc ions (Fig. 4a). The distorted $\{ZnO_6\}$

octahedra are edge-sharing and form a flat honeycomb layer parallel to the ab plane (Fig. 4b and c). The 2D-$\{Zn(\mu_6\text{-}O_3PC\text{-})\}$ layers are connected by the biphenyl-carboxylic acid part of the ligand to a supramolecular 3D network through the carboxylic acid groups which are oriented towards each other with the typical tail-to-tail arrangement, also known as $R_2^2(8)$-motif in the Etter-notation (Fig. 4d and Table S5 in ESI†).[76]

Similarly compound $[Co(\mu_6\text{-}O_3P\text{-}(C_6H_4)_2\text{-}CO_2H)]$ (**9**) was prepared from an equimolar ratio of $CoCl_2$ and H_3BPPA in water. The single-crystal data set of **9** was not of sufficient quality to present a publishable structure determination. Yet, the isostructural nature of **6** and **9** could be established and also confirmed by comparison of the powder X-ray diffractograms (see Fig. S24 in ESI†).

The cadmium compound $[Cd_3(\mu_6\text{-}O_3P\text{-}(C_6H_4)_2\text{-}CO_2\text{-}\mu_2)(\mu_6\text{-}O_3P\text{-}(C_6H_4)_2\text{-}CO_2\text{-}\mu_3)]$ (**7**) was obtained from a 3:2 molar ratio

Table 1 Selected distances (Å) and angles (°) in **5**[a]

Zn1–O3	1.940(4)	Zn2–O4[xi]	1.909(5)
Zn1–O5[x]	2.010(5)	Zn2–O6[i]	1.970(4)
Zn1–O6	2.007(4)	Zn2–O7[vii]	1.974(4)
Zn1–O6[v]	2.256(5)	Zn3–O1	2.133(4)
Zn1–O7	2.014(5)	Zn3–O2[ii]	2.013(5)
Zn2–O1	1.991(4)	Zn3–O7[ii]	2.264(4)
O3–Zn1–O6[v]	110.82(18)	O4[xi]–Zn2–O1	103.41(19)
O3–Zn1–O5[x]	96.31(18)	O6[i]–Zn2–O1	104.64(19)
O6–Zn1–O5[x]	99.97(18)	O7[vii]–Zn2–O1	89.09(18)
O3–Zn1–O7	116.73(18)	O2[ii]–Zn3–O2[vii]	97.0(3)
O6–Zn1–O7	128.57(19)	O2[ii]–Zn3–O1	86.30(16)
O5[x]–Zn1–O7	93.40(18)	O2[vii]–Zn3–O1	175.21(18)
O3–Zn1–O6[v]	90.79(17)	O1[vi]–Zn3–O1	90.6(2)
O6–Zn1–O6[v]	77.4(2)	O2[ii]–Zn3–O7[ii]	98.01(16)
O5[x]–Zn1–O6[v]	172.90(17)	O2[ii]–Zn3–O7[vii]	90.37(16)
O7–Zn1–O6[v]	83.34(17)	O1–Zn3–O7[ii]	92.64(16)
O4[xi]–Zn2–O6[i]	110.3(2)	O1[vi]–Zn3–O7[ii]	78.43(15)
O4[xi]–Zn2–O7[vii]	126.2(2)	O2[ii]–Zn3–O7[vii]	90.37(16)
O6[i]–Zn2–O7[vii]	116.62(19)	O2[vii]–Zn3–O7[vii]	98.01(16)
		O1–Zn3–O7[vii]	78.32(15)
Zn1–O6–Zn2[iii]	127.5(2)	O1[vi]–Zn3–O7[vii]	92.64(16)
Zn2–O1–Zn3	97.19(17)	O7[ii]–Zn3–O7[vii]	167.4(2)
Zn1–O7–Zn3[iv]	110.38(19)		

[a] Symmetry transformations: i = x, 1 + z; ii = x, 1 + y, z; iii = x, y, −1 + z; iv = x, −1 + y, z; v = −x, y, −z; vi = −x, y, 1 − z; vii = −x, 1 + y, 1 − z; viii = −x, −1 + y, 1 − z; ix = 1/2 − x, 1/2 + y, 1 − z; x = 1/2 − x, −1/2 + y, 1 − z; xi = 1/2 − x, 1/2 + y, 2 − z; xii = 1/2 − x, −1/2 + y, 2 − z.

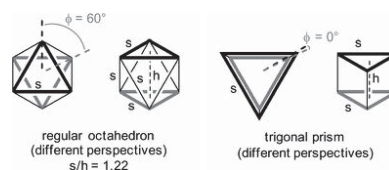**Table 2** Selected distances (Å) and angles (°) in **6**[a]

Zn–O1	1.931(4)	Zn–O1[xii]	2.620(4)
Zn–O2[iii]	1.973(6)		
O1–Zn–O1[i]	93.2(3)	O1[iv]–Zn–O1[xii]	171.1(3)
O1–Zn–O2[ii]	162.8(3)	O1–Zn–O1[xii]	82.8(4)
O1–Zn–O2[iii]	93.7(2)	Zn–O1–Zn[iv]	76.6(2)
O2[ii]–Zn–O2[iii]	84.2(4)	Zn[ii]–O2–Zn[vii]	95.8(4)
O1[i]–Zn–O1[xii]	103.4(3)		

[a] Symmetry transformations: i = −x + 1, y, −z + 1; ii = −x + 3/2, −y + 3/2, −z + 1; iii = x − 1/2, y + 1/2, z; iv = −x + 1/2, −y + 3/2, −z + 1; vii = x + 1/2, y − 1/2, z; xii = 1/2 + x, 3/2 − y, z.

Scheme 4 Octahedron and trigonal prism with enhanced triangular faces and relevant parameters for the assessment of their relationship. ϕ is the twist angle between the enhanced triangles around the C_3 axis.

polyhedra in compound **7** can be regarded as distorted trigonal prisms (see average values in Scheme 5 from the data in Table S12 in ESI†).

The −PO_3^{2-} oxygens bridge between five Cd atoms, while the −COO^- groups bridge either two or three Cd atoms (Fig. 5a, Scheme 3 and Fig. S31 in ESI†). Overall, the BPPA[3−] ligand bridges seven or eight Cd atoms. The edge- and vertex-sharing {CdO_6} trigonal prisms with their bridging μ_5-PO_3^{2-} and μ_2/μ_3-COO^- groups are arranged in flat layers (parallel to
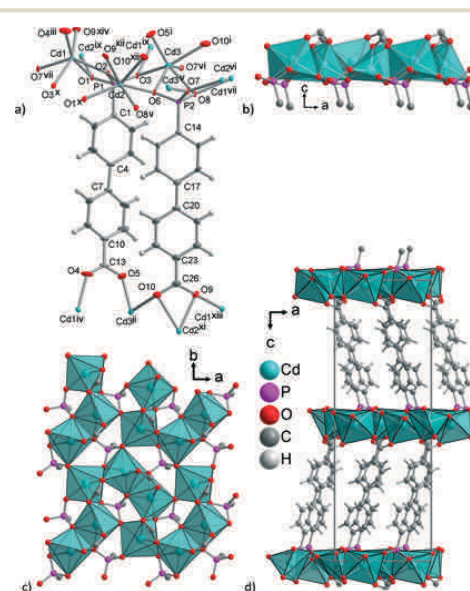
Fig. 5 (a) Expanded asymmetric unit of the cadmium compound **7** (Cd and P 70%, C and O 50% thermal ellipsoids) and (b, c) layers of cadmium ions, bridged by phosphonate and carboxylate groups, {$Cd_3(\mu_5$-O_3PC-$)_2(−CO_2$-$\mu_2/\mu_3)_2$} with the {CdO_6} trigonal prisms depicted as polyhedra. (d) Projection of the three-dimensional packing on the ac plane. Symmetry transformations: i = 1/2 − x, y, 1/2 + z; ii = 1/2 − x, y, −1/2 + z; iii = −x, 2 − y, 1/2 + z; iv = −x, 2 − y, −1/2 + z; v = −1/2 + x, 1 − y, z; vi = 1/2 + x, 1 − y, z; vii = x, −1 + y, z; ix = 1/2 + x, 2 − y, z; x = −1/2 + x, 2 − y, z; xi = −x, 1 − y, −1/2 + z; xii = −x, 1 − y, 1/2 + z; xiii = 1/2 − x, −1 + y, −1/2 + z; xiv = 1/2 − x, 1 + y, 1/2 + z. Selected distances are given in Table 3. Angles are listed in Table S6 in ESI.†

of Cd(OAc)₂ and H₃BPPA in water in the presence of oxalic acid (added to allow stable pH values).

In the crystal structure of **7**, the asymmetric unit consists of three different Cd atoms and two fully deprotonated BPPA[3−] ligands. The Cd atoms are coordinated by six oxygen atoms from both μ_2- and μ_3-COO^- and μ_5-PO_3^{2-} groups (Fig. 5a).

Significant distortion from classical octahedral towards trigonal-prismatic (TP) geometry around Cd is clearly revealed in the structure of **7** (see Cd-polyhedra in Table S12 in ESI†). An idealized octahedron has two exactly parallel, staggered equilateral triangles and all edges of side s (Scheme 4). Consideration of the angular parameters θ, ρ and ω (Scheme 5) in the comparison between octahedral and trigonal prismatic limiting structures[77,78] indicates that the Cd

86

Scheme 5 Angular parameters involved in the comparison between the octahedral and trigonal-prismatic limiting structures. θ = angle between the mean plane of the two O_3 triangles and the chelate planes defined by the metal and each pair of near eclipsed O vertices. ρ = angle between the metal and *trans* O-donor sites. ω = angle between the triangular faces defined by the metal and near eclipsed O atoms. The angle for Cd*i* is the average of three angles, which are listed in Table S12 in ESI.†

Table 3 Selected distances (Å) in **7**[a]

Cd1–O1	2.370(7)	Cd2–O8[v]	2.273(8)
Cd1–O2	2.294(7)	Cd2–O9[xii]	2.387(9)
Cd1–O3[x]	2.359(8)	Cd2–O10[xii]	2.458(9)
Cd1–O4[iii]	2.177(9)	Cd3–O3	2.328(8)
Cd1–O7[vii]	2.263(7)	Cd3–O5[i]	2.132(9)
Cd1–O9[xiv]	2.406(9)	Cd3–O6	2.324(8)
Cd2–O1[x]	2.286(8)	Cd3–O7[vi]	2.201(7)
Cd2–O2	2.226(7)	Cd3–O8	2.328(8)
Cd2–O6	2.289(8)	Cd3–O10[i]	2.541(10)

[a] For angles see Table S6 in ESI. Symmetry transformations: i = 1/2 − x, y, 1/2 + z; ii = 1/2 − x, y, −1/2 + z; iii = −x, 2 − y, 1/2 + z; v = −1/2 + x, 1 − y, z; vi = 1/2 + x, 1 − y, z; vii = x, −1 + y, z; ix = 1/2 + x, 2 − y, z; x = −1/2 + x, 2 − y, z; xii = −x, 1 − y, 1/2 + z; xiii = 1/2 − x, −1 + y, −1/2 + z; xiv = 1/2 − x, 1 + y, 1/2 + z.

the *ab* plane) (Fig. 5b and c) and these layers are connected by the biphenyl part of the ligand to a 3D network (Fig. 5d).

Compound **7** crystallizes in the non-centrosymmetric orthorhombic space group *Pca*2₁. The non-centrosymmetric packing (Flack parameter 0.007(9))[68] originates from the identical orientation of the phosphonato ends (or the carboxylato ends, respectively) of the $^{2-}O_3P–(C_6H_4)_2–CO_2^-$ linkers along the crystallographic *c* axis (Fig. 5d).

Five edge- and vertex-sharing $\{CdO_6\}$ polyhedra form a pentagon, which assembles into a 2D **mcm**-net (Fig. 6a).[79] In its regular form this pentagon tiling consists of two kinds of vertices (5^3 and 5^4, connecting 3 or 4 pentagons, respectively), two kinds of edges and one kind of face.

The mercury(ɪ) compound with the sum formula $[Hg(\mu_3\text{-}HO_3P–(C_6H_4)_2–CO_2H)]$ (**8**) was obtained from an equimolar ratio of mercury(ɪɪ) acetate, $Hg(OAc)_2$, and H₃BPPA in water in the presence of oxalic acid to allow stable pH values. In **8**, the mercury oxidation state assignment depends on the pres-
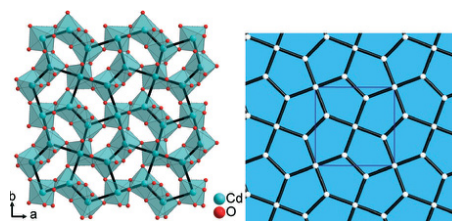
Fig. 6 Left: Layer of $\{CdO_6\}$ polyhedra in **7** with the Cd atoms connected by black lines to illustrate the pentagonal **mcm** tiling. Right: **mcm** net from http://rcsr.net/layers/mcm.[79]

ence or absence of the calculated proton on the phosphonato group, $^-HO_3P$.

The phosphonate group of the ligand remains singly protonated (or is only singly deprotonated), that is, $-PO_3H^-$ with the O3 atom carrying the H atom. The carboxyl group remains protonated as is clearly evidenced by the tail-to-tail hydrogen-bonding arrangement. The H3 atom on O3 of $-PO_3H^-$ could be found and refined with $U_{iso}(H)$ = $1.5U_{eq}(O)$ and the DFIX restraint 0.90 ± 0.05 Å.

Bond valence sum calculations[80,81] done on the Hg atom of **8** gave a value of 0.83 when assuming a valence of 1 and a value of 1.00 when assuming a valence of 2. The calculated values support the valence of 1.

In the structure of **8**, two mercury ions form a handle with C_2-symmetry-related Hg atoms at a Hg–Hg distance of 2.5116(14) Å, presumably the well-known dinuclear Hg_2^{2+} dication. A possible Hg_2^{4+} cation is rare. The di-mercury(ɪɪ) complex bis(μ-*P*,*N*-1-benzyl-2-imidazolyl-diphenylphosphine)(μ-*O*,*O'*-diperchloratedimercury(ɪɪ)) diperchlorate ($C_{44}H_{38}N_4O_{16}P_2$-Cl_4Hg_2) is one example,[82] but the Hg–Hg distance with 3.071(1) Å is longer than in **8**. The short Hg–Hg distance of ∼2.5 Å falls in the distance range of 2.46–2.60 Å observed for a $Hg(ɪ)_2^{2+}$ cation.[83]

Hence, we assume a Hg(ɪ) oxidation state with single-deprotonated H₃BPPA ligand. The asymmetric unit contains one unique Hg atom and one H₂BPPA⁻ ligand. Each Hg atom is coordinated by three oxygens from three different $^-HO_3P$-groups (Fig. 7a) with a severely distorted tripodal HgO_3 coordination, which is tilted with respect to the Hg–Hg bond (Fig. 7b and Fig. S32, ESI†). There is one short Hg1–O1 contact of 2.118(13) Å and two considerably longer contacts Hg1–O2[iii] = 2.566(16) Å and Hg1–O3[iv] = 2.729(15) Å (Table 4 and Fig. 7a). This coordination environment agrees with a classical L–Hg(ɪ)–Hg(ɪ)–L species. For Hg(ɪɪ), a higher coordination number of four to eight is expected, whereas a coordination number of three for H(ɪɪ) is very rare.[84] More importantly, no direct Hg–Hg bonds are found in coordination polymers of mercury(ɪɪ).[84] For Hg_2^{2+}, there are several examples of complexes in the Cambridge Structure Database in which the overall coordination number of a Hg(ɪ) atom is four.[85] Furthermore, an *in situ* reduction of Hg^{2+} to Hg_2^{2+} was also observed by Su *et al.*[85c]
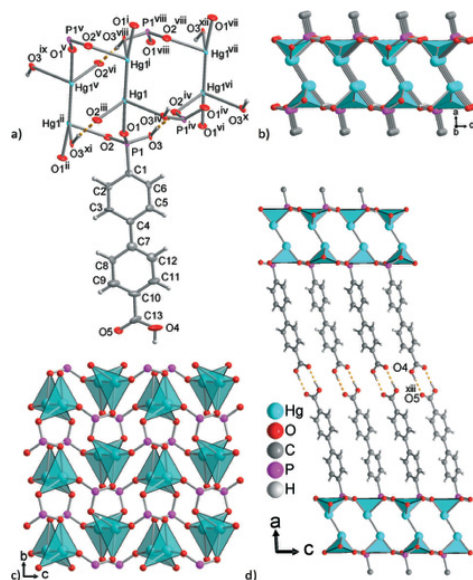
Fig. 7 (a) Expanded asymmetric unit of **8** (Hg and P 70%, C and O 50% thermal ellipsoids; H bonds are orange dashed lines) and (b, c) layers of Hg_2^{2+} handles, bridged by phosphonate groups, $\{Hg_2(\mu_3\text{-}HO_3PC\text{-})_2\}$ with the $\{HgO_3\}/\{Hg_2O_6\}$ depicted as polyhedra. (d) Section of the supramolecular three-dimensional packing through the tail-to-tail hydrogen-bonding arrangement (orange dashed lines) of the carboxylic acid groups. Symmetry transformations: i = 1 − x, y, 1/2 − z; ii = x, −y, 1/2 + z; iii = x, −y, −1/2 + z; iv = x, 1 − y, −1/2 + z; v = 1 − x, −y, 1 − z; vi = x, 1 + y, z; vii = 1 − x, 1 + y, 1/2 − z; viii = 1 − x, 1 − y, 1 − z; ix = 1 − x, −1 + y, 3/2 − z; x = x, 2 − y, −1/2 + z; xi = x, −1 + y, z; xii = 1 − x, 2 − y, 1 − z. Selected distances and angles are given in Table 4; hydrogen bonding interactions in Table S8 in ESI.†

Table 4 Selected bond distances (Å) and angles (°) in **8**[a]

Hg1–O1	2.118(13)	Hg1–O3[iv]	2.729(15)
Hg1–O2[iii]	2.566(16)	Hg1–Hg1[i]	2.5116(14)
O1–Hg1–Hg1[i]	171.7(4)	P1–O1–Hg1	133.6(9)
O1–Hg1–O2[iii]	78.3(5)	P1–O2–Hg1[ii]	120.1(8)
Hg1[i]–Hg1–O2[iii]	108.9(3)	O3[iv]–Hg1–Hg1[i]	101.3(3)
O3[iv]–Hg1–O2[iii]	97.0(5)		

[a] Symmetry transformations: i = 1 − x, y, 1/2 − z; ii = x, −y, 1/2 + z; iii = x, −y, −1/2 + z; iv = x, 1 − y, −1/2 + z.

The phosphonate groups of six ligands (three on each Hg) are bridging the Hg–Hg handles to a flat 2D-$\{Hg_2(\mu_3\text{-}HO_3P\text{-})\}$ layer (Fig. 7b and c). These 2D-layers are connected by the biphenyl-carboxylic acid part of the ligand to a supramolecular 3D network through the carboxylic acid groups which are oriented towards each other in the tail-to-tail arrangement $(R_2^2(8)$-motif in the Etter-notation)[76] (Fig. 7d and S32, Table S8, ESI†).

A mixed-valent mercury complex with ʟ-alanine, [Hg_{12}(ʟ-ala)$_8$(NO$_3$)$_8$]·2H$_2$O showed a coordination environment for Hg similar to the one found for **8**.[86] A compound of mercury with a phosphono-carboxylate linker has been unknown.

There are seven entries in the Cambridge Structure Database, CSD, with a –P–O–Hg coordination, from which only two (AFIWES[87] and SARSAF[88]) contain phosphonates coordinated to Hg(ɪɪ) and of which none has Hg–Hg handles.

All metal-linker compound **5**–**9** share the layer motif for the $\{MO_x\}$ polyhedra. The driving force appears to be the separation of polar and nonpolar parts of molecules, which is a common packing motif.[89–91]

CH-π contacts between neighbouring biphenyl systems in **5**–**8** are listed in Tables S9–S11 in ESI† with angles and distances of significant interactions.

A listing of the dihedral angles in the BPPA linker in complexes **5**–**8** is given in Table S13 in the ESI.† With dihedral angles ranging from 0.1(6)° (**5**) to 2.0(2)° (**8**), the aryl systems are nearly co-planar (0°) to each other, favouring the π-electron delocalisation. The aryl-COO(H) angles vary from 2.0(2)° (**6**, **7**) to 16.3(9)° (**5**), which is explained by the different state of protonation and coordination of the –COO group. Still, a close to planar geometry of the ligand is observed in all complexes.

Hydrothermal stability

The noteworthy water stability of the complexes **5**–**9** has been investigated by long-time exposure of the complexes in water. IR and powder X-ray diffraction, PXRD, did not indicate any structural changes within months. Furthermore, the hydrothermal synthesis conditions (water at 180–200 °C) would not allow the formation of water-unstable structures.

The thermogravimetric behavior in Fig. 8 (detailed Fig. S19–S23 in ESI†) reveals a high thermal stability for **5** and **7**. The thermally stable ligand (m.p. >350 °C) contributes to the overall stability of the compounds through the strong metal-phosphonate coordination. The mass loss of ∼5% in **4** (see Fig. S18 in ESI†) can be explained by a dehydration (−1H$_2$O,
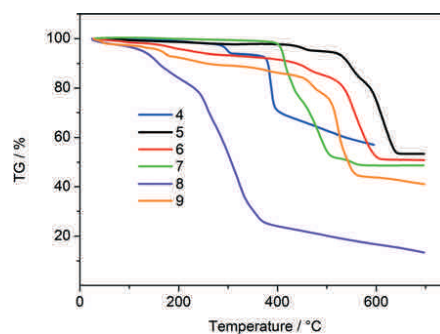

Fig. 8 Thermogravimetric analysis (TGA) curves of compounds **4**–**9**.

18 g mol^{-1}, 6%) through the condensation of phosphonic acid groups to give anhydrides.[92]

Compounds **5** and **7**, where the ligand is fully deprotonated without a remaining –COOH group, start to decompose at ~400 °C. The isostructural compounds **6** and **9**, where only the phosphono group is deprotonated (–PO$_3{}^{2-}$) and the carboxyl group still protonated (–COOH), show a steady weight loss starting at ~150–200 °C, presumably first by a condensation (–1H$_2$O, 18 g mol^{-1}: 5.3% in **6** and **9**) followed by a decarboxylation (–1CO$_2$, 44 g mol^{-1}: 13% in **6**; 13.5% in **9**). The mercury compound **8** undergoes a rapid mass loss, starting already at ~100 °C, which can also be observed in other Hg complexes.[93] A decarboxylation is observed in the temperature range from 120 to 180 °C (–1CO$_2$, 45 g mol^{-1}, 9.5%). Hg complexes vaporize completely because of the high volatility of elemental Hg above 500 °C. Elemental Hg is formed by decomposition of intermediate HgO to its elements.

Luminescence

Many organic molecules are only fluorescent in solution because in their solid-state they are subject to self-quenching with concomitant low quantum yield of their luminescence.[94] Immobilization/rigidification of organic molecules as linkers or as guest molecules in a solid framework like a coordination polymer[95] or MOF with d^{10} metal ions such as Zn^{2+} and Cd^{2+} will reduce non-radiative relaxation caused by free rotation and vibration and, therefore, lead to stronger emissions.[96,97]

The emission spectrum of **4** (Fig. 9) shows a broad band with a maximum at around 365 nm when excited at 316 nm. The spectrum is comparable to that of dihydroxybiphenyls, such as 4,4′-dihydroxybiphenyl (λ_{max} = 354 nm) and 2,2′-di-

hydroxybiphenyl (λ_{max} = 356 nm) and many other previously reported substituted biphenyl systems (λ_{max} = 318–420 nm).[98]

It is well documented that the luminescence observed in MOFs or coordination polymers of transition metal ions without unpaired electrons (such as Cd^{2+} and Zn^{2+}) are typically ligand centered.[99,100] The emission spectra of the Zn compound **5** (λ_{ex} = 354 nm), the Cd compound **7** (λ_{ex} = 350 nm), the Hg compound **8** (λ_{ex} = 345 nm) and the Co compound **9** (λ_{ex} = 360 nm) also exhibit broad emission bands in the visible range at 410–420 nm suggesting that the luminescence in all compounds originate from the electronic transitions of the ligand. The emission spectra of the complexes are red shifted compared to that of the ligand, **4**, due to the different coordination and crystal packing interactions. The positions of the emission bands may be explained by different dihedral angles of the aromatic rings in the ligand and the complexes. Smaller dihedral angles result in enhanced π electron interactions, which in turn shift the emission bands to lower energies.[101] Although the dihedral angle in the ligand **4** is not known, in the metal compounds it is consistently very close to 0°: 0.1(6)° (**5**), 1.5(1)° (**6**), 0.5(2)° (**7**) and 2.0(2)° (**8**). Even though the dihedral angles in the excited states cannot be determined, it may be assumed that due to the crystal in rigid structures the conformations do not change significantly. To the best of our knowledge, no luminescent phosphonate–carboxylate compounds with Zn^{2+}, Hg$_2{}^{2+}$ and Cd^{2+} ions have been reported so far.

Conclusions

We have presented the crystal structures of five complexes with the new BPPA^{3-} or HBPPA^{2-} ligand. The new mixed-functional linker assumes (five) different metal–oxygen(ligand) coordination modes depending on the metal. Yet, all metal-linker compounds **5–9** share the common motif of {MO$_x$} polyhedra arranged in a mostly flat layer, which are connected by the biphenyl part, either directly or through tail-to-tail carboxyl groups. This way, polar and nonpolar parts of the molecules are separated, which is a common packing motif. In the flat {MO$_x$} layers in **6** and **7** the Zn and Cd metal nodes represent a honeycomb and an **mcm** net, respectively. Between the biphenyl groups, CH-π contacts are present (see ESI†). The coordination polyhedra of the Cd atoms in compound **7** were analyzed towards a trigonal-prismatic coordination environment. When the linker is fully deprotonated to BPPA^{3-} the metal–ligand networks feature a high thermal stability of ~400 °C. When the carboxyl group is still protonated (–COOH in HBPPA^{2-}) a decarboxylation starts at ~150–200 °C, yet further decomposition only occurs above 400 °C. All compounds are very resistant against hydrolysis as they were synthesized in water at up to 200 °C and were stored in either water or air. The fluorescence emission of the H$_3$BPPA ligand is red shifted by about 50 nm upon deprotonation and metal complexation. It was our aim to demonstrate, that the combination of the phosphonato, –PO$_3{}^{2-}$
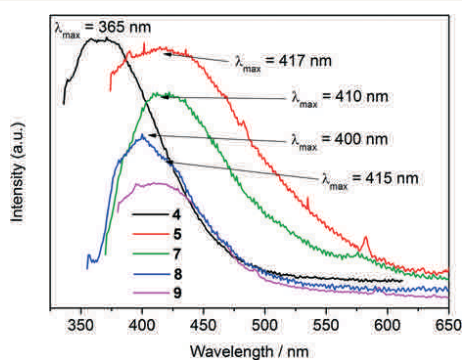

Fig. 9 Solid-state luminescence spectra of complexes **5** (λ_{ex} = 354 nm), **7** (λ_{ex} = 350 nm), **8** (λ_{ex} = 345 nm) and **9** (λ_{ex} = 360 nm) in comparison with the spectrum of the ligand, **4** (λ_{ex} = 316 nm). The spikes in the emission spectra are probably due to the lamp fluctuations or random pickup by the photomultiplier.

and carboxylato, –COO⁻ function leads to hydrothermally stable network compounds.

Experimental section

Materials and methods

All reactants were commercially available and used without further purification. Doubly de-ionized (DI) water was used.

Elemental (CHN) analyses were performed on a Perkin Elmer CHN 2400. ^{1}H, ^{13}C and ^{31}P NMR spectra were measured with a Bruker Avance DRX-200, Bruker Avance DRX-500 or Bruker Avance DRX-600. High-resolution electron-spray ionization mass spectra (HR-ESI-MS) were collected with a UHR-QTOF maXis 4G from Bruker Daltonics. Electron impact (EI) mass spectra were collected on a TSQ 7000 by Finnigan MAT. FT-IR spectra were recorded in ATR mode (Platinum ATR-QL, Diamond) on a Bruker TENSOR 37 IR spectrometer in the range of 4000–500 cm^{-1}. The absorbance bands have been described by the following terms: strong (s), medium (m), weak (w) and broad (br). Solid-state fluorescence spectra (2D) were obtained with a FluoroMax spectrometer from Horiba at room temperature. The samples were ground to a powder and pressed to fit securely in the sample holder (the mercury compound **8** has not been measured because of its toxicity). The reflection angle was set to be 60°. For thermogravimetric analysis (TGA) a Netzsch TG 209 F3 Tarsus was used, equipped with Al-crucible and a measurement range from 20 to 700 °C with a heating rate of 10 K min^{-1} under inert atmosphere (N$_2$). Programmable ovens with heating and cooling ramps were from Memmert.

Melting points were determined using a Büchi Melting Point B540. For powder X-ray diffraction patterns (PXRD) a Bruker D2 Phaser powder diffractometer was used with flat panel low background sample holder, CuKα radiation (λ = 1.5418 Å) at 30 kV, 10 mA, a scan speed of 0.2 s per step and a step size of 0.02° (2θ).

Circular dichroism (CD) spectra of **5** were recorded on a J-810 spectropolarimeter (JASCO) with KBr pellets (0.05 wt% of **5**). To correct for linear anisotropy artifacts the KBr pellets were rotated during a measurement by the use of a motor-driven sample holder (20 rpm). The detector integration time was set to 16 s (scan rate: 20 nm min^{-1}). Each pellet was measured on the front and the reverse side. The resulting spectra (see Fig. S33 in ESI†) were averaged.

Single crystal X-ray diffractometry

Suitable crystals were carefully selected under a polarizing microscope, covered in protective oil and mounted on a 0.05 mm cryoloop. *Data collection.* Bruker Kappa APEX2 CCD X-ray diffractometer with microfocus tube, Mo-Kα radiation (λ = 0.71073 Å), multi-layer mirror system, ω- and θ-scans. Data collection with APEX II,[102] cell refinement with SMART, data reduction with SAINT[103] and experimental absorption correction with SADABS.[104] *Structure analysis and refinement*: The structures were solved by direct methods, SHELXS-97, refinement was done by full-matrix least squares on F^2 using the SHELX-97 program suite.[105] Non-hydrogen atoms were refined with anisotropic displacement parameters. Hydrogen atoms were positioned geometrically and refined using riding models [AFIX 43 for aromatic CH with C–H = 0.93 Å, AFIX 23 for CH$_2$ with C–H = 0.97 and U_{iso}(H) = 1.2U_{eq}(C), AFIX 137 for CH$_3$ with C–H = 0.96 Å and U_{iso}(H) = 1.5U_{eq}(C); AFIX 83 for –COOH and U_{iso}(H) = 1.5U_{eq}(O)]. Hydrogen atoms H1 and H7 on the OH groups in **5** have been freely refined in position and U_{iso}. Crystals of **5**–**9** were of very small size. It is known that very small crystals diffract weaker than larger crystals,[106] resulting in lower data quality and subsequent problems during refinement. Some of the *checkcif* alerts are due to the small crystal size, *e.g.*, poor data/parameter ratio (**6**, **7**). In **6** the disorder of the biphenyl moiety (treated with the PART command in SHELX) and –COOH group, which can have two different orientations, is causing level B alerts. The large residual electron density near the Hg atoms in **8** gave level A and B alerts. Nine of the 13 largest peaks of the residual electron density (including the three largest) are within 2 Å of the Hg atom in **8**. Crystal data and details on the structure refinement are given in Tables 5 and 6. Graphics were drawn with DIAMOND.[107] Analyses on the supramolecular C–H⋯O-, C–H⋯π- and π–π-stacking interactions were done with *PLATON* for Windows.[108] The crystallographic data have been deposited with the Cambridge Crystallographic Data Center (CCDC-numbers 1465329–1465334 for **3**, **6**, **8**, **5**, **2**, **7**, respectively).

Syntheses

4-Iodo-4′-biphenylcarboxylic acid (1). According to a method of Merkushev and Yudina,[66] 10.0 g (0.05 mol) of 4-biphenylcarboxylic acid, 21.7 g (0.05 mol) of bis(trifluoroacetoxy)iodobenzene and 12.7 g (0.05 mol) of freshly ground iodine were placed in a 50 mL flask together with 20 mL of CCl$_4$. The deep-violet suspension was stirred for two hours at room temperature. The solid was filtered and washed with 3 × 10 mL of CCl$_4$. The resulting white powder was dried in vacuum (10^{-1} mbar) to afford 13.3 g of pure product (82% yield). Mp = 310 °C (lit: 312 °C).[109] FT-IR (ATR) $\tilde{v}$/cm^{-1} = 2976 (w, br), 2820 (w, br), 2668 (w), 2546 (w), 1827 (vs), 1677 (m), 1605 (m), 1572 (m), 1549 (m), 1514 (m), 1474 (m), 1424 (m), 1386 (m), 1321 (m), 1298 (m), 1280 (m), 1196 (s), 1177(m), 1123 (m), 1104 (m), 1062 (m), 1019 (m), 1010 (m), 996 (m), 954 (m), 871 (m), 818 (m), 767 (m), 744 (vs), 710 (m), 698 (m), 661 (m), 623 (m). ^{1}H-NMR (200 MHz; DMSO-d_6) δ/ppm = 7.53 (d, 2H, J = 8.0 Hz), 7.79 (d, 2H, J = 8.0 Hz), 7.84 (d, 2H, J = 8.0 Hz), 8.01 (d, 2H, J = 8.0 Hz). Spectra are given in Fig. S1 and S2 in the ESI.†

4-Iodo-4′-biphenylcarboxylic acid methyl ester (2). In a 50 mL glass flask 5.0 g (15.4 mmol) of **1** were suspended in 10 mL of a mixture of CCl$_4$ and N,N′-dimethylformamide (v : v = 1 : 1). Then 6.2 g (45.0 mmol) of K$_2$CO$_3$ were added to the suspension under stirring. A portion of 6.4 g (45.0 mmol) of methyliodide was added dropwise over one hour resulting in the formation of a yellowish, oily layer. The layers were

Table 5 Crystal data and structure refinement for **2** and **3**

Compound	2	3
Chemical formula	$C_{14}H_{11}IO_2$	$C_{18}H_{21}O_5P$
M_r	338.13	348.32
Crystal system	Orthorhombic	Triclinic
Space group	$Pca2_1$	$P\bar{1}$
Temperature (K)	150	296
a (Å)	6.0355 (4)	8.094(2)
b (Å)	7.2980(4)	8.186(2)
c (Å)	27.8833(18)	13.626(4)
α (°)	90	104.044(15)
β (°)	90	92.510(15)
γ (°)	90	99.071(14)
V (Å^3)	1228.18(13)	861.7(4)
Z	4	2
μ (mm^{-1})	2.593	0.18
Crystal size (mm)	$0.10 \times 0.10 \times 0.05$	$0.90 \times 0.20 \times 0.20$
T_{min}, T_{max}	0.724, 0.745	0.620, 0.744
No. measured, indep. and obs. $[I > 2\sigma(I)]$ reflect.	10 290, 2382, 2325	11 291, 3248, 2650
R_{int}	0.049	0.053
$(\sin \theta/\lambda)_{max}$ (Å^{-1})	0.624	0.613
$R_1 [F^2 > 2\sigma(F^2)]$, wR_2 (F^2),^{b} S^c	0.030, 0.099, 1.24	0.060, 0.175, 1.07
No. of reflect./restraints/parameters	2382/1/155	3248/0/220
Weight. scheme w; a/b^d	0.050/0.6335	0.0925/0.6193
Max./min. $\Delta\rho$ (e Å^{-3})^a	0.81, −0.82	0.53, −0.47
Absolute structure (Flack) parameter^e	0.080(17)	—

^{a} Largest difference peak and hole. ^{b} $R_1 = [\sum(||F_o| - |F_c||)/\sum|F_o|]$; $wR_2 = [\sum[w(F_o^2 - F_c^2)^2]/\sum[w(F_o^2)^2]]^{1/2}$. ^{c} Goodness-of-fit, $S = [\sum[w(F_o^2 - F_c^2)^2]/(n - p)]^{1/2}$. ^{d} $w = 1/[\sigma^2(F_o^2) + (aP)^2 + bP]$ where $P = (\max(F_o^2 \text{ or } 0) + 2F_c^2)/3$. ^{e} Ref. 68.

Table 6 Crystal data and structure refinement for **5–8**

Compound	5	6	7	8
Chemical formula	$C_{26}H_{20}O_{14}P_2Zn_5$	$C_{13}H_9O_5PZn$	$C_{26}H_{16}Cd_3O_{10}P_2$	$C_{13}H_{10}HgO_5P$
M_r	945.31	341.54	887.53	477.77
Crystal system	Monoclinic	Monoclinic	Orthorhombic	Monoclinic
Space group	$C2$	$C2/m$	$Pca2_1$	$C2/c$
Temperature (K)	173	173	173	173
a (Å)	32.8388(12)	5.2848(12)	9.3961(7)	59.003(11)
b (Å)	5.3763(19)	8.1031(18)	9.5450(7)	5.4907(9)
c (Å)	7.913(3)	27.371(6)	27.3230(19)	7.8375(12)
β (°)	103.531(11)	91.766(12)	90	93.644(9)
V (Å^3)	1358.2(9)	1171.6(5)	2450.5(3)	2534.0(7)
Z	2	4	4	8
μ (mm^{-1})	4.55	2.25	2.77	12.29
Crystal size (mm)	$0.10 \times 0.01 \times 0.01$	$0.03 \times 0.03 \times 0.03$	$0.10 \times 0.07 \times 0.05$	$0.01 \times 0.01 \times 0.01$
T_{min}, T_{max}	0.502, 0.748	0.724, 0.745	0.685, 0.747	0.515, 0.746
No. measured, indep. and obs. $[I > 2\sigma(I)]$ reflect.	8001, 3360, 2930	5207, 1106, 912	48 627, 4301, 4281	11 056, 2121, 1633
R_{int}	0.060	0.054	0.043	0.089
$(\sin \theta/\lambda)_{max}$ (Å^{-1})	0.703	0.594	0.595	0.594
$R_1 [F^2 > 2\sigma(F^2)]$, wR_2 (F^2),^{b} S^c	0.041, 0.085, 1.01	0.068, 0.163, 1.05	0.032, 0.077, 1.13	0.070, 0.176, 1.03
No. of reflections/restraints/parameters	3360/1/220	1106/0/129	4301/1/310	2121/0/155
Weight. scheme w; a/b^d	0.0302/0	0.0504/40.479198	0.008/37.947201	0.0831/363.958771
Max./min. $\Delta\rho$ (e Å^{-3})^a	1.67, −1.09	3.63, −1.72	1.73, −2.15	8.07, −3.81
Absolute structure (Flack) parameter^e	0.030(3)	—	0.007(9)	—

^{a} Largest difference peak and hole. ^{b} $R_1 = [\sum(||F_o| - |F_c||)/\sum|F_o|]$; $wR_2 = [\sum[w(F_o^2 - F_c^2)^2]/\sum[w(F_o^2)^2]]^{1/2}$. ^{c} Goodness-of-fit, $S = [\sum[w(F_o^2 - F_c^2)^2]/(n - p)]^{1/2}$. ^{d} $w = 1/[\sigma^2(F_o^2) + (aP)^2 + bP]$ where $P = (\max(F_o^2 \text{ or } 0) + 2F_c^2)/3$. ^{e} Ref. 68.

separated, the upper DMF layer was discarded, the solvent from the yellowish CCl$_4$ was removed in vacuum affording an off-white powder (5.0 g; 98% yield). Alternatively: In a 250 mL flask 2.5 g (7.9 mmol) of **1** were suspended in 100 mL of dry methanol. Conc. sulphuric acid (5 mL) was added and the suspension heated to reflux for 4 h. The solid was filtered and washed with plenty of water (>100 mL) to remove the acid and methanol. The product was dried to afford 2.4 g

(90%) of an off-white powder. Mp = 188 °C (lit.: 189 °C).[110] FT-IR (ATR) $\tilde{v}$/cm^{-1} = 3399 (w, br), 2998 (w), 2944 (w), 2842 (w), 1936 (m), 1902 (m), 1781 (m), 1708 (s), 1602 (m), 1576 (m), 1474 (m), 1453 (m), 1431 (m), 1387 (m), 1330 (m), 1287 (m), 1269 (s), 1209 (m), 1186 (m), 1136 (m), 1110 (s), 1066 (m), 1018 (m), 995 (m), 949 (m), 860, 819 (s), 764 (vs), 697 (m), 662 (m), 622 (m), 588 (m). ^{1}H-NMR (200 MHz, CDCl$_3$) δ/ppm = 3.92 (s, 3H), 7.34 (d, 2H, J = 8.6 Hz), 7.59 (d, 2H, J = 8.6 Hz), 7.77 (d, 2H, J = 8.6 Hz), 7.08 (d, 2H, J = 8.6 Hz). Spectra are given in Fig. S3 and S4 in ESI.†

4-Diethylphosphono-4′-biphenylcarboxylic acid methyl ester (3). In a two necked 50 mL flask 5.0 g (14.8 mmol) of **2** and 0.33 g (1.47 mmol) of anhydrous NiBr$_2$ were suspended in 10 mL of mesitylene. The suspension was placed under nitrogen and heated to 180 °C with constant stirring and refluxing. After one hour 3.5 g (22.3 mmol) of triethylphosphite were added drop-wise over 2 hours at 180 °C with the suspension changing its colour from greenish yellow to red and back again with each drop of triethylphosphite added. After refluxing another two hours for completion of the reaction the light green suspension was allowed to cool to room temperature. The excess of triethylphosphite and solvent was removed under reduced pressure. The resulting solid was washed with water and dried to afford 4.4 g (85% yield) of pure product. Mp = 77–79 °C. FT-IR (ATR) $\tilde{v}$/cm^{-1} = 3785 (w), 2969 (w), 2911 (w), 1637 (w), 1593 (w), 1521 (w), 1428 (m), 1329 (m), 1250 (s), 1198 (m), 1091 (m), 1032 (m), 1010 (m), 962 (m), 824 (w), 768 (m), 686 (m), 611 (vs). ^{1}H-NMR (500 MHz, DMSO-d_6) δ/ppm = 1.22 (t, 6H), 3.87 (s, 3H), 4.01 (q, 4H), 7.33–8.35 (m, 8H). ^{13}C-NMR (125.7 MHz, DMSO-d_6) δ/ppm = 16.5 (–CH_3), 39.8 (–CH_2–), 52.5 (O–CH_3), 62.1 (O–CH_2), 127.6 (d), 130.1 (d), 132.1 (d), 142.5, 143.3 (aromatic C), 176.5 (–COOH). ^{31}P{H}-NMR (121.5 MHz, DMSO-d_6) δ/ppm = 17.53. Spectra are given in Fig. S5–S8 in ESI.† EI-MS(+) at 100 °C (M = C$_{18}$H$_{21}$O$_5$P (348.11) m/z (%) 348 (15) [M], 320 (28) [M–C$_2$H$_4$]$^+$, 292 (41) [M–C$_2$H$_5$–C$_2$H$_4$]$^+$, 261 (22) [M–C$_2$H$_4$–C$_2$H$_3$O$_2$]$^+$, 152 (65) [M–PO$_3$(C$_2$H$_5$)$_2$–CO$_2$CH$_3$ = C$_{12}$H$_8$]$^+$. Calcd. for C$_{18}$H$_{21}$O$_5$P·H$_2$O (366.35 g mol^{-1}): C 59.01, H 6.33%. Found C 58.79, H 5.99%.

4-Phosphonato-4′-biphenylcarboxylic acid (4), H$_3$BPPA. In a 100 mL glass flask 1.0 g (2.87 mmol) of **3** were suspended in 15 mL of 37% hydrochloric acid and refluxed for 20 h. The off-white product was filtered and washed with plenty of water to remove any residual hydrochloric acid from the product. The product was dried to give 0.74 g (93%) of **4**. Mp > 350 °C (decomp.). FT-IR (ATR) $\tilde{v}$/cm^{-1} = 3324 (w, b), 2955 (w, br), 2849 (w, br), 2677 (m), 2557 (m), 2166 (m), 1935 (m), 1808 (m), 1677 (vs), 1605 (m), 1574 (w), 1550 (w), 1429 (m), 1391 (m), 1302 (m), 1214 (m), 1179 (m), 1145 (m), 1102 (m), 1002 (vs), 946 (m), 868 (m), 831 (m), 799 (m), 771 (m), 755 (m), 722 (m), 689 (m), 577 (vs). ^{1}H-NMR (200 MHz, DMSO-d_6) δ/ppm = 7.70–7.90 (m, 6H), 8.04 (d, 2H, J = 7.70 Hz), 8.2–9.0 (broad signal, P–OH) ^{13}C-NMR (125.7 MHz, DMSO-d_6) δ/ppm = 127.1, 127.2, 127.5, 127.6, 129.5, 130.5, 131.7, 133.6, 134.8, 138.3, 141.7, 143.9 (aromatic C), 167.5 (–COOH). ^{31}P-NMR (121.5 MHz, DMSO-d_6) δ/ppm = 10.91. Spectra are given in

Fig. S9–S12 in ESI.† EI-MS(+) at 260 °C, M = C$_{13}$H$_{11}$O$_5$P, (278): m/z (%) 278 (100) [M], 198 (22) [M–PO$_3$H]$^+$, 152 (40) [M–PO$_3$H$_2$–CO$_2$H = C$_{12}$H$_8$]$^+$. Calcd. for C$_{13}$H$_{11}$O$_5$P (278.2 g mol^{-1}): C 56.13, H 3.99%. Found C 56.17, H 4.10%.

[Zn$_5$(μ$_3$-OH)$_4$(μ$_4$-O$_3$P–(C$_6$H$_4$)$_2$–CO$_2$-μ$_2$)$_2$] (5). In a Teflon-lined stainless-steel autoclave portions of 9.9 mg (0.054 mmol) of anhydrous zinc acetate (Zn(OAc)$_2$), 10.0 mg (0.036 mmol) of H$_3$BPPA and 2.4 mg (0.03 mmol) of oxalic acid dihydrate (C$_2$H$_2$O$_4$·2H$_2$O) were mixed in 1 mL of doubly deionized water and heated to 190 °C for 72 h. After cooling to ambient temperature within 24 h colorless, needle-shaped crystals were obtained. Crystal yield 17.0 mg (51%); adjustment of the reactant stoichiometry to the ratio found in the X-ray structure of the product does have little effect on the yield. The synthesis of **5** also led to the formation of plate-like, colorless crystals, which were found at the bottom of the reaction vessel. It was shown through the independent synthesis of **6** that those were crystals of **6**, which had been formed as by-product to **5** (Fig. S25 and S26 in ESI†). Mp > 300 °C. FT-IR (ATR) $\tilde{v}$/cm^{-1} = 3460 (w), 3069 (w), 1691 (w), 1586 (w), 1553 (w), 1519 (w), 1423 (m), 1167 (m), 1143 (m), 1073 (vs), 962 (vs), 925 (s), 869 (m), 830 (s), 775 (vs), 728 (m), 700 (m), 595 (vs) (Fig. S13, ESI†). Calc. for C$_{26}$H$_{20}$O$_{14}$P$_2$Zn$_5$ (945.29 g mol^{-1}): C 33.04, H 2.13%. Found C 33.71, H 2.39%.

[Zn(μ$_6$-O$_3$P–(C$_6$H$_4$)$_2$–CO$_2$H)] (6). In a Teflon-lined stainless-steel autoclave 18.8 mg (0.072 mmol) of Zn(NO$_3$)$_2$·4H$_2$O and 20.0 mg (0.072 mmol) of H$_3$BPPA combined with 2 mL of DI water. The suspension was stirred briefly and then kept in a programmable oven at 200 °C for 48 h and then cooled to ambient temperature within 24 h. An off-white crystalline powder was obtained, which was washed with portions of DI water (3 × 5 mL) and dried in air. Crystal yield 13.0 mg (54%). Mp > 300 °C. FT-IR (ATR) $\tilde{v}$/cm^{-1} = 2988 (w, br), 2875 (w, br), 2669 (w, b), 2543 (w, br), 1681 (m), 1606 (w), 1427 (w), 1275 (w), 1179 (m), 1146 (s), 1059 (vs), 958 (vs), 828 (m), 756 (m), 691 (w), 599 (vs), 562 (s) (Fig. S14, ESI†). Calc. for C$_{13}$H$_9$O$_5$PZn (341.56 g mol^{-1}): C 45.71, H 2.66%. Found C 45.69, H 2.54%.

[Cd$_3$(μ$_6$-O$_3$P–(C$_6$H$_4$)$_2$–CO$_2$-μ$_2$)(μ$_6$-O$_3$P–(C$_6$H$_4$)$_2$–CO$_2$-μ$_3$)] (7). Portions of 14.0 mg (0.053 mmol) of Cd(OAc)$_2$·2H$_2$O, 10.0 mg (0.036 mmol) of H$_3$BPPA, 3.6 mg (0.029 mmol) of oxalic acid dihydrate (C$_2$H$_2$O$_4$·2H$_2$O) and 3 mL of DI water were placed in a Teflon-lined stainless-steel autoclave, which was heated to 190 °C within six hours, kept at this temperature for 48 h and then cooled to room temperature over 24 h. The product was filtered, washed with water (3 × 10 mL) and dried in air to obtain a white powder. Yield 15.0 mg (94%). Mp > 300 °C. FT-IR (ATR) $\tilde{v}$/cm^{-1} = 3402 (m, b), 3284 (m), 2855 (w, b), 2546 (w), 1684 (vs), 1604 (m), 1425 (s), 1126 (m), 1089 (s), 1031 (m), 948 (s), 823 (s), 765 (s), 719 (s), 687 (m), 578 (s) (Fig. S15, ESI†). Calc. for C$_{26}$H$_{16}$Cd$_3$O$_{10}$P$_2$ (887.59 g mol^{-1}): C 35.18, H 1.82%. Found C, 35.26, H 2.0%.

[Hg(μ$_3$-HO$_3$P–(C$_6$H$_4$)$_2$–CO$_2$H)] (8). *Caution: Elemental mercury and its compounds are highly toxic and should be handled under adequate safety conditions, wearing gloves, dust mask and using fumehoods!*

Inside a Teflon-lined stainless-steel autoclave 11.0 mg (0.034 mmol) of $Hg(OAc)_2$ and 3.6 mg (0.029 mmol) of oxalic acid dihydrate were weighed and dissolved in 4 mL of DI water. A portion of 10.0 mg (0.036 mmol) of H_3BPPA was added and the suspension stirred to homogeneity. The reactor was heated to 120 °C within 24 h and kept at this temperature for 72 h. After cooling to room temperature within 24 h the solids were filtered and washed with water (3 × 10 mL). Colorless block-shaped crystals of very small size (0.01 × 0.01 × 0.01 mm) were isolated, which were used for X-ray structure determination. Crystal yield 8.0 mg (50%). Mp > 300 °C. FT-IR (ATR) $\tilde{\nu}/cm^{-1}$ = 2969 (m, br) 2849 (m, br), 2674 (w), 2547 (w), 2323 (w), 1807 (w), 1682 (vs), 1604 (m), 1573 (w), 1426 (m), 1392 (m), 1280 (m), 1139 (m), 1070 (m), 824 (s), 765 (s), 752 (m), 720 (m), 582 (s) (Fig. S16, ESI†). Calc. for $C_{13}H_{10}HgO_5P$ (477.78 g mol^{-1}): C 32.68, H 2.11%. Found C 30.84, H 1.91%.

[$Co(\mu_6-O_3P-(C_6H_4)_2-CO_2H)$] (9). In a Teflon-lined stainless-steel autoclave 9.32 mg (0.036 mmol) of anhydrous $CoCl_2$ and 10.0 mg (0.036 mmol) of H_3BPPA were suspended in 2 mL DI water and heated at 220 °C for 48 h. After cooling to ambient temperature over 24 h very thin pink-colored hexagonal plate-shaped crystals were formed with dimensions of 0.01 × 0.01 × 0.001 mm. Crystal yield 16.0 mg (61%). Mp = >300 °C. FT-IR (ATR) $\tilde{\nu}/cm^{-1}$ = 3445 (w, b), 2961 (w, br), 2777 (w, br), 1681 (m), 1602 (w), 1419 (m), 1390 (m), 1138 (m), 944 (vs), 828 (s), 768 (s), 753 (m), 723 (m), 579 (m) (Fig. S17, ESI†). Calc. for $C_{13}H_9CoO_5P$ (335.12 g mol^{-1}): C 46.59, H 2.71%. Found: C 46.16, H 3.24%.

Acknowledgements

Notes and references

1 N. Stock and S. Biswas, *Chem. Rev.*, 2012, **112**, 933–969; M. Gaab, N. Trukhan, S. Maurer, R. Gummaraju and U. Müller, *Microporous Mesoporous Mater.*, 2012, **157**, 131–136; C. Janiak and J. K. Vieth, *New J. Chem.*, 2010, **34**, 2366–2388; C. Janiak, *Dalton Trans.*, 2003, 2781–2804.

2 S. Li and F. Huo, *Nanoscale*, 2015, 7, 7482–7501.

3 A. H. Chughtai, N. Ahmad, H. A. Younus, A. Laypkov and F. Verpoort, *Chem. Soc. Rev.*, 2015, **44**, 6804–6849.

4 Y. Xu, M. Wu, Y. Liu, X.-Z. Feng, X.-B. Yin, X.-W. He and Y.-K. Zhang, *Chem. – Eur. J.*, 2013, **19**, 2276–2283.

5 B. Gole, A. K. Bar and P. S. Mukherjee, *Chem. – Eur. J.*, 2014, **20**, 13321–13336.

6 R. B. Getman, Y.-S. Bae, C. E. Wilmer and R. Q. Snurr, *Chem. Rev.*, 2012, **112**, 703–723; L. Wu, M. Xue, S.-L. Qiu, G. Chaplais, A. Simon-Masseron and J. Patarin, *Microporous Mesoporous Mater.*, 2012, **157**, 75–81; R. J. Kuppler, D. J.

Timmons, Q.-R. Fang, J.-R. Li, T. A. Makal, M. D. Young, D. Yuan, D. Zhao, W. Zhuang and H.-C. Zhou, *Coord. Chem. Rev.*, 2009, **253**, 3042–3066; M. P. Suh, H. J. Park, T. K. Prasad and D. W. Lim, *Chem. Rev.*, 2012, **112**, 782–835; H. Wu, Q. Gong, D. H. Olson and J. Li, *Chem. Rev.*, 2012, **112**, 836–868; L. J. Murray, M. Dincă and J. R. Long, *Chem. Soc. Rev.*, 2009, **38**, 1294–1314.

7 J. A. Mason, M. Veenstra and J. R. Long, *Chem. Sci.*, 2014, **5**, 32–51; R. Sathre and E. Masanet, *RSC Adv.*, 2013, **3**, 4964–4975; J. Liu, P. K. Thallapally, B. P. McGrail, D. R. Bown and J. Liu, *Chem. Soc. Rev.*, 2012, **41**, 2308–2322; H. Amrouche, B. Creton, F. Siperstein and C. Nieto-Draghi, *RSC Adv.*, 2012, **2**, 6028–6035.

8 J. R. Li, J. Sculley and H. C. Zhou, *Chem. Rev.*, 2012, **112**, 869–932; Z. Zhang, Y. Zhao, Q. Gong, Z. Li and J. Li, *Chem. Commun.*, 2013, **49**, 653–661; H. B. Tanh Jeazet, C. Staudt and C. Janiak, *Dalton Trans.*, 2012, **41**, 14003–14027; X. Y. Chen, V.-T. Hoang, D. Rodrigue and S. Kaliaguine, *RSC Adv.*, 2013, **3**, 24266–24279; G. Férey, C. Serre, T. Devic, G. Maurin, H. Jobic, P. L. Llewellyn, G. De Weireld, A. Vimont, M. Daturi and J. S. Chang, *Chem. Soc. Rev.*, 2011, **40**, 550–562; J.-R. Li, Y. Ma, M. C. McCarthy, J. Sculley, J. Yu, H.-K. Jeong, P. B. Balbuena and H.-C. Zhou, *Coord. Chem. Rev.*, 2011, **255**, 1791–1823; N. Hara, M. Yoshimune, H. Negishi, K. Haraya, S. Hara and T. Yamaguchi, *RSC Adv.*, 2013, **3**, 14233–14236; J. H. Yoon, D. Kim, X. Song, S. Han, J. Shin, S. B. Hong and M. Soo Lah, *RSC Adv.*, 2012, **2**, 11566–11573; M. Fischer, F. Hoffmann and M. Fröba, *RSC Adv.*, 2012, **2**, 4382–4396; L. Ge, A. Du. M. Hou, V. Rudolph and Z. Zhu, *RSC Adv.*, 2012, **2**, 11793–11800; Z. R. Herm, R. Krishna and J. R. Long, *Microporous Mesoporous Mater.*, 2012, **157**, 94–100; M. G. Plaza, A. F. P. Ferreira, J. C. Santos, A. M. Ribeiro, U. Müller, N. Trukhan, J. M. Loureiro and A. E. Rodrigues, *Microporous Mesoporous Mater.*, 2012, **157**, 101–111.

9 S. Qiu, M. Xue and G. Zhu, *Chem. Soc. Rev.*, 2014, **43**, 6116–6140.

10 F. Jeremias, D. Fröhlich, C. Janiak and S. Henninger, *New J. Chem.*, 2014, **4**, 24073–24082; C. Janiak and S. K. Henninger, *Chimia*, 2013, **67**, 419–424; M. Taddei, A. Ienco, F. Costantino and A. Guern, *RSC Adv.*, 2013, **3**, 26177–26183; P. Küsgens, M. Rose, I. Senkovska, H. Fröde, A. Henschel, S. Siegle and S. Kaskel, *Microporous Mesoporous Mater.*, 2009, **120**, 325–330; J. J. Low, A. I. Benin, P. Jakubczak, J. F. Abrahamian, S. A. Faheem and R. R. Willis, *J. Am. Chem. Soc.*, 2009, **131**, 15834–15842.

11 G. Férey, *Dalton Trans.*, 2009, 4400–4415; G. Férey and C. Serre, *Chem. Soc. Rev.*, 2009, **38**, 1380–1399; G. Férey, *Chem. Soc. Rev.*, 2008, 37, 191–214.

12 G. Férey, C. Serre, C. Mellot-Draznieks, F. Millange, S. Surble, J. Dutour and I. Margiolaki, *Angew. Chem., Int. Ed.*, 2004, **43**, 6296–6301; P. Horcajada, S. Surble, C. Serre, D.-Y. Hong, Y.-K. Seo, J.-S. Chang, J.-M. Grenèche, I. Margiolaki and G. Férey, *Chem. Commun.*, 2007, 2820–2822; L. Kurfiřtová, Y.-K. Seo, Y.-K. Hwang, J.-S. Chang and J. Čejka, *Catal. Today*, 2012, **179**, 85–90.

13 G. Férey, C. Mellot-Draznieks, C. Serre, F. Millange, J. Dutour, S. Surble and I. Margiolaki, *Science*, 2005, **309**, 2040–2042.

14 G. Akiyama, R. Matsuda and S. Kitagawa, *Chem. Lett.*, 2010, **39**, 360–361.

15 M. Kandiah, M. H. Nilsen, S. Usseglio, S. Jakobsen, U. Olsbye, M. Tilset, C. Larabi, E. A. Quadrelli, F. Bonino and K. P. Lillerud, *Chem. Mater.*, 2010, **22**, 6632–6640; J. H. Cavka, S. Jakobsen, U. Olsbye, N. Guillou, C. Lamberti, S. Bordiga and K. P. Lillerud, *J. Am. Chem. Soc.*, 2008, **130**, 13850–13851.

16 N. C. Burtch, H. Jasuja and K. S. Walton, *Chem. Rev.*, 2014, **114**, 10575–10612.

17 J. Canivet, A. Fateeva, Y. Guo, B. Coasnec and D. Farrusseng, *Chem. Soc. Rev.*, 2014, **43**, 5594–5617.

18 F. Jeremias, V. Lozan, S. Henninger and C. Janiak, *Dalton Trans.*, 2013, **42**, 15967–15973; A. Khutia, H. U. Rammelberg, T. Schmidt, S. Henninger and C. Janiak, *Chem. Mater.*, 2013, **25**, 790–798; J. Ehrenmann, S. K. Henninger and C. Janiak, *Eur. J. Inorg. Chem.*, 2011, 471–474.

19 C. Heering, I. Boldog, V. Vasylyeva, J. Sanchiz and C. Janiak, *CrystEngComm*, 2013, **15**, 9757–9768.

20 C. Montoro, F. Linares, E. Quartapelle Procopio, I. Senkovska, S. Kaskel, S. Galli, N. Masciocchi, E. Barea and J. A. R. Navarro, *J. Am. Chem. Soc.*, 2011, **133**, 11888–11891.

21 P. O. Adelani, L. J. Jouffret, J. E. S. Szymanowski and P. C. Burns, *Inorg. Chem.*, 2012, **51**, 12032–12040.

22 P. O. Adelani, G. E. Sigmon and P. C. Burns, *Inorg. Chem.*, 2013, **52**, 6245–6247.

23 Reviews: K. Maeda, *Microporous Mesoporous Mater.*, 2004, **73**, 47–55; A. Clearfield and Z. Wang, *J. Chem. Soc., Dalton Trans.*, 2002, 2937–2947; A. Clearfield, *Curr. Opin. Solid State Mater. Sci.*, 2002, **6**, 495–506.

24 S. Kirumakki, J. Huang, A. Subbiah, J. Yao, A. Rowland, B. Smith, A. Mukherjee, S. Samarajeewa and A. Clearfield, *J. Mater. Chem.*, 2009, **19**, 2593–2603.

25 F. Zhai, Q. Zheng, Z. Chen, Y. Ling, X. Liu, L. Wenig and Y. Zhou, *CrystEngComm*, 2013, **15**, 2040–2043.

26 S. Kirumakki, J. Huang, A. Subbiah, J. Yao, A. Rowland, B. Smith, A. Mukherjee, S. Samarajeewa and A. Clearfield, *J. Mater. Chem.*, 2008, **19**, 2593–2603.

27 X. Zhao, J. G. Bell, S.-F. Tang, L. Li and K. M. Thomas, *J. Mater. Chem. A*, 2016, **4**, 1353–1365.

28 A. Clearfield and K. Demadis, *Metal Phosphonate Chemistry: From Synthesis to Applications*, Royal Society of Chemistry, Oxford, 2012, ch. 2–4, pp. 45–128.

29 M. Deng, X. Liu, Q. Zheng, Z. Chen, C. Fang, B. Yue and H. He, *CrystEngComm*, 2013, **15**, 7056–7061.

30 K. J. Gagnon, H. P. Perry and A. Clearfield, *Chem. Rev.*, 2012, **112**, 1034–1054.

31 J. M. Taylor, R. Vaidhyanathan, S. S. Iremonger and G. K. H. Shimizu, *J. Am. Chem. Soc.*, 2012, **134**, 14338–14340.

32 T. L. Kinnibrugh, A. A. Ayi, V. I. Bakhmutov, J. Zon and A. Clearfield, *Cryst. Growth Des.*, 2013, **13**, 2973–2981.

33 T. Zheng, J. M. Clemente-Juan, J. Ma, L. Dong, S.-S. Bao, J. Huang, A. Coronado and L.-M. Zheng, *Chem. – Eur. J.*, 2013, **19**, 16394–16402.

34 M. Taddei, F. Costantino, A. Lenco, A. Comotti, P. V. Dau and S. M. Cohen, *Chem. Commun.*, 2013, **49**, 1315–1317.

35 R. El Osta, M. Frigoli, J. Marrot, N. Guillou, H. Chevreau, R. I. Walton and F. Millange, *Chem. Commun.*, 2012, **48**, 10639–10641.

36 A. Clearfield and K. D. Demadis, *Metal Phosphonate Chemistry*, RSC Publishing, Cambridge, 2011.

37 A. R. Patterson, W. Schmitt and R. C. Evans, *J. Phys. Chem. C*, 2014, **118**, 10291–10301.

38 L. Jiménez-García, A. Kaltbeitzel, W. Pisula, J. S. Gutmann, M. Klapper and K. Müllen, *Angew. Chem., Int. Ed.*, 2009, **48**, 9951–9953.

39 A. Corma, H. García and F. X. Llabrés i Xamena, *Chem. Rev.*, 2010, **110**, 4606–4655.

40 G. K. H. Shimizu, R. Vaidhyanathan and J. M. Taylor, *Chem. Soc. Rev.*, 2009, **38**, 1430–1449.

41 Review: T. Rojo, J. L. Mesa, J. Lago, B. Bazan, J. L. Pizarro and M. I. Arriortua, *J. Mater. Chem.*, 2009, **19**, 3793–3818.

42 Cobalt compounds: (*a*) S.-Z. Hou, D.-K. Cao, X.-G. Liu, Y.-Z. Li and L.-M. Zheng, *Dalton Trans.*, 2009, 2746–2750; (*b*) Y. S. Ma, Y. Song and L.-M. Zheng, *Inorg. Chim. Acta*, 2008, **361**, 1363–1371; (*c*) Z.-C. Zhang, S. Gao and L.-M. Zheng, *Dalton Trans.*, 2007, 4681–4684; (*d*) L.-M. Zheng, S. Gao, P. Yin and X.-Q. Xin, *Inorg. Chem.*, 2004, **43**, 2151–2156; (*e*) P. Yin, S. Gao, L.-M. Zheng and X.-Q. Xin, *Chem. Mater.*, 2003, **15**, 3233–3236; (*f*) P. Yin, S. Gao, L.-M. Zheng, Z.-M. Wang and X.-Q. Xin, *Chem. Commun.*, 2003, 1076–1077; (*g*) P. Yin, X.-C. Wang, S. Gao and L.-M. Zheng, *J. Solid State Chem.*, 2005, **178**, 1049–1054.

43 Iron compounds: H. A. Habib, B. Gil-Hernández, K. Abu-Shandi, J. Sanchiz and C. Janiak, *Polyhedron*, 2010, **29**, 2537–2545; K. Abu-Shandi, H. Winkler and C. Janiak, *Z. Naturforsch. B*, 2006, **632**, 629–633; K. Abu-Shandi and C. Janiak, *Z. Naturforsch. B.*, 2005, **60**, 1250–1254; Y. Lalatonne, C. Paris, J. M. Serfaty, P. Weinmann, M. Lecouvey and L. Motte, *Chem. Commun.*, 2008, 2553–2555; C. A. Merrill and A. K. Cheetham, *Inorg. Chem.*, 2005, **44**, 5273–5277; H.-H. Song, L.-M. Zheng, G.-S. Zhu, Z. Shi, S.-H. Feng, S. Gao, Z. Hu and X.-Q. Xin, *J. Solid State Chem.*, 2002, **164**, 367–373; M. Riou-Cavellec, C. Serre, J. Robino, M. Noguès, J.-M. Grenèche and G. Férey, *J. Solid State Chem.*, 1999, **147**, 122–131; L.-M. Zheng, H.-H. Song, C.-H. Lin, S.-L. Wang, Z. Hu, Z. Yu and X.-Q. Xin, *Inorg. Chem.*, 1999, **38**, 4618–4619; A. W. Herlinger, J. R. Ferraro, J. A. Garcia and R. Chiarizia, *Polyhedron*, 1998, **17**, 1471–1475.

44 J.-S. Feng, S.-S. Bao, M. Ren, Z.-S. Cai and L.-M. Zheng, *Chem. – Eur. J.*, 2015, **21**, 17336–17343.

45 X.-J. Yang, S.-S. Bao, M. Ren, N. Hoshino, T. Akutagawa and L.-M. Zheng, *Chem. Commun.*, 2014, **50**, 3979–3981.

46 Y.-Z. Zheng and R. E. P. Winpenny, *Sci. China: Chem.*, 2012, **55**, 910–913.

47 Z.-Y. Du, H.-R. Wen, C.-M. Liu, Y.-H. Sun, Y.-B. Lu and Y.-R. Xie, *Cryst. Growth Des.*, 2010, **10**, 3721–3726.

48 Y.-Y. Zhang, M.-H. Zeng, Y. Qi, S.-Y. Sang and Z.-M. Liu, *Inorg. Chem. Commun.*, 2007, **10**, 33–36.

49 M. Menelaou, M. Dakanali, C. P. Raptopoulou, C. Drouza, N. Lalioti and A. Salifoglou, *Polyhedron*, 2009, **28**, 3331–3339; S. Kunnas-Hiltunen, M. Matilainen, J. J. Vepsäläinen and M. Ahlgrén, *Polyhedron*, 2009, **28**, 200–204; P. J. Byrne, D. S. Wragg, J. E. Warren and R. E. Morris, *Dalton Trans.*, 2009, 795–799; C.-Y. Fang, Z.-X. Chen, X.-F. Liu, Y.-T. Yang, M.-L. Deng, L.-H. Weng, Y. Jia and Y.-M. Zhou, *Inorg. Chim. Acta*, 2009, **362**, 2101–2107; K. Latham, K. F. White, K. B. Szpakolski, C. J. Rix and J. M. White, *Inorg. Chim. Acta*, 2009, **362**, 1872–1886; G. Yucesan, J. E. Valeich, H. X. Liu, W. Ouellette, C. J. O'Connor and J. Zubieta, *Inorg. Chim. Acta*, 2009, **362**, 1831–1839; J. Galezowska, P. Kafarski, H. Kozlowski, P. Mlynarz, V. M. Nurchi and T. Pivetta, *Inorg. Chim. Acta*, 2009, **362**, 707–713; Z. Y. Du, Y. R. Xie and H. R. Wen, *Inorg. Chim. Acta*, 2009, **362**, 351–354; S. M. Ying, X. F. Li, J. G. Huang, J. Y. Lin, W. T. Chen and G. P. Zhou, *Inorg. Chim. Acta*, 2008, **361**, 1547–1551; D. R. Jansen, J. R. Zeevaart, Z. I. Kolar, K. Djanashvili, J. A. Peters and G. C. Krijger, *Polyhedron*, 2008, **27**, 1779–1786; R. Murugavel and S. Shanmugan, *Dalton Trans.*, 2008, 5358–5367; V. Chandrasekhar, P. Sasikumar and R. Boomishankar, *Dalton Trans.*, 2008, 5189–5196.

50 C. Heering, B. Nateghi and C. Janiak, *Crystals*, 2016, **6**, 22.

51 J. Svoboda, V. Zima, L. Beneš, K. Melánová, M. Trchová and M. Vlček, *Solid State Sci.*, 2008, **10**, 1533–1542.

52 A.-M. Pütz, L. M. Carrella and E. Rentschler, *Dalton Trans.*, 2013, **42**, 16194–16199.

53 J.-M. Rueff, N. Barrier, S. Boudin, V. Dorcet, V. Caignaert, P. Boullay, G. B. Hix and P.-A. Jaffrès, *Dalton Trans.*, 2009, 10614–10620.

54 J.-M. Rueff, O. Perez, A. Leclaire, H. Couthon-Gourvès and P.-A. Jaffrès, *Eur. J. Inorg. Chem.*, 2009, 4870–4876.

55 J.-T. Li, L.-R. Guo, Y. Shen and L.-M. Zheng, *CrystEngComm*, 2009, **11**, 1674–1678.

56 J.-M. Rueff, O. Perez, V. Caignaert, G. Hix, M. Berchel, F. Quentel and P.-A. Jaffrès, *Inorg. Chem.*, 2015, **54**, 2152–2159.

57 V. Zima, J. Svoboda, L. Beneš, K. Melánová, M. Trchová and J. Dybal, *J. Solid State Chem.*, 2007, **180**, 929–939.

58 P. O. Adelani and T. E. Albrecht-Schmitt, *Inorg. Chem.*, 2010, **49**, 5701–5705.

59 K. Melánová, J. Klevcov, L. Beneš, J. Svoboda and V. Zima, *J. Phys. Chem. Solids*, 2012, **73**, 1452–1455.

60 J.-T. Li, D.-K. Cao, T. Akutagawa and L.-M. Zheng, *Dalton Trans.*, 2010, **39**, 8606–8608.

61 Z. Chen, Y. Zhou, L. Weng and D. Zhao, *Cryst. Growth Des.*, 2008, **8**, 4045–4053.

62 Y. Ling, M. Deng, Z. Chen, B. Xia, X. Liu, Y. Yang, Y. Zhou and L. Wenig, *Chem. Commun.*, 2013, **49**, 78–80.

63 B. A. Breeze, M. Shanmugam, F. Tuna and R. E. P. Winpenny, *Chem. Commun.*, 2007, 5185–5187.

64 J.-M. Rueff, O. Perez, A. Leclaire, H. Couthon-Gourvès and P.-A. Jaffrès, *Eur. J. Inorg. Chem.*, 2009, 4870–4876.

65 T.-B. Liao, Y. Ling, Z.-X. Chen, Y.-M. Zhou and L.-H. Weng, *Chem. Commun.*, 2010, **46**, 1100–1102.

66 E. B. Merkushev and N. D. Yudina, *Zh. Org. Khim.*, 1982, **17**, 2598–2601.

67 C. P. Brock, J. R. Blackburn and K. L. Haller, *Acta Crystallogr., Sect. B: Struct. Sci.*, 1984, **40**, 493–498.

68 H. D. Flack, M. Sadki, A. L. Thompson and D. J. Watkin, *Acta Crystallogr., Sect. A: Found. Crystallogr.*, 2011, **67**, 21–34; H. D. Flack and G. Bernardinelli, *Chirality*, 2008, **20**, 681–690; H. D. Flack and G. Bernardinelli, *Acta Crystallogr., Sect. A: Found. Crystallogr.*, 1999, **55**, 908–915; H. Flack, *Acta Crystallogr., Sect. A: Found. Crystallogr.*, 1983, **39**, 876–881; S. Parsons, H. D. Flack and T. Wagner, *Acta Crystallogr., Sect. B: Struct. Sci.*, 2009, **69**, 249–259.

69 R. B. DeVasher, L. R. Moore and K. H. Shaughnessy, *J. Org. Chem.*, 2004, **69**, 7919–7927.

70 A. W. Addison, T. N. Rao, J. Reedijk, J. van Rijn and G. C. Verschoor, *J. Chem. Soc., Dalton Trans.*, 1984, 1349–1356.

71 A.-C. Chamayou, G. Makhloufi, L. A. Nafie, C. Janiak and S. Lüdeke, *Inorg. Chem.*, 2015, **54**, 2193–2203.

72 B. Gil-Hernández, J. K. Maclaren, H. A. Höppe, J. Pasan, J. Sanchiz and C. Janiak, *CrystEngComm*, 2012, **14**, 2635–2644; B. Gil-Hernández, H. Höppe, J. K. Vieth, J. Sanchiz and C. Janiak, *Chem. Commun.*, 2010, **46**, 8270–8272.

73 M. Enamullah, A. Sharmin, M. Hasegawa, T. Hoshi, A.-C. Chamayou and C. Janiak, *Eur. J. Inorg. Chem.*, 2006, 2146–2154; C. Janiak, A.-C. Chamayou, A. K. M. R. Uddin, M. Uddin, K. S. Hagen and M. Enamullah, *Dalton Trans.*, 2009, 3698–3709.

74 W. Dan, X. Liu, M. Deng, Y. Ling, Z. Chen and Y. Zhou, *Inorg. Chem. Commun.*, 2013, **37**, 93–96.

75 Z. Chen, Y. Zhou, L. Weng, C. Yuan and D. Zhao, *Chem. – Asian J.*, 2007, **2**, 1549–1554.

76 M. C. Etter, *Acc. Chem. Res.*, 1990, **23**, 120–126; M. C. Etter, J. C. MacDonald and J. Bernstein, *Acta Crystallogr., Sect. B: Struct. Sci.*, 1990, **46**, 256–262; M. C. Etter, *J. Phys. Chem.*, 1991, **95**, 4601–4610.

77 E. I. Stiefel and G. F. Brown, *Inorg. Chem.*, 1972, **11**, 434.

78 S. Banerjee, A. Ghosh, B. Wu, P.-G. Lassahn and C. Janiak, *Polyhedron*, 2005, **24**, 593–599.

79 The three letter symbols, proposed by M. O'Keeffe, can be retrieved with examples and further information from the Reticular Chemistry Structure Resource database, http://rcsr.anu.edu.au/.

80 Bond valences (*s*) calculated from the Hg–O bond lengths (*R*) according to $s = \exp(R_0 - R)/B$ and $R_0 = 1.900$ for Hg(I)–O or 1.972 for Hg(II)–O, $B = 0.37$; program VALENCE as implemented in PLATON.

81 I. D. Brown and R. D. Shannon, *Acta Crystallogr., Sect. A: Cryst. Phys., Diffr., Theor. Gen. Crystallogr.*, 1973, **29**, 266; I. D. Brown and K. K. Wu, *Acta Crystallogr., Sect. B: Struct. Crystallogr. Cryst. Chem.*, 1976, **32**, 1957; I. D. Brown and D. Altermatt, *Acta Crystallogr. B*, 1985, **41**, 244; N. E. Brese and M. O'Keeffe, *Acta Crystallogr., Sect. B: Struct. Sci.*, 1991, **47**, 192–197; I. D. Brown, *J. Appl. Crystallogr.*, 1996, **29**, 479; I. D. Brown, *The Chemical*

Bond in Inorganic Chemistry: The Bond Valence Model, Oxford University Press, Oxford, 2002.

82 R. Galassi, F. Bachechi and A. Burini, *J. Mol. Struct.*, 2006, **791**, 82–88.

83 S. T. Liddle, in *Molecular Metal–Metal Bonds: Compounds, Synthesis, Properties*, Wiley-VCH Verlag, Weinheim, Germany, 2015, ch. 12.2.1.1.

84 A. Morsali and M. Y. Masoomi, *Coord. Chem. Rev.*, 2009, **253**, 1882–1905.

85 (*a*) K. Brodersen, R. Dölling and G. Liehr, *Z. Anorg. Allg. Chem.*, 1980, **464**, 17–29; (*b*) S. Panda, H. B. Singh and R. J. Butcher, *Inorg. Chem.*, 2004, **43**, 8532–8537; (*c*) Y. Li, J.-A. Zhang, Y.-B. Wang, M. Pan and C. Y. Su, *Inorg. Chem. Commun.*, 2013, **34**, 4–7.

86 C. D. L. Saunders, N. Burford, U. Werner-Zwanziger and R. McDonald, *Inorg. Chem.*, 2008, **47**, 3693–3699.

87 C. R. Samanamu, E. N. Zamora, J.-L. Montchamp and A. F. Richards, *J. Solid State Chem.*, 2008, **181**, 1462–1471.

88 B. Kamenar, A. Hergold-Brundic and M. Bruvo, *Z. Kristallogr.*, 1988, **184**, 103.

89 T. Dorn, A.-C. Chamayou and C. Janiak, *New J. Chem.*, 2006, **30**, 156–167.

90 J. K. Maclaren, J. Sanchiz, P. Gili and C. Janiak, *New J. Chem.*, 2012, **36**, 1596–1609.

91 M. Enamullah, V. Vasylyeva and C. Janiak, *Inorg. Chim. Acta*, 2013, **408**, 109–119.

92 S. Vairam and S. Govindarajan, *Thermochim. Acta*, 2004, **414**, 263–270.

93 L. W. Collins, E. K. Gibson and W. W. Wendlandt, *Thermochim. Acta*, 1975, **11**, 177–185.

94 T. Gunnlaughson, M. Glynn, G. M. Tocci, P. E. Kruger and F. M. Pfeffer, *Coord. Chem. Rev.*, 2006, **250**, 3094–3117; Y. Cui, Y. Yue, G. Qian and B. Chen, *Chem. Rev.*, 2012, **112**, 1126–1162.

95 H. A. Habib, A. Hoffmann, H. A. Höppe, G. Steinfeld and C. Janiak, *Inorg. Chem.*, 2009, **48**, 2166–2180; H. A. Habib, A. Hoffmann, H. A. Höppe and C. Janiak, *Dalton Trans.*, 2009, 1742–1751; H. A. Habib, J. Sanchiz and C. Janiak, *Dalton Trans.*, 2008, 1734–1744.

96 Z. Hu, B. J. Deibert and J. Li, *Chem. Soc. Rev.*, 2014, **43**, 5815–5840; J. Heine and K. Müller-Buschbaum, *Chem. Soc.*

Rev., 2013, **42**, 9232–9242; M. D. Allendorf, C. A. Bauer, R. K. Bhakta and R. J. T. Houk, *Chem. Soc. Rev.*, 2009, **38**, 1330–1352.

97 L. E. Kreno, K. Leong, O. K. Farha, M. Allendorf, R. P. Van Duyne and J. T. Hupp, *Chem. Rev.*, 2012, **112**, 1105–1125.

98 J. W. Bridges, P. J. Creaven and R. T. Williams, *Biochem. J.*, 1965, **96**, 872–878.

99 Q. Gong, Z. Hu, B. J. Deibert, T. J. Emge, S. J. Teat, D. Banerjee, B. Mussman, N. D. Rudd and J. Li, *J. Am. Chem. Soc.*, 2014, **136**, 16724–16727.

100 A. Majumder, G. M. Rosair, A. Mallick, N. Chattopadhyay and S. Mitra, *Polyhedron*, 2006, **25**, 1753–1762.

101 (*a*) W. W. Lestari, P. Lonnecke, M. B. Sarosi, H. C. Streit, M. Adlung, C. Wickleder, M. Handke, W.-D. Einicke, R. Glaser and E. Hey-Hawkins, *CrystEngComm*, 2013, **15**, 3874–3884; (*b*) W. W. Lestari, H. C. Streit, P. Lönnecke, C. Wickleder and E. Hey-Hawkins, *Dalton Trans.*, 2014, **43**, 8188–8195.

102 APEXII, *Data collection program for the APEXII CCD area-detector system*, Bruker Analytical X-ray Systems, Madison, Wisconsin, USA, 2010.

103 SMART, Data Collection Program for the CCD Area-Detector System, *SAINT: Data Reduction and Frame Integration Program for the CCD Area-Detector System*, Bruker Analytical X-ray Systems, Madison, Wisconsin, USA, 1997.

104 G.-M. Sheldrick, *Program SADABS: Area-detector absorption correction*, University of Göttingen, Germany, 1996.

105 C. B. Hübschle, G. M. Sheldrick and B. Dittrich, *J. Appl. Crystallogr.*, 2011, **44**, 1281–1284.

106 J. Newman, *Acta Crystallogr., Sect. D: Biol. Crystallogr.*, 2006, **62**, 27–31.

107 K. Brandenburg, *DIAMOND (Version 3.2)*, Crystal and Molecular Structure Visualization, Crystal Impact – K. Brandenburg & H. Putz, Gbr: Bonn, Germany, 2009.

108 A. Spek, *Acta Crystallogr., Sect. D: Biol. Crystallogr.*, 2009, **65**, 148–155; A. L. Spek, *PLATON – A multipurpose crystallographic tool*, Utrecht University, Utrecht, The Netherlands, 2005.

109 H. O. Wirth, W. Kern and E. Schmitz, *Makromol. Chem.*, 1963, **68**(1), 66–69.

110 R. Pummerer and L. Seligsberger, *Ber. Dtsch. Chem. Ges.*, 1931, **64**, 2477–2486.

Electronic Supplementary Information (ESI)

Syntheses, structures and properties of group 12 element (Zn, Cd, Hg) coordination polymers with a mixed-functional phosphonate-biphenyl-carboxylate linker

Christian Heering,[a] Biju Francis,[a,b] Bahareh Nateghi,[a] Gamall Makhloufi,[a] Christoph Janiak [a] *

a Institut für Anorganische Chemie und Strukturchemie, Universitätsstr. 1
40225 Düsseldorf, Germany
Emails: christian.heering@hhu.de, bijufrancis85@gmail.com, Bahareh.Nateghi@hhu.de, gamall.makhloufi@hhu.de, *janiak@hhu.de

b Permanent address: CSIR-Network of Institutes for Solar Energy
National Institute for Interdisciplinary Science & Technology(NIIST) Thiruvananthapuram-695 019, India

Content:

Fig. S1 FT-IR (ATR) spectrum of 4-iodo-4'-biphenylcarboxylic acid, **1**.

Fig. S2 ^{1}H-NMR spectrum of 4-iodo-4'-biphenylcarboxylic acid, **1** at 200 MHz in DMSO-d_6.
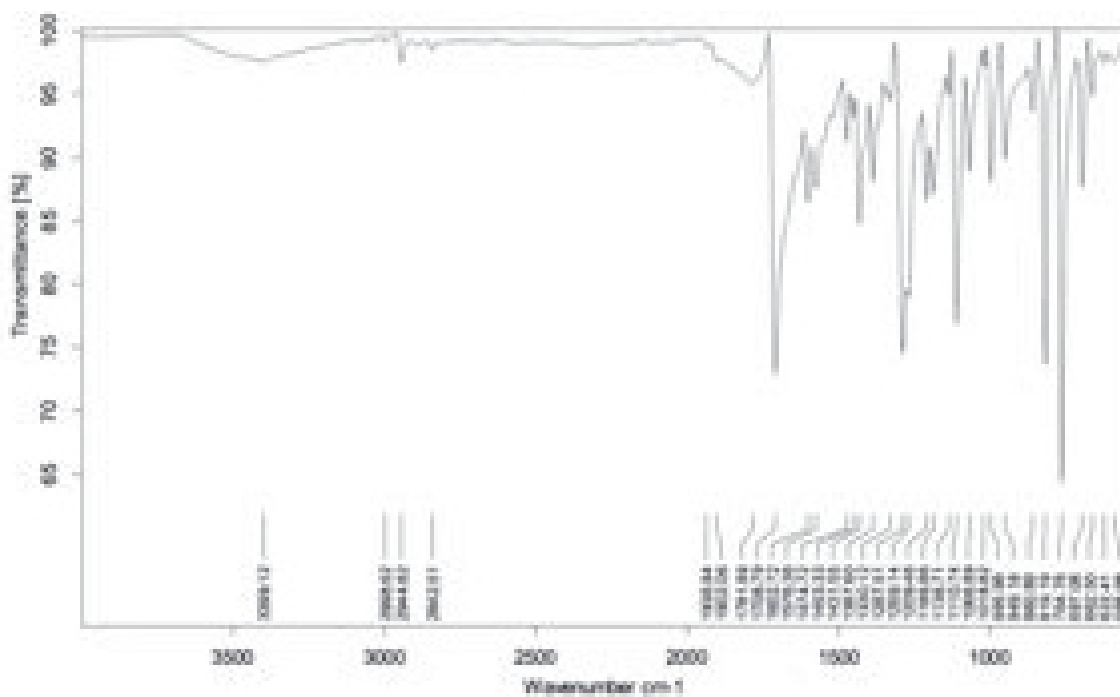
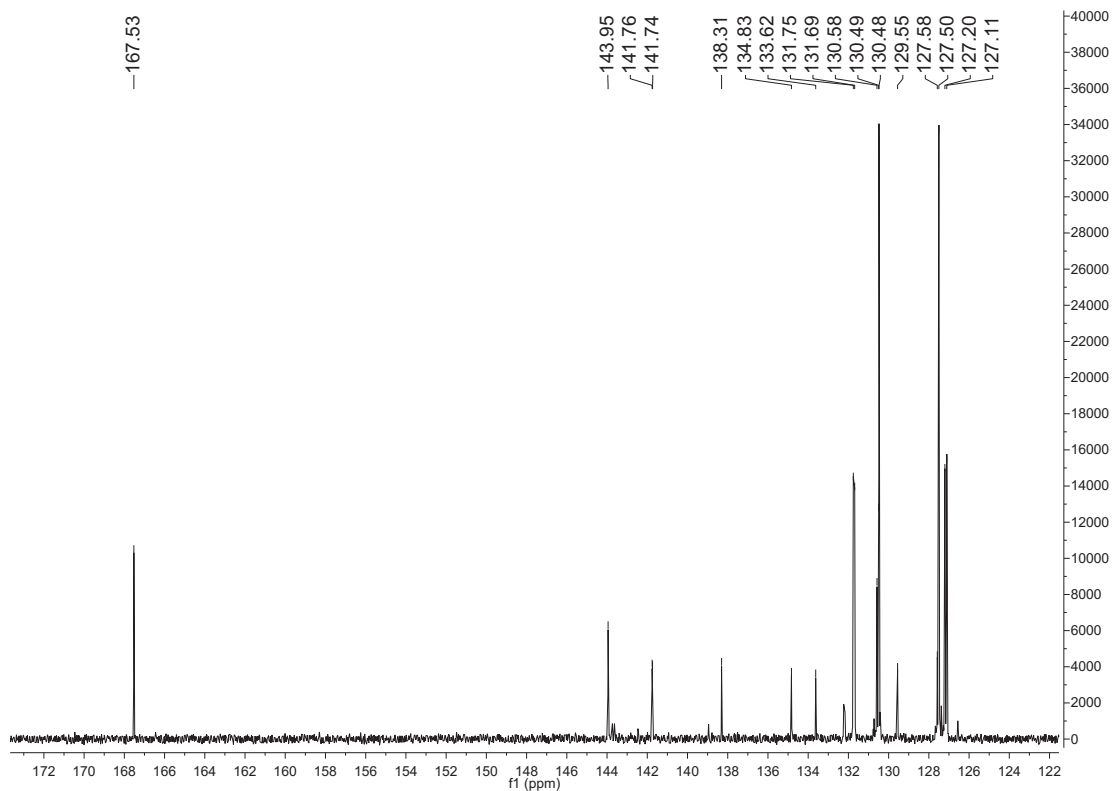**Fig. S3** FT-IR (ATR) spectrum of 4-iodo-4'-biphenylcarboxylic acid methyl ester, **2**.
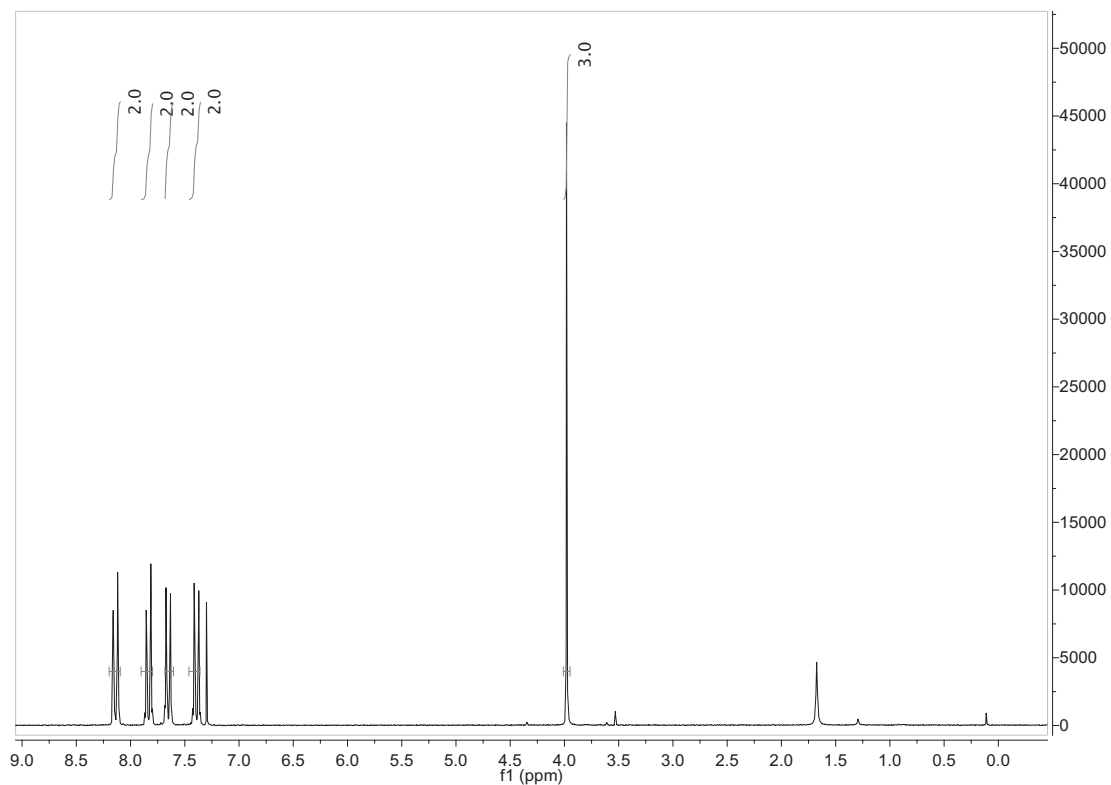
Fig. S4 ^{1}H-NMR spectrum of 4-iodo-4'-biphenylcarboxylic acid methyl ester, **2** at 200 MHz in CDCl$_3$.
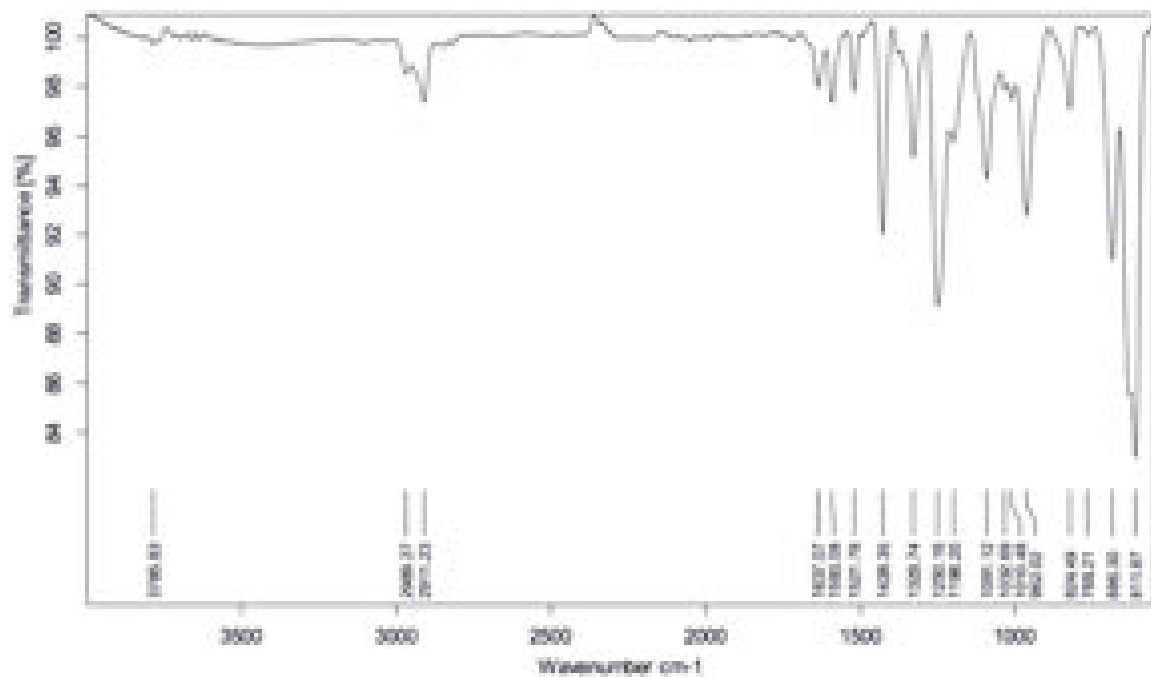
Fig. S5 FT-IR (ATR) spectrum of 4-diethylphosphono-4'-biphenylcarboxylic acid methyl ester, **3**.
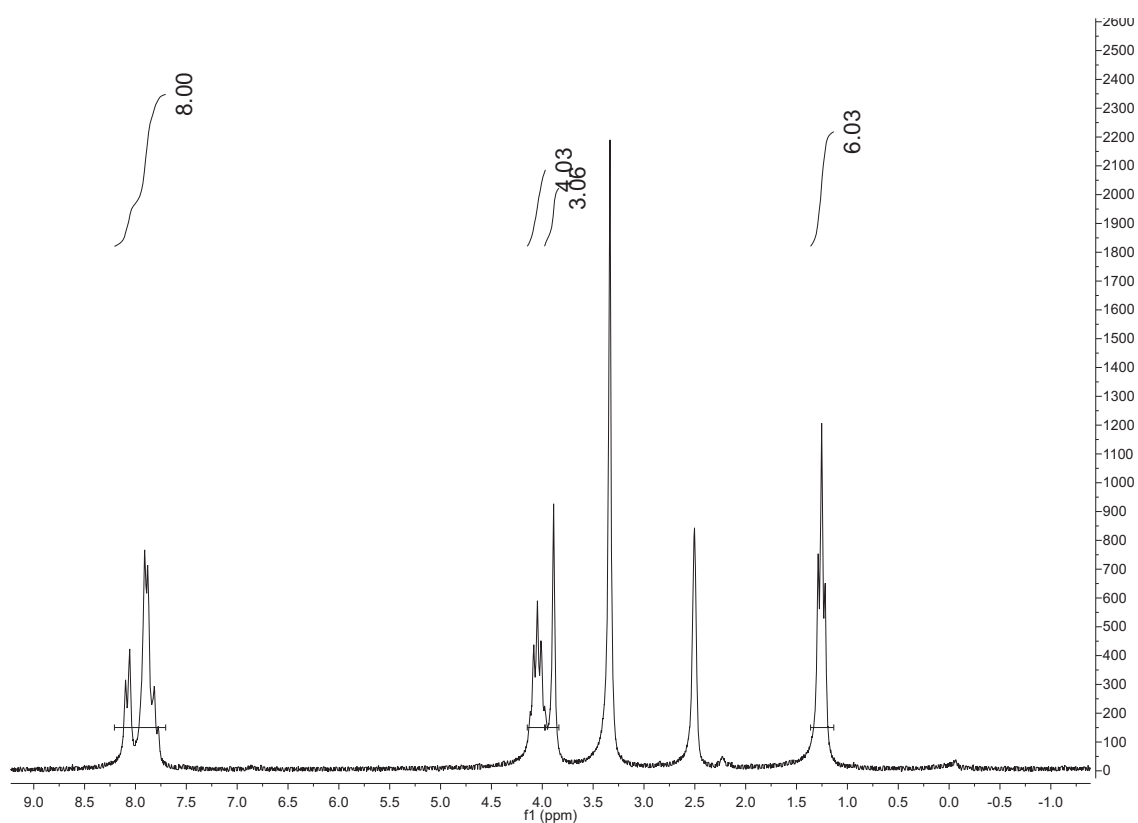
Fig. S6 ^{1}H-NMR spectrum of 4-diethylphosphono-4'-biphenylcarboxylic acid methyl ester, **3** at 200 MHz in DMSO-d_6.
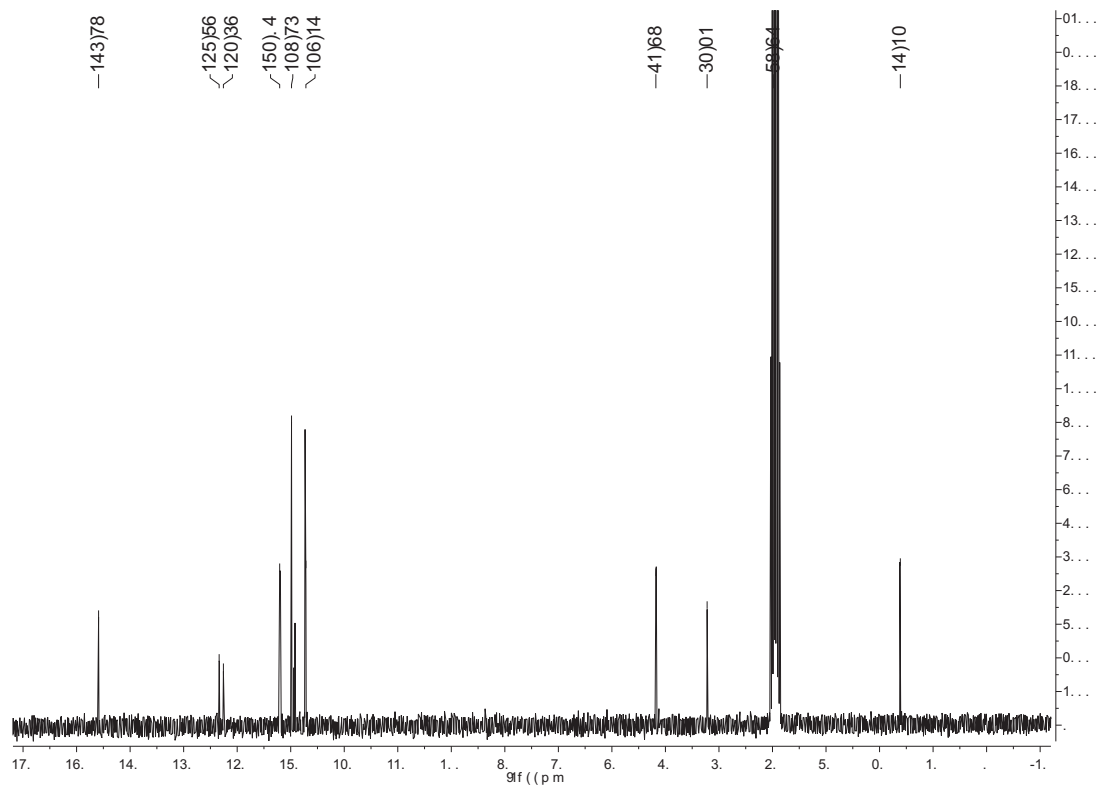
Fig. S7 ^{13}C-NMR spectrum of 4-diethylphosphono-4'-biphenylcarboxylic acid methyl ester, **3** at 75 MHz in DMSO-d_6.
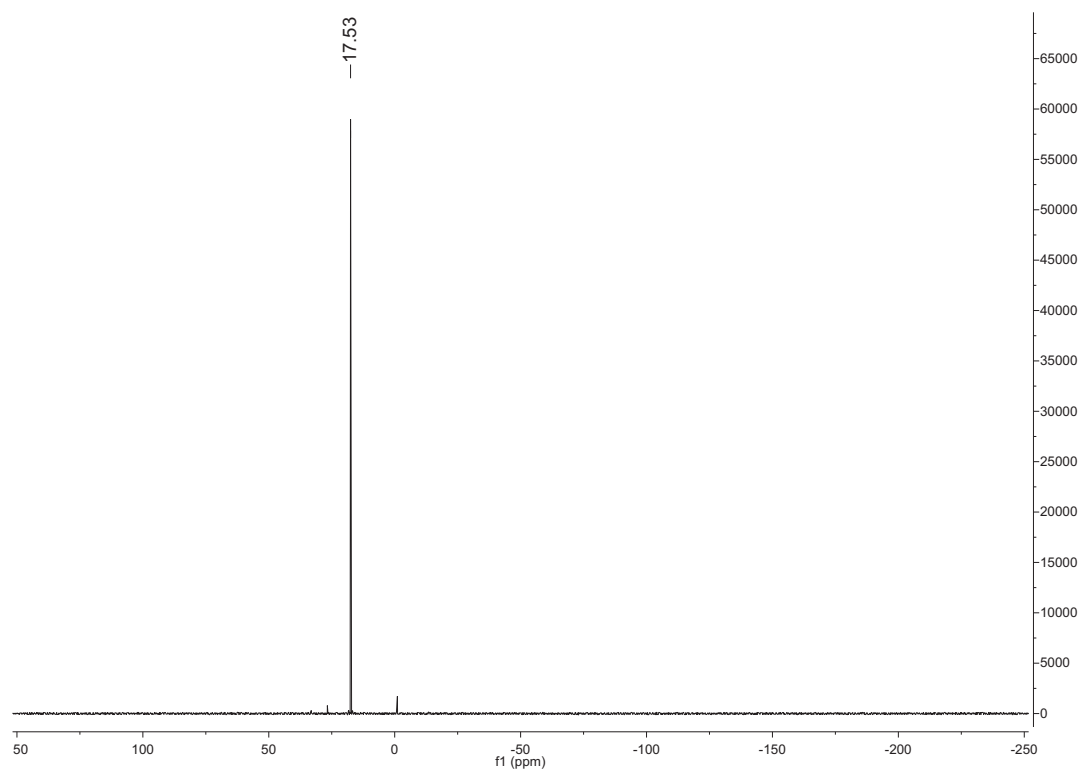
Fig. S8 ^{31}P{H}-NMR spectrum of 4-diethylphosphono-4'-biphenylcarboxylic acid methyl ester, **3** at 121 MHz in DMSO-d_6.
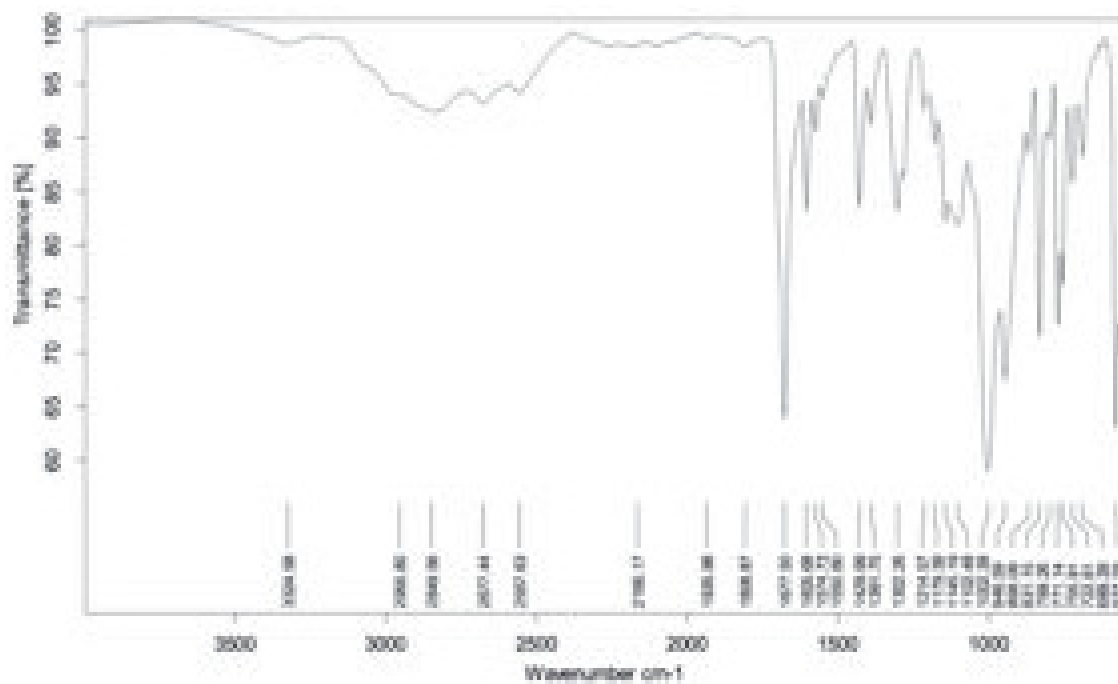
Fig. S9 FT-IR (ATR) spectrum of 4-phosphonato-4'-biphenylcarboxylic acid, **4**.
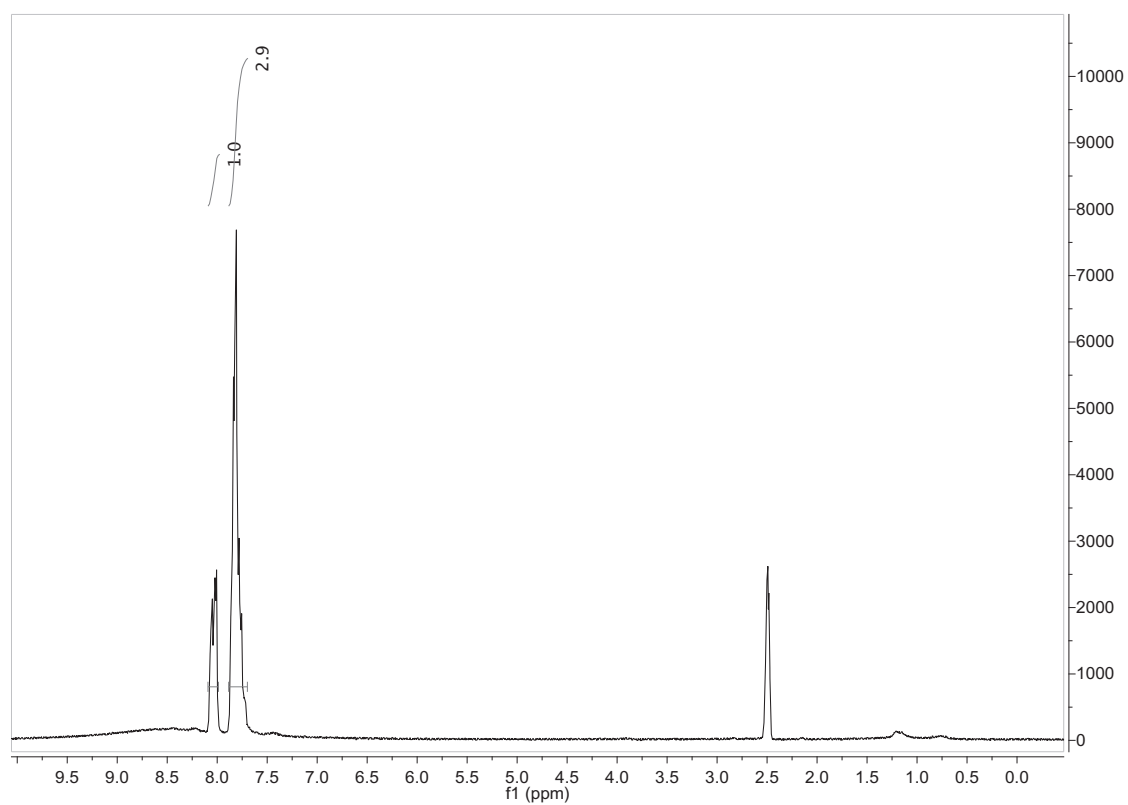
Fig. S10 ^{1}H-NMR spectrum of 4-phosphonato-4'-biphenylcarboxylic acid, **4** at 200 MHz in DMSO-d_6.

Fig. S11 ^{13}C-NMR spectrum of 4-phosphonato-4'-biphenylcarboxylic acid, **4** at 125.7 MHz in DMSO-d_6.
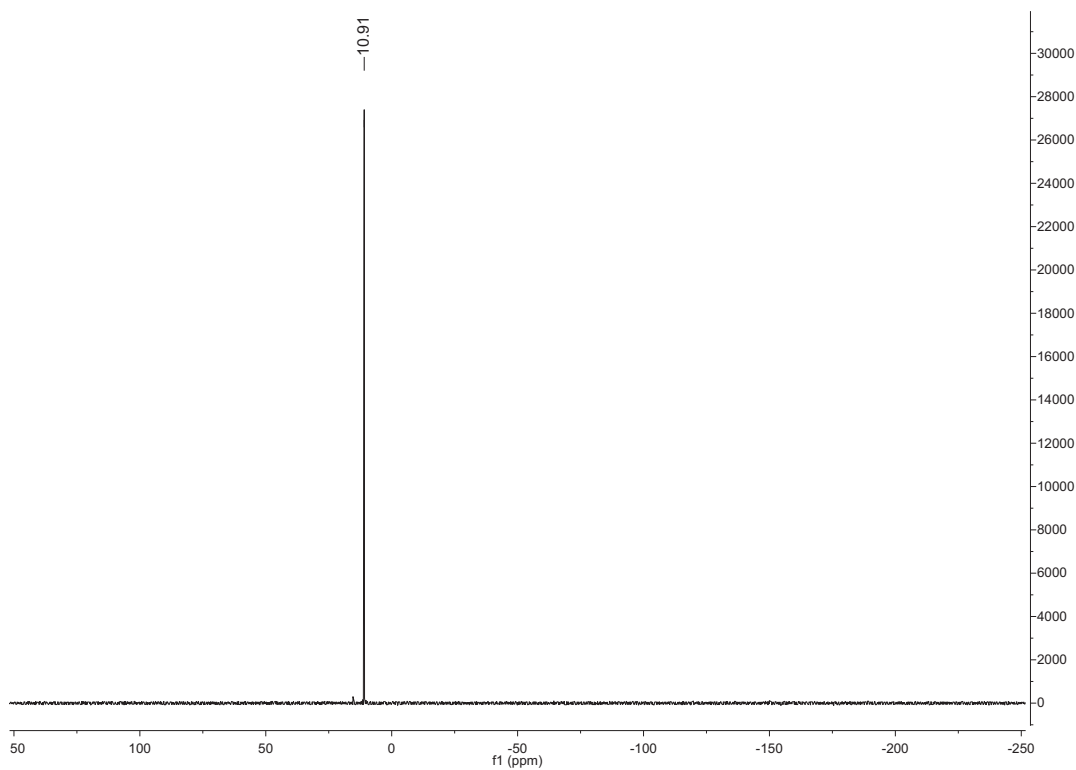
Fig. S12 ^{31}P{H}-NMR spectrum of 4-phosphonato-4'-biphenylcarboxylic acid, **4** at 121.5 MHz in 25% ND$_3$ in D$_2$O.
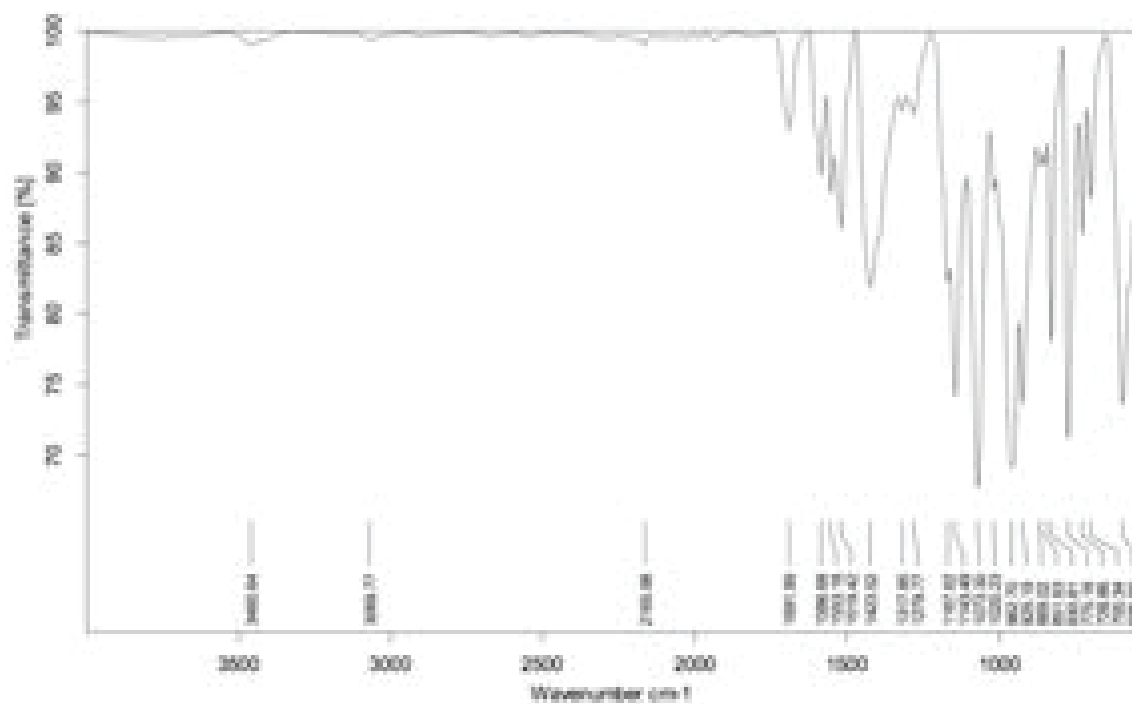
Fig. S13 FT-IR (ATR) spectrum of [Zn$_5$(μ_3-OH)$_4$(μ_4-O$_3$P-(C$_6$H$_4$)$_2$-CO$_2$-μ_2)$_2$], **5**.
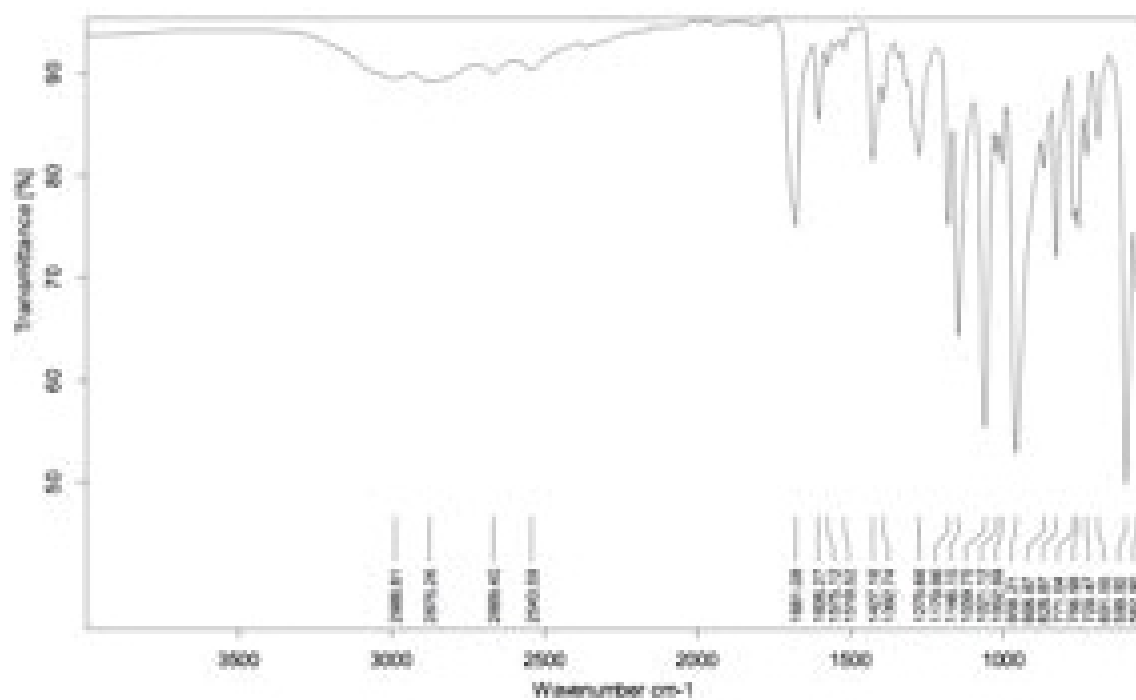
Fig. S14 FT-IR(ATR) spectrum of [Zn(μ_6-O$_3$P-(C$_6$H$_4$)$_2$-CO$_2$H)], **6**.
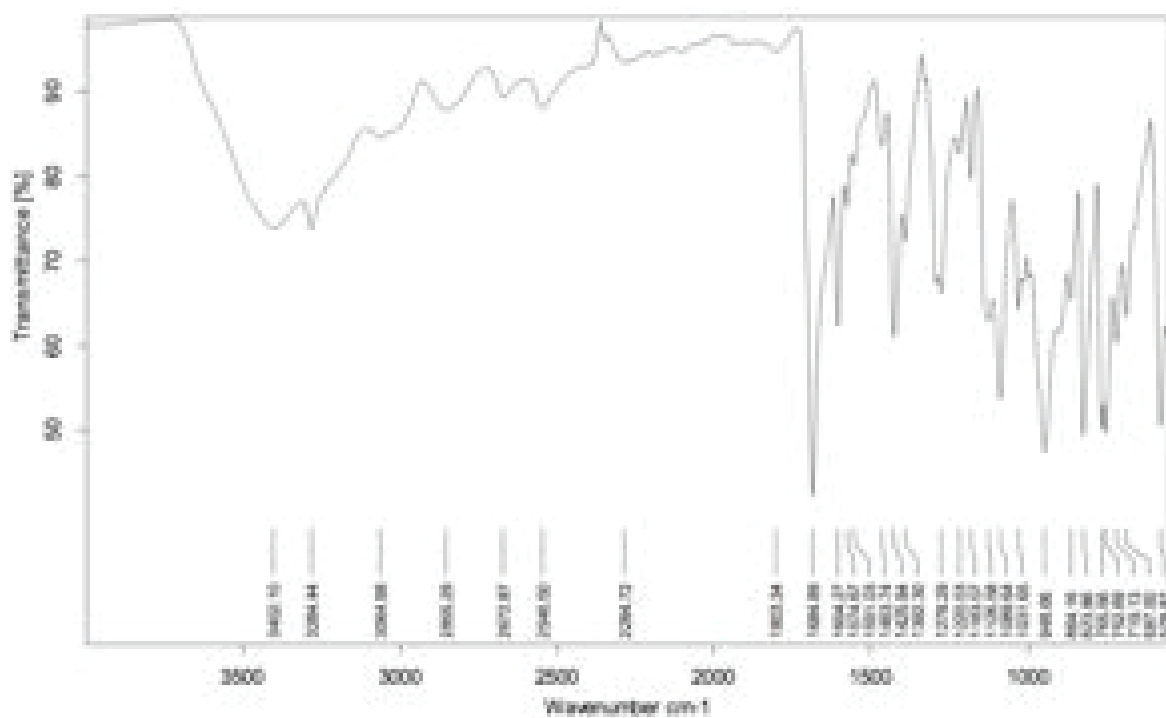
Fig. S15 FT-IR (ATR) spectrum of [Cd$_3$(μ_6-O$_3$P-(C$_6$H$_4$)$_2$-CO$_2$-μ_2)(μ_6-O$_3$P-(C$_6$H$_4$)$_2$-CO$_2$-μ_3)], **7**.
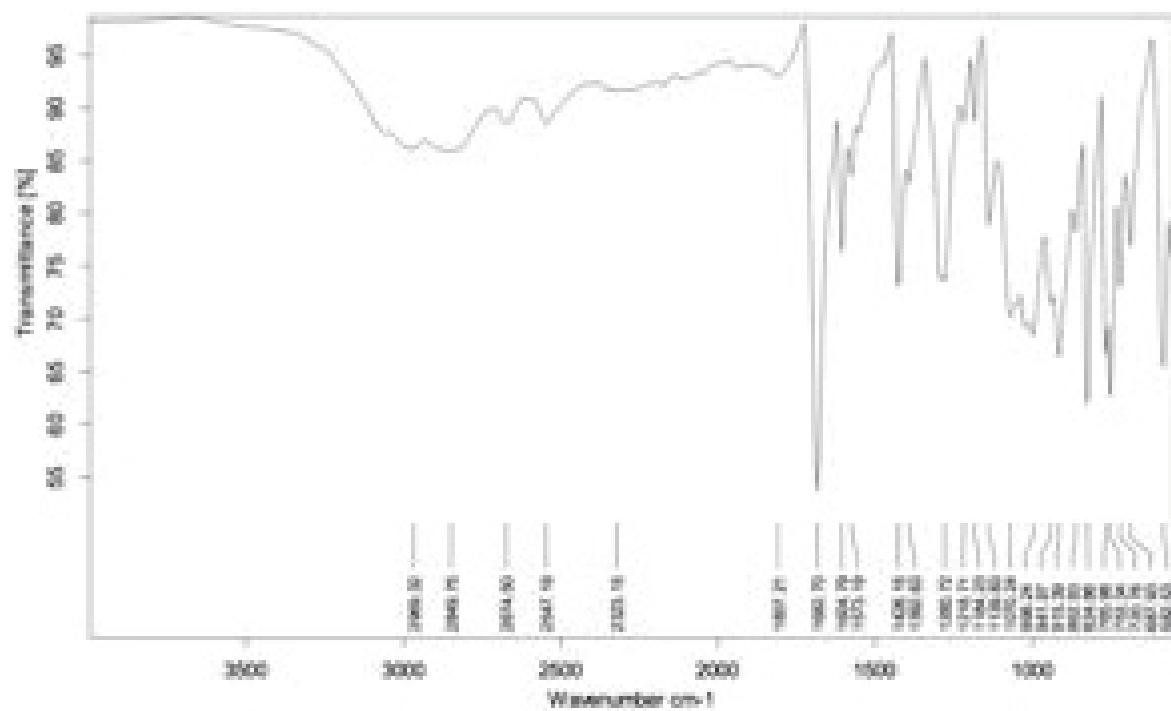
Fig. S16 FT-IR (ATR) spectrum of [Hg(μ_3-HO$_3$P-(C$_6$H$_4$)$_2$-CO$_2$H)], **8**.

Fig. S17 FT-IR (ATR) spectrum of [Co(μ_6-O$_3$P-(C$_6$H$_4$)$_2$-CO$_2$H)], **9**.

Thermogravimetric measurements
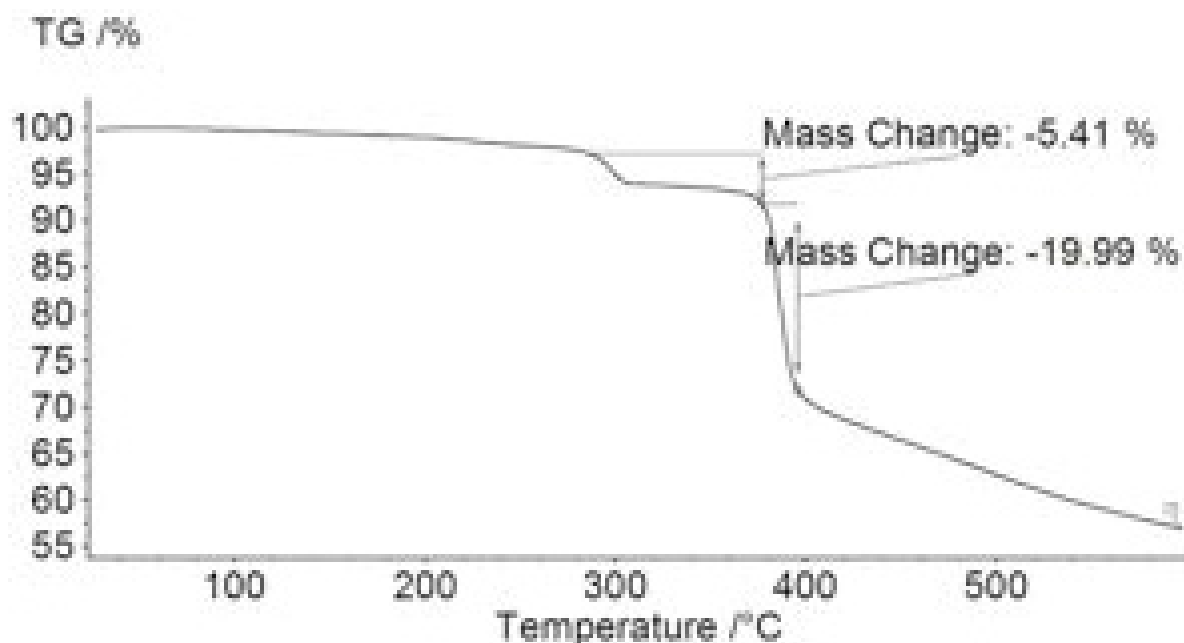
Fig. S18 TGA curve of 4-phosphonato-4'-biphenylcarboxylic acid, **4**.
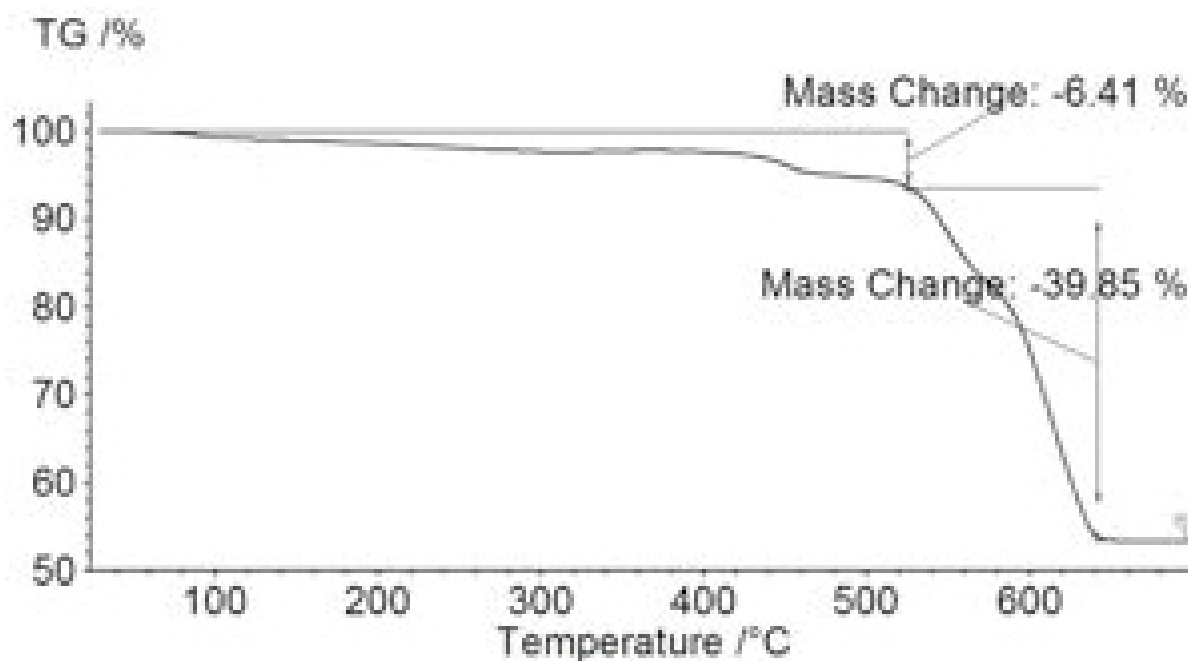
Fig. S19 TGA curve of $[Zn_5(\mu_3\text{-}OH)_4(\mu_4\text{-}O_3P\text{-}(C_6H_4)_2\text{-}CO_2\text{-}\mu_2)_2]$, **5**.
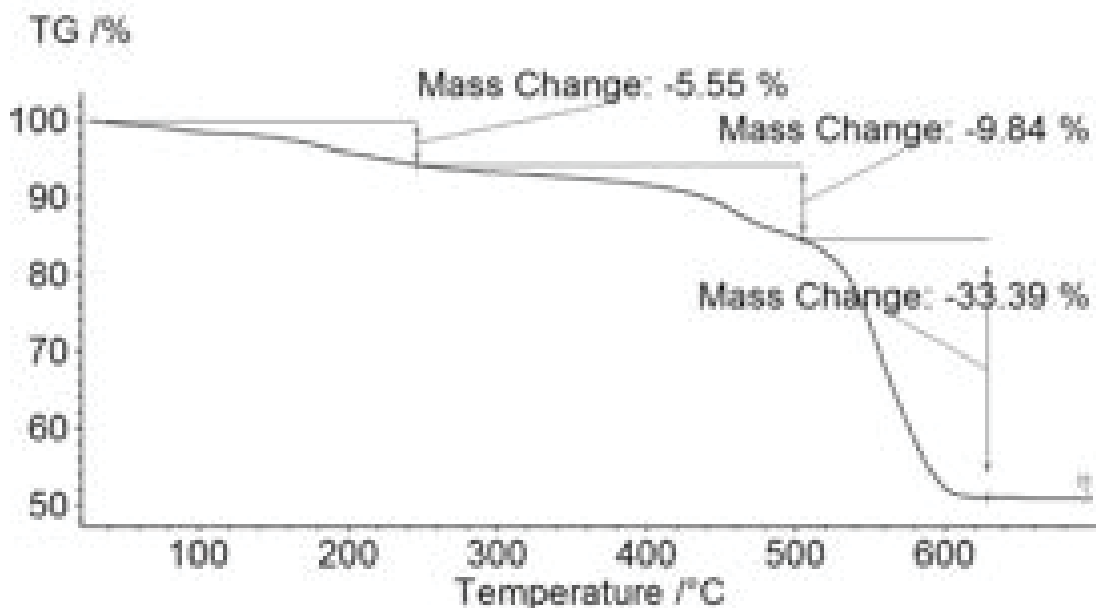
Fig. S20 TGA curve of [Zn(μ_6-O$_3$P-(C$_6$H$_4$)$_2$-CO$_2$H)], **6**.
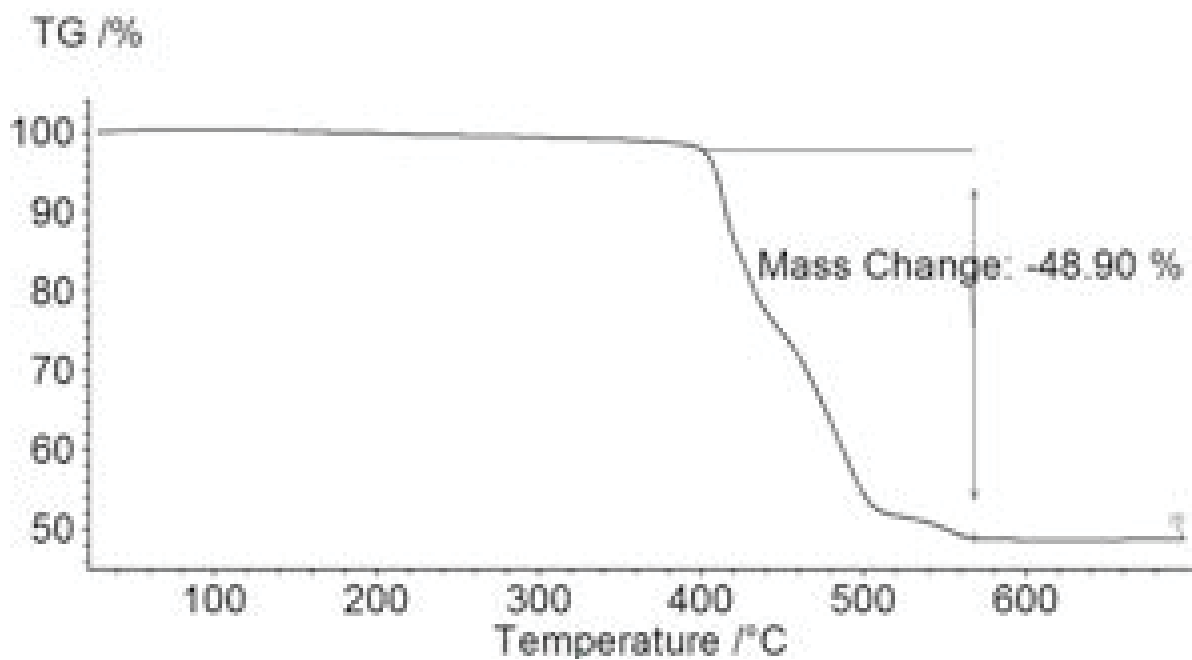
Fig. S21 TGA curve of [Cd$_3$(μ_6-O$_3$P-(C$_6$H$_4$)$_2$-CO$_2$-μ_2)(μ_6-O$_3$P-(C$_6$H$_4$)$_2$-CO$_2$-μ_3)], **7**.
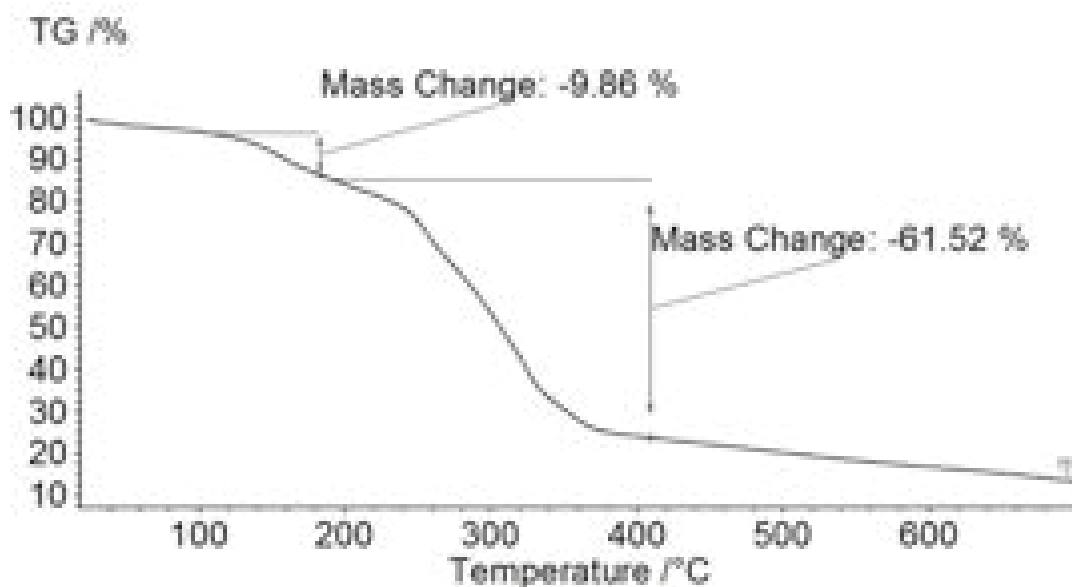
Fig. S22 TGA curve of $[Hg(\mu_3\text{-}HO_3P\text{-}(C_6H_4)_2\text{-}CO_2H)]$, **8**.
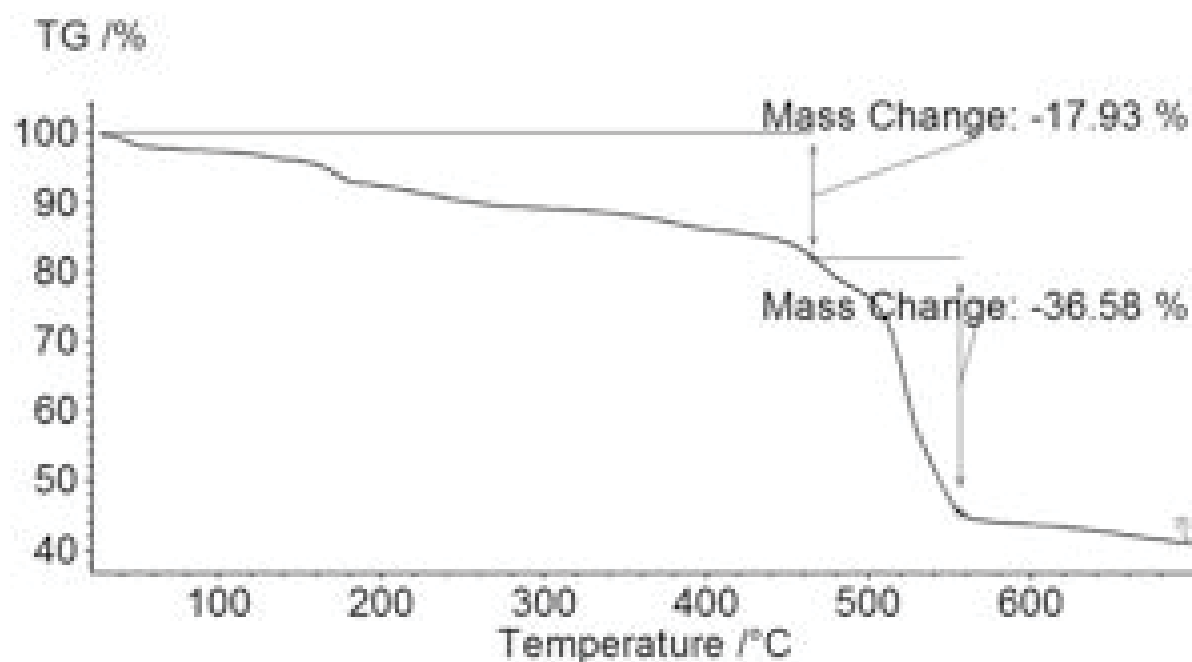
Fig. S23 TGA curve of $[Co(\mu_6\text{-}O_3P\text{-}(C_6H_4)_2\text{-}CO_2H)]$, **9**.
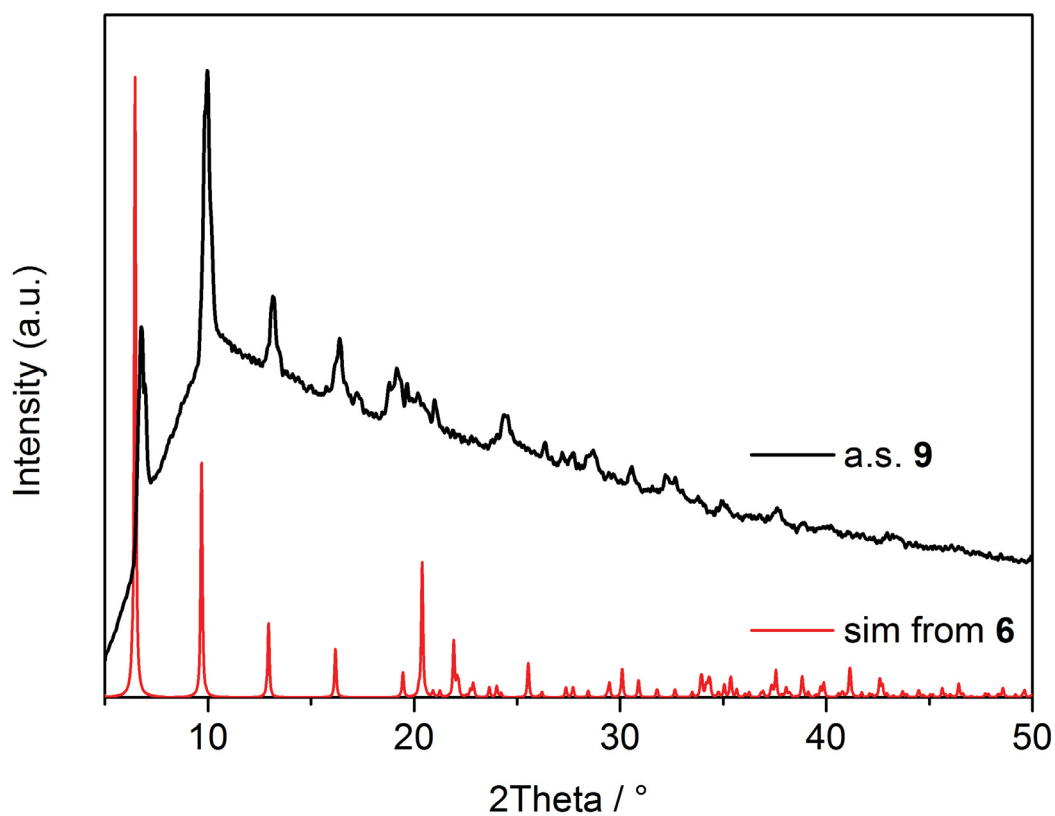
Powder X-ray diffraction

Fig. S24 PXRD comparison of **6** (red, simulated from single-crystal X-ray data set, SCXRD) and **9** (black, as synthesized, a.s.) for demonstration of isostructural relation. The strong background for the a.s. sample is due to the fluorescence of Co(II) ions towards CuKα radiation.[92].

Fig. S25 PXRD comparison of **5** and **6**. The pattern of "**5**" obtained after synthesis (black) with the simulated patterns of **5** and **6** (red and blue, respectively, from SCXRD). The green pattern is the experimental pattern of the crystalline powder of the H$_3$BPPA ligand **4**.
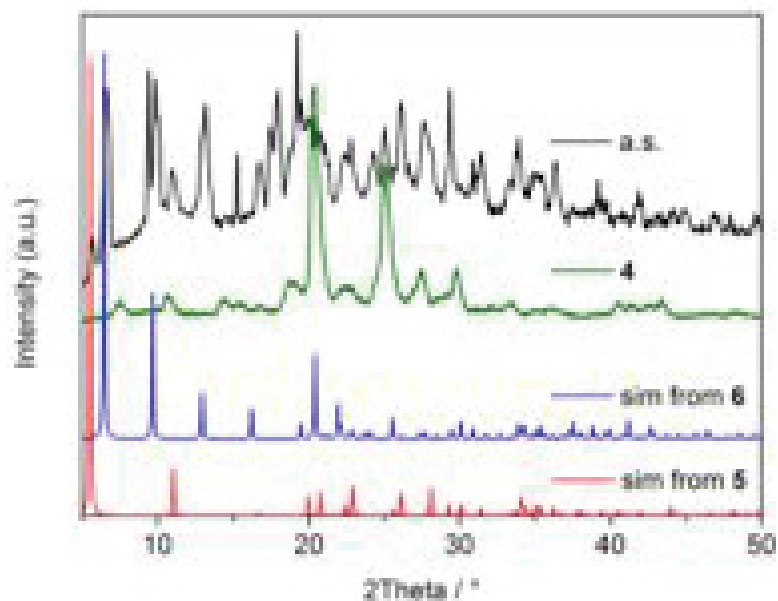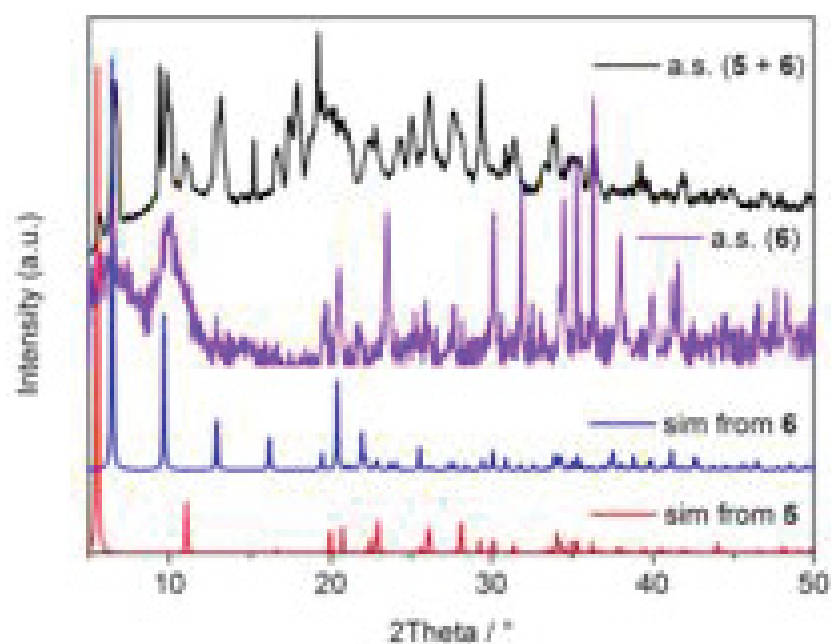

Fig. S26 PXRD comparison of **5** and **6**. The pattern of "**5**" obtained after synthesis (black) with the simulated patterns of **5** and **6** (red and blue, respectively, from SCXRD) and the experimental pattern of **6** (purple, as synthesized, a.s.).

Additional structure graphics
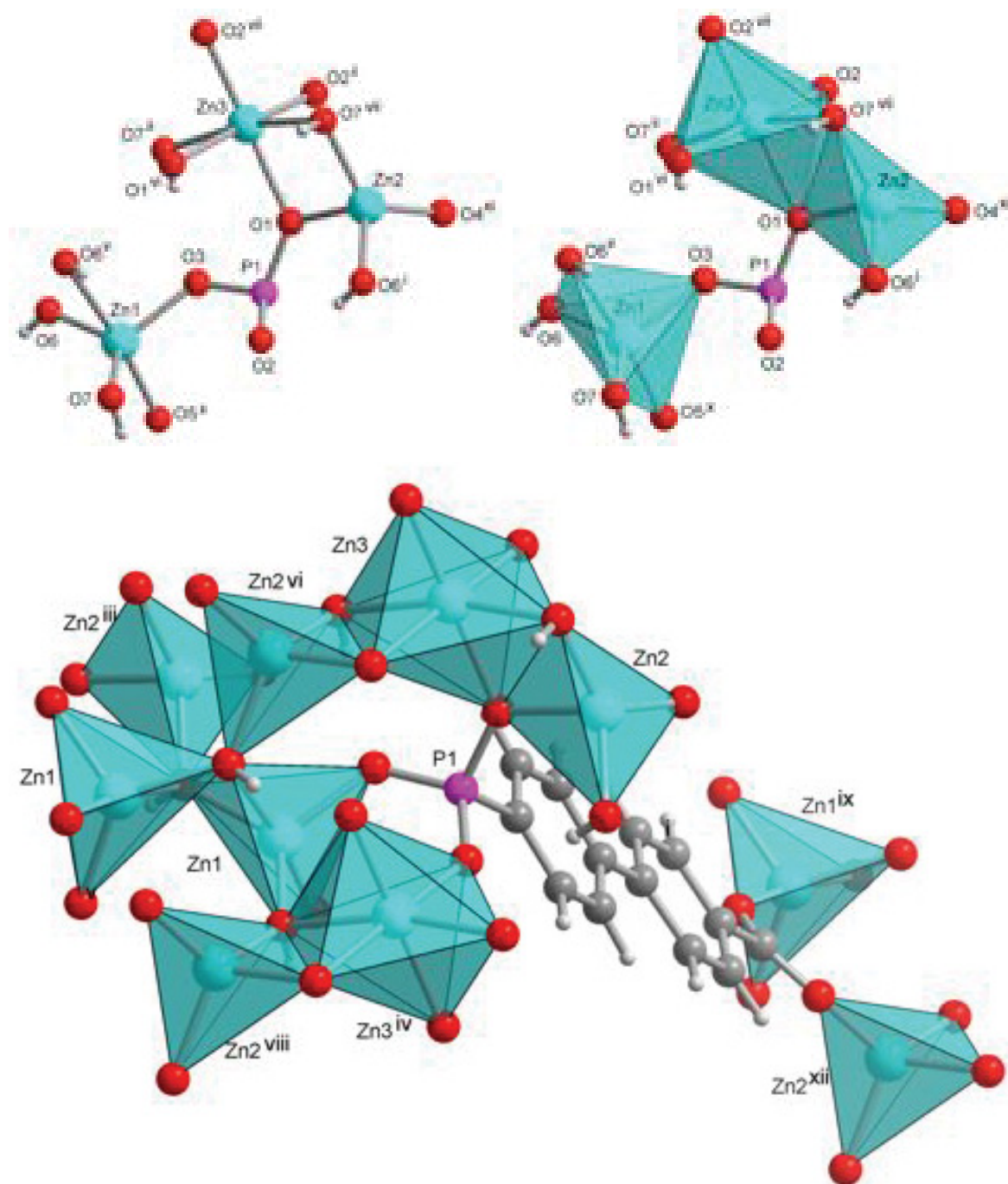
Fig. S27 Coordination sphere around the crystallographic different Zn atoms 1, 2 and 3 in **5**. Hydrogen bonds from OH are depicted in Fig. S29.

Symmetriy transformations: i = x, y, 1+z; ii = x, 1+y, z; iii = x, y, -1+z; iv = x, -1+y, z; v = -x, y, -z; vi = -x, y, 1-z; vii = -x, 1+y, 1-z; viii = -x, -1+y, 1-z; ix = 0.5-x, 0.5+y, 1-z; x = 0.5-x, -0.5+y, 1-z; xi = 0.5-x, 0.5+y, 2-z; xii = 0.5-x, -0.5+y, 2-z.
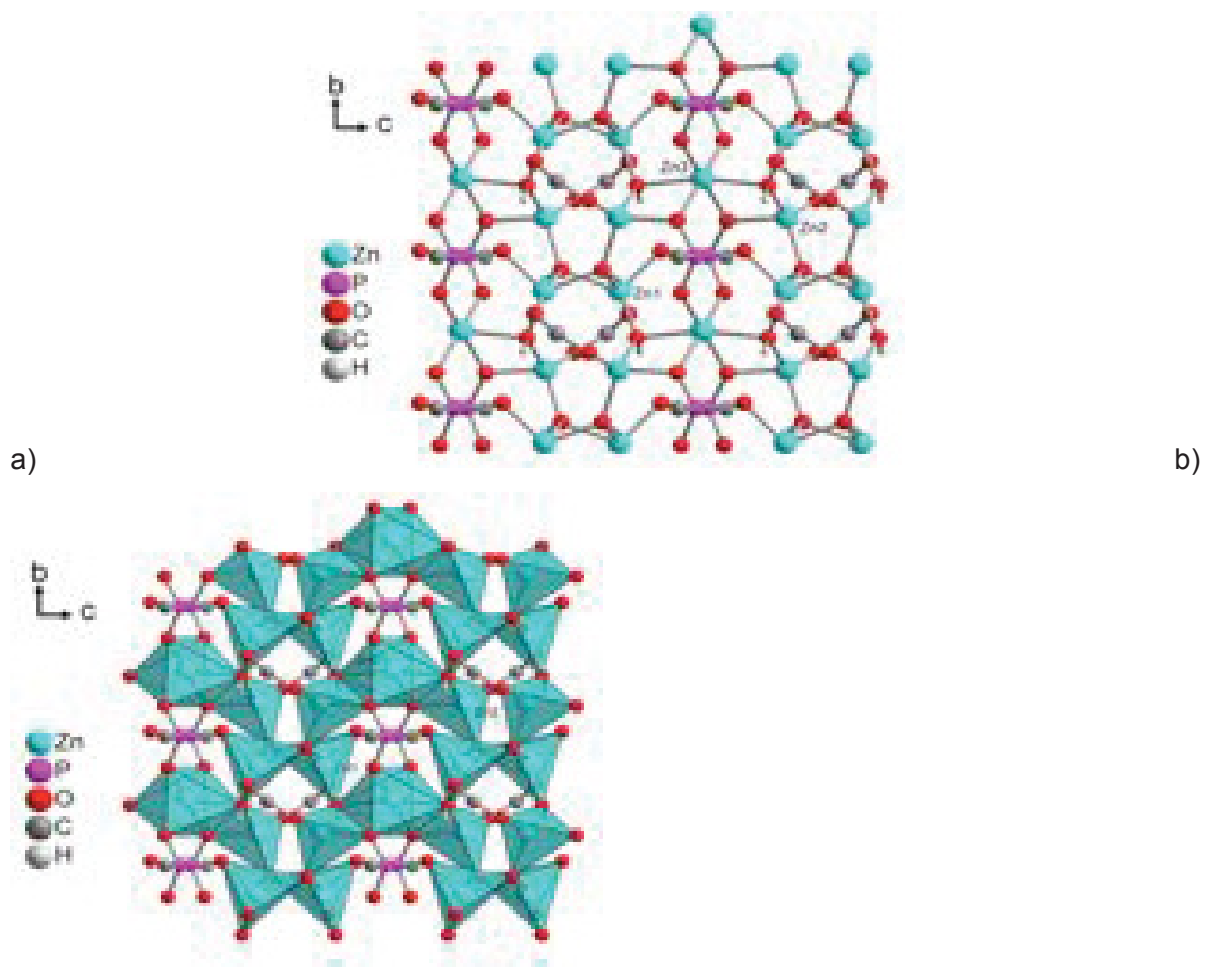
Fig. S28 Ball-and-stick drawing of the ZnO-layer along a-axis (a) and with ZnO_x polyhedra (b) of complex **5**.
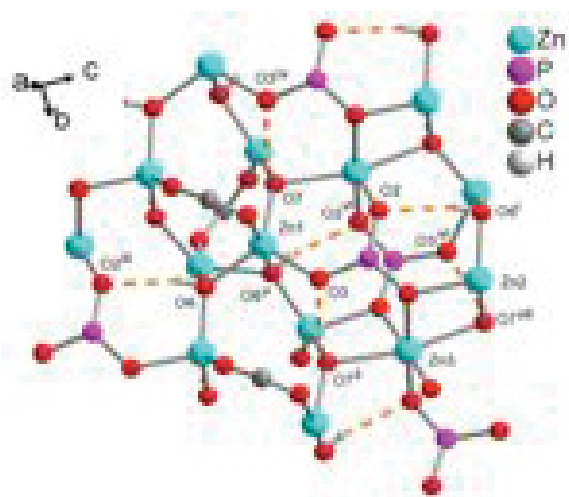
Fig. S29 Hydrogen bonds from OH$^-$ to phosphonato group in **5**. For details of the H-bonds see Table S5. Symmetry transformations i = x, 1+y, z; iii = -x, 1+y, 1-z; iv = 0.5-x, 0.5+y, 1-z; v = 0.5+x, 0.5+y, 1+z; vi = 0.5-x, 1.5+y, 1-z; vii = x, y-1, z.
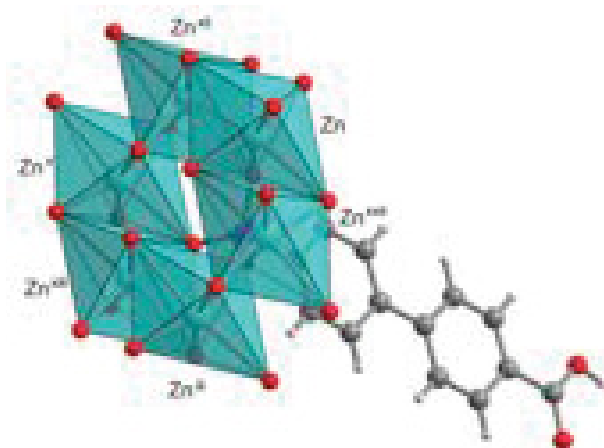
Fig. S30 Expanded asymmetric unit of **6** with {ZnO$_6$} octahedra. Symmetry transformations iii: 1-x, y, 1-z, v: 3/2-x, 1/2+y, 1-z, xii: 1-x, 1+y, 1-z, xiii: 1-x, 2-y, 1-z, xxii: -x, 1-y, 1-z.
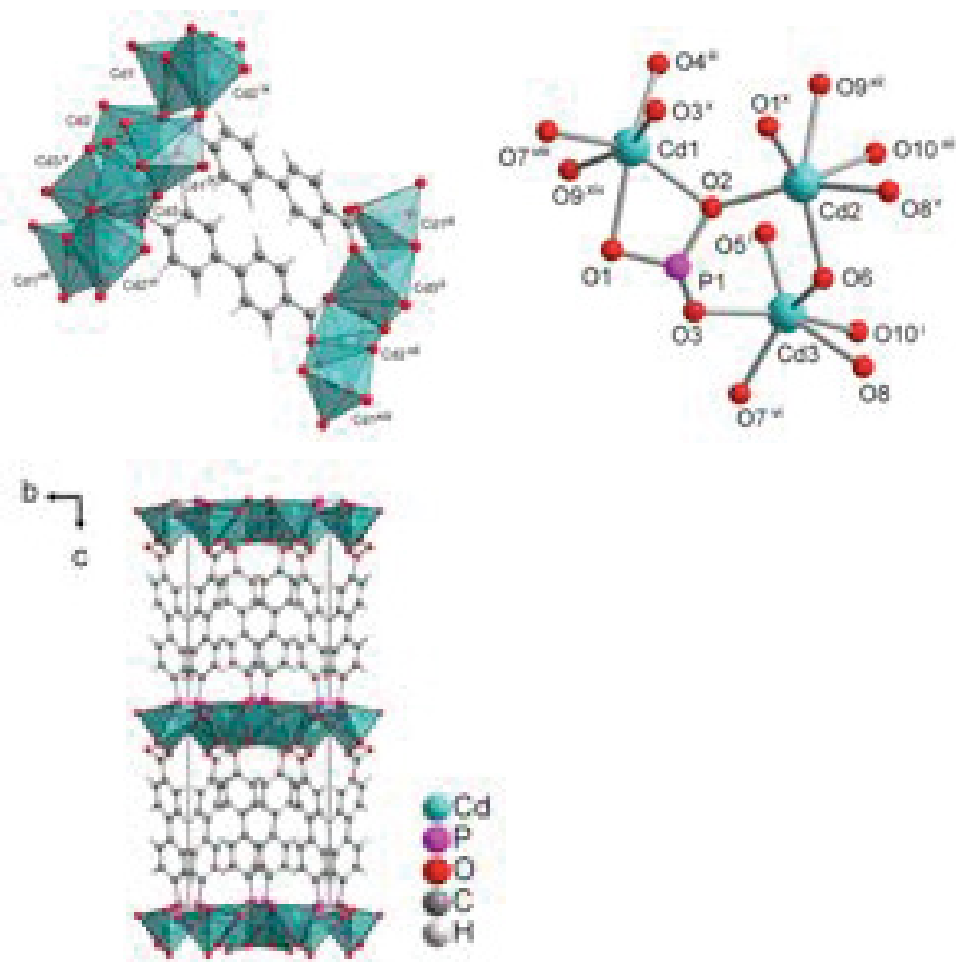
Fig. S31 Expanded asymmetric unit of **7** with drawing of ball-and-stick model and CdO$_x$ polyhedra highlighted(left). Coordination sphere around the crystallographic different Cd atoms 1, 2 and 3 in **7** (right). Symmetry transformations i: 1/2-x, y, 1/2+z, ii: 1/2-x, y, -1/2+z, iii: -x, 2-y, 1/2+z, v: -1/2+x, 1-y, z, vi: 1/2+x, 1-y, z, vii: x, -1+y, z, ix: 1/2+x, 2-y, z, x: -1/2+x, 2-y, z, xii: -x, 1-y, 1/2+z, xiii: 1/2-x, -1+y, -1/2+z, xiv: 1/2-x, 1+y, 1/2+z.

114

Fig. S32 Top: Expanded asymmetric unit of **8** with drawing of ball-and-stick model and Hg$_2$O$_3$ polyhedra highlighted. Bottom: Projection of the packing diagram on the *ab* plane. Symmetry transformations ii: +x, 1-y, -1/2+z, iii: 1-x, +y, 1/2-z, v: +x, -y, -1/2+z, vi: 1-x, 1-y, 1-z, xv: 1-x, -y, 1-z.

Structure Tables

Tables were created with publCIF.[93]

Table S1 Bond lengths and angles (Å, °) for **2**.

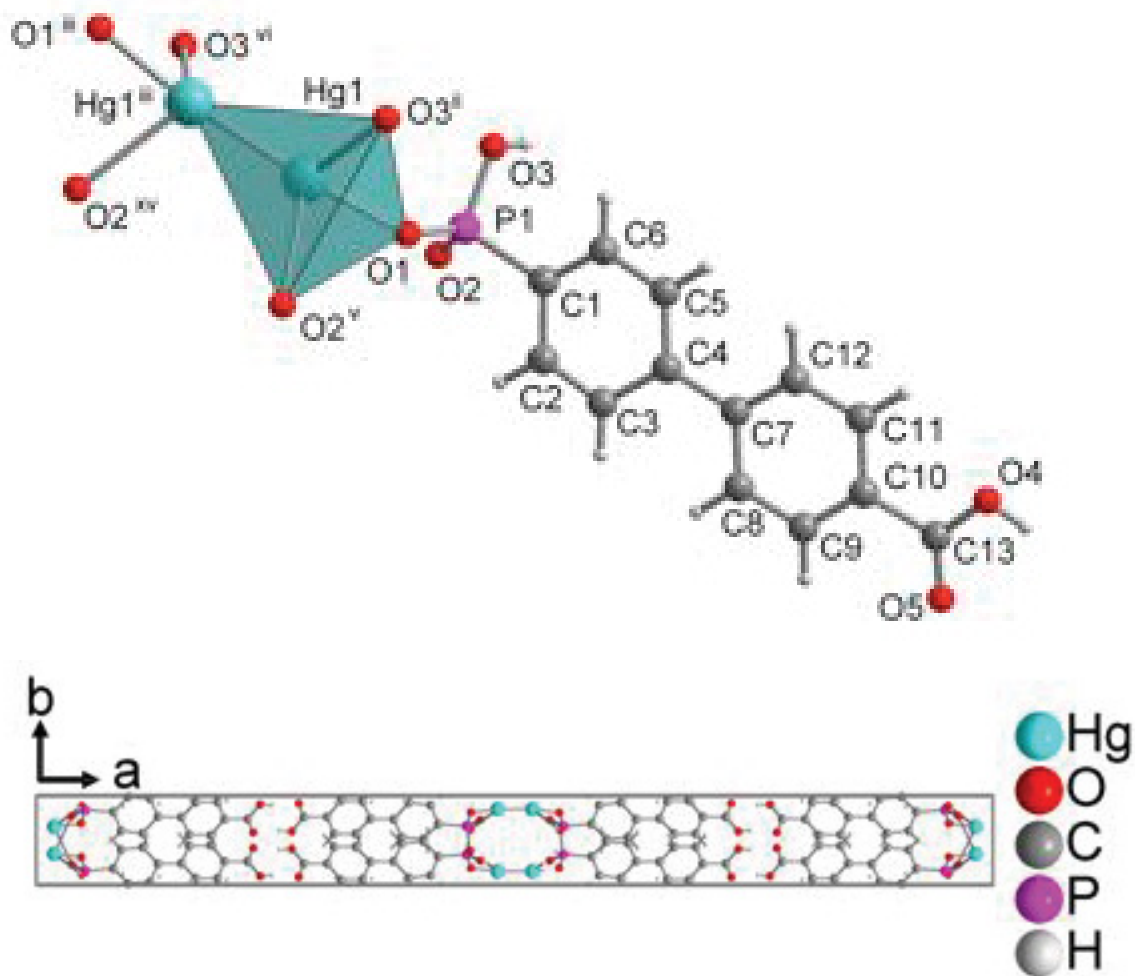|			
I1—C1	2.082(9)	C8—C9	1.375(12)
C1—C2	1.383(12)	C8—C7	1.405(11)
C1—C6	1.400(13)	C13—C10	1.490(13)
O1—C13	1.202(13)	C10—C11	1.395(12)
C2—C3	1.379(15)	C10—C9	1.398(12)
O2—C13	1.303(12)	C11—C12	1.377(12)
O2—C14	1.440(18)	C12—C7	1.409(11)
C3—C4	1.397(13)	C5—C4	1.390(10)
C5—C6	1.376(12)	C4—C7	1.484(12)
C2—C1—C6	118.4(8)	C9—C8—C7	122.5(8)
C2—C1—I1	121.2(7)	C11—C10—C9	118.1(8)
C6—C1—I1	120.4(6)	C11—C10—C13	119.0(8)
C3—C2—C1	120.3(8)	C9—C10—C13	122.9(8)
C13—O2—C14	117.9(10)	C2—C3—C4	122.2(7)
C5—C4—C3	116.7(8)	C6—C5—C4	121.7(8)
C5—C4—C7	121.2(7)	O1—C13—O2	123.6(10)
C3—C4—C7	122.1(7)	O1—C13—C10	123.4(9)
C5—C6—C1	120.6(7)	O2—C13—C10	112.9(8)
C8—C9—C10	120.7(8)	C11—C12—C7	122.3(6)
C12—C11—C10	120.8(7)	C8—C7—C12	115.7(8)
C6—C1—C2—C3	1.5(12)	C8—C7—C4	122.2(7)
I1—C1—C2—C3	-179.3(7)	C12—C7—C4	122.1(7)
C1—C2—C3—C4	-0.5(14)	C12—C7—C4	122.1(7)
C6—C5—C4—C3	0.6(11)	O2—C13—C10—C9	-6.7(10)
C6—C5—C4—C7	-178.2(7)	C7—C8—C9—C10	-0.4(11)
C2—C3—C4—C5	-0.6(12)	C11—C10—C9—C8	0.0(11)
C2—C3—C4—C7	178.3(8)	C13—C10—C9—C8	178.8(7)
C4—C5—C6—C1	0.4(13)	C9—C10—C11—C12	0.5(12)
C2—C1—C6—C5	-1.4(12)	C13—C10—C11—C12	-178.4(7)
I1—C1—C6—C5	179.3(6)	C10—C11—C12—C7	-0.5(12)

C14—O2—C13—O1	2.2(14)	C9—C8—C7—C12	0.4(11)
C14—O2—C13—C10	-175.8(8)	C9—C8—C7—C4	-179.9(6)
O1—C13—C10—C11	-5.9(12)	C11—C12—C7—C8	0.1(11)
O2—C13—C10—C11	172.2(7)	C11—C12—C7—C4	-179.6(7)
O1—C13—C10—C9	175.3(9)	C5—C4—C7—C8	179.7(7)
C3—C4—C7—C8	0.9(10)		

Table S2 Bond lengths and angles (Å, º) for **3**.

P1—O2	1.462(2)	C5—C6	1.384(4)
P1—O1	1.560(2)	O5—C13	1.195(3)
P1—O3	1.567(2)	C7—C12	1.394(3)
P1—C1	1.788(3)	C7—C8	1.397(4)
O1—C15	1.446(4)	C8—C9	1.380(4)
O4—C13	1.341(3)	C1—C6	1.400(3)
O4—C14	1.449(3)	C2—C3	1.378(4)
C1—C2	1.387(4)	C9—C10	1.395(4)
C3—C4	1.403(3)	C10—C11	1.388(4)
O3—C17	1.437(5)	C10—C13	1.494(4)
C4—C5	1.397(4)	C11—C12	1.389(4)
C4—C7	1.481(4)	C6—C5—C4	121.0(2)
C16—C15	1.486(4)	C5—C6—C1	120.6(2)
C18—C17	1.338(7)	C12—C7—C8	117.9(2)
O2—P1—O1	116.11(13)	C12—C7—C4	121.3(2)
O2—P1—O3	113.98(13)	C8—C7—C4	120.8(2)
O1—P1—O3	102.44(13)	C9—C8—C7	121.9(2)
O2—P1—C1	113.48(13)	C8—C9—C10	119.7(2)
O1—P1—C1	101.48(11)	C11—C10—C9	119.2(2)
O3—P1—C1	108.04(11)	C11—C10—C13	122.8(2)
C15—O1—P1	121.6(2)	C9—C10—C13	117.9(2)
C13—O4—C14	115.3(2)	O5—C13—O4	123.5(2)
C2—C1—C6	118.4(2)	O5—C13—C10	124.4(2)
C2—C1—P1	118.48(18)	O4—C13—C10	112.2(2)
C6—C1—P1	123.1(2)	C10—C11—C12	120.7(2)
C3—C2—C1	121.3(2)	C11—C12—C7	120.7(2)

C2—C3—C4	120.8(2)	C18—C17—O3	115.5(5)
C17—O3—P1	122.1(3)	P1—C1—C6—C5	179.36(19)
C5—C4—C3	117.9(2)	C5—C4—C7—C12	-36.2(3)
C5—C4—C7	121.7(2)	C3—C4—C7—C12	144.3(2)
C3—C4—C7	120.4(2)	C5—C4—C7—C8	144.6(2)
O1—C15—C16	107.6(3)	C3—C4—C7—C8	-34.9(3)
O2—P1—O1—C15	-46.8(3)	C12—C7—C8—C9	0.1(4)
O3—P1—O1—C15	78.1(3)	C4—C7—C8—C9	179.4(2)
C1—P1—O1—C15	-170.3(3)	C7—C8—C9—C10	0.0(4)
O2—P1—C1—C2	-23.6(3)	C8—C9—C10—C11	-0.3(4)
O1—P1—C1—C2	101.7(2)	C8—C9—C10—C13	179.8(2)
O3—P1—C1—C2	-151.0(2)	C14—O4—C13—O5	-0.7(4)
O2—P1—C1—C6	156.8(2)	C14—O4—C13—C10	178.8(2)
O1—P1—C1—C6	-77.9(2)	C11—C10—C13—O5	-166.8(2)
O3—P1—C1—C6	29.4(2)	C9—C10—C13—O5	13.1(4)
C6—C1—C2—C3	1.2(4)	C11—C10—C13—O4	13.8(3)
P1—C1—C2—C3	-178.4(2)	C9—C10—C13—O4	-166.3(2)
C1—C2—C3—C4	-1.6(4)	C9—C10—C11—C12	0.5(4)
O2—P1—O3—C17	-37.5(3)	C13—C10—C11—C12	-179.6(2)
O1—P1—O3—C17	-163.7(3)	C10—C11—C12—C7	-0.4(4)
C1—P1—O3—C17	89.7(3)	C8—C7—C12—C11	0.1(3)
C2—C3—C4—C5	1.0(4)	C4—C7—C12—C11	-179.1(2)
C2—C3—C4—C7	-179.4(2)	P1—O3—C17—C18	-104.0(6)
P1—O1—C15—C16	160.8(2)	C4—C5—C6—C1	-0.3(4)
C3—C4—C5—C6	-0.1(4)	C2—C1—C6—C5	-0.2(4)
C7—C4—C5—C6	-179.6(2)		

Table S3. Hydrogen-bond geometry (Å, º) for **3**.

D—H···A	D—H	H···A	D···A	D—H···A
C17—H17A···O2	0.97	2.56	3.039(5)	111
C17—H17B···O5[i]	0.97	2.56	3.507(7)	164

Symmetry code: i = x-1, y, z-1.

Table S4 Hydrogen-bond geometry (Å, °) for **5**.

D—H$\cdots A$	D—H	H$\cdots A$	$D\cdots A$	D—H$\cdots A$
O6—H1$\cdots$O2^{xi}	0.76 (11)	2.17 (11)	2.860 (6)	150 (12)
O6—H1$\cdots$O7^{ii}	0.76(11)	2.34 (12)	2.845 (7)	125 (11)
O7—H7$\cdots$O3^{viii}	0.79 (8)	2.03 (7)	144 (7)	144 (7)

Symmetry codes: ii = x, 1+y, z; ; viii = -x, -1+y, 1-z;; xi = 0.5-x, 0.5+y, 2-z.

Table S5 Hydrogen-bond geometry (Å, °) for **6**.

D—H$\cdots A$	D—H	H$\cdots A$	$D\cdots A$	D—H$\cdots A$
O3—H3A$\cdots$O4^{xiii}	0.83(1)	1.77(1)	2.61(2)	170.90(8)

Symmetry transformation: xiii = 2-x, 1-y, -z.

Table S6 Selected angles (°) for 7.

O4^{iii}—Cd1— O7^{vii}	108.8(4)	O2—Cd2—O8^{vi}	157.5(3)
O4^{iii}—Cd1—O2	106.6(4)	O2—Cd2—O1^{x}	92.7(3)
O7^{vii}—Cd1—O2	139.4(3)	O8^{vi}—Cd2— O1^{x}	88.1(3)
O4^{iii}—Cd1—O3^{x}	89.7(3)	O2—Cd2—O6	83.2(3)
O7^{vii}—Cd1—O3^{x}	71.0(3)	O8^{vi}—Cd2—O6	82.9(3)
O2—Cd1—O3^{x}	90.3(3)	O1^{x}—Cd2—O6	143.7(3)
O4^{iii}—Cd1—O1	158.0(3)	O2—Cd2— O9^{xii}	107.1(3)
O7^{vii}—Cd1—O1	88.3(3)	O5^{i}—Cd3—O7^{v}	117.0(4)
O2—Cd1—O1	63.9(3)	O5^{i}—Cd3—O6	102.6(4)
O3^{x}—Cd1—O1	109.5(3)	O7^{v}—Cd3—O6	134.4(3)
O4^{iii}—Cd1—O9^{xiv}	91.5(3)	O5^{i}—Cd3—O3	89.3(3)
O7^{vii}—Cd1—O9^{xiv}	88.3(3)	O7^{v}—Cd3—O3	72.6(3)
O2—Cd1—O9^{xiv}	110.0(3)	O6—Cd3—O3	86.9(3)
O3^{x}—Cd1—O9^{xiv}	158.4(3)	O5^{i}—Cd3—O8	144.2(3)
O1—Cd1—O9^{xiv}	74.7(3)	O7^{v}—Cd3—O8	92.3(3)
O8^{vi}—Cd2—O9^{xii}	94.9(3)	O6—Cd3—O8	63.5(3)
O1^{x}—Cd2—O9^{xii}	76.6(3)	O3—Cd3—O8	120.6(3)
O6—Cd2—O9^{xii}	139.0(3)	O5^{i}—Cd3—O10^{i}	85.5(4)
O2—Cd2—O10^{xii}	119.3(3)	O7^{v}—Cd3—O10^{i}	87.7(3)
O8^{vi} —Cd2—O10^{xii}	77.2(3)	O6—Cd3—O10^{i}	118.5(3)
O1^{x}—Cd2—O10^{xii}	126.4(3)	O3—Cd3—O10^{i}	154.6(3)
O6—Cd2—O10^{xii}	85.7(3)	O8—Cd3—O10^{i}	74.9(3)
O9^{xii}—Cd2—O10^{xii}	54.3(3)		
		Cd2^{xi}—O10—Cd3^{ii}	95.5(3)
Cd2—O2—Cd1	126.7(3)	Cd2^{xi}—O9—Cd1^{xiii}	97.8(3)
Cd3—O3—Cd1^{ix}	86.8(3)	Cd3^{v}—O7—Cd1^{ii}	92.3(3)
Cd2^{vi}—O8—Cd3	106.5(3)	Cd2—O6—Cd3	119.0(3)

Symmetry transformations: i = 1/2-x, y, 1/2+z; ii = 1/2-x, y, -1/2+z; iii = -x, 2-y, 1/2+z; v = -1/2+x, 1-y, z; vi = 1/2+x, 1-y, z; vii = x, -1+y, z; ix = 1/2+x, 2-y, z; x = -1/2+x, 2-y, z; xi = -x, 1-y, -1/2+z; xii = -x, 1-y, 1/2+z; xiii = 1/2-x, -1+y, -1/2+z; xiv = 1/2-x, 1+y, 1/2+z.

Table S7 Hydrogen-bond geometry (Å, °) for 7.

D—H⋯*A*	*D*—H		H⋯*A*	*D*⋯*A*	*D*—H⋯*A*

C15—H15···O8^{vi}	0.95		2.61	3.262(17)	126

Symmetry transformation: vi = 1/2+x, 1-y, z

Table S8 Hydrogen-bond geometry (Å, º) for **8**.

D—H$\cdots A$	D—H	H$\cdots A$	$D\cdots A$	D—H$\cdots A$
O3—H10$\cdots$O2^{iv}	0.84	1.69	2.516(18)	168
O4—H4$\cdots$O5^{xiii}	0.84	1.78	2.619(19)	174
C2—H2$\cdots$O1^{iii}	0.95	2.49	3.37(2)	154

Symmetry codes:iii = x, -y, -z+1/2; iv = x, 1-y, -1/2+z; xiii = -x+1/2, -y+1/2, -z+2.

Supramolecular Packing Analyses

Packing Analysis by PLATON((a) A. Spek, *Acta Crystallographica Section D*, 2009, **65**, 148-155;(b) A. L. Spek *PLATON – A multipurpose crystallographic tool*, Utrecht University: Utrecht, The Netherlands, 2005.)

Despite the presence of biphenyl π-systems in compounds **1** and **2**, there are no π-π interactions [94] and only few intermolecular C-H⋯π [95] evident.
The supramolecular packing analyses of the biphenyl rings are tabulated below(Tables S12 – S14).

The listed "Analysis of Short Ring-Interactions" for possible π-stacking interactions yielded rather long centroid-centroid distances(>4.0 Å) together with non-parallel ring planes(α >> 0°) and large slip angles(β, γ > 30°).
In comparison, significant π-stacking shows rather short centroid-centroid contacts(<3.8 Å), near parallel ring planes(alpha < 10° to ~0° or even exactly 0° by symmetry), small slip angles(β, γ < 25°) and vertical displacements(slippage < 1.5 Å) which translate into a sizable overlap of the aryl-plane areas [95,96].

Significant intermolecular C-H⋯π contacts start around 2.7 Å for the(C-)H⋯ring centroid distances with H-Perp also starting at 2.6-2.7 Å and C-H⋅⋅Cg > 145° [95,[97],98].
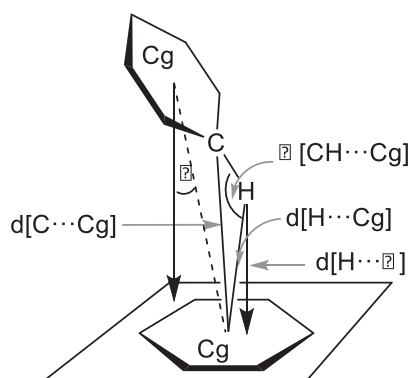
Scheme S1 Graphical presentation of the parameters used for the description of CH-π interactions.

Packing Analysis for possible **CH-π interactions** (see Scheme S1 for explanation)**:**
==
=====
Analysis of X-H...Cg(π -Ring) Interactions(H..Cg < 3.0 Ang. - Gamma < 30.0 Deg)
==
=====
- Cg(J)   = Center of gravity of ring J(Plane number above)
- H-Perp = Perpendicular distance of H to ring plane J
- Gamma   = Angle between Cg-H vector and ring J normal
- X-H..Cg = X-H-Cg angle(degrees)
- X..Cg   = Distance of X to Cg(Angstrom)
- X-H, π = Angle of the X-H bond with the π-plane(i.e.' Perpendicular = 90 degrees, Parallel = 0 degrees)

Table S9 Analysis of X-H...Cg(π -Ring) Interactions in **5.**

X--H(I)	Cg(J)	[ARU(J)]	H..Cg	H-Perp	Gamma	C-H..Cg	C..Cg	X-H,π
C(9)-H(9)	->Cg(8)	[4547.01]	2.95	2.89	12.05	140	3.734(7)	53
C(11)-H(11)	->Cg(8)	[4556.01]	2.95	-2.91	9.17	138	3.709(8)	54
		Min. or max.	2.950	-2.907	9.2	140	3.709	54.0

[4547] = 1/2-X,-1/2+Y,2-Z

[4556] = 1/2-X,1/2+Y,1-Z

Ring8: C1-C2-C3-C4-C5-C6

Table S10 Analysis of X-H...Cg(π -Ring) Interactions in **7.**

X--H(I)	Cg(J)	[ARU(J)]	H..Cg	H-Perp	Gamma	C-H..Cg	C..Cg	X-H,π
C(2)-H(2)	->Cg(1)	[1555.01]	2.69	-2.65	9.1	101	3.023(17)	3
C(6)-H(6)	->Cg(15)	[4565.01]	3.00	-2.96	9.13	138	3.758(16)	57
C(12)-H(12)	->Cg(16)	[4565.01]	2.91	-2.83	13.87	142	3.707(18)	59
		Min. or max.	2.690	-2.959	9.1	142.0	3.023	59.0

[1555] = X,Y,Z

[4565] = 1/2+X,1-Y,Z

Ring1: C1-C2-C3-C4-C5-C6

Ring15: C14-C15-C16-C17-C18-C19

Ring16: C20-C21-C22-C23-C24-C25

Table S11 Analysis of X-H...Cg(π -Ring) Interactions in **8.**

X--H(I)	Cg(J)	[ARU(J)]	H..Cg	H-Perp	Gamma	C-H..Cg	C..Cg	X-H,π
C(6)-H(6)	->Cg(1)	[4564.01]	2.88	2.73	18.77	123	3.49(2)	51
C(9)-H(9)	->Cg(2)	[4555.01]	2.86	-2.80	12.04	133	3.57(3)	51
C(12)-H(12)	->Cg(2)	[4564.01]	2.87	2.84	8.02	139	3.64(2)	54
		Min. or max.	2.860	-2.801	8.0	139	3.490	54.0

[4564] = X,1-Y,-1/2+Z

[4555] = X,-Y,1/2+Z

Ring1: C1-C2-C3-C4-C5-C6

Ring2: C7-C8-C9-C10-C11-C12

Table S12 Angles (°) for comparison of octahedral and trigonal prismatic geometry in **7**. Angles between planes of atoms are denoted with plane through atoms / plane through atoms.

<u>Cd-polyhedra with atom numbers</u> (symmetry labels not given)
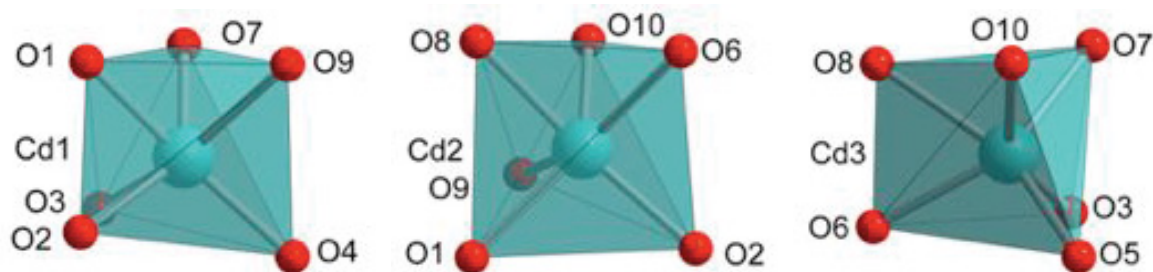
octahedron	trigonal prism	geometric relation	angle	averaged
θ_{ideal}: 54.7	θ_{ideal}: 90	O1 O7^{vii} O9^{xiv} / O4^{iii} Cd1 O9^{xiv}	63.2	
		O1 O7^{vii} O9^{xiv} / O1 Cd1 O2	86.1	<u>71.9</u>
		O1 O7^{vii} O9^{xiv} / O3^{x} Cd1 O7^{vii}	66.3	
		O6 O8^{vi} O10^{xii} / O9^{xii} Cd2 O10^{xii}	68.2	
		O6 O8^{vi} O10^{xii} / O2 Cd2 O6	75.4	<u>77.3</u>
		O6 O8^{vi} O10^{xii} / O1^{x} Cd2 O8^{vi}	88.4	
θ = angle between the mean plane of the two O$_3$ triangles and the chelate planes defined by the metal and each pair of near eclipsed O vertices		O3 O5^{i} O6 / O5 Cd3 O10^{i}	69.1	
		O3 O5^{i} O6 / O3 Cd3 O7^{vi}	79.0	<u>79.1</u>
		O3 O5^{i} O9 / O6 Cd3 O8	89.2	
ρ_{ideal}: 180	ρ_{ideal}: 135.4	O3^{x} Cd1 O9^{xiv}	158.4(3)	
		O4^{iii} Cd1 O1	158.0(3)	<u>151.9</u>
		O7^{vii} Cd1 O2	139.4(3)	
		O2 Cd2 O8^{vi}	157.5(3)	
		O1^{xi} Cd2 O10^{xii}	126.4(3)	<u>141.0</u>
		O6 Cd2 O9^{xii}	139.0(3)	
ρ = angle between the metal and *trans* O-donor sites.		O3 Cd3 O10^{i}	154.6(3)	
		O5^{i} Cd3 O8	144.2(3)	<u>144.4</u>
		O7^{vi} Cd3 O6	134.4(3)	
ω_{ideal}: 180	ω_{ideal}: 120	O1 O2 Cd1 / O4^{iii} O9^{xiv} Cd1	115.8	
		O1 O2 Cd1 / O3^{x} O7^{vii} Cd1	107.2	<u>110.5</u>
		O4^{iii} O9^{xiv} Cd 1 / O3^{x} O7^{vii} Cd1	108.6	
		O2 O6 Cd2 / O1^{x} O8^{vi} Cd2	139.0	
		O2 O6 Cd2 / O9^{xii} O10^{xii} Cd2	119.9	<u>116.5</u>
		O1^{x} O8^{vi} Cd2 / O9^{xii} O10^{xii} Cd2	90.8	
ω = angle between the		O6 O8 Cd3 / O7^{vi} O3 Cd3	114.6	

126

triangular faces defined by the metal and near eclipsed O atoms.	O3 O7^{vi} Cd3 / O5^i O10^i Cd3	115.7	<u>116.7</u>
	O6 O8 Cd3 / O5^i O10^i Cd3	119.9	

Symmetry transformations: i = 1/2-x, y, 1/2+z; ii = 1/2-x, y, -1/2+z; iii = -x, 2-y, 1/2+z; iv = v = -1/2+x, 1-y, z; vi = 1/2+x, 1-y, +z; vii = x, -1+y, z; ix = 1/2+x, 2-y, z; x = -1/2+x, 2-y, z; xii = -x, 1-y, 1/2+z; xiii = 1/2-x, -1+y, -1/2+z; xiv = 1/2-x, 1+y, 1/2+z.

Table S13 Dihedral angles between aryl rings in the biphenyl system and between –COO(H) group and ary rings in **5**-**8**.

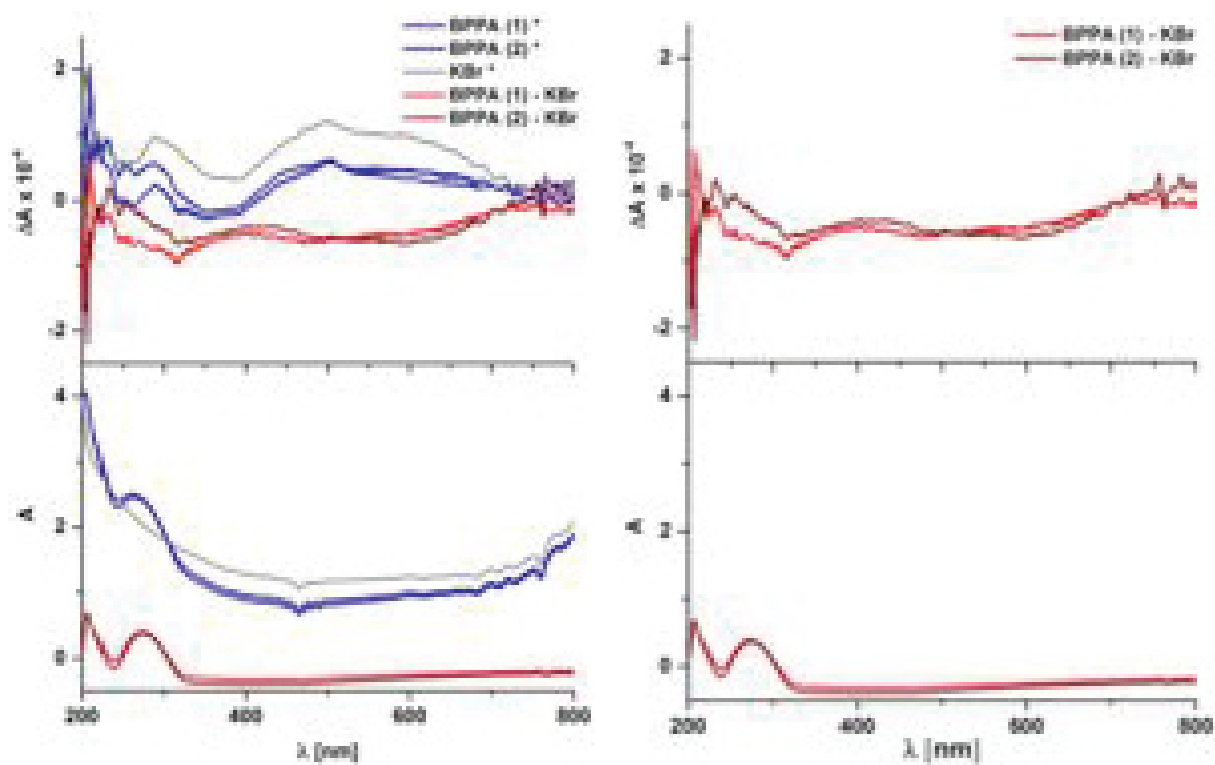|	**5**	**6**	**7**	**8**
Biphenyl, dihedral	0.1(6)	1.5(1)	0.5(2)	2.0(2)
-COO(H) group to benzyl, dihedral	16.3(9)	2(2)	2.0(2)	5.0(4)

Fig. S33. CD-spectra of **5**.
* averaged front- and reverse-side spectra (0.05% w/w of BPPA in KBr pellet)
** in light and dark red depicted the difference spectra (KBr subtracted from BPPA)

3 Unpublished work

The following work is formatted for submission as a publication to an ACS journal. The figures, schemes and tables within are not following the numbering of those of the main thesis text and shall be considered as separated from the main text. Apart form that, the references are following the order of the main text.

3.1 Single crystal-to-single crystal transformations upon solvent exchange and guest removal in a flexible water-stable copper MOF with a mixed-functional pyrazole-carboxylate linker.

Christian Heering, Ishtvan Boldog, Birger Dittrich and Christoph Janiak

Institut für Anorganische Chemie und Strukturchemie, Heinrich-Heine Universität Düsseldorf, Universitätsstraße 1, D-40225 Düsseldorf, Germany.

Abstract

The solvent exchange in the new flexible metal-organic framework $[Cu(HL)_2] \cdot nSolv$ ($1 \cdot nSolv$; Solv = DMF, MeOH, EtOH, *n*-hexane, water) is followed by single crystal-to-single crystal transformations $[Cu(HL)_2]$ is based on the heteroditopic, mixed- or bifunctional 4-(3,5-dimethylpyrazol-4-yl)phenylcarboxylate (HL^-) linker and consists of a three-fold interpenetrated 3D framework with **lvt** topology. The copper(II) carboxylate MOF is stable in MeOH and in water. Compound **1** is thermally stable up to 240 °C and demonstrates single crystal-to-single crystal transformations as a 'breathing' MOF upon solvent substitution from a parent crystal, $[Cu(HL)_2] \cdot 1.25DMF$, by methanol to $[Cu(HL)_2] \cdot 5H_2O \cdot 1MeOH$ and by water to $[Cu(HL)_2] \cdot 9H_2O$ or even degassing to $[Cu(HL)_2] \cdot H_2O$. The

framework adapts to the change in solvent guest molecules and even upon desolvating with retention of crystallinity as confirmed by single crystal and powder X-ray diffraction studies. The maximum shrinkage in unit cell volume from 6532.5(9) $Å^3$ for **1** · 1.25DMF to 4951.2(11) $Å^3$ for **1** · H_2O caused by the 'breathing' effect reaches ~25 % for the desolvated sample $[Cu(HL)_2]$ · H_2O, which is accompanied by H-bond switching from NH···$^-$OOC to NH···O_{Solv} and formation of Cu-O_{solv} bonds, regarded as one of the driving forces of the process. Solvent exchange from **1** · 1.25DMF with *n*-hexane yields the *n*-hexane exchanged crystals, $[Cu(EtOH)(HL)_2Cu(HL)_2]$ · 1.4*n*-hexane (**2** · 1EtOH · 1.4*n*-hexane). Different from the **1** · nSolv structures, **2** · 1EtOH · 1.4*n*-hexane has two crystallographically different Cu centers of which one had undergone a transformation from distorted octahedral (in **1**) to square-pyramidal geometry. Unlike the notable solvent uptake of up to 46 wt% (for methanol), for **1** · H_2O the N_2 sorption is low (S_{BET} = 157 m^2/g) due to small pore openings of the structure in its desolvated state. Consequently the sorption of the smaller H_2 (0.8 wt%, 77 K) and CO_2 molecules (0.7 wt% at 760 Torr, 273 K) is higher and in accordance with the crystallographically found porosity of the desolvated form.

Introduction

Porous coordination polymers (PCPs),[99] alternatively known as metal organic frameworks (MOFs)[100] are a competitively investigated class of porous materials having potential applications[101] such as gas storage,[102,,103] gas[104,105,106] and liquid[107] separation, selective drug delivery,[108,109] heterogeneous catalysis,[110] magnetism[111] and recently water sorption for heat transformation.[112,113,114]

Many of the classical PCPs, like zinc carboxylates such as MOF-5 and the IRMOF-series cannot withstand prolonged contact with water or moisture even at room temperature.[115] HKUST-1 ($Cu_3(BTC)_2$) is intermediate in water stability but eventually decomposes.[112,115] MIL-type compounds, including MIL-100(Fe),[113, 116] MIL-101(Cr),[114, 117 , 118] NH_2-MIL-

101(Cr)[119] as well as Al-fumarate,[120,121] CAU-10-H,[122,123] ZIF-8[124] and in part UiO-66[125,126,127] exhibit higher water stability.[128,129] Their modification and extension within the isoreticular approach is a significant part of research activities in the field.

One of the most hydrolytically stable PCPs, which can withstand boiling in water at a broad pH range except for strongly alkaline conditions, is ZIF-8, [Zn(2-methylimidazolate)$_2$],[124] which owes its stability to its hydrophobicity but also to more covalent, M-N coordination bonds between the 3d metal ion and imidazolate. The same stability is expected with the more versatile pyrazolate PCPs, which are less well investigated, except for the MFU-1 material,[130] an isostructural pyrazolate analogue of MOF-5.

In our recent report, dedicated to complexes of bi- or mixed-functional pyrazolate-carboxylate ligands[131,132] we and other demonstrated the increased water stability of zinc MOFs with mixed-functional 3,5-dimethyl-pyrazolate-4-carboxylate, $^-Me_2pzCO_2^-$ and 4-(3,5-dimethylpyrazolate)phenylcarboxylate, $^-Me_2pzC_6H_4CO_2^-$ linkers compared to the isostructural zinc-benzene-1,4-dicarboxylate MOF-5.

Inspired by these results we also probed the synthesis of copper complexes of these novel bifunctional or mixed pyrazolate-carboxylate ligands to elaborate the possible synergism of the two different donor groups. The apparently water-stable porous copper complex of the short 3,5-dimethylpyrazolate-4-carboxylate linker and its capability to capture small hydrophobic molecules like mustard gas derivatives was described recently.[133,134] The longer, fully deprotonated 4-(3,5-dimethylpyrazolate)phenylcarboxylate linker (L^{2-}, Scheme 1) is known in MOF-5 isoreticular structures with Zn^{2+} and Co^{2+},[131] the mono-deprotonated 4-(3,5-dimethylpyrazol-4-yl)phenylcarboxylate (HL$^-$, Scheme 1) in a hydrogen bonded network with Co^{2+}, in interpenetrated 3D-coordination networks with Zn^{2+} and Co^{2+}, 2D coordination networks with Cd^{2+} and Cu^{2+}, and in a triply polycatenated 2D **lvt** coordination network of Cu^{2+}.[135]
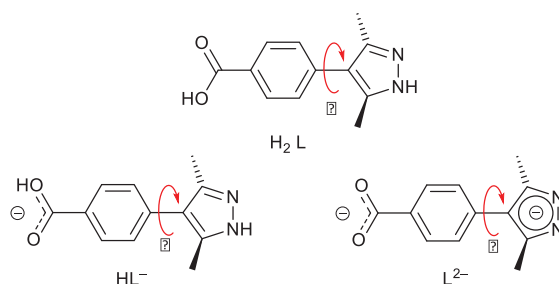
Scheme 1. 4-(3,5-dimethylpyrazol-4-yl)phenylcarboxylic acid, H_2L and its mono- and bis-deprotonated linkers. The φ angle is the dihedral angle between the pyrazolyl and phenylene ring.

The flexibility of some MOFs and their response to solvent exchange or removal is part of the investigation of breathing structures.[136] For example: $[Ln_2(bpydc)_3(H_2O)_3] \cdot nDMF$ (Ln = Nd, Sm, Eu, Gd, Tb, Dy, Ho, and Er), underwent single-crystal-to-single crystal (SC-SC) transformation upon guest removal with a remarkable change of the unit cell volume of 24%.[137] In the diamondoid network, $\{[Zn(pyeb)_2](DMF)(H_2O)\}_n \cdot$ solvent the solvent molecules DMF, acetone and MeCN replace each other within the voids of the structure.[138] In $[Mn(pybimc)_2] \cdot 2H_2O \cdot G$ (G = toluene, THF, pybimc = 2-(2′-pyridyl)-benzimidazole-5-carboxylate) an irreversible SC-SC transformation is triggered by solvent guest exchange.[139] $[Cu_2(L)_2(SO_4)(Br)_2] \cdot H_2O$ (L=4,4'-(1,4-(*trans*-2-butene)diyl)bis(1,2,4-triazole) is a 'breathing' structure upon reversible dehydration.[140] The structure of $[Zn_4O(CPMA)_3] \cdot$ 6DMF showed solvent-induced reversible SC-SC transformation upon guest exchange of DMF with benzene, *n*-hexane and methanol.[141] The 3D networks $\{[Ni_3(\mu_3-btc)_2(\mu_4-btre)_2(\mu-H_2O)_2]\cdot\sim22H_2O\}$ and $\{[Zn_3(\mu_4-btc)_2(\mu_4-btre)(H_2O)_2]\cdot2H_2O\}$ can be dehydrated to $\{[Ni_3(\mu_2-btc)_2(\mu_4-btre)_2(\mu-H_2O)_2(H_2O)_2] \cdot 4H_2O\}$ and $\{[Zn_3(\mu_6-btc)_2(\mu_4-btre)_2] \cdot \sim0.67H_2O\}$ in SC-SC transitions (btre = 1,2-bis(1,2,4-triazol-4-yl)ethane) with the unit cell of the Ni compound reduced to 60%.[142]

In this contribution we report the synthesis, the reversible solvent removal and solvent exchange of the PCP [Cu(HL)₂], and its gas-sorption properties.

Experimental Section

Materials: $Cu(NO_3)_2 \cdot 2.5H_2O$ (99%+, Alfa Aesar), DMF (ACS grade, VWR), anhydrous EtOH, anhydrous MeOH, *n*-hexane (all ACS grade, VWR) were used as received. Water was de-ionized (DI water). The synthesis of 4-(3,5-dimethylpyrazol-4-yl)phenylcarboxylic acid, also named 4-carboxyphenyl-3,5-dimethylpyrazole (H_2L), was done according to our earliear report.[131]

Methods: FT-IR measurements were carried out on a Bruker TENSOR 37 IR spectrometer at ambient temperature in the range of 500 to 4000 cm⁻¹ using an ATR unit (Platinum ATR-QL, diamond window) (abbreviations used: s – strong, m – medium, w – weak, br – broad, sh – shoulder, v- 'very' prefix). Solid state fluorescence spectra were recorded with a Horiba Fluoromax4 with slit openings of 3 nm for both, excitation and emission windows, with an increment of 0.5 nm. Elemental analyses were obtained on a Perkin Elmer CHN 2400 instrument. Thermogravimetric analyses were done under nitrogen on a Netzsch TG 209 F3 Tarsus at 10 K/min heating rate using corundum sample holders. Powder X-ray diffraction (PXRD) measurements were carried out on samples at ambient temperature with a Bruker D2 Phaser using a low-background silicon sample holder and Cu-K_α radiation ($\lambda = 1.54184$ Å) at 30 kV of source voltage and 0.04 °/s scan rate. Simulated powder X-ray diffractograms were obtained from single-crystal data using MERCURY 3.5.1 software.[143] Gas sorption measurements were carried out on an ASAP 2020 automatic sorption analyser (Micromeritics). The freshly synthesized and also the solvent exchanged sample (both yielded the desolvated **1** · H_2O, see details for solvent exchange under syntheses of **1** · xSolv and **2** · 1EtOH · 1.4*n*-hexane, respectively; in detail: up to 10 mg of **1** · 1.25DMF were suspended in at least 10 mL of solvent, with which the solvent exchanged

took place. Stirring at low frequency (1/s) with a magnetic stirring bar for 7 days and replacement with fresh solvent once a day led to the solvent exchanged products) were pre-dried at 10^{-3} Torr at 120 °C for at least 24 h, and then dried at a vacuum of 10^{-8} mbar at 120 °C for 24 h. The gas sorption measurements were performed on 30 mg sample (in activated form). H_2 and N_2 sorption measurements were carried out at 77 K, CO_2 sorption studies at 273 K through cooling with an ice/water mixture.

Synthesis of $[Cu(HL)_2] \cdot DMF \cdot EtOH \cdot 6H_2O$, **1** $\cdot DMF \cdot EtOH \cdot 6H_2O$. A solution of 20 mg (0.092 mmol) of H_2L and 11 mg (0.047 mmol) of $Cu(NO_3)_2 \cdot 2.5H_2O$ in 1.5 mL of absolute ethanol, 0.15 ml of deionized water and 0.15 ml *N,N'*-dimethylformamide (DMF) was sealed in a glass vial with screw cap and heated to 40 °C. Deep blue columnar crystals with sizes up to 0.2x0.2x0.8 mm formed after three days (Fig. 1). Yield: 12.0 mg (21 %). FT-IR (ATR), $\tilde{v}$, cm^{-1}: 3667 (m, br), 2928 (m, br), 1611 (s), 1587 (s), 1530 (m), 1397 (vs), 1398 (vs), 1371 (vs), 1267 (m), 1180 (w), 1059 (w), 1012 (m), 855 (m), 799 (w), 775 (s), 719 (vs), 638 (w), 605 (w), 574 (w) (Fig. S1). Elemental analysis for **1** $\cdot$ 1.25DMF ($C_{27.75}H_{30.75}CuN_{5.25}O_{6.25}$, 583.36 g/mol) calcd C 55.42, H 5.15, N 10.57%; found C 55.25, H 4.24, N 10.83%.

Syntheses of **1** $\cdot$ 5H_2O $\cdot$ 1MeOH, **1** $\cdot$ 9H_2O, desolvated **1** $\cdot$ H_2O and **2** $\cdot$ 1EtOH $\cdot$ 1.4*n*-hexane. The general solvent exchange procedure, which is similar to the one published by Kitagawa *et al*. in 2012,[144] (Scheme 3) was carried out as follows: **1** $\cdot$ 1.25DMF (10.0 mg) was dried in air at 40 °C for 24 h and then gently stirred in 5 mL of solvent S (S = MeOH, H_2O or *n*-hexane) for seven days, being replaced with fresh solvent every 24 hours. The color of the crystals changed from deep blue to purple, yielding 9.0 mg **1** $\cdot$ 5H_2O $\cdot$ 1MeOH (from S = MeOH, Fig. 1B), 8.4 mg **1** $\cdot$ 9H_2O (from S = H_2O) (Fig. 1) and 9.0 mg **2** $\cdot$ 1EtOH $\cdot$ 1.4*n*-hexane (from S = *n*-hexane, Fig. 1). The crystals were stored in the substituted solvent.

Desolvation of 20 mg of **1** · 1.25DMF was performed by heating to 100 °C with evacuating for 48 h at 10^{-6} mbar yielding **1** · H_2O. The crystals turned from purple to greenish turquoise (Fig. 1). The larger crystals fragmented to pieces or cracked several times, but the single-crystal integrity of the smaller crystal fragments was retained (Fig. 1). This behaviour was also described by Bryant *et al*. upon desolvating $[Cu(HL)_2]$ · 4MeOH · H_2O.[135] The crystals were stored under inert gas in case of the desolvated sample. For single-crystal analysis, suitable crystals were selected. **1** · $5H_2O$ · 1MeOH: FT-IR (ATR), $\tilde{v}$, cm^{-1}: 3342 (m, br), 2940(m, br), 2829 (m), 1588 (s), 1528 (s), 1383 (vs), 1311 (w), 1263 (w), 1180 (m), 1104 (w), 1027 (vs), 852 (m), 798 (m), 771 (m), 719 (m), 609 (w), 578 (w) (Fig. S2). **1** · $9H_2O$: FT-IR (ATR), $\tilde{v}$, cm^{-1}: 3353 (vs, vb), 1608 (s), 1525 (s) 1374 (vs), 1265 (m), 1179 (m), 1056 (w), 1011 (m), 865 (br, m), 841 (vs), 794 (vs), 771 (m), 604 (v) (Fig. S3). **1** · H_2O: FT-IR (ATR), $\tilde{v}$, cm^{-1}: 3203 (vbr, sh, w), 2927 (br, w), 1589 (s), 1524 (s), 1372 (vs), 1264 (m), 1177 (s), 1100 (w), 1054 (w), 1011 (s), 867 (w), 843 (m), 795, 771 (s), 716 (s), 607 (w) (Fig. S4). **2** · *n*-hexane: FT-IR (ATR), $\tilde{v}$, cm^{-1}: 2956 (m), 2926(m), 2871 (w), 1609 (s), 1530 (s), 1372 (vs), 1169 (s), 1212 (s), 1180 (m), 1104 (w), 1027 (vs), 857 (s), 771 (m), 719 (vs), 604 (w) (Fig. S5).

For the elemental analyses we note that meaningful elemental analyses of MOFs are difficult to obtain due to solvent loss and different sample states (different states of dryness vs. not dried). We have rationally combined all methods, IR, SQUEEZE data and CHN results to give the most likely solvent content for CHN calculation: **1** · $5H_2O$ · 1MeOH ($C_{25}H_{36}CuN_4O_{11}$, 632.13 gmol^{-1}) calcd: C 47.50, H 5.74, N 8.86; found: C 47.30, H 4.90, N 7.92%.

1 · $9H_2O$ ($C_{24}H_{40}CuN_4O_{13}$, 656.14 gmol^{-1}) calcd: C 43.93; H 6.14; N 8.54; found: C 44.02, H 6.37, N 10.13%.

1 · $1H_2O$ (desolvated) ($C_{24}H_{24}CuN_4O_5$, 513.03 gmol^{-1}) calcd: calcd: C 54.39, H 4.94, N, 10.57; found: C 53.70, H 4.89, N 10.44%.

2 · 1EtOH · 1.4*n*-hexane ($C_{58.4}H_{65.6}Cu_2N_8O_9$, MW = 1041.09 gmol^{-1}) calcd: C 60.87, H 5.88, N 9.72; found: C 61.0, H 4.57, N 11.09%.

Single crystal X-ray structure determination: Suitable crystals (Fig. 1) were chosen with a polarized light microscope and mounted in a perfluorinated oil drop. The diffraction data was collected using a Bruker Kappa APEX2 CCD diffractometer with microfocus source of Cu–Kα radiation (λ = 1.54178 Å) or Mo–Kα radiation (λ = 0.71073 Å) and multi-layer monochromator. The data were collected with a nitrogen gas-stream cooling device at 173 ± 2 K using the APEX2 software[145] for unit-cell determination and data collection. Data reduction was performed by SAINT 8.34A (integration) and SADABS (empirical absorption correction).[146] The structures were solved by dual-space direct methods using SHELXT.[147] Full-matrix least squares refinements on F^2 were carried out with SHELXL-2014/6.[147]

Solvent molecules in the voids of the **1** · nSolv compounds and **2** · *n*-hexane are disordered and it was not possible to locate them precisely. However, the type of solvent could be determined by the found and refined carbon/oxygen/nitrogen atoms and their relative positioning. The most probable solvent localization became evident. In parallel the option SQUEEZE in PLATON[148] was used to better refine the framework structure without the disordered solvent atoms in the voids. Also, SQUEEZE provided a total electron count in the voids by also including non-refined Q-peaks. This total electron count was compared with the number of located solvent molecules (Table 1). In the **1** · nSolv structures only a hydrogen-bonded water oxygen atom remained within the refinement. All non-hydrogen atoms in the **1** · nSolv structures were refined anisotropically. The structure of **2** · *n*-hexane showed twinning by inversion with a batch scale factor of 0.519(6)).

The quality of the structure of **1** · H_2O is low compared with the other structures presented here. Due to removal of solvate molecules the unit-cell volume is reduced and visible cracks on the crystal surface and interior appear (see Figure 1). The structure of **1** · H_2O reveals a solvent-filled and void volume which is much lower than in the other **1** · nSolv structures. Pronounced disorder, especially affecting the pyrazole, is also observed in the structure of **1** · H_2O leading to a high number of alerts in PLATON *Checkcif*. The PXRD patterns of

structure of **1** · H_2O were influenced by the aforementioned problems as well, which can be seen in Figure 6. A similar observation was made by Bryant *et al*. when desolvating crystals of $[Cu(HL)_2]$ · 4MeOH · H_2O to $[Cu(HL)_2]$ · H_2O. From the latter they could obtain a low resolution structure model in monoclinic space group *I2/a* with synchrotron radiation.[135] The problem of poor quality data from desolvated crystals is a known issue and has been described in the literature. In all structures the hydrogen atoms of the CH- or CH_3 groups were positioned geometrically and refined in a riding model (AFIX 43 for NH, AFIX 33 or 137 for CH_3) with $U_{iso}(H) = 1.2U_{eq}(CH, CH_2)$ and $U_{iso}(H) = 1.5U_{eq}(CH_3)$. Graphical material has been prepared using DIAMOND.[149] Crystal structure and refinement details are given in Table 1. The structural data has been deposited with the Cambridge Crystallographic Data Center (CCDC-numbers 1059795-1059798, 1485358).

Table 1. Crystal data and structure refinement for **1** · nSolv, desolvated **1** · H_2O and **2** · 1EtOH · 1.4*n*-hexane (all squeezed data).

Compound	**1** · 1.25DMF	**1** · 5H_2O · 1MeOH	**1** · 9H_2O	**1** · H_2O	**2** · 1EtOH · 1.4C_6H_{14}
Empirical formula	$C_{24}H_{22}CuN_4O_6$ [a]	$C_{24}H_{22}CuN_4O_6$ [a]	$C_{24}H_{22}CuN_4O_4$ [a]	$C_{24}H_{24}CuN_4O_6$	$C_{50}H_{50}Cu_2N_8O_9$
CCDC no.	1059798	1059795	1059796	1485358	1059797
M_r /g mol^{-1}	525.99	525.99	493.99	530.03	1034.06
T /K	173(2)	173(2)	173(2)	173(2)	173(2)
Wavelength / Å	1.54178	0.71073	0.71073	0.71073	0.71073
Crystal system	Tetragonal	Tetragonal	Tetragonal	Tetragonal	Tetragonal
Space group	$I\,4_1/a$	$I\,4_1/a$	$I\,4_1/a$	$I\,4_1/a$	$P\bar{4}$
a /Å	23.5135(15)	22.9623(15)	23.2432(12)	19.2917(19)	23.0848(10)
b /Å	23.5135(15)	22.9623 (15)	23.2432(12)	19.2917(19)	23.0848(10)
c /Å	11.8153(8)	12.0329(8)	11.9130(7)	13.3035(14)	11.9672(6)

V /Å^3	6532.5(9)	6344.5(9)	6436.0(8)	4951.2(11)	6377.4(6)
Z	8	8	8	8	4
Calc. density /g cm^{-3}	1.074	1.101	1.02	1.422	1.077
μ / mm^{-1}	1.24	0.72	0.71	0.93	0.72
F(000)	2184	2168	2040	2200	2144
Reflections collected (R$_{int}$)	23952 (0.034)	31771 (0.027)	48055 (0.0123)	16041 (0.0680)	66346 (0.036)
Independent reflections	2805	8924	3300	969	29767
Max. and min. transmission	0.752/0.378	0.748/0.640	0.745/0.623	0.649/0.744	0.747/0.577
Data / restraints / parameters	2805 / 1 / 166	8927 / 0 / 162	3300 / 0 / 153	969 / 221 / 212	29767 / 0 / 633
Largest diff. peak and hole, eÅ^{-3}	0.43 / -0.31	0.74 / -0.36	0.37 / -0.39	0.40 / -0.39 [d]	1.20 / -0.47
R_1/wR_2 [I>2σ(I)] [b]	0.0390/0.1212	0.0371/0.1008	0.0388/0.1032	0.1510/0.3196	0.0394/0.0916
R_1/wR_2 (all data) [b]	0.0400/0.1221	0.0532/0.1092	0.0414/0.1047	0.1785/0.3362	0.0530/0.0960
Goodness-of-fit on F^2 [c]	1.075	1.022	1.061	1.082	0.994
Squeezed e Å^{-3} [d]	395	453	720	-	550

[a] Largest difference peak and hole. [b] $R_1 = [\sum(||F_o| - |F_c||)/\sum|F_o|]$; $wR_2 = [\sum[w(F_o^2 - F_c^2)^2]/\sum[w(F_o^2)^2]]^{1/2}$. [c] Goodness-of-fit $= [\sum[w(F_o^2 - F_c^2)^2]/(n - p)]^{1/2}$. [d] Void electron count is matched to potential solvent molecules (with consideration of IR and CHN analysis, see above) according to Z x $\sum i$(solvent molecule i electron count x number of solvent molecules i in formula unit). The sum ($\sum i$) is formed over the possible different solvent molecules i. Electron count for solvent molecules i: DMF (C_3H_7NO) 40 e, EtOH 26 e, MeOH 18 e, H_2O 10, n-hexane (C_6H_{14}) 50 e.

For the structures of **1** · 1.25DMF and **1** · 5H$_2$O · 1MeOH one crystal water molecules per formula unit were found and refined, hence, its electron contribution is not included in the void count of electrons.

For the structure of **2** · n-hexane one copper-coordinated ethanol molecule is part of the formula unit.

Results and Discussion

The ligand 4-(3,5-dimethylpyrazol-4-yl)phenylcarboxylic acid, H_2L (Scheme 1), was synthesized through Cu(I) catalysed coupling of 4-iodobenzoic acid and acetyl-acetone with subsequent conversion to the substituted pyrazole by treatment with aqueous hydrazine monohydrate solution.[131] The H_2L ligand is fluorescent in the solid state under excitation with λ_{ex} = 250 nm with an emission maximum of λ_{max} = 370 nm in the UV region (Fig. S7). This in accordance with other substituted benzene derivatives and benzoic acids, which have emission maxima in the region from 290 to 365 nm (in solution).[150] The red shift to 370 nm for H_2L from 330-340 nm for benzoic acid[151] can be assigned to the HMe_2pz- group, which has an electron donating character causing the red shift. In solution H_2L showed no fluorescence presumably due to the non-radiative relaxation caused by free rotation and vibration. Immobilization/rigidification of organic molecules as linkers in a coordination polymer[152] with d^{10} metal ions such as Zn^{2+} and Cd^{2+} can reduce such non-radiative processes and, therefore, lead to emission.[153,154] In the copper compounds **1** · nSolv and **2** · 1EtOH · 1.4n-hexane the emission was quenched due to coordination to a metal ion with unpaired electrons.

Heating of a solution of an excess of copper(II) nitrate and the H_2L ligand in an optimized 10:1:1 solvent mixture of $EtOH/DMF/H_2O$ at 40 °C in a closed vessel afforded deep-blue columnar crystals of **1** · 1.25DMF (Fig. 1). Bryant *et al*. synthesized an analogous complex, $[Cu(HL)_2]$ · 4MeOH · H_2O, from $CuSO_4$ · $5H_2O$ by using methanol as solvent. The isolated complex with the copper-ligand formula of $[Cu(HL)_2]$ contained non-deprotonated pyrazole (see below), as the temperature of synthesis was apparently too low to cause formation of a pyrazolate complex. Our attempt to prepare a [CuL] compound resulted in isolation of $[Cu(HL)_2]$ · nSolv compounds, in which only the carboxylate group is deprotonated. Pyrazole complexes are much weaker coordinated compared to the charge-assisted pyrazolates, but, surprisingly, the isolated **1** · nSolv compounds demonstrated significant

hydrolytic stability as became evident by stirring in water for 7 days for the solvent-to-water exchange and by water vapour sorption measurements (see below). The involvement of NH-pyrazoles is interesting in the context of increased hydrophilicity of otherwise quite hydrophobic PCPs with 3,4-dimethylpyrazolate groups. On the other hand higher synthesis temperatures up to 90 °C did not yield any products in monocrystalline form suitable for single crystal XRD structure determination.
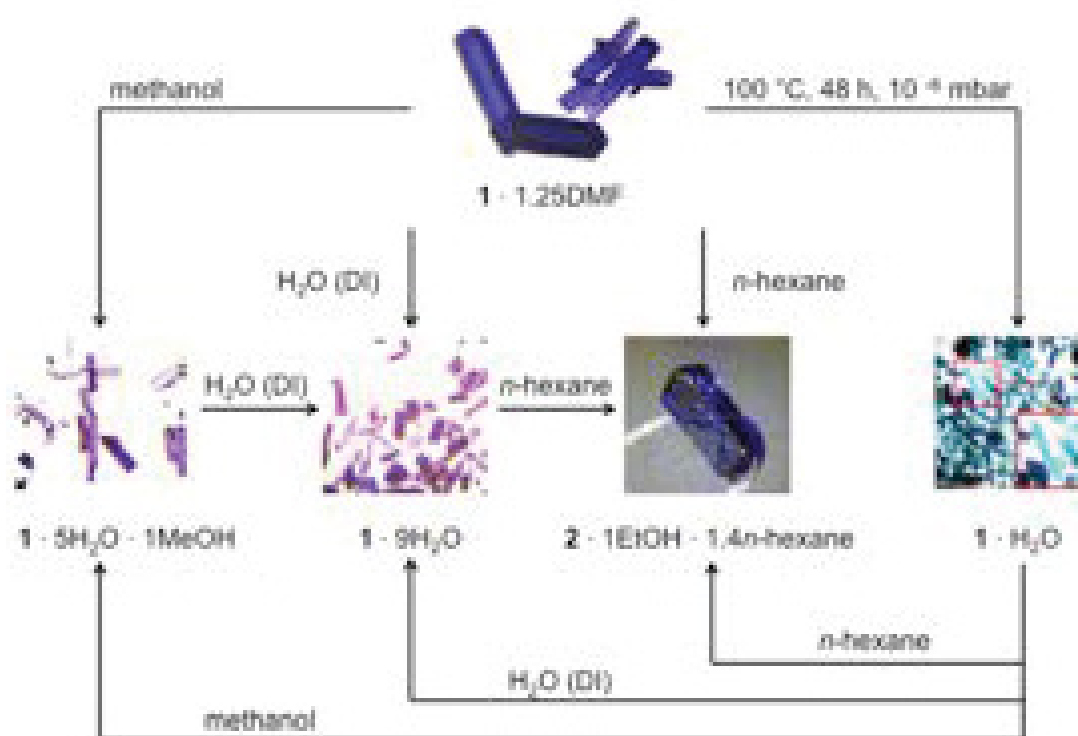

Figure 1. Schematic explanation of the solvent exchange process starting from **1** · 1.25DMF and light microscopy images of crystals of **1** · 1.25DMF, **1** · 5H$_2$O · 1MeOH, **1** · 9H$_2$O, **2** · 1EtOH · 1.4n-hexane and **1** · H$_2$O (desolvated) with zoom (red square) on a selected crystal with visible cracks. The solvent exchange process involved drying of **1** · 1.25DMF at 40 °C in air for 24 h. The crystals were then gently stirred in 5 mL of chosen solvent for seven days, with the solvent replaced every 24 h.

The crystal solvent in the **1** · nSolv compounds can be exchanged with retention of the crystal host structure. Specifically, the exchange of the DMF in **1** · 1.25DMF was carried out at room temperature over 7 days by gently stirring the crystals in the chosen new solvent and replacing the solution with fresh solvent every 24 hours. By this procedure the compounds **1** · 5H_2O · 1MeOH (from stirring in MeOH), **1** · 9H_2O (from stirring in H_2O) and **2** · 1EtOH · 1.4*n*-hexane (from stirring n *n*-hexane) could be obtained (see crystal images in Fig. 1). Also, from **1** · H_2O the structures **1** · 5H_2O · 1MeOH, **1** · 9H_2O and **2** · 1EtOH · 1.4*n*-hexane were obtained from stirring in the corresponding solvents. Successful solvent exchange to the given stoichiometry in **1** · nSolv and **2** · 1EtOH · 1.4*n*-hexane was supported by the electron count of the squeezed electron density (see Table S4 in Supp. Info.), by CHN and IR analyses. The solvent formulation of **1** · 1.25DMF the other **1** · nSolv compounds, of desolvated **1** · H_2O and **2** · 1EtOH · 1.4*n*-hexane was done by combining the evidence from all available measurements, (single crystal X-ray, CHN, TGA and IR), noting that an exact formula cannot be derived by using one method alone. The stated solvent content nSolv in **1** is therefore our most rational proposal that is supported by all techniques that were used to determine the right solvent content. A still missing method is thermogravimetric analysis with mass spectrometric coupling. From IR spectra analyses we found that the solvent exchange took place, as we could prove with an overlay of solvent specific IR-spectra measured by us.

Substitution of solvent takes place in a single crystal-to-single crystal transformation. From continuous observation of the stirred crystals we have no evidence for dissolution and re-crystallization. Storage of minimal amounts (<1 mg) of sample in large volumes of solvent (>20 mL) for weeks did not result in dissolution or re-crystallization of the sample from visual inspection. Furthermore, in freshly synthesized samples the crystals had formed on the glass wall of the reaction vessel, and even after solvent exchange had not moved or appeared dislocated.

In the following structure discussion the term **1** · nSolv includes **1** · 1.25DMF, **1** · 5H$_2$O · 1MeOH, **1** · 9H$_2$O and also [Cu(HL)$_2$] · 4MeOH · H$_2$O[135] but excludes desolvated **1** · H$_2$O. The **1** · nSolv structures with polar guest solvents crystallize in the centrosymmetric tetragonal space group *I* 4$_1$/a. The crystallographically unique Cu(II) ion in **1** · 1.25DMF and in the other **1** · nSolv structures has a centrosymmetric *trans*-{CuN$_2$O$_4$} environment of a Jahn-Teller distorted octahedron (Fig. 2a, b). Two carboxylate groups participate in one short (1.936 Å) and one long (2.765 Å) Cu-O bond each, along with two pyrazole groups for the Cu-N (1.996 Å) coordination bonds (Table 2). This gives rise to an essentially square-planar {CuN$_2$O$_2$} node. The NH-donor of the pyrazole function in the **1** · nSolv structures does not participate in the typical formation of an H-bond with the adjacent carboxylate group of the copper atom, but is bound to an oxygen atom of a water molecule (N-H · O$_{solv}$; 2.82 Å). While the dihedral phenylene-pyrazolyl angle φ (Scheme 1) of 40.2° in the ligand is seen as the torsion energy minimum of H$_2$L,[161] the dihedral angle φ for HL$^-$ in **1** · nSolv structures is between 45-47° (44° in **2** · 1EtOH · 1.4*n*-hexane) (Table S4) which is still close to this energy minimum (energy maxima are estimated at 0° and 90° for φ).

(a)
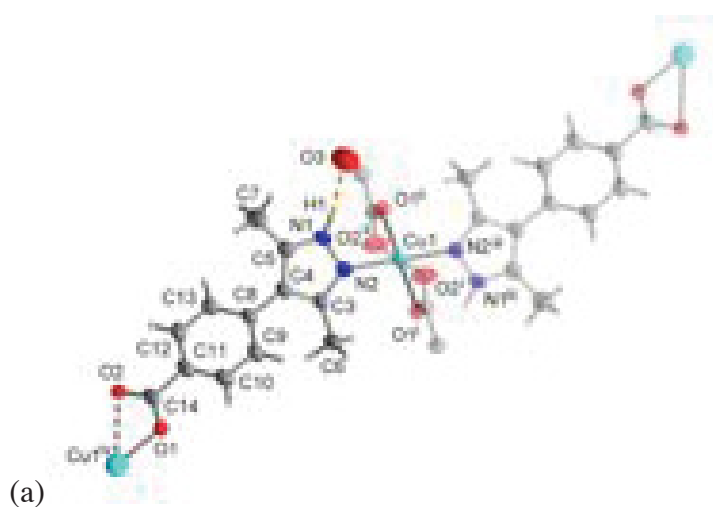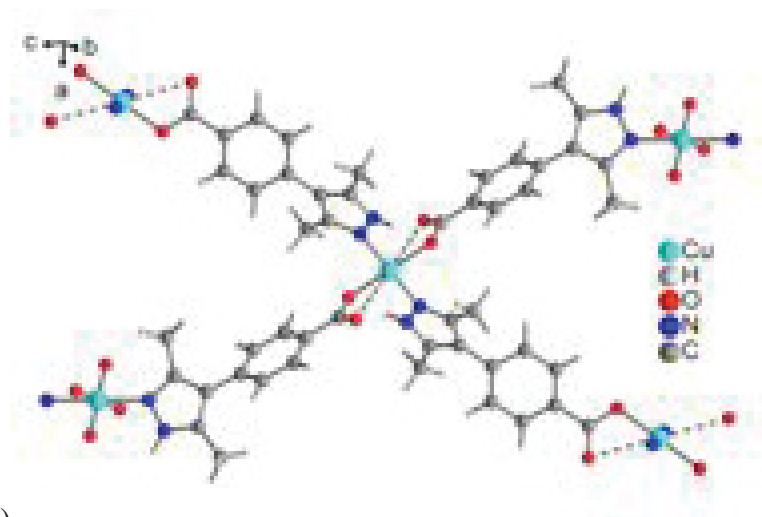
(b)

Figure 2. (a) Extended asymmetric unit showing the Cu coordination sphere (50% thermal ellipsoids, H atoms at arbitrary radii) in the structure of **1** · 1.25DMF (identical to the other **1** · nSolv structures). The symmetry-generated parts are shown with 50% transparency. The hydrogen bond to the crystal water oxygen atom is given as dashed orange line. Symmetry transformation i = y+1/4, -x+3/4, -z+3/4; ii: -y+3/4, x+1/4, z-3/4; iii: -x+1, -y+1, -z; iv: 3/4-y, -1/4+x, 3/4-z. (b) Bridging action of the pyrazolyl-carboxylate ligands between the four-connected Cu atoms. Selected distances and angles are given in Table 2.

In **2** · 1EtOH · 1.4n-hexane a slightly changed structure is observed, though not visible by judging the crystal morphology and violet colour (Fig. 1), which does not change during the solvent-exchange procedure. Yet, a tetragonal primitive $P\bar{4}$ symmetry is observed in **2** · 1EtOH · 1.4n-hexane. The crystal transformation from **1** · 1.25DMF to **2** · 1EtOH · 1.4n-hexane is accompanied by rearrangement of the environment around every second Cu centre (Fig. 3) giving two crystallographically different Cu ions. In **2** · 1EtOH · 1.4n-hexane, an ethanol molecule coordinates to the apical position of a square-pyramidal environment in what now becomes Cu1. The previous elongated Cu···O contacts to the second carboxylate oxygen atoms become even longer. Cu2 retains the same square-planar geometry as seen in the **1** · nSolv structures. The -C_2H_5 tails from the coordinated ethanol molecules point into the cavity, forming a dominantly hydrophobic area (Fig. S15). This adjustment in ethanol coordination to Cu must be seen as a synergistic effect to the incorporation of non-polar n-

hexane, which fills the now non-polar voids as guest molecule. Still, for the Cu nodal topology in the extended network both Cu1 and Cu2 in **2** · 1EtOH · 1.4*n*-hexane have an essentially square-planar configuration.

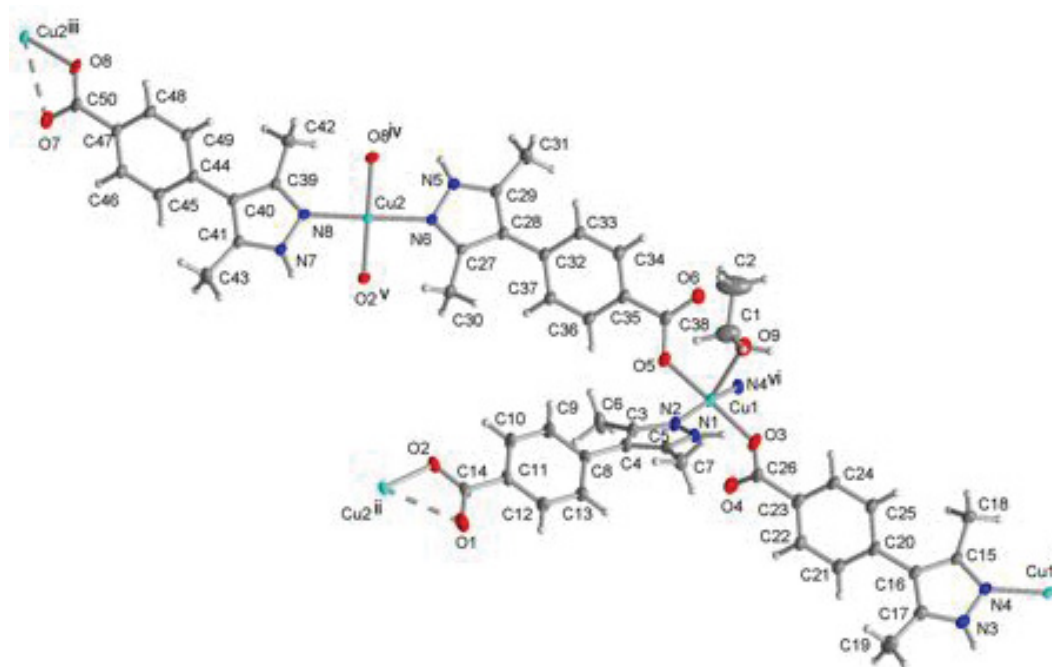**Figure 3.** Extended asymmetric unit of **2** · 1EtOH · 1.4*n*-hexane (50% thermal ellipsoids, H atoms at arbitrary radii). Symmetry transformations: i = -x, y, 3-z; ii = 1-x, -y, z; iii = x, 1-y, -z; iv = 1-x, y, -z; v = 1-x, -y, z; vi = x, -y, 3-z. Detailed view of the square-pyramidal coordination environment of Cu1 in Fig. S15 in Supp. Info. Selected distances and angles are given in Table 2 and in Table S2 in Supp. Info.

Table 1. Selected bond lengths (Å) and angles (°) for **1** · nSolv, **1** · H$_2$O and **2** · 1EtOH · 1.4n-hexane.[a]

Compound	**1** · 1.25DMF	**1** · 5H$_2$O ·1MeOH	**1** · 9H$_2$O	**1** · H$_2$O	**2** · 1EtOH · 1.4n-hexane [b]
Cu1-N2	1.9964(16)	1.9809(7)	1.9858(17)	1.93(2)	1.9897(16) [b]
Cu1-O1^i	1.9356(13)	1.9391(6)	1.9417(14)	1.938(15)	1.9445(14) [b]
Cu1-O2^i	2.765	2.743	2.727	2.140(18)	1.9477(14) [b]
Cu-O(EtOH)	--	--	--	--	2.398(1)
N(-H)···O[c]	2.823(3)	2.7944(14)	[d]	2.80(30)	3.040(2)
N2-Cu1-O1^{ii}	88.48(6)	88.63(3)	88.40(7)	90.7(9)	89.46(6)
O1^i-Cu1-N2	91.53(6)	91.37(3)	91.60(7)	89.6(9)	90.28(6)
N2-Cu1-N2^{iii}	180	180	180(6)	141.3(5)	166.81(7)
O-Cu-O [c]	180(6)	180(3)	180(7)	160.8(9)	178.29(7)

[a] Symmetry transformations: (**1** · nSolv) i: y+1/4, -x+3/4, -z+3/4; ii: -y+3/4, x+1/4, z-3/4; iii: -x+1, -y+1, -z. (**1** · H$_2$O) ii: y+3/4, -x+5/4, -z+1/4; iii: -y+5/4, x-1/4, z+3/4.

[b] For **2** · 1EtOH · 1.4n-hexane average distances are given here in view of the two crystallographically different Cu atoms and four crystallograpically different linkers with a larger number of individual Cu-N and Cu-O contacts. The individual contacts are listed in Table S2 in Supp. Info.

[c] N1-H···O3, O1^i-Cu1-O1^{ii} in **1** · nSolv, except for N1A···O1^{iii}, O1^{ii}-Cu1-O2^{iii} in **1** · H$_2$O; see Table S1 in Supp. Info. for further details on hydrogen bonding interaction to the refined crystal water molecule.

[d] water O atom was not refined but is included in the squeezed electron density.

According to the effectively square-planar coordination environment of the copper atom, the extended framework structures of **1** · nSolv (including [Cu(HL)$_2$] · 4MeOH · H$_2$O)[135] and of **2** · 1EtOH · 1.4n-hexane represent one of the expected topologies for this case, the **lvt** net topology[155,156] (Fig. 3a-c; point symbol: $4^2.8^4$, extended point symbol: $4.4.8_4.8_4.8_8.8_8$).[157] The

overall structures of **1** · nSolv and **2** · *n*-hexane consist of three interpenetrated[158,159] and symmetry-related **lvt** frameworks (Fig. 3d).

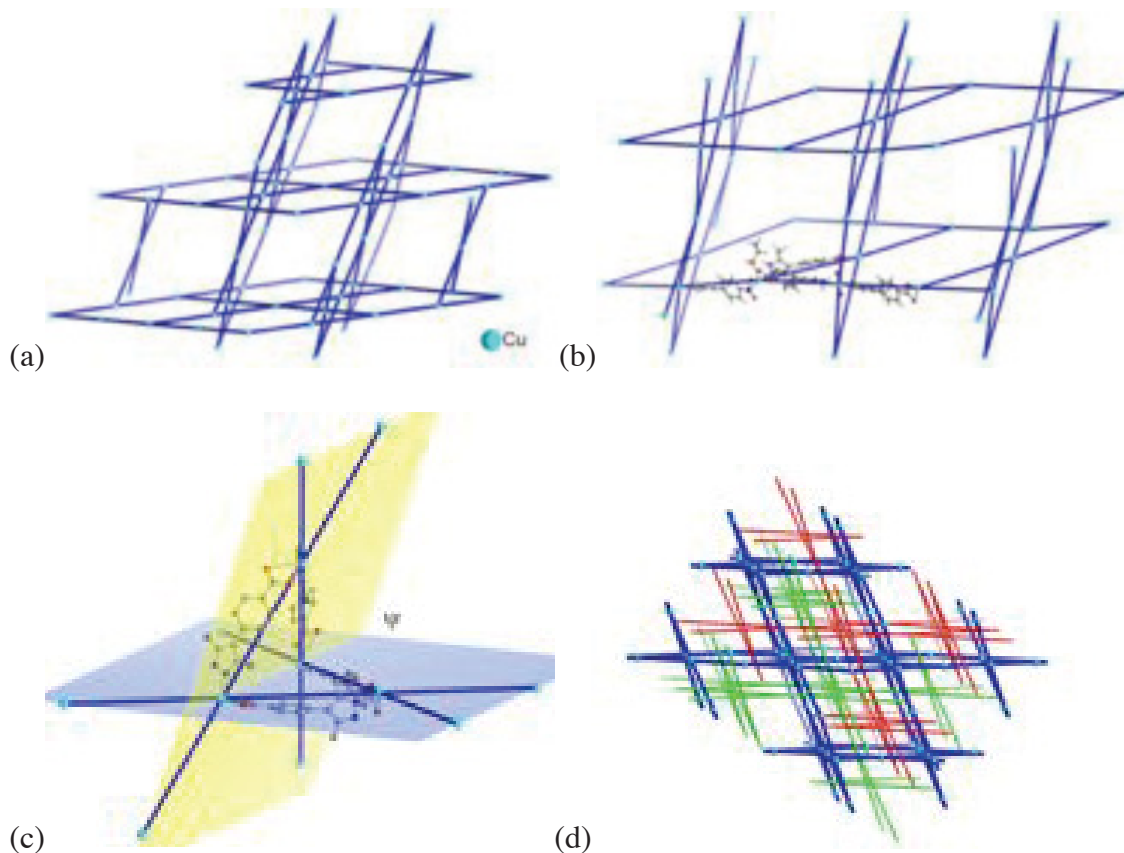**Figure 3.** (a) The Cu-Cu-node connected **lvt** net in **1** · nSolv, with the inclined horizontal and near vertical **sql** rhombic planes. (b) The corrugated **lvt** net **2** · *n*-hexane. (c) Each topological Cu-Cu-connection (Cu-Cu = 12.15 Å) is spanned by an HL^- ligand. Ψ is the acute angle between the sets of tilted rhombic nets crossing each other at their Cu nodes. (d) Triple interpenetration of the **lvt** nets. The drawing of the blue-violet net is enhanced for better visibility.

The **lvt** net in **1** · nSolv can be conceptualized as two sets of symmetry related rhombic nets (**sql**, Fig. 3a,b), which are inclined and intersect each other in the middle of the respective edges. In **2** · 1EtOH · 1.4*n*-hexane the individual rhombic **sql** nets are corrugated

concomittant to the symmetry lowering. The acute angle Ψ between the rhombic net planes (Fig. 3c) lies between 64-67° for **1** · nSolv, except for **1** · H_2O (68.99°) and **2** · *n*-hexane (59°) (Table S4). The **lvt** framework is rather porous (pore openings tend to be ~1.7 times larger compared to pores of a square planar, **sql** net; when taking in account the pore sizes the ratio increases even more), which explains the interpenetration observed in **lvt** nets[160] and also in the **1** · nSolv structures.

For a zinc(II) coordination polymer with HL, [Zn(HL)$_2$] · nSolv [161] a fourfold interpenetrated **dia** net is formed instead of a **lvt** net seen in **1** · nSolv. The reason for this difference is that in [Zn(HL)$_2$] · nSolv a tetrahedral [ZnN$_2$O$_2$] node exists, whereas the square-planar [CuN$_2$O$_2$] node is found in **1** · nSolv.

Despite the threefold interpenetration of the **lvt** nets, there is still substantial solvent accessible inter-framework space (31-39% in the squeezed structures of **1** · nSolv, 35% in **2** · *n*-hexane as calculated by PLATON SQUEEZE, VOID or SOLV, Table S4), which is filled with the determined disordered solvent molecules. Only for the desolvated and contracted structure of **1** · H_2O no solvent accessible void was found anymore. The change in crystal solvent is accompanied by only small adjustment of the unit cell volume, the solvent accessible voids as well as slight changes in the geometry of the copper coordination environment (Table 1 and 2, Table S4, Fig. S14 for comparison of simulated PXRD).

Desolvation of **1** · nSolv to **1** · H_2O leads to pronounced structural changes. However, the crystal space-group symmetry ($I4_1/a$) and the structure organization (Fig. S16 and S17 in Supp. Info.) principally remain the same. Obvious mechanical stress caused by the desolvating procedure influenced the morphology of the crystals with formation of cracks (Fig. 1). In desolvated **1** · H_2O the structure refinement indicates disorder of the Cu atom and the pyrazole ring over two positions (Fig. S18 in Supp. Info.). Still, structure refinement allowed to discuss the following features: Significant contraction of the long axial Cu1-O2

contacts from 2.766(2) Å to 2.14(2) Å occurs and, hence, the color changes from bluish violet to greenish turquoise (Fig. 1), concomitant with a change of the ligand φ angle between the pyrazole and phenylene ring from ~46° to 64° (Scheme 1, Table 3).

The unit-cell volume decreases from ~6340-6530 $Å^3$ for **1** · nSolv to 4951 $Å^3$ for **1** · H_2O (Fig. 4, Table 1 and Table S4 in Supp. Info.), which is in direct relation to edge to edge distance (*d*) across the diagonal of the rhombic openings in the nets. Along the *c* axis this edge to edge diagonal is reduced from 36.2-35.6 Å in **1** · nSolv to 13.6 Å in **1** · H_2O (Table S5 in Supp. Info.).
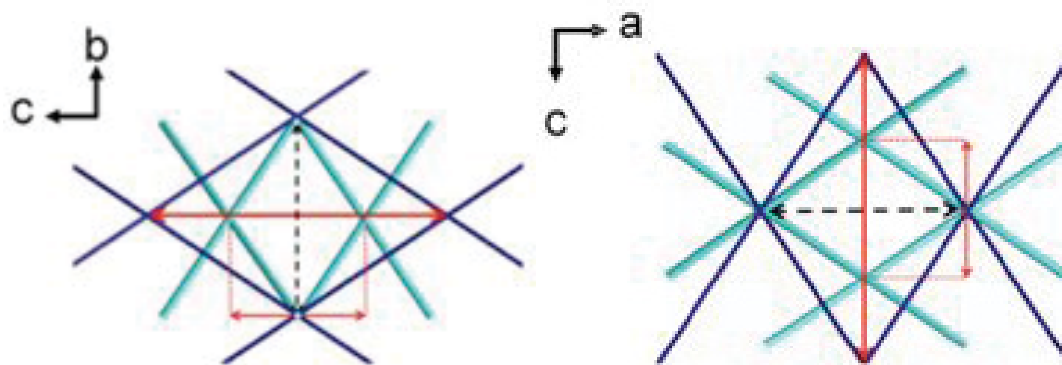
Figure 4. Breathing illustrated by the adjustment in the network between **1** · nSolv (violet blue net) and **1** · H_2O (desolvated, turquoise net) projected on the *bc* and *ac* plane. The reduction of the unit-cell volume in **1** · H_2O is traced to the reduction in the diagonal edge-to-edge distance (red and black arrows) along the *c* axis leading to a contraction of the channels parallel to the *a*- and *b*-axes. (View on unchanged *ab*-plane, channel along *c* axis is given in Fig. S15 and edge-to-edge distances for **1** · $5H_2O$ · 1MeOH, **1** · $9H_2O$ and **2** · hexane in Table S5 in Supp. Info)

Heating compound **1** · 1.25DMF up to ~200 °C in a thermogravimetric analysis leads to removal of DMF, 10.45% (1.25 DMF, 73.09 g/mol = 9%; see Fig. S6 in Supp. Info.). Rapid mass loss of 50% follows in the range from 200 to 400 °C, wherein the complex disintegrates and is finally carbonized.
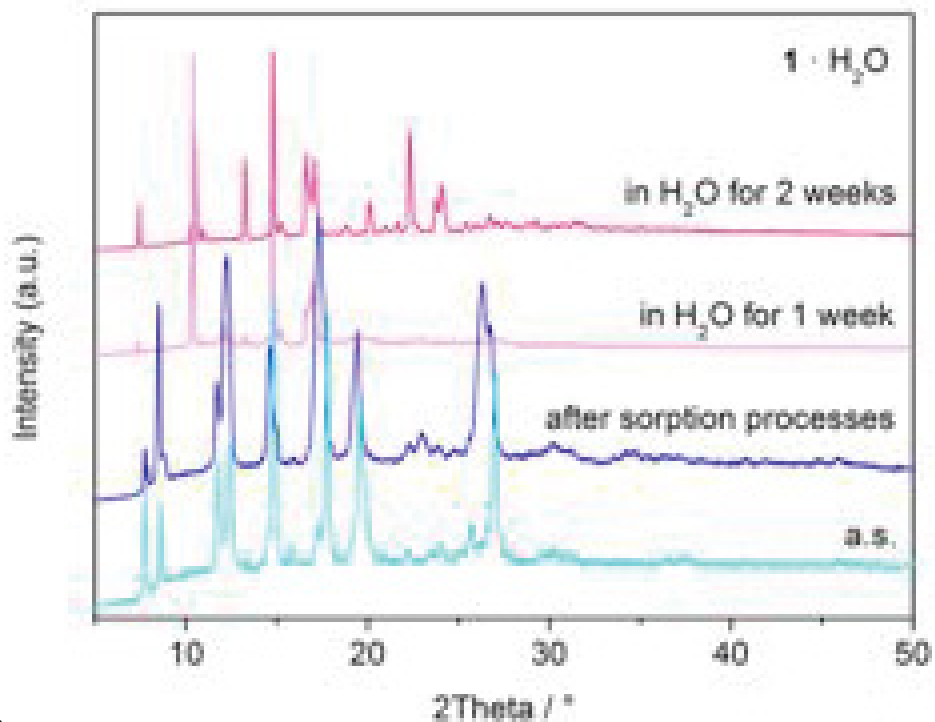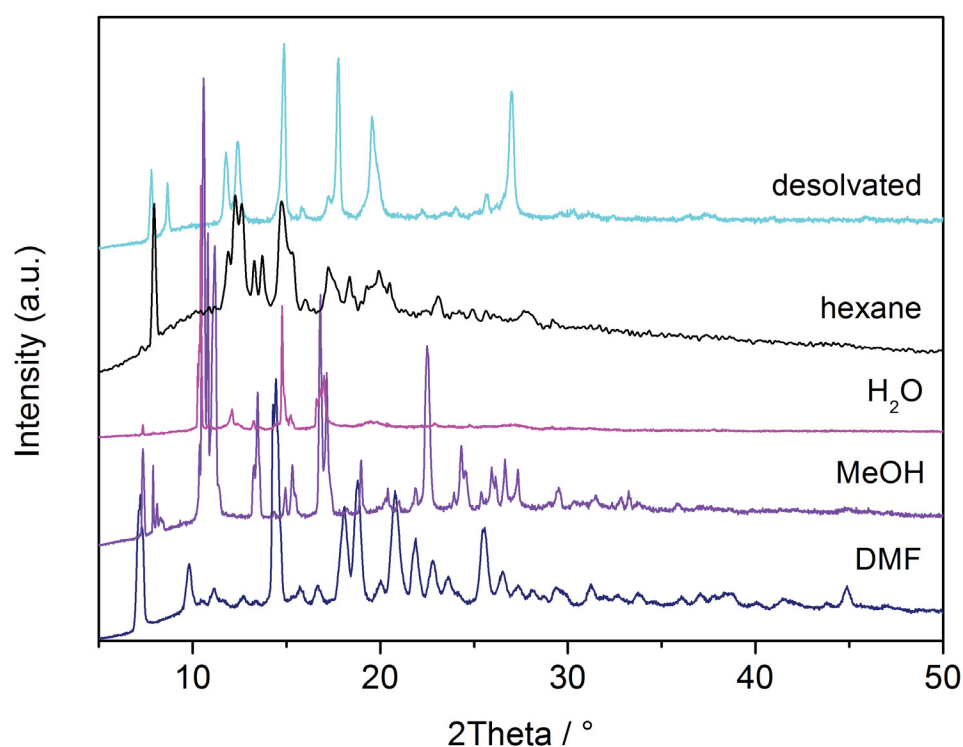
Figure 6. a) Experimental powder diffraction patterns of **1** · H$_2$O (cyan), re-immersed with solvent, after use in sorption experiments and after two weeks storage in water. b) Experimental powder diffraction patterns of **1** · 1.25DMF (dark blue) to **1** · 5H$_2$O · 1MeOH (violet), **1** · 9H$_2$O (pink), **2** · 1EtOH · 1.4*n*-hexane and desolvated **1** · H$_2$O (cyan). The

differences in the experimental diffractograms are due to the different solvent contributions. The simulated diffractograms for the **1** · nSolv structures (except **1** · H_2O) are very similar and reflect the rather unchanged network upon solvent exchange (Fig. S14 in Supp. Info.). (Additional diffractograms and comparison between experimental and simulated pattern in Fig. S9-13 in Supp. Info.)

A reversible uptake of solvent starting with **1** · H_2O in order to 'reload' the desolvated sample was successful. However, because of the mechanical stress during desolvation (see above and Fig. 1), it was not possible to obtain even microcrystals of adequate quality to prove the isostructural nature to other **1** · nSolv samples by means of PXRD and other techniques. We were only able to select a few crystals, which showed similar unit cell dimensions as the 'mother' crystals after the solvent uptake procedure that is immersion of **1** · H_2O into the solvent. Therefore, we can assume that a reversible solvent uptake process is indeed possible..

The sorption properties of the activated compound **1** · 1.25DMF (activation was carried out by drying **1** · 1.25DMF for 48h at 100 °C and at 10^{-6} bar using the degassing port of a Quantachrome NOVA sorption apparatus) against gases were investigated for N_2 (Fig. 8), H_2, CO_2 and water vapors (Fig. S6-8 in Supp. Info.). Small pore openings (Fig. 7) and the possibly flexible threefold interpenetration in **1** do not allow effective N_2 sorption (~55 cm^3 N_2(STP), P/P$_0$~0.95, 77 K), which corresponds to the observed surface area (BET) of 157 m^2/g. At cryogenic temperature of 77 K diffusion of N_2 molecules into small micropores is very slow. Diffusion limitations at this temperature influence adsorption in ultramicropores (pores smaller than 7 Å diameter). Such materials then require time-consuming N_2 adsorption measurements and may still have under-equilibration of measured adsorption isotherms, which will give lower than real surface areas. Such errors can be avoided by

using CO_2 adsorption analysis at 273 K. The saturation pressure of CO_2 at 0 °C is very high (~26141 Torr), so that low relative pressure measurements for the micropore analysis are achieved in the range of moderate absolute pressures (1–760 Torr). At 273 K CO_2 molecules can more easily access ultramicropores than N_2 at 77 K. The kinetic diameter of CO_2 (3.3 Å) is also slightly smaller than for N_2 (3.64 Å). Thus micropore analysis by CO_2 sorption at 273 K is advantageous over N_2 analysis at 77 K because (i) faster analysis and (ii) better adsorption point equilibration (both due to higher diffusion rates) and (iii) extension of the pore analysis to smaller sizes that are accessible to CO_2 molecules but not to N_2.[162]
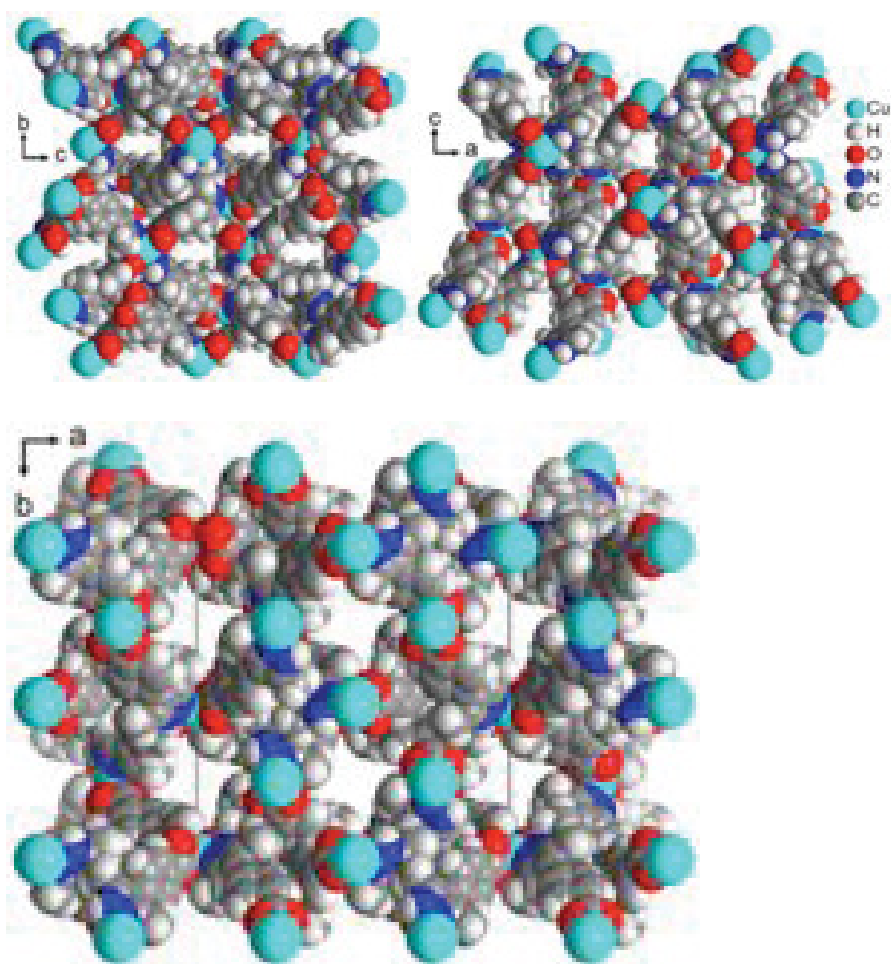
Figure 7. Projections of the packing diagrams in space-filling mode on the three different planes for the full, three-fold interpenetrated network of **1** · 1.25DMF to illustrate the small channel cross-sections of ~2.5 Å x 4 Å along *b* and *c* and of 3.7 Å x 3.7 Å along *c*.

H_2, having a smaller kinetic diameter (2.9 Å), as well as CO_2, with its higher mobility at 273 K could enter in the pores. The uptake of H_2 (~90 cm^3/g, or 0.8 wt% at 77 K) and CO_2 (~80 cm^3/g, 0.7 wt% or 3.6 mmol/g, 273.15 K) at 1 bar corresponds to the expectation from the potential void volume in **1** · nSolv.

It is interesting to note that desolvated **1** · H_2O represents a densely packed structure (Fig. S19 in Supp. Info) for which no gas sorption would be expected. The low N_2 sorption supports the formation dense structure of **1** · H_2O. The significant uptake values for hydrogen and CO_2 than reflect flexibility or breathing of the framework. The weak N-H⸱⸱O$_2$C$_{(gas)}$ interactions might contribute to the CO_2 uptake.
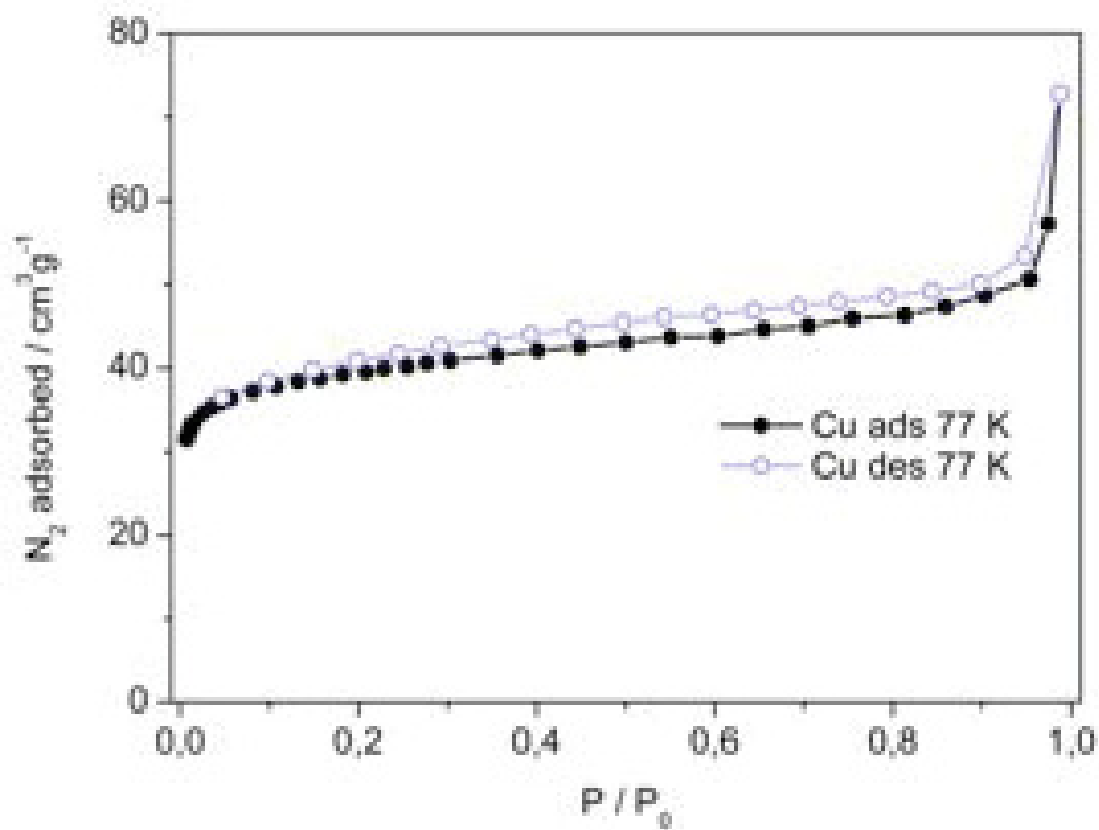
Figure 8. Nitrogen sorption isotherms for [Cu(HL)$_2$], **1**, at 77 K.

Conclusions

The hydrolytic and thermal stability of the reported copper(II) compound [Cu(HL)$_2$] with the mixed- or bifunctional 4-(3,5-dimethylpyrazol-4-yl)phenylcarboxylate (HL⁻) linker demonstrates the somewhat underestimated potential of this mixed-functinonal pyrazolyl-carboxylate linkers. While the initial goal to isolate a pyrazolate-carboxylate compound failed, the presence of an NH group on the non-deprotonated pyrazole endows the complex with increased hydrophilicity. Compound [Cu(HL)$_2$] crystallizes as a 3D triply-interpenetrated network of **lvt** topology. The incorporated solvent molecules (DMF and H$_2$O) can be exchanged with methanol, water and hexane or removed almost completely (desolvated) under retention of the single crystallinity and network topology. The observed reversible single-to-single crystal transformation, during which the cell volume remains rather constant during exchange but decreases from ~6340-6532 Å^3 to 4951 Å^3 upon desolvation is due to a framework flexibility or breathing property., Similar long pyrazolyl-carboxylate ligands could also be efficient in the context of induced framework flexibility of porous solids, which are of increasing interest.[163] The adoption of a different coordination environment due to guest exchange was shown in the case of *n*-hexane as solvent, where a response of the network from polar towards non-polar guests was observed and discussed.

Associated content

IR spectra, thermogravimetric and gas sorption data. Single crystal X-ray data has been deposited as CCDC deposition numbers 1059795-1059798 and 1485358 with the Cambridge Crystallographic Data Centre from which it can be obtained upon request at www.ccdc. cam.ac.uk/data_request/cif.

Supporting Information. A document containing CHN analyses, IR-spectra, TGA analysis, PXRD diffractograms, sorption isotherms for H_2, CO_2 and H_2O vapor, structure graphics and tables and geometry calculations are available free of charge.

Corresponding Author

*E-mail: janiak@hhu.de

Institut für Anorganische Chemie und Strukturchemie, Heinrich-Heine Universität Düsseldorf, Universitätsstraße 1, D-40225 Düsseldorf, Germany.

Graphical abstract:
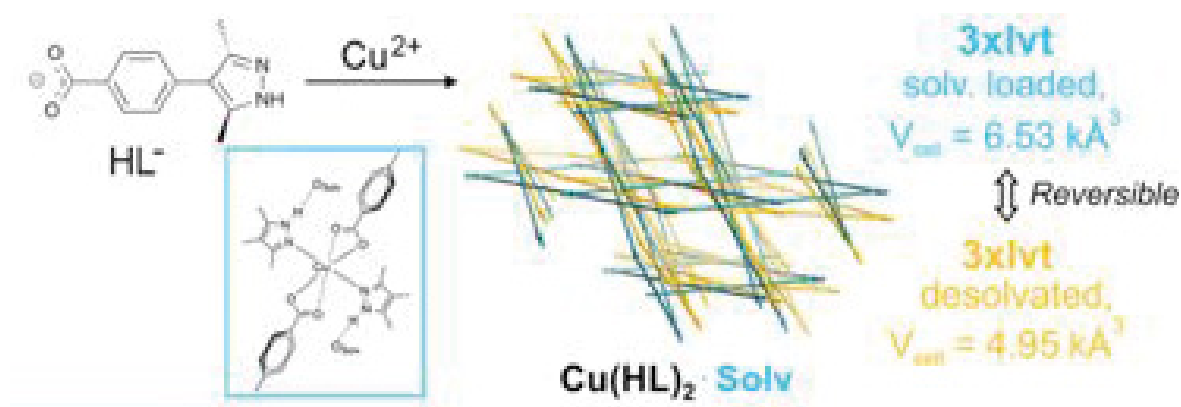
3.2   Supporting Information

Single crystal-to-single crystal transformations upon solvent exchange and guest removal in a flexible water-stable copper MOF with a mixed-functional pyrazole-carboxylate linker.

Christian Heering, Ishtvan Boldog, Birger Dittrich and Christoph Janiak*

a Institut für Anorganische Chemie und Strukturchemie, Heinrich-Heine Universität Düsseldorf, Universitätsstraße 1, D-40225 Düsseldorf, Germany.

*E-mail: janiak@hhu.de
christian.heering@hhu.de
birger.dittrich@hhu.de
ishtvan.boldog@gmail.com

Elemental analyses data

We note, that meaningful elemental analyses of porous compounds with exceptional large voids are difficult to obtain due to solvent loss and different sample states (different volatilities of the used solvents, partial solvent loss, i.e., partial dryness during sample preparation before weighing for elemental analysis). Even a total removal or replacement of guest molecules could not be reached because of physical limits. Therefore, we give the detailed analysis data for all compounds and the measured EA. A reasonable proposed composition is given, in accordance with structural data.

1 (theoretical structure without solvents) $C_{24}H_{22}CuN_4O_4$, 494.01 g/mol) calcd: C 58.35; H 4.49; N 11.34%

1 · 1.25DMF ($C_{27.75}H_{30.75}CuN_{5.25}O_{6.25}$, 583.36 g/mol) calcd: C 55.42, H 5.15, N 10.57; found: C 55.25, H 4.24, N 10.83%.

1 · 5H$_2$O · 1MeOH ($C_{25}H_{38}CuN_4O_{11}$, 634.14 gmol^{-1}) calcd: C 47.35, H 6.04, N 8.84; found: C 47.30, H 4.90, N 7.92%.

1 · 9H$_2$O ($C_{24}H_{40}CuN_4O_{13}$, 656.14 gmol^{-1}) calcd: C 43.93; H 6.14; N 8.54; found: C 44.02, H 6.37, N 10.13%.

1 · H$_2$O (desolvated) ($C_{24}H_{24}CuN_4O_5$, 513.03 gmol^{-1}) calcd: C 54.39, H 4.94, N, 10.57; found: C 53.70, H 4.89, N 10.44%.

2 · 1EtOH · 1.4*n*-hexane ($C_{58.4}H_{65.6}Cu_2N_8O_9$, MW = 1041.09 gmol^{-1}) calcd: C 60.87, H 5.88, N 9.72; found: C 61.0, H 4.57, N 11.09%.
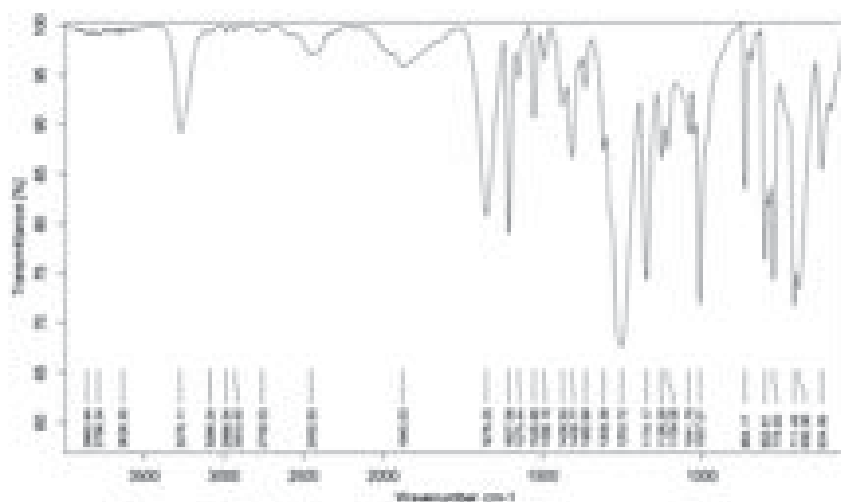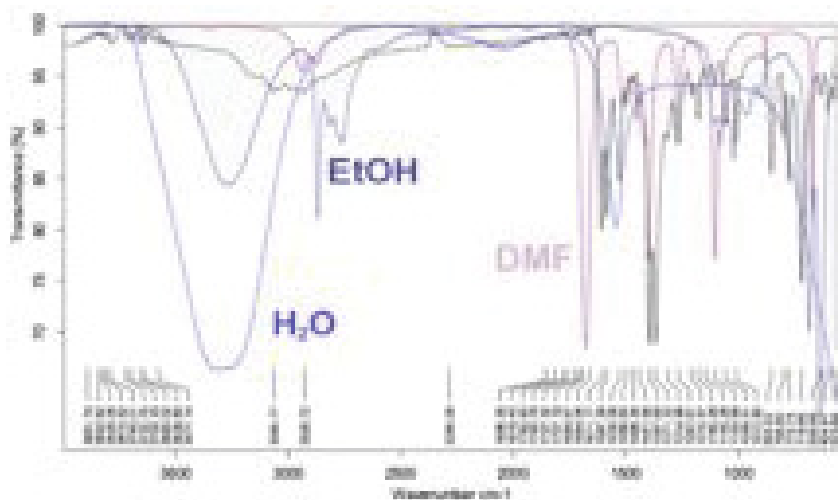
IR spectra

Figure S0 IR-spectrum (ATR) of H$_2$L.
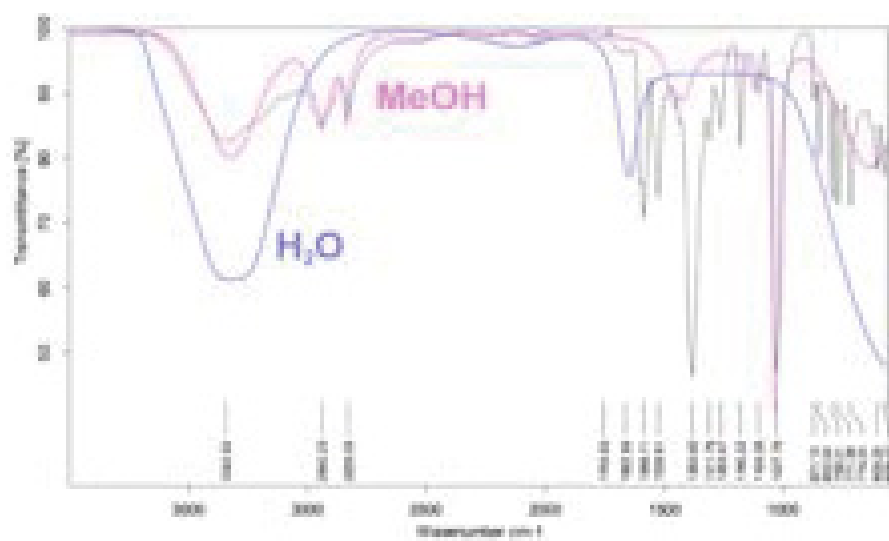
Figure S1 IR spectrum (ATR) of **1** · 1.25DMF

Figure S2. IR spectrum (ATR) of **1** · 5H$_2$O · 1MeOH.
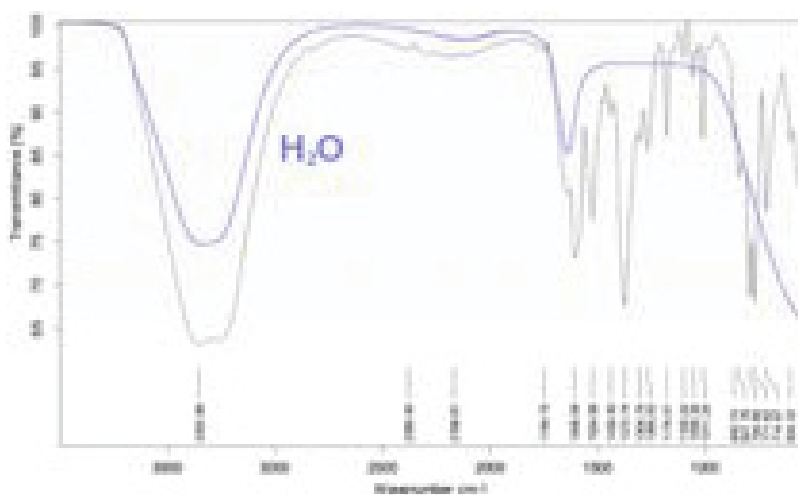
Figure S3. IR spectrum (ATR) of **1** · 9H$_2$O.
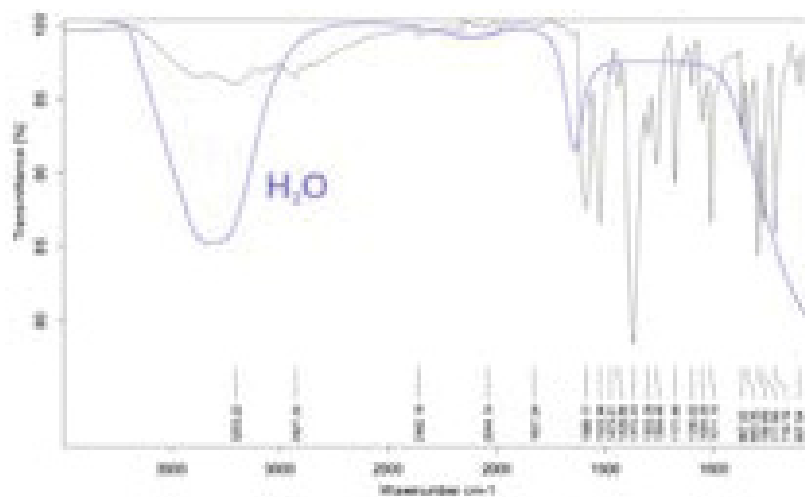
Figure S4. IR spectrum (ATR) of desolvated **1** · 1H$_2$O.
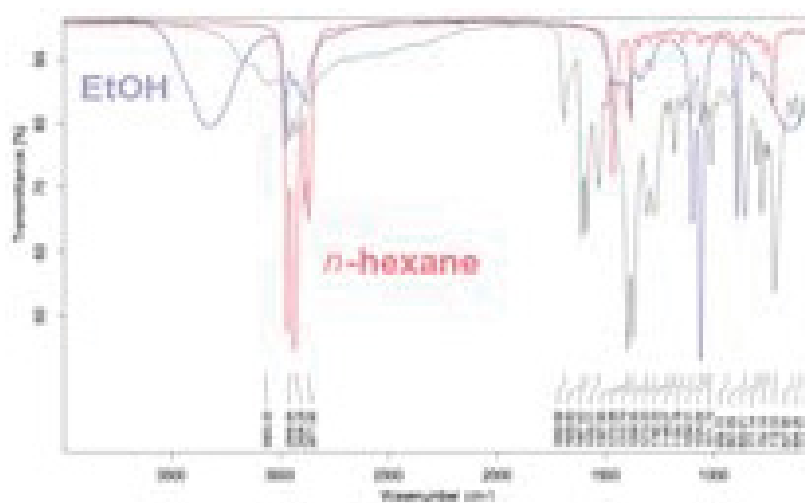
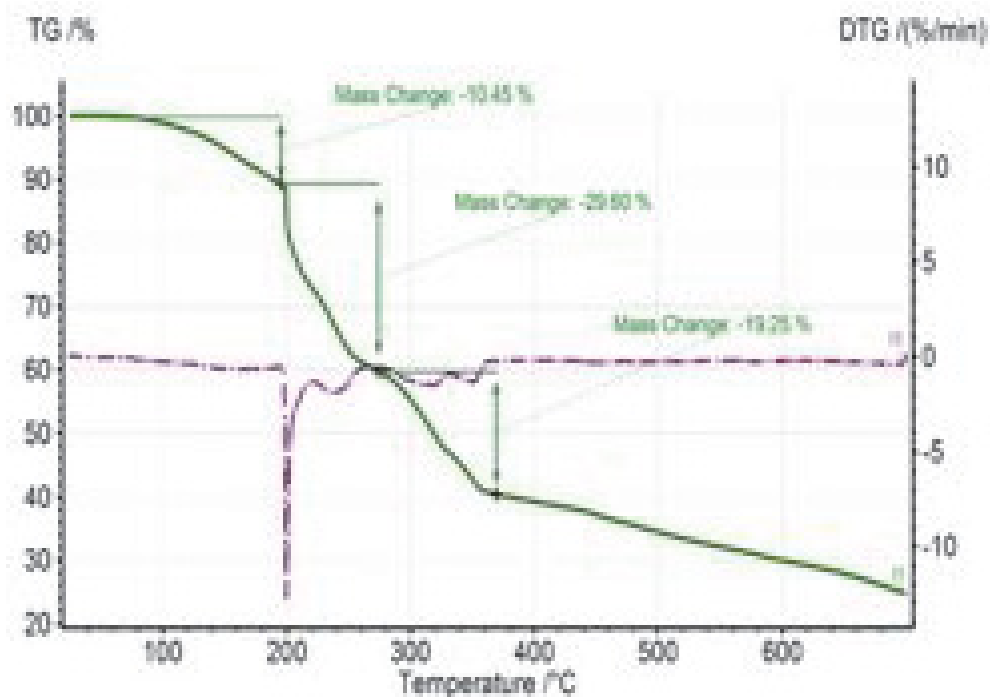**Figure S5.** IR spectrum of **2** · 1EtOH · 1.4*n*-hexane.

TGA

Figure S6. TG/DTG of **1** · 1.25DMF. (10.45% correspond to 1.25 DMF; MW = 73.09, 9%)
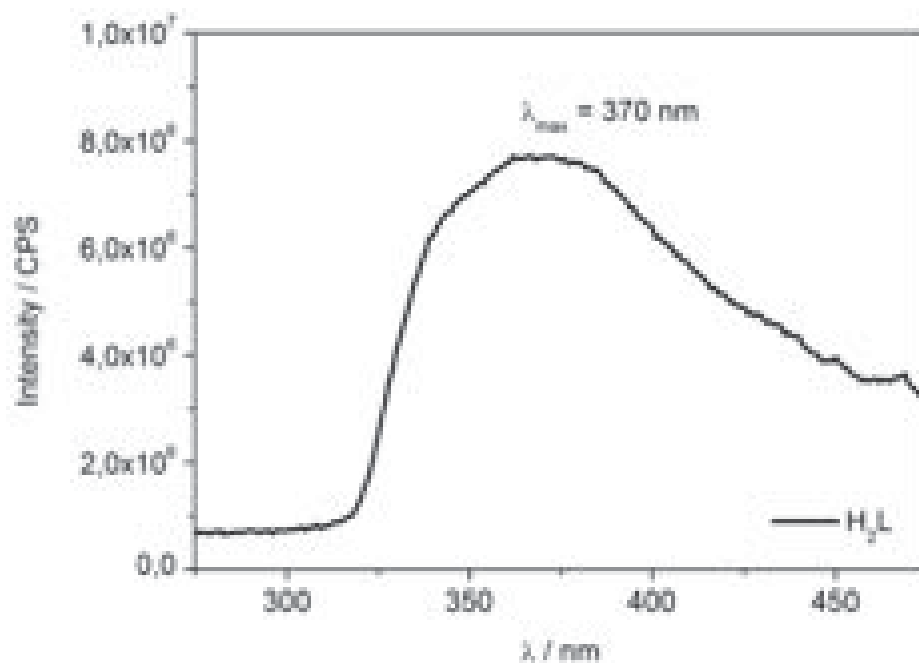

Figure S7. Fluorescence emission spectrum of H_2L at λ_{ex} = 250 nm.

Sorption measurements

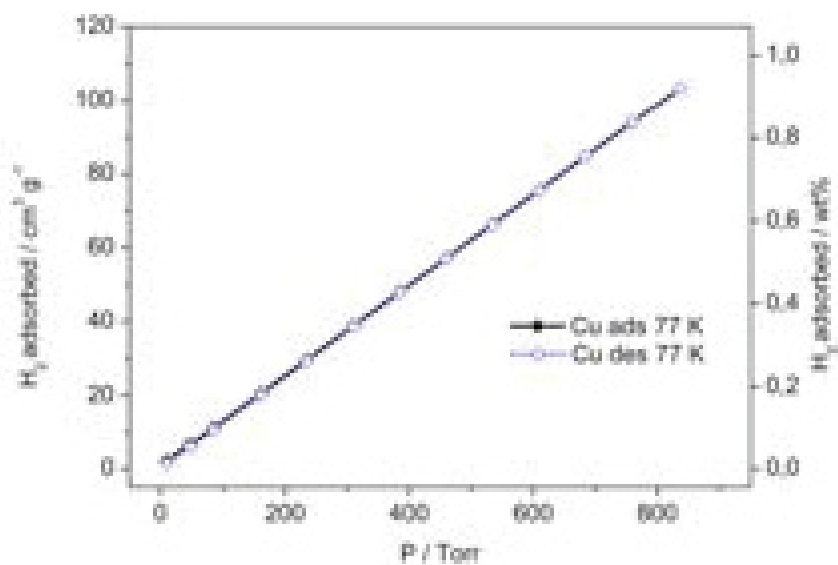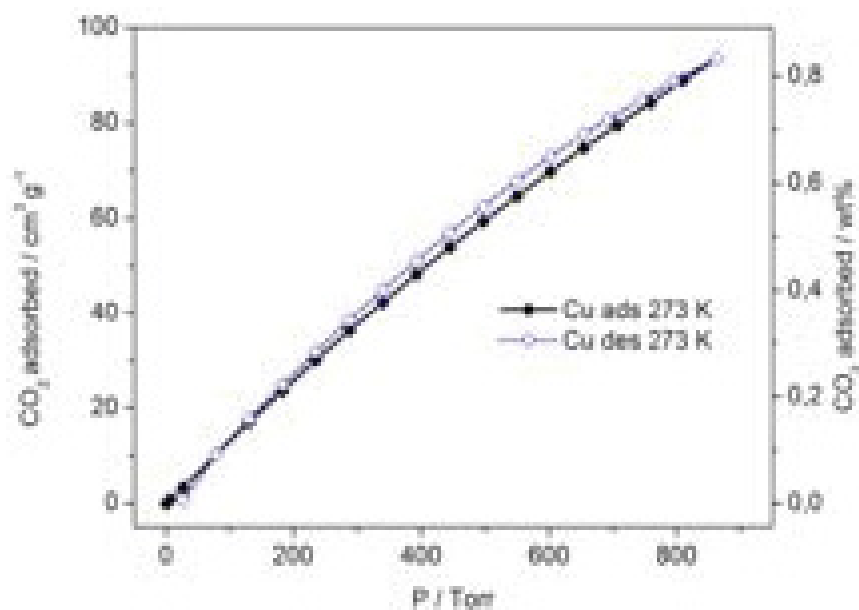**Figure S8.1.** Hydrogen adsorption isotherms for **1** · H_2O at 77 K.

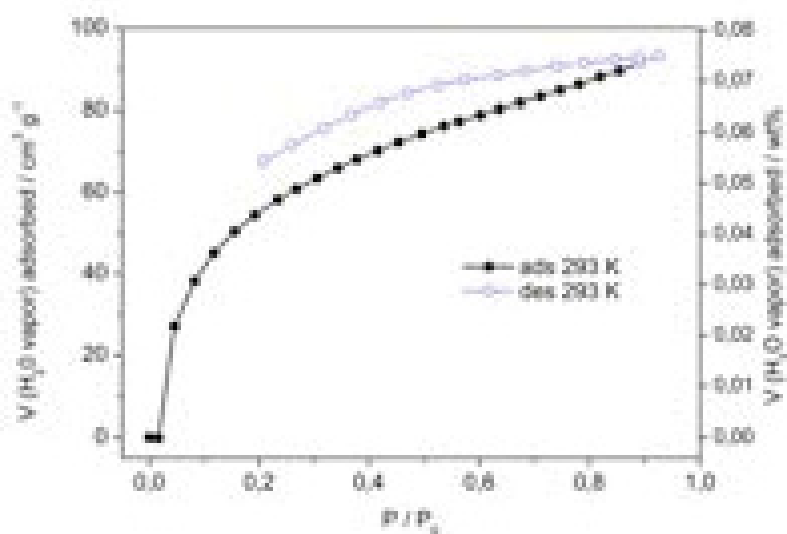**Figure S8.2.** Carbon dioxide adsorption isotherms for **1** · H_2O at 273 K.

Figure S8.3. Water vapor adsorption isotherms for **1** · H_2O at 293 K.

Powder X-ray diffraction
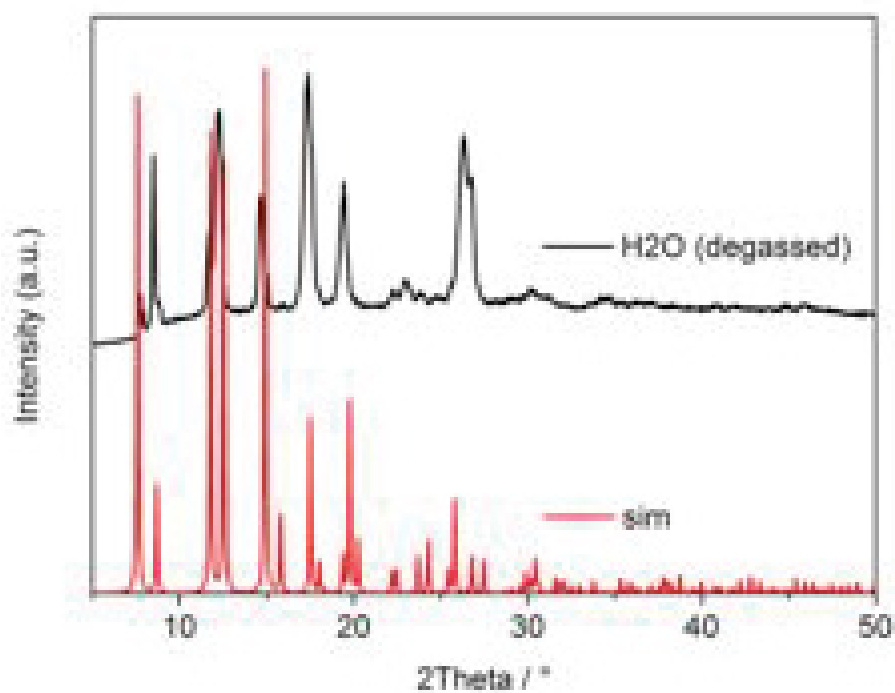
Figure S9. Experimental powder patterns for desolvated **1** · H_2O (black) and simulated pattern from SCXRD measurement (red).
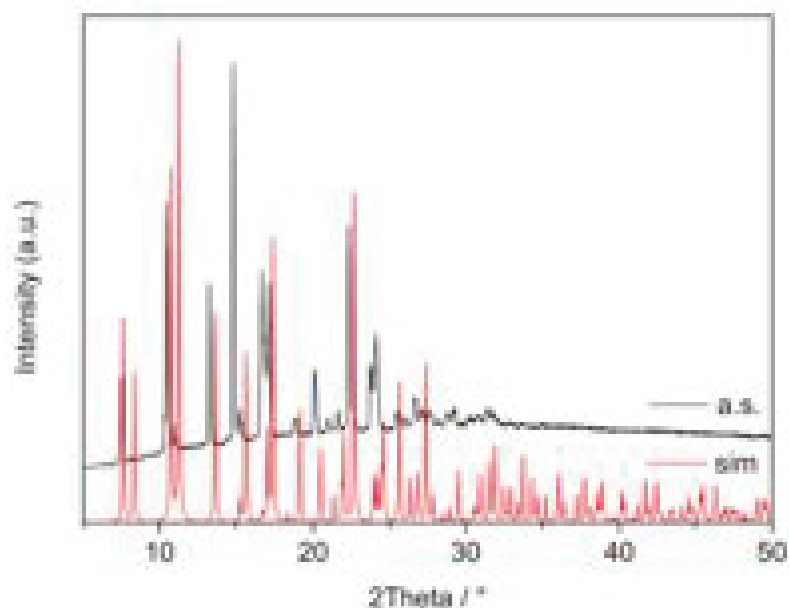
Figure S10. Experimental powder patterns for **1** · 9H$_2$O (as synthesized, black) and simulated pattern from SCXRD measurement (red). Note that the simulation is based on the refined network where the solvent contribution was removed by PLATON SQUEEZE, hence, a deviation between the experimental (with solvent) and simulated (without solvent) pattern is expected.

Figure S11. Experimental powder patterns for **1** · 5H$_2$O · 1MeOH (black) and simulated pattern from SCXRD measurement (red). Note that the simulation is based on the refined network where the solvent contribution was removed by PLATON SQUEEZE, hence, a deviation between the experimental (with solvent) and simulated (without solvent) pattern is expected.

Figure S12. Experimental powder patterns for **1** · 1.25DMF (black) and simulated pattern from SCXRD measurement (red). Note that the simulation is based on the refined network where the solvent contribution was removed by PLATON SQUEEZE, hence, a deviation between the experimental (with solvent) and simulated (without solvent) pattern is expected.
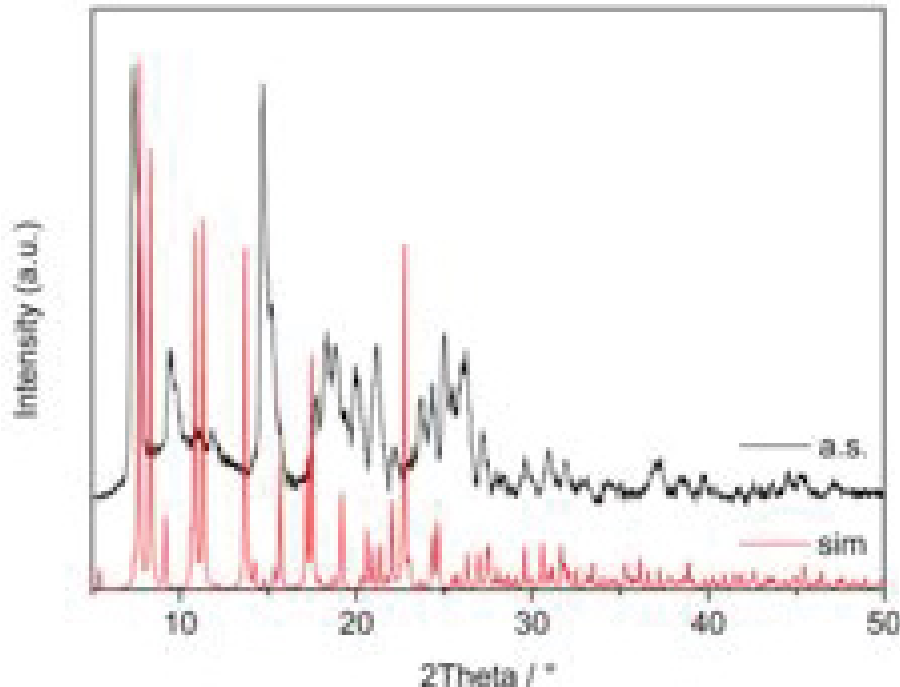
Figure S13. Experimental powder patterns for **2** · 1EtOH · 1.4*n*-hexane (black) and simulated pattern from SCXRD measurement (red). Note that the simulation is based on the refined network where the solvent contribution was removed by PLATON SQUEEZE, hence, a deviation between the experimental (with solvent) and simulated (without solvent) pattern is expected.
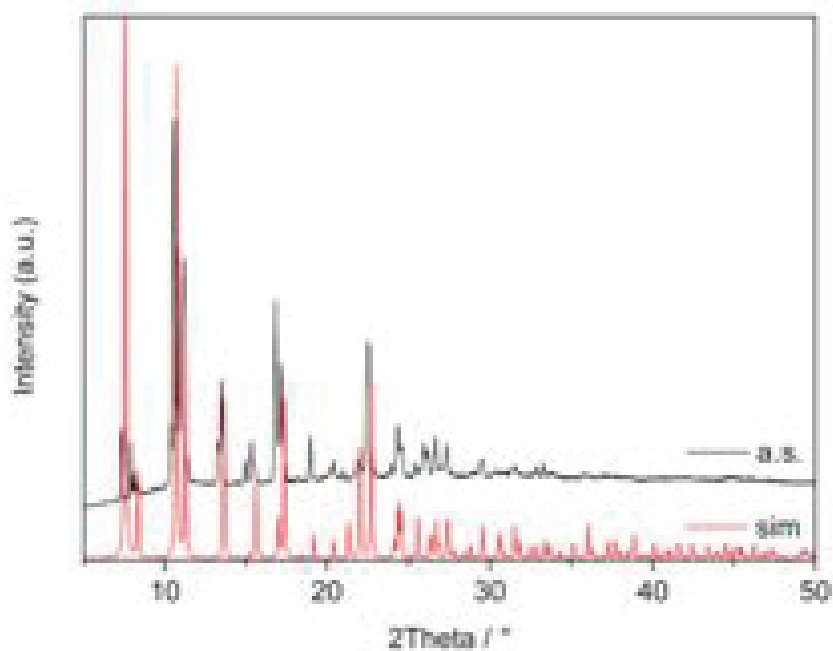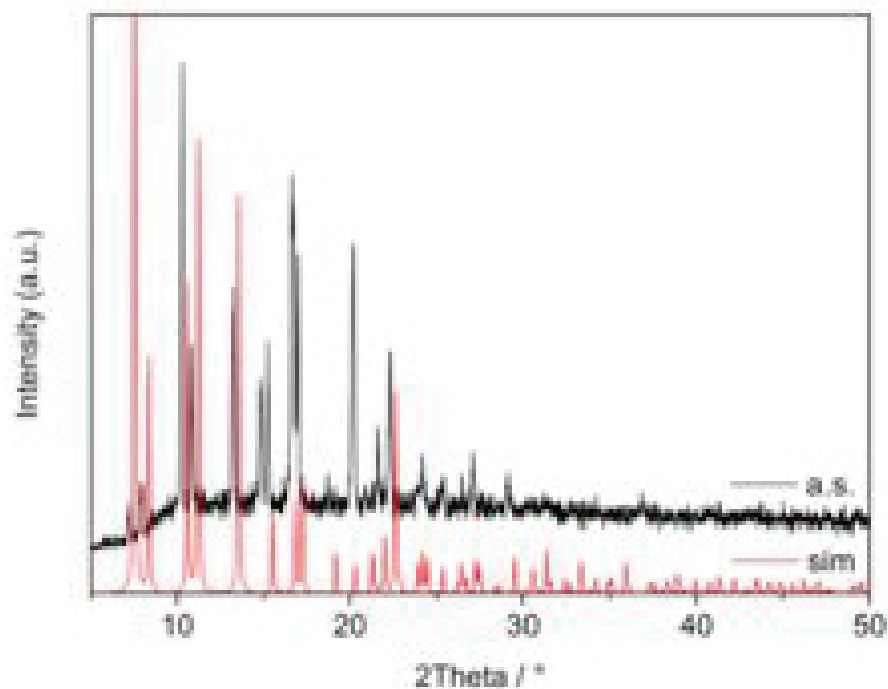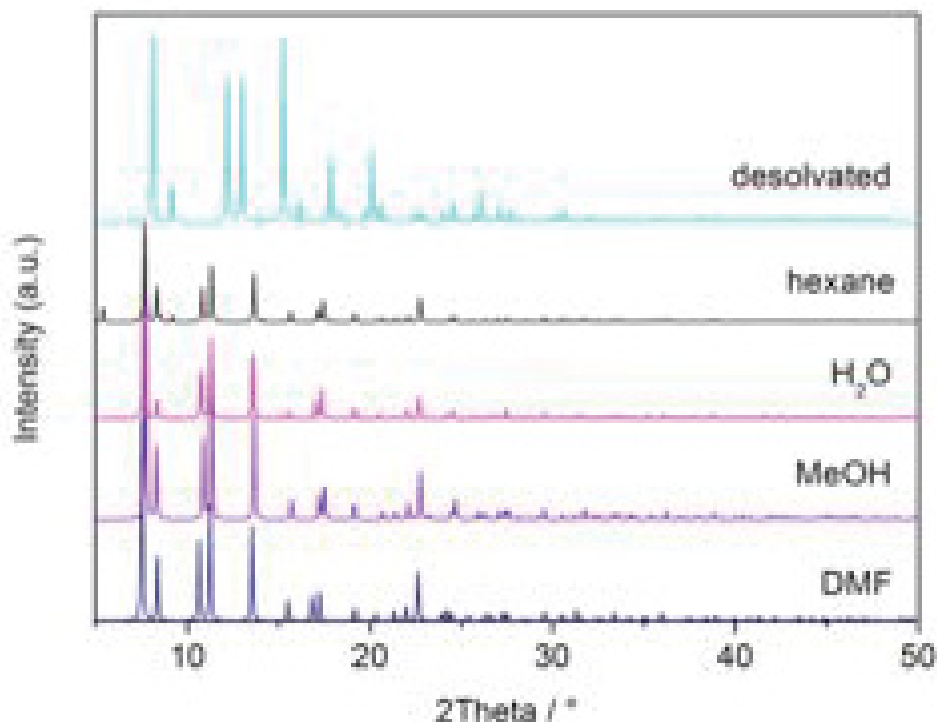
Figure S14. Overlay of the simulated patterns from the SCXRD measurements. The similarity of the simulated patterns for the **1** · nSolv structures (except **1** · H₂O) reflects the rather unchanged network upon solvent exchange.

Structure refinement details

The structures could not be fully refined, regarding all highly disordered solvent molecules inside the voids.

In the special case of the desolvated or "fully" degassed sample **1** (1H₂O remains), where exceptional high disorder was observed, even the structure solution itself was of poor quality. The "desolvated structure **1** is presented for comparison and for showing that it is possible to determine and refine the structure of a desolvated/degassed PCP.

In all other cases of the **1**·nSolv structures and for **2** Q-peaks inside the voids were removed by SQUEEZE in PLATON.

PLATON was used with the CALC SQUEEZE option to determine the electron count within the voids (see Table 3).

Table S1. Hydrogen-bond geometry (Å, °)

for **1** · 1.25DMF.

D—H⋯*A*	*D*—H	H⋯*A*	*D*⋯*A*	*D*—H⋯*A*
N1—H1⋯O3	0.88(2)	1.95(2)	2.823(3)	168(3)

for **1** · 5H$_2$O · 1MeOH

D—H⋯A	*D*—H	H⋯A	*D*⋯A	*D*—H⋯A
N1---H1...O3	0.88	1.99	2.7944(14)	152.1°

for **2** · 1EtOH · 1.4*n*-hexane.

D—H⋯*A*	*D*—H	H⋯*A*	*D*⋯*A*	*D*—H⋯*A*
N1—H1⋯O6[i]	0.88	2.28	3.040(2)	144
C2—H2*C*⋯O6	0.98	2.58	3.298(4)	130
C7—H7*C*⋯N3[ii]	0.98	2.68	3.329(3)	124
C7—H7*C*⋯O6[i]	0.98	2.49	3.117(3)	122
C18—H18*A*⋯O9[iii]	0.98	2.51	3.412(3)	153

Symmetry transformations: i = *y*, -*x*, -*z*+2; ii = *x*, *y*, *z*-1; iii = *y*, -*x*, -*z*+3.
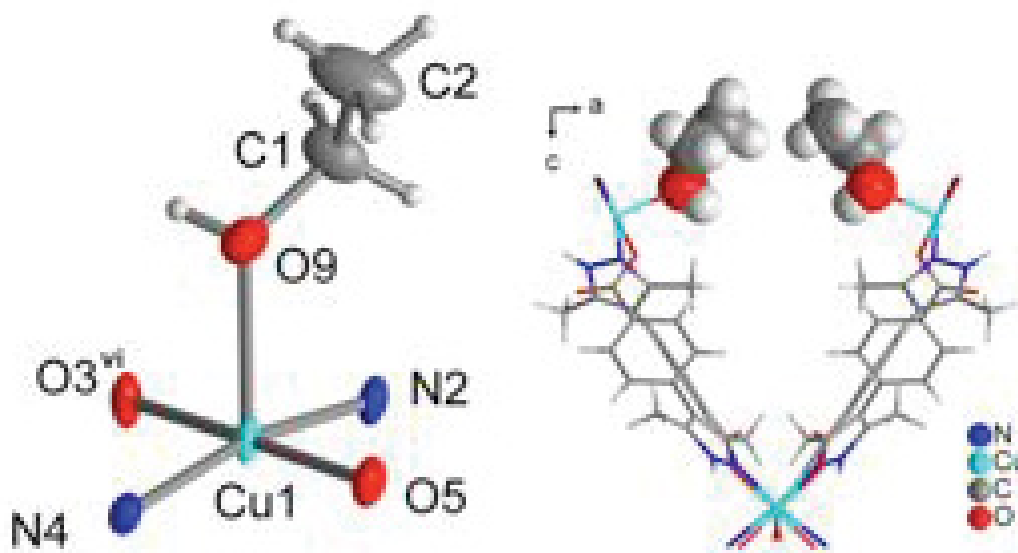
Figure S15. Square-pyramidal environment around Cu1 in the structure of **2** · 1EtOH · 1.4*n*-hexane (left). Visualization of the proximity of the ethanol molecules, which coordinate to Cu1 each (right). Symmetry transformation: iv = 1-x, y, -z.

Table S2. Selected bond lengths (Å) and angles (°) for **2** · 1EtOH · 1.4*n*-hexane.

Cu1—O3	1.9444(14)	Cu2—O2[v]	1.9393(13)

Cu1—O5	1.9477(14)	Cu2—N6	1.9866(15)
Cu1—N4^{vi}	1.9900(16)	Cu2—N8	1.9913(16)
Cu1—N2	2.0021(16)	O8—Cu2^{v}	1.9295(13)
Cu1—O9	2.3975(18)	Cu2—O8^{ii}	1.9295(13)
N4—Cu1^{i}	1.9899(16)	O2—Cu2^{ii}	1.9393(13)
O3—Cu1—O5	178.28(7)	N4^{i}—Cu1—O9	99.74(7)
O3—Cu1—N4^{i}	90.63(6)	N2—Cu1—O9	93.45(7)
O5—Cu1—N4^{vi}	89.49(6)	O8^{ii}—Cu2—O2^{v}	179.84(7)
O3—Cu1—N2	89.23(6)	O8^{iv}—Cu2—N6	88.22(6)
O5—Cu1—N2	90.26(6)	O2^{v}—Cu2—N6	91.77(6)
N4^{vi}—Cu1—N2	166.80(7)	O8^{iv}—Cu2—N8	91.25(6)
O3—Cu1—O9	92.04(7)	O2^{v}—Cu2—N8	88.75(6)
O5—Cu1—O9	89.63(6)	N6—Cu2—N8	177.85(7)

Symmetry transformations: i = -x, y, 3-z; ii = 1-x, -y, z; iii = x, 1-y, -z; iv = 1-x, y, -z; v = 1-x, -y, z; vi = x, -y, 3-z.

1 · 1.25DMF   **1** · H$_2$O (desolvated)

A

B

C
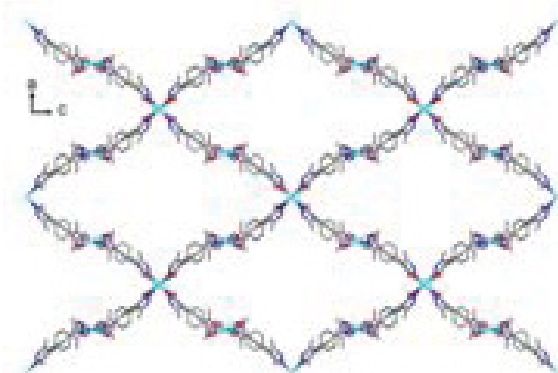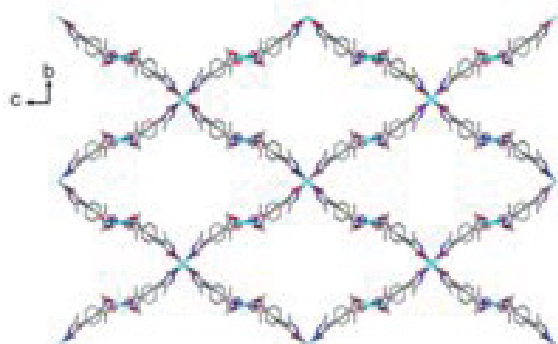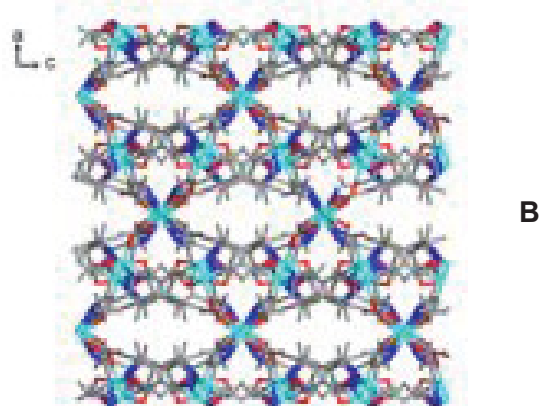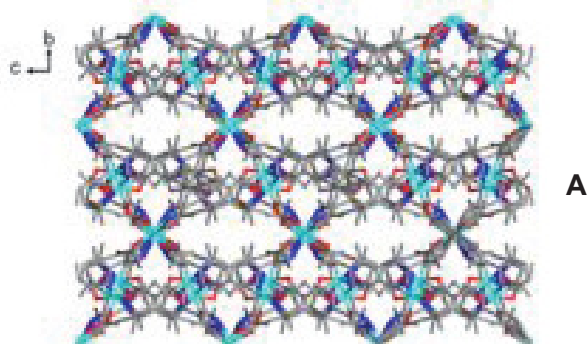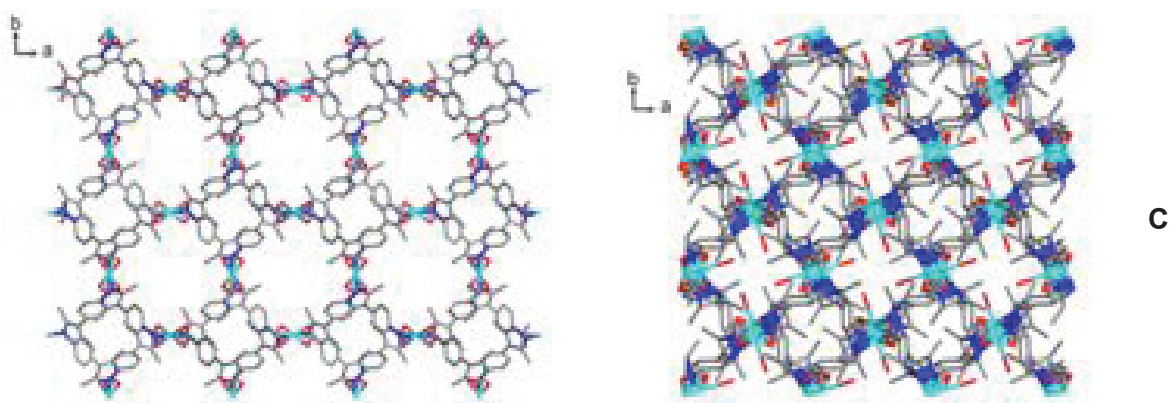
Figure S16. The structures of **1** · 1.25DMF and **1** · H_2O (desolvated) in comparison (wires and sticks modelling). View along *a*- (line A), *b*- (line B) and *c*-axis (line C).
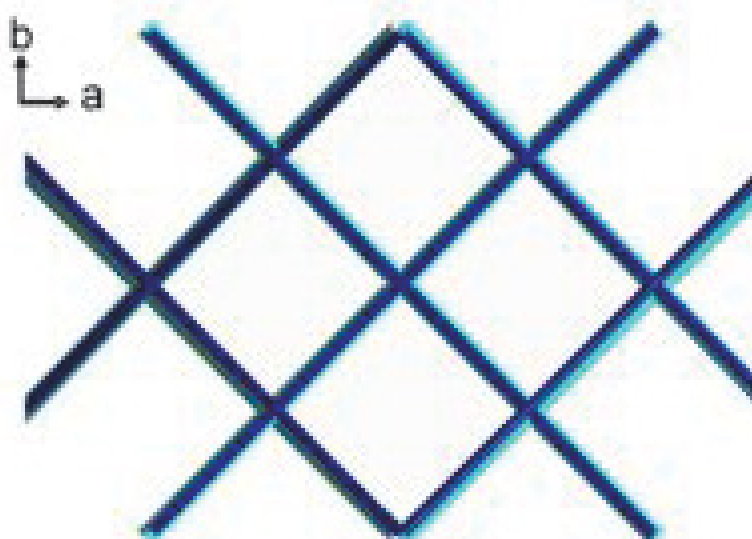
Figure S17. Visualization of one Cu-Cu-node connected network (from triple interpenetration) in **1** · 1.25DMF (dark blue net) and **1** · H_2O (desolvated, turquoise net) with view along *c*-axis (perpendicular to *ab*-plane)
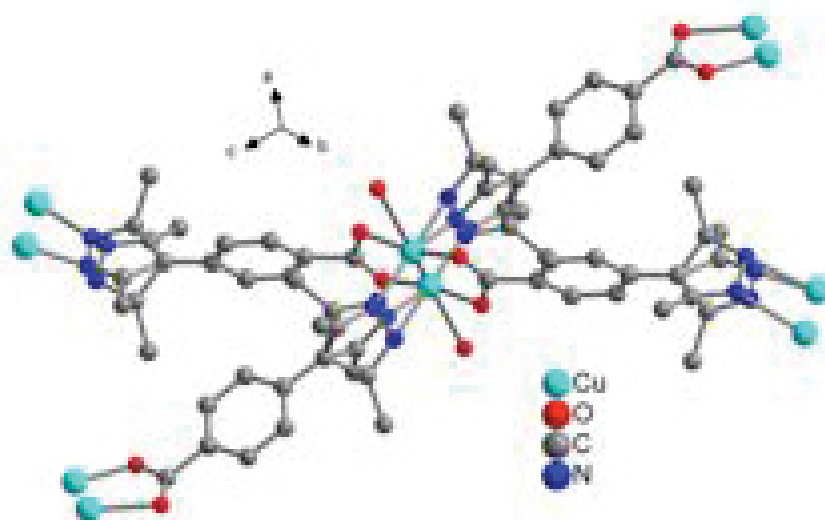
Figure S18. Connectivity of the mononuclear copper node in the network of **1** · H_2O to its four neighbours. Note the disorder of Cu atom and the pyrazole function of HL over two positions. This gives the wrong appearance of a dinuclear Cu-paddle-wheel unit.
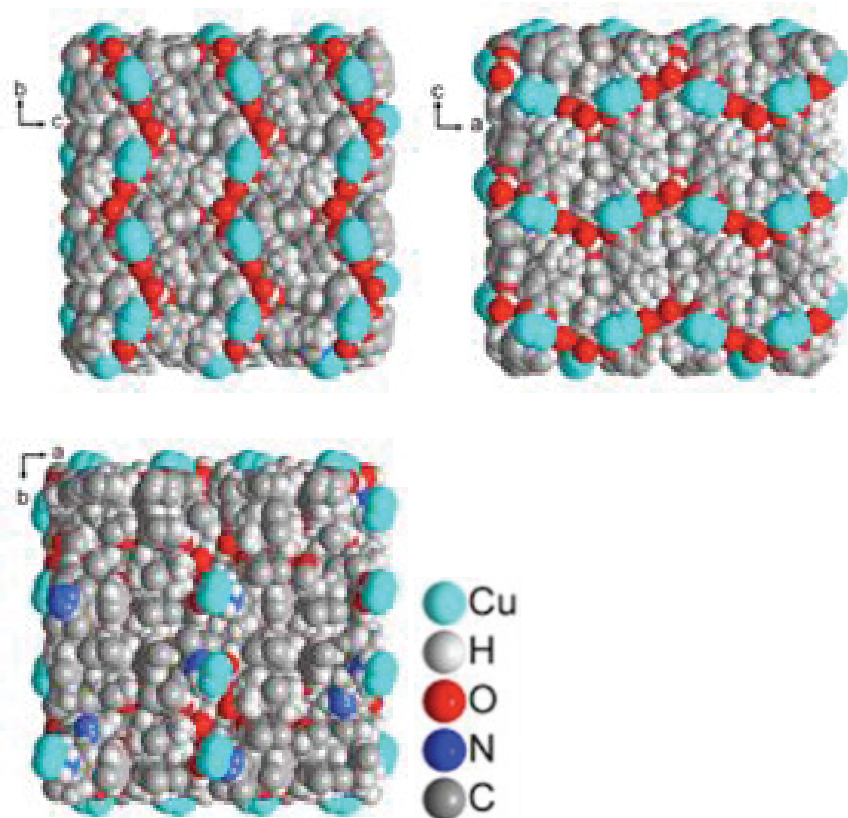
Figure S19 Projections of the packing diagrams in space-filling mode on the three

different planes for the full, three-fold interpenetrated network of **1** · H_2O to illustrate

the dense packing.

Table S4. Cell volume, solvent occupied / accessible voids, void electron count and φ and ψ geometric parameters for **1** · nSolv, **2** · 1EtOH · 1.4*n*-hexane and desolvated **1** · H_2O.

Sample	Unit cell vol. / Å^3	Void vol. in unit cell [a] / Å^3; %		Void count electrons [a] in total void vol. (matched) [b] / e Å^{-3}	Geometry, φ, ψ
1 · 1.25 DMF (*Z*=8)	6532	2033; 31		395 (400)	45.2, 67.1
1 · 5H_2O · 1MeOH (*Z*=8)	6344	2037; 32		453 (544)	47.1, 66.4
1 · 9H_2O (*Z*=8)	6436	2536; 39		720 (720)	46.1, 64.6
2 · 1.4 *n*-hexane (*Z*=4)	6377	2209;35		550 (560)	43.8, 58.7
1 · H_2O (desolvated)	4951	-[c]		-[c]	64[d], 68.99

[a] - Total solvent accessible void volume in unit cell and void count of electrons calculated by PLATON SQUEEZE routine.

[b] – Void electron count is matched to potential solvent molecules (with consideration of IR and CHN analysis, see above) according to Z x Σi(solvent molecule i electron count x number of solvent molecules i in formula unit). The sum (Σi) is formed over the possible different solvent molecules i. Electron count for solvent molecules: DMF (C_3H_7NO) 40 e, EtOH 26 e, MeOH 18 e, H_2O 10, hexane (C_6H_{14}) 50 e.

For the structures of **1** · 1.25DMF and **1** · 5H_2O · 1MeOH one crystal water molecule per formula unit was found and refined, hence, its electron contribution is not included in the void count of electrons.

For the structure of **2** · *n*-hexane one copper-coordinated ethanol molecule is part of the formula unit.

[c] – no solvent accessible void was found and estimated with V = 0 by SQUEEZE (PLATON).

[d] – Because of the disorder of the pyrazole group in **1** · H_2O (degassed), two φ angles, 55.6° and 72.5°, can be determined, of which the average was calculated.

Table S5. Edge to edge distances (Å) (see explanation in main text).

Edge-to-edge distance along axis	**1** · 1.25 DMF	**1** · 5H$_2$O · 1MeOH	**1** · 9H$_2$O	**2** · 1EtOH · 1.4 *n*-hexane	**1** · H$_2$O (desolvated)
a	23.6	23.0	23.3	23.0	19.7
b	23.7	23.1	23.1	23.2	19.4
c	35.4	35.9	35.9	36.1	13.3

4 Conclusions

In this work it was demonstrated that bifunctional ligands with the strongly coordinating groups pyrazolate or phosphonate and carboxylate could be used to synthesize coordination polymers that exhibit high water and thermal stabilitiy. With the herein for the first time presented 4-phosphono-biphenyl-4'-carboxylic acid and with 3,5-dimethyl-(pyrazol-4-yl)-benzoic acid various complexes were synthesized with different metals, which all show interesting properties apart from the mentioned stabilities. The group 12 elements Zn, Cd and Hg gave luminescent coordination polymers with 4-phosphono-biphenyl-4'-carboxylic acid, Zn and Co gave MOF-5 analogues with 3,5-dimethyl-(pyrazol-4-yl)-benzoic acid, which are porous compounds with high surface areas (BET) up to 1,600 m^2/g (Co). With Cu and 3,5-dimethyl-(pyrazol-4-yl)-benzoic acid single-crystal to single-crystal transformations were investigated and a 'breathing' effect was described with this flexible network. Charge assisted hydrogen-bonded networks with NH_4^+ and $[Co(NH_3)_6]^{3+}$ in complexes with 4-phosphono-biphenyl-4'-carboxylic acid were presented and inclusion properties and hydrogen bonding were investigated. In conclusion, the mixed-functional ligand approach as a tool for highly stable CPs and PCPs was proven successful and important new insights were contributed to the area of Metal-organic frameworks.

5 References

[1] Cui, Y.; Li, B.; He, H.; Zhou, W.; Chen, B.; Qian, G. *Acc. Chem. Res.*, **2016**, *49*, 483-493.

[2] Lee, J.-Y.; Farha, O. K.; Roberts, J.; Scheidt, K. A.; Nguyen, S.-B. T.; Hupp, J. T. *Chem. Soc. Rev.*, **2009**, *38*, 1450-1459.

[3] Zhou, H.-Z.; Long, J. R.; Yaghi, O. M. *Chem. Rev.*, **2012**, *112*, 673-674.

[4] Hu, Z.; Deibert, B. J.; Li, J. *Chem. Soc. Rev.*, **2014**, *43*, 5815-5840.

[5] Kreno, L. E.; Leong, K.; Farha, O. K.; Allendorf, M.; Van Duyne, R. P.; Hupp, J. T. *Chem. Rev.*, **2012**, *112*, 1105-1125.

[6] Cui, Y.; Yue, Y.; Qian, G.; Chen, B. *Chem. Rev.*, **2012**, *112*, 1126–1162.

[7] Kurmoo, M. *Chem. Soc. Rev.*, **2009**, *38*, 1353-1379.

[8] Murray, L. J.; Dinca, M.; Long, J. R. *Chem. Soc. Rev.*, **2009**, *38*, 1294-1314.

[9] Phan, A.; Doonan, C. J.; Uribe-Romo, F. J.; Knobler, C. B.; O'Keeffe, M.; Yaghi, O. M. *Acc. Chem. Res.*, **2010**, *43*, 58-67.

[10] Park, K. S.; Ni, Z.; Côté, A. P.; Choi, J. Y.; Huang, R.; Uribe-Romo, F. J.; Chae, H. K.; O'Keeffe, M.; Yaghi, O. M. *PNAS*, **2006**, *103*, 10186-10191.

[11] Czaja, A. U.; Trukhan, N.; Müller, U. *Chem. Soc. Rev.*, **2009**, *38*, 1284-1293.

[12] Furukawa, H.; Cordova, K. E.; O'Keeffe, M.; Yaghi, O. M. *Science*, **2013**, *341*.

[13] Zhou, H.-C.; Kitagawa, S. *Chem. Soc. Rev.*, **2014**, *43*, 5415-5418.

[14] Falcaro, P.; Ricco, R.; Doherty, C. M.; Liang, K.; Hill, A. J.; Styles, M. J. *Chem. Soc. Rev.*, **2014**, *43*, 5513-5560.

[15] Hoskins, B. F.; Robson, R. *JACS*, **1990**, *112*, 1546-1554.

[16] Li, H.; Eddaoudi, M.; O'Keeffe, M.; Yaghi, O. M. *Nature*, **1999**, *402*, 276-279.

[17] Baerlocher, C. H.; Meier, W. M.; Olson, D. H.: Atlas of Zeolite Framework Types (5th ed.), **2001**, Elsevier, New York

[18] Müller, U.; Schubert, M.; Teich, F.; Pütter, H.; Schierle-Arndt, K.; Pastre, J. *J. Mater. Chem.*, **2006**, *16*, 626-636.

[19] Assfour, B.; Leoni, S.; Seifert, G. *J. Phys. Chem. C*, **2010**, *114*, 13381-13384.

[20] Liu, X.; Li, Y.; Ban, Y.; Peng, Y.; Jin, H.; Bux, H.; Xu, L.; Caro, J.; Yang, W. *Chem. Comm.*, **2013**, *49*, 9140-9142.

[21] Nováković, S. B.; Bogdanović, G. A.; Heering, C.; Makhloufi, G.; Francuski, D.; Janiak, C. *Inorg. Chem.*, **2015**, *54*, 2660-2670.

[22] Zhou, H.-C.; Long, J. R.; Yaghi, O. M. *Chem. Rev.*, **2012**, *112*, 673-674.

[23] Stock, N., Biswas, S., **2012**, *112*, 933-969.

[24] Eddaoudi, M.; Moler, D. B.; Li, H.; Chen, B.; Reineke, T. M.; O'Keeffe, M.; Yaghi, O. M. *Acc. Chem. Res.*, **2001**, *34*, 319-330.

[25] Deng, H.; Grunder, S.; Cordova, K. E.; Valente, C.; Furukawa, H.; Hmadeh, M.; Gándara, F.; Whalley, A. C.; Liu, Z.; Asahina, S.; Kazumori, H.; O'Keeffe, M.; Terasaki, O.; Stoddart, J. F.; Yaghi, O. M. *Science*, **2012**, *336*, 1018-1023.

[26] Aakeroy, C. B.; Champness, N. R.; Janiak, C. *CrystEngComm*, **2010**, *12*, 22-43.

[27] Tranchemontagne, D. J.; Mendoza-Cortes, J. L.; O'Keeffe, M. Yaghi, O. M. *Chem. Soc. Rev.*, **2009**, *38*, 1257-1283.

[28] Millange, F.; Guillou, N.; Walton, R. I.; Greneche, J.-M.; Margiolaki, I.;Férey, G. *Chem. Comm.*, **2008**, 4732-4734.

[29] Ferey, G.; Serre, C. *Chem. Soc. Rev.*, **2009**, *38*, 1380-1399.

[30] Serre, C.; Millange, F.; Thouvenot, C.; Noguès, M.; Marsolier, G.; Louër, D.; Férey, G. *JACS*, **2002**, *124*, 13519-13526.

[31] Alhamami, Mays and Doan, Huu and Cheng, Chil-Hung *Materials*, **2014**, *7*, 3198-3250.

[32] Alhamami, M.; Doanm H.; Cheng, C.-H. *Materials*, **2014**, *7*, 3198-3250.

[33] A. Schneemann, A.; Bon, V.; Schwedler, I.; Senkovska, I.; Kaskel, S.; Fischer, R. A. *Chem. Soc. Rev.*, **2014**, *43*, 6062-6096.

[34] Rao, C. N. R.; Natarajan, S.; Vaidhyanathan, R. *Angew. Chem. Int. Ed.*, **2004**, *43*, 1466-1496.

[35] Farha, O. K. ; Özgür Yazaydın, A.; Eryazici, I.; Malliakas, C. D.; Hauser, B. G.; Kanatzidis, M G.; Nguyen, S. B. T.; Snurr, R. Q.; Hupp, J. T. *Nat. Chem.*, **2010**, *2*, 944-948.

[36] Furukawa, H.; Ko, N.; Go, Y. B.; Aratani, N.;Choi, S. B. Choi, E.; Yazaydin, A. Ö.; Snurr, R. Q.; O'Keeffe, M.; Kim, J.; Yaghi, O. M. *Science*, **2010**, *329*, 424-428.

[37] Eddaoudi, M.; Moler, D. B.; Li, H.; Chen, B.; Reineke, T. M.; O'Keeffe, M.; Yaghi, O. M. *Acc. Chem. Res.*, **2001**, *34*, 319-330.

[38] Férey, G.; Mellot-Draznieks, C.; Serre, C.; Millange, F.; Dutour, J.; Surblé, S.; Margiolaki, I. *Science*, **2006**, *309*, 2040-2042.

[39] Deng, H.; Grunder, S.; Cordova, K. E.; Valente, C.; Furukawa, H.; Hmadeh, M.; Gándara, F.; Whalley, A. C.; Liu, Z.; Asahina, S.; Kazumori, H.; O'Keeffe, M.; Terasaki, O.; Stoddart, J. F.; Yaghi, O. M. *Science*, **2012**, *336*, 1018-1023.

[40] Férey, G.; Mellot-Draznieks, C.; Serre, C.; Millange, F.; Dutour, J.; Surblé, S.; Margiolaki, I., *Science*, **2005**, *309*, 2040-2042.

[41] Cychosz, K. A.; Matzger, A. J. *Langmuir*, **2010**, *26*, 17198-17202.

[42] Guillerm, V.; Ragon, F.; Dan-Hardi, M.; Devic, T.; Vishnuvarthan, M.; Campo, B.; Vimont, A.; Clet, G.; Yang, Q.; Maurin, G.; Férey, G.; Vittadini, A.; Gross, S.; Serre, C. *Angew. Chem. Int. Ed.*, **2012**, *51*, 9267–9271.

[43] Low, J. J.; Benin, A. I.; Jakubczak, P.; Abrahamian, J. F.; Faheem, S. A.; Willis, R. R. *JACS*, **2009**, *131*, 15834-15842.

[44] Yang, J.; Grzech, A.; Mulder, F. M.; Dingemans, T. J. *Chem. Comm.*, **2011**, *47*, 5244-5246.

[45] Chui, S. S.-Y.; Lo, S. M.-F.; Charmant, J. P. H.; Orpen, A. G.; Williams, I. D. *Science*, **1999**, *283*, 1148-1150.

[46] Alvarez, E.; Guillou, N.; Martineau, C.; B. Bueken, B.; Van de Voorde, B.; Le Guillouzer, C.; P. Fabry, P.; Nouar, F.; Taulelle, F.; de Vos, D.; Chang, J. S.; Cho, K. H.; Ramsahye, N.; Devic, T.; Daturi, M.; Maurin, G.; C. Serre, C. *Angew. Chem. Int. Ed.*, **2015**, *54*, 1521-3773.

[47] Trofimenko, S. *Chem. Rev.*, **1972**, *72*, 497-509.

[48] S. Trofimenko, *J. Am. Chem. Soc.*, 1967, **89**, 3170-3177.

[49] Trofimenko, S.: *The Coordination Chemistry of Pyrazole-Derived Ligands*, John Wiley and Sons, Inc., **2007**.

[50] Aromí, G.; Barrios, L. A.; Roubeau, O.; Gamez, P. *Coord. Chem. Rev.*, **2011**, *55*, 485-546.

[51] Tsupreva, V.N.; Titov, A. A.; Filippov, O. A.; Bilyachenko, A. N.; Smoljyakov, A. F.; Dolgushin, F. M.; Agapkin, D. V.; Godovikov, I. A.; Epstein, L. M.; Shubina, E. S. *Inorg. Chem.*, **2011**, *50*, 3325-3331.

[52] Boldog, I.; Rusanov, E. B.; Sieler, J.; Blaurock, S.; Domasevitch, K. V. *Chem. Comm.*, **2003**, *9*, 740-741.

[53] Colombo, V.; Montoro, C.; Maspero, A.; Palmisano, G.; Masciocchi, N.; Galli, S.; Barea, E.; Navarro, J. A. R. *JACS*, **2012**, *134*, 12830-12843.

[54] Mulyana, Y.; Kepert, C. J.; Lindoy, L. F.; Parkin, A.; Turner, P. *Dalton Trans.*, **2005**, 1598-1601.

[55] Heering, C.; Boldog, I.; Vasylyeva, V.; Sanchíz, J.; Janiak, C. *CrystEngComm*, **2013**, *15*, 9757-9768.

[56] Qi, X.-L.; Zhang, C.; Wang, B.-Y.; Xue, W.; He, C.-T.; Liu, S.-Y.; Zhang, W.-X.; Chen, X.-M., *CrystEngComm*, **2013**, *15*, 9530-9536.

[57] Muñoz, S.; Guerrero, M.; Ros, J.; Parella, T.; Font-Bardia, M.; Pons, J., *Cryst. Growth & Des.*, **2012**, *12*, 6234-6242.

[58] Furukawa, H.; Gándara, F.; Zhang, Y.-B.; Jiang, J.; Queen, W. L.; Hudson, M. R.; Yaghi, O. M. *JACS*, **2014**, *136*, 4369-4381.

[59] Wade, Casey R. and Corrales-Sanchez, Tachmajal and Narayan, T. C.; Dinca, M. *Energy Environ. Sci.*, **2013**, *6*, 2172-2177.

[60] Clearfield, A.: Metal Phosphonate Chemistry: From Synthesis to Applications, RSC, **2012**, 1-44.

[61] G. Alberti and U. Costantino and S. Allulli and N. Tomassini Journal of Inorganic and Nuclear Chemistry, 1978, 40, 1113-1117.

[62] Gagnon, K. J.; Perry, H. P.; Clearfield, A., *Chem. Rev.*, **2012**, *112*, 1034-1054.

[63] Albrecht-Schmitt, Thomas and Bujoli, Bruno and Cahill, Christopher and Murugavel, R and Rocha, Joao and Hix, Gary and Shimizu, George and Zubieta, Jon and Zon, Jerzy and Brunet, Ernesto and Winpenny, Richard and Wright, Paul A and Stock, Norbert and Mao, Jiang Gao and Zheng, Li-Min: *Metal Phosphonate Chemistry* **2012**, RSC, all chapters.

[64] Iremonger, S. S.; Liang, J.; Vaidhyanathan, R.; Martens, I.; Shimizu, G. K. H.; Daff, T. D.; Aghaji, M. Z.; Yeganegi, S.; Woo, T. K. *JACS*, **2011**, *133*, 20048-20051.

[65] Iremonger, S. S.; Liang, J.; Vaidhyanathan, R.; Martens, I.; Shimizu, G. K. H.; Daff, T. D.; Aghaji, M. Z.; Yeganegi, S.; Woo, T. K., *JACS*, **2011**, *133*, 20048-20051.

[66] Taylor, J. M.; Vaidhyanathan, R.; Iremonger, S. S.; Shimizu, G. K. H. *JACS*, **2012**, *134*, 14338-14340.

[67] Brunet, E.; Cerro, C.; Juanes, O.; Rodríguez-Ubis, J. C.; Clearfield, A. *J. Mat. Sci.*, **2008**, *43*, 1155-1158.

[68] Pramanik, M. Patra, A. K.; Bhaumik, A. *Dalton Trans.*, **2013**, *42*, 5140-5149.

[69] Shimizu, G. K. H.; Vaidhyanathan, R.; Taylor, J. M. *Chem. Soc. Rev.*, **2009**, *38*, 1430-1449.

[70] Yao, H.-C.; Li, Y.-Z.; Gao, S.; Song, Y.; Zheng, L.-M.; Xin, X.-Q. *J. Solid State Chem.*, **2004**, *177*, 4557-4563.

[71] Gao, W.-Y.; Pham, T.; Forrest, K. A.; Space, B.; Wojtas, L.; Chen, Y.-S.; Ma, S., *Chem. Comm.*, **2015**, *51*, 9636-9639.

[72] Galli, S.; Masciocchi, N.; Colombo, V.; Maspero, A.; Palmisano, G.; López-Garzón, F. J.; Domingo-García, M.; Fernández-Morales, I.; Barea, E.; Navarro, J. A. R., Chem. of Materials, **2010**, *22*, 1664-1672.

[73] Clearfield, A.; Demadis, K.: Metal Phosphonate Chemistry*, **2012**, *RSC*.

[74] Ling, Y.; Deng, M.; Chen, Z.; Xia, B.; Liu, X.; Yang, Y.; Zhou, Y. Weng, L. *Chem. Comm.*, **2013**, *49*, 78-80.

[75] Cabeza, A.; Aranda, M. A. G.: Metal Phosphonate Chemistry: From Synthesis to Applications, RSC, **2012**, 107-132.

[76] Zhang, J.; Li, J.; Sun, Z.-G.; Hua, R.-N.; Zhu, Y.-Y.; Zhao, Y.; Zhang, N.; Liu, L.; Lu, X.; Wang, W.-N.; Tong, F. *Inorg. Chem. Comm.*, **2009**, 12, 276-279.

[77] Rueff, J.-M.; Barrier, N.; Boudin, S.; Dorcet, V.; Caignaert, V.; Boullay, P.; Hix, G. B.; Jaffrès, P.-A. *Dalton Trans.*, **2009**, 10614-10620.

[78] Mao, J.-G.; Clearfield, A. *Inorg. Chem.*, **2002**, *41*, 2319-2324.

[79] Midollini, S.; Orlandini, A.; Rosa, P.; Sorace, L., *Inorg. Chem.*, **2005**, *44*, 2060-2066.

[80] Bauer, S.; Bein, T.; Stock, N., *Inorg. Chem.*, **2005**, *44*, 5882-5889.

[81] Sheikh, J. A.; Jena, H. S.; Adhikary, A.; Khatua, S.; Konar, S., *Inorg. Chem.* **2013**, *52*, 9717-9719.

[82] Zhai, F.; Zheng, Q.; Chen, Z.; Ling, Y.; Liu, X.; Weng, L.; Zhou, Y. *CrystEngComm*, **2013**, *15*, 2040-2043.

[83] Beatty, A. M. Coord. *Chem. Rev.*, **2003**, *246*, 131-143.

[84] Beatty, A. M. *CrystEngComm*, **2001**, *3*, 243-255.

[85] Brunet, P.; Simard , M.; Wuest, J. D. *JACS*, **1997**, *119*, 2737–2738.

[86] Yaghi, O. M.; Li, H.; Groy, T. L. *JACS*, **1996**, *118*, 9096–9101.

[87] Morgan, K. R.; Gainsford, G. J.; Milestone, N. B. *Chem. Commun.*, **1997**, 61-62.

[88] Wang, X.-Y.; Justice, R.; Sevov, S. C., *Inorg. Chem.*, **2007**, *46*, 4626-4631.

[89] Ward, M. D. *ChemInform*, **2006**, 37.

[90] Reddy, D. S.; Duncan, S. Shimizu, G. K. H. *Angew. Chem. Int. Ed.*, **2003**, *42*, 1360-1364.

[91] Sekiya, R.; Nishikiori, S., *CrystEngComm*, **2011**, *13*, 6405-6414.

[92] A. R. West: "Solid State Chemistry and Its Applications" John Wiley & Sons, 1987, p 177.

[93] S. P. Westrip, *J. Apply. Cryst.*, 2010, **43**, 920-925.

[94] C. Janiak, *J. Chem. Soc., Dalton Trans.*, 2000, 3885-3896.

[95] M. Nishio, *CrystEngComm*, 2004, **6**, 130-158; M. Nishio, M. H. Y. Umezawa, *The CH/p interaction* (Evidence, Nature and consequences), Wiley-VCH, 1998; M. H. Y. Umezawa, S. Tsuboyama, K. Honda, J. Uzawa and M. Nishio, *Bull. Chem. Soc. Jpn.*, 1998, **71**, 1207-1213; C. Janiak, S. Temizdemir, S. Dechert, W. Deck, F. Girgsdies, J. Heinze, M. J. Kolm, T. G. Scharmann and O. M. Zipffel, *Eur. J. Inorg. Chem.*, 2000, 1229-1241.

[96] π-Interactions between pyridyl-type ligands for comparison: V. Lozan, P.-G. Lassahn, C. Zhang, B. Wu, C. Janiak, G. Rheinwald and H. Lang, *Z. Naturforsch. B*, 2003, **58**, 1152-1164; C. Zhang and C. Janiak, *Z. Anorg. Allg. Chem.*, 2001, **627**, 1972-1975; C. Zhang and C. Janiak, *J. Chem. Crystallogr.*, 2001, **31**, 29-35; H.-P. Wu, C. Janiak, G. Rheinwald and H. Lang, *J. Chem. Soc., Dalton Trans.*, 1999, 183-190; C. Janiak, L. Uehlin, H.-P. Wu, P. Klüfers, H. Piotrowski and T. G. Scharmann, *J. Chem. Soc., Dalton Trans.*, 1999, 3121-3131; H.-P. Wu, C. Janiak, L. Uehlin, P. Klüfers and P. Mayer, *Chem. Commun.*, 1998, 2637-2638.

[97] X.-J. Yang, F. Drepper, B. Wu, W.-H. Sun, W. Haehnel and C. Janiak, *Dalton Trans.*, 2005, 256-267 and ESI therein;

[98] N. N. L. Madhavi, A. K. Katz, H. L. Carrell, A. Nangia and G. R. Desiraju, *Chem. Commun.*, 1997, 1953-1954; H.-C. Weiss, D. Bläser, R. Boese, B. M. Doughan and M. M. Haley, *Chem. Commun.*, 1997, 1703-1704; T. Steiner, M. Tamm, B. Lutz and J. van der Maas, *Chem. Commun.*, 1996, 1127-1128; P. L. Anelli, P. R. Ashton, R. Ballardini, V. Balzani, M. Delgado, M. T. Gandolfi, T. T. Goodnow, A. E. Kaifer, D. Philp, M. Pietraszkiewicz, L. Prodi, M. V. Reddington, A. M. Z. Slawin, N. Spencer, J. F. Stoddart, C. Vicent and D. J. Williams, *J. Am. Chem. Soc.*, 1992, **114**, 193-218.

[99] Kitagawa, S.; Matsuda R. *Coord. Chem. Rev.* **2007**, *251*, 2490-2509. (b) Maji, T. K.; Kitagawa, S. *Pure Appl. Chem.* **2007**, *79*, 2155-2177.

[100] Introductions to special MOF issues: (a) Long, J. R.; Yaghi, O. M. *Chem. Soc. Rev.* **2009**, *38*, 1213-1214. (b) Biradha, K.; Zaworotko, M. J. *New. J. Chem.* **2010**, *34*, 2353-2356. (c) Kitagawa, S.; Natarajan, S. *Eur. J. Inorg. Chem.* **2010**, 3685. (d) Zhou, H. -C.; Long, J. R.; Yaghi, O. M. *Chem. Rev.* **2012**, *112*, 673-674.

[101] (a) Janiak, C. *Dalton Trans.* **2003**, 2781-2804. (b) Janiak, C.; Vieth, J. K. *New. J. Chem.* **2010**, *34*, 2366-2388.

[102] Wu, H.; Gong, Q.; Olson, D. H.; Li, J. *Chem. Rev.* **2012**, *112*, 836-868.

[103] (a) Murray, L. J.; Dinca, M.; Long, J. R. *Chem. Soc. Rev.* **2009**, *38*, 1294-1314. (b) Morris, R. E.; Wheatley, P. S. *Angew. Chem. Int. Ed.* **2008**, *47*, 4966-4981. (c) Düren, T.; Bae, Y. -S..; Snurr, R. Q. *Chem. Soc. Rev.* **2009**, *38*, 1237-1247. (d) Wang, S.; Yang, Q.; Zhang, J.; Zhang, X.; Zhao, C.; Jiang, L.; Su C.-Y. *Inorg. Chem.* **2013**, *52*, 4198–4204.

[104] (a) Li, J.-R.; Sculley, J.; Zhou, H.-C. *Chem. Rev.* **2012**, *112*, 869-932. (b) Reboul, J.; Furukawa, S.; Horike, N.; Tsotsalas, M.; Hirai, K.; Uehara, H.; Kondo, M.; Louvain, N.; Sakata, O.; Kitagawa, S. *Nat. Mater.* **2012**, *11*, 717-723. (c) Wang, H.; Jia, L.; Hou, L.; Shi, W.; Zhu, Z.; Wang, Y. *Inorg. Chem.*, **2015**, *54*, 1841-1846. (d) Karagiaridi, O.; Bury, W.; Fairen-Jimenez, D.; Wilmer, C. E.; Sarjeant, A. A.; Hupp, J. T.; Farha, O. K. *Inorg. Chem.* **2014**, *53*, 10432-10436.

[105] (a) Tanh Jeazet, H. B.; Staudt, C.; Janiak, C. *Chem. Commun.* **2012**, *48*, 2140-2142. (b) Hunger, K.; Schmeling, N.; Tanh Jeazet, H. B.; Janiak, C.; Staudt, C.; Kleinermanns, K. *Membranes* **2012**, *2*, 727-763.

[106] (a) Tanh Jeazet, H. B.; Staudt, C.; Janiak, C. *Dalton Trans.* **2012**, *41*, 14003-14027. (b) Zornoza, B.; Tellez, C.; Coronas, J.; Gascon, J.; Kapteijn, F. *Microporous Mesoporous Mater.* **2013**, *166*, 67-78. (b) Bastani, D.; Esmaeili, N.; Asadollahi, M. *J. Ind. Eng. Chem.* **2013**, *19*, 375-393.

[107] Cychosz, K. A.; Ahmad, R.; Matzger, A. J. *Chem. Sci.* **2010**, *1*, 293-302.

[108] (a) Lohe, M. R.; Gedrich, K.; Freudenberg, T.; Kockrick, E.; Dellmann, T.; Kaskel, S. *Chem. Commun.* **2011**, *47*, 3075-3077. (b) Férey, G. *Chem. Soc. Rev.* **2008**, *37*, 191-214.

[109] Horcajada, P.; Gref, R.; Baati, T.; Allan, P. K.; Maurin, G.; Couvreur, P.; Férey, G.; Morris, R. E.; Serre, C. *Chem. Rev.* **2012**, *112*, 1232-1268.

[110] (a) Lee, J.-Y.; Farha, O. K.; Roberts, J.; Scheidt, K. A.; Nguyen, S. T.; Hupp, J. T. *Chem. Soc. Rev.* **2009**, *38*, 1450-1459. (b) Dhakshinamoorthy, A.; Opanasenko, M.; Čejka, J.; Garcia, H. *Adv. Synth. Catal.* **2013**, *355*, 247-268. (c) Yoon, M.; Srirambalaji, R.; Kim, K. *Chem. Rev.* **2012**, *112*, 1196-1231. (d) Zahmakiran, M. *Dalton Trans.* **2012**, *41*, 12690-12696. (e) Lin, X.-M.; Li, T.-T.; Chen, L.-F.; Zhang, L.; Su, C.-Y. *Dalton Trans.* **2012**, *41*, 10422-10429. (f) Saha, D.; Sen, R.; Maity, T.; Koner, S. *Dalton Trans.* **2012**, *41*, 7399-7408. (g) Savonnet, M.; Camarata, A.; Canivet, J.; Bazer-Bachi, D.; Bats, N.; Lecocq, V.; Pinel, C.; Farrusseng, D. *Dalton Trans.* **2012**, *41*, 3945-3948. (h) Cirujano, F. G.; Llabres i Xamena, F. X.; Corma, A. *Dalton Trans.* **2012,** *41*, 4249-4254.

[111] (a) Gil-Hernández, B.; Maclaren, J. K.; Höppe, H. A.; Pasan, J.; Sanchiz, J.; Janiak, C. *CrystEngComm* **2012**, *14*, 2635-2644. (b) Kurmoo, M. *Chem. Soc. Rev.* **2009**, *38*, 1353-1379.

[112] (a) Jeremias, F.; Fröhlich, D.; Janiak, C.; Henninger, S. *New J. Chem.* **2014**, *4*, 24073-24082; (b) Janiak, C.; Henninger, S. K. *Chimia* **2013**, *67*, 419-424. (c) Henninger, S. K.; Jeremias, F.; Kummer, H.; Janiak, C. *Eur. J. Inorg. Chem.* **2012**, 2625–2634. (d) Akiyama, G.; Matsuda, R.; Sato, H.; Hori, A.; Takata, M.; Kitagawa, S. *Microporous Mesoporous Mater.* **2012**, *157*, 89-93. (e) Zhang, J.-P.; Zhu, A.-X.; Lin, R.-B.; Qi, X.-L.; Chen, X.-M. *Adv. Mater.* **2011**, *23*, 1268-1271. (f) Akiyama, G.; Matsuda, R.; Kitagawa, S. *Chem. Lett.* **2010**, *39*, 360-361. (g) Henninger, S. K.; Habib, H. A.; Janiak, C. *J. Am. Chem. Soc.* **2009**, *131*, 2776-2777. (h) Biemmi, E.; Darga, A.; Stock, N.; Bein, T. *Microporous Mesoporous Mater.* **2008**, *114*, 380-386. (i) Aristov, Y. I. *J. Chem. Eng. Jpn.* **2007**, *40*, 1242-1251.

[113] Jeremias, F.; Khutia, A.; Henninger, S. K.; Janiak, C. *J. Mater. Chem.* **2012**, *22*, 10148-10151.

[114] Ehrenmann, J. ; Henninger, S. K.; Janiak, C. *Eur. J. Inorg. Chem.* **2011**, 471-474.

[115] Low, J. J.; Benin, A. I.; Jakubczak, P.; Abrahamian, J. F.; Faheem, S. A.; Willis, R. R. *J. Am. Chem. Soc.* **2009**, *131*, 15834-15842.

[116] Horcajada, O.; Surble, S.; Serre, C.; Hong, D. Y.; Seo, Y. K.; Chang, J. S.; Grenèche, J. M.; Margiolaki, I.; Férey, G. *Chem. Commun.*, 2007, 2820-2822.

[117] Llewellyn, P. L.; Bourrelly, S.; Serre, C.; Vimont, A.; Daturi, M.; Hamon, L.; De Weireld, G.; Chang, J.-S.; Hong, D.-Y.; Hwang, Y. K.; Jhung, S. H.; Férey, G. *Langmuir* **2008**, *24*, 7245–7250.

[118] Férey, G.; Mellot-Draznieks, C.; Serre, C.; Millange, F.; Dutour, J.; Surble, S.; Margiolaki, I. *Science*, 2005, **309**, 2040–2042.

[119] Khutia, A.; Rammelberg, H. U.; Schmidt, T.; Henninger, S.; Janiak, C. *Chem. Mater.* **2013**, *25*, 790-798.

[120] (a) Karmakar, S.; Dechnik, J.; De, S.; Janiak, C.; *J. Hazardous Mater.* **2016**, *303*, 10-20. (b) Jeremias, F.; Fröhlich, D.; Janiak, C.; Henninger, S. K. *RSC Adv.* **2014**, *4*, 24073-24082.

[121] Coelho, J. A.; Ribeiro, A. M.; Ferreira, A. F. P.; Lucena, S. M. P.; Rodrigues, A. E.; de Azevedo, D. C. S. *Ind. Eng. Chem. Res.* **2016**, *55* , 2134-2143.

[122] Fröhlich, D.; Henninger, S. K.; Janiak, C. *Dalton Trans.* **2014**, *43*, 15300-15304.

[123] Reinsch, H.; van der Veen, M. A.; Gil, B.; Marszalek, B.; Verbiest, T.; de Vos, D.; Stock, N. *Chem. Mater.*, 2013, **25**, 17-26.

[124] (a) Huang, X.-C.; Lin, Y.-Y.; Zhang, J.-P.; Chen, X.-M. *Angew. Chem. Int. Ed.* **2006**, *45*, 1557-1559. (b) Park, K. S.; Ni, Z.; Côté, A. P.; Choi, J. Y.; Huang, R.; Uribe-Romo, F. J.; Chae, H. K.; O'Keeffe, M.; Yaghi, O. M. *PNAS* **2006**, *103*, 10186-10191; (c) Novaković, S. B.; Bogdanović, G. A.; Heering, C.; Makhloufi, G.; Francuski, D.; Janiak, C. *Inorg. Chem.* **2015**, *54*, 2660-2670.

[125] Jeremias, F.; Lozan, V.; Henninger, S.; Janiak, C. *Dalton Trans.* **2013**, *42*, 15967-15973.

[126] Wu, H.; Yildirim, T.; Zhou, W. *J. Phys. Chem. Lett.* **2013**, *4*, 925-930.

[127] Cavka, J. H.; Jakobsen, S.; Olsbye, U.; Guillou, N.; Lamberti, C.; Bordiga, S.; Lillerud, K. P. *J. Am. Chem. Soc.*, 2008, **130**, 13850-13851.

[128] Küsgens, P.; Rose, M.; Senkovska, I.; Fröde, H.; Henschel, A.; Siegle, S.; Kaskel, S. *Micropor. Mesopor. Mater.* **2009**, *120*, 325-330.

[129] Wu, T.; Shen, V.; Luebbers, M.; Hu, C.; Chen, Q.; Ni, Z.; Masel, R. I. *Chem. Commun.* **2010**, *46*, 6120-6122.

[130] Tonigold, M., Lu, Y., Bredenkötter, B., Rieger, B., Bahnmüller, S., Hitzbleck, J., Langstein, G. and Volkmer, D. *Angew. Chem. Int. Ed.* **2009**, *48*: 7546-7550.

[131] Heering, C.; Boldog, I.; Vasylyeva, V.; Sanchiz, J.; Janiak, C. *CrystEngComm* **2013**, *15*, 9757-9768.

[132] (a) Colombo, V.; Montoro, C.; Maspero, A.; Palmisano, G.; Masciocchi, N.; Galli, S.; Barea, E.; Navarro, J. A. R. *J. Am. Chem. Soc.* **2012**, *134*, 12830-12843. (b) Masciocchi, N.; Galli, S.; Colombo, V. Maspero, A.; Palmisano, G.; Seyyedi, B.; Lamberti, C.; Bordiga, S. *J. Am. Chem. Soc.* **2010**, *132*, 7902-7904.

[133] Tonigold, M.; Lu, Y.; Mavrandonakis, A.; Puls, S.; Staudt, R.; Maellmer, J.; Sauer, J.; Volkmer, D. *Chem. Eur. J.* **2011**, *17*, 8671-8695.

[134] (a) Quartapelle Procopio, E.; Fukushima, T.; Barea, E.; Navarro, J. A. R.; Horike, S.; Kitagawa, S. *J. Chem. Eur.* **2012**, *18*, 13117-13125 (b) Montoro, C.; Linares, F.; Quartapelle Procopio, E.; Senkovska, I.; Kaskel, S.; Galli, S.; Masciocchi, N.; Barea, E.; Navarro, J. A. R. *J. Am. Chem. Soc.* **2011**, *133* (31), 11888–11891 (c) He, C.-T.; Tian, J.-Y.; Liu, S.-Y.; Ouyang, G.; Zhang, J.-P.; Chen, X.-M. *Chem. Sci.* **2013**, *4*, 351-356 (d) Padial, N. M.; Quartapelle Procopio, E.; Montoro, C.; López, E.; Oltra, J. E.; Colombo, V.; Maspero, A.; Masciocchi, N.; Galli, S.; Senkovska, I.; Kaskel, S.; Barea E.; Navarro, J. A. R. *Angew. Chem.* **2013**, *125*, 8448-8452.

[135] Bryant,M. R.; Burrows, A. D.; Fitchett, C. M.; Hawes, C. S.; Hunter, S. O.; Keenan, L. L.; Kelly, D. J.; Kruger, P. E.; Mahon, M. F.; Richardson, C. *Dalton Trans.* **2015**, *44*, 9269-9280.

[136] (a) Alhamami, M.; Doan, H.; Cheng, C.-H. *Materials,* **2014**, 7, 3198-3250 (b) Férey, G.; Serre, C. *Chem. Soc. Rev.* **2009**, 38, 1380-1399 (c) Millange, F.; Guillou, N.; Walton, R. I.; Grenèche, J.-M.; Margiolakid, I.; Férey, G. *Chem. Commun.* **2008**, 4732–4734. (d) Liu, M.-M.; Bi, Y.-L.; Dang, Q.-Q.; Zhang, X.-M. *Dalton Trans.* **2015**, *44*, 19796-19799. (e) Reinsch, H.; Pillai, R. S.; Siegel, R.; Senker, J.; Lieb, A.; Maurin, G.; Stock, N. *Dalton Trans.* **2016**, *45*, 4179-4186. (f) Kim, Y.; Haldar, R.; Kim, H.; Koo, J.; Kim, K. *Dalton Trans.,* **2016**,*45*, 4187-4192. (g) Zheng, B.; Wang, L. L.; Hui, J. C.; Du, L.; Du, H.; Zhu, M. *Dalton Trans.,* **2016**, *45*, 4346-4351. (h) Chen, L.; Mowat, J. P. S.; Fairen-Jimenez, D.; Morrison, C. A.; Thompson, S. P.; Wright, P. A.; Düren, T. *J. Am. Chem. Soc.* **2013**, *135*, 15763-15773. (i) Tian, Y.; Allan, P. K.; Renouf, C. L.; He, X.; McCormicka, L. J.; Morris, R. E. *Dalton Trans.* **2014**, *43*, 1519–1523. (j) Li, H.; Wang, X.; Jia, Y.; Zhao, B.; Ding, R.; Hou, H.; Fan, Y. *CrystEngComm* **2012**,

[14], 5155–5157. (k) Low, Z.-X.; Yao, J.; Liu, Q.; He, M.; Wang, Z.; Suresh, A. K.; Bellare, J.; Wang, H. *Cryst. Growth Des.* **2014**, *14*, 6589-6598.

[137] Gustafsson, M.; Su, J.; Yue, H.; Yao, Q.; Zou, X. *Cryst. Growth Des.* **2012**, *12*, 3243-3249.

[138] Sharma, M. K.; Lama, P.; Bharadwaj, P. K. *Cryst. Growth Des.* **2011**, *11*, 1411-1416.

[139] Ho, T.-Y.; Huang, S.-M.; Wu, J.-Y.; Hsu, K.-C.; Lu, K.-L. *Cryst. Growth Des.* **2015**, *15*, 4266-4271.

[140] Murdock, C. R.; Lu, Z.; Jenkins, D. M. *Inorg. Chem.*, **2013**, *52*, 2182-2187.

[141] Lee, J. H.; Kim, T. K.; Suh, M. P.; Moon, H. R. *CrystEngComm*, **2015**, *17*, 8807-8811.

[142] Habib, H. A..; Sanchiz, J.; Janiak, C. *Dalton Trans.*, **2008**, 1734-1744.

[143] Mercury 3.5.1: visualization and analysis of crystal structures: Macrae, C. F.; Edgington, P. R.; McCabe, P.; Pidcock, E.; Shields, G. P.; Taylor, R.; Towler, M.; van de Streek, J. *J. Appl. Cryst.* **2006**, *39*, 453-457.

[144] Quartapelle Procopio, E.; Fukushima, T.; Barea, E.; Navarro, J. A. R.; Horike, S.; Kitagawa, S. *Chem. Eur. J.*, **2012**, *18*, 13117-13125.

[145] Apex2 - Data Collection Program for the CCD Area-Detector System; SAINT - Data Reduction and Frame Integration Program for the CCD Area-Detector System. Bruker Analytical X-ray Systems, Madison, Wisconsin, USA, 1997-2014.

[146] (a) Sheldrick, G. Program SADABS: Area-detector absorption correction, University of Göttingen, Germany, 1996-2014. (b) Krause, L., Herbst-Irmer, R., Sheldrick, G.M., Stalke, D. *J. Appl. Cryst.* **2015**, *48*, 3-10.

[147] Sheldrick, G. M. *Acta Crystallogr. A* **2015**, *71*, 3-8.

[148] Spek, A. L. *Acta Crystallographica Section D*, 2009, **65**, 148-155;; PLATON – A Multipurpose Crystallographic Tool, Utrecht University, Utrecht, The Netherlands, A. L. Spek (2008); Windows implementation: L. J. Farrugia, University of Glasgow, Scotland, Version 40608, 2008.

[149] Brandenburg, K. Diamond (Version 3.2 or Version 4.0), crystal and molecular structure visualization, Crystal Impact. K. Brandenburg & H. Putz Gbr, Bonn, Germany, 2007-2016

[150] Bridges, J. W.; Williams, R. T. *Nature* **1962**, *196*, 59-61.

[151] Martin, R.; Clarke, G. A. *J. Phys. Chem.* **1978**, *82*, 81-86.

152 (a) Habib, H. A.; Hoffmann, A.; Höppe, H. A.; Steinfeld, G.; Janiak, C. *Inorg. Chem.*, **2009**, *48*, 2166-2180. (b) Habib, H. A.; Hoffmann, A.; Höppe H. A.; Janiak, C. *Dalton Trans.,* 2009, 1742-1751. (c) Habib, H. A.; Sanchiz, J.; Janiak, C. *Dalton Trans.*, **2008**, 1734-1744.

153 (a) Hu, Z.; Deibert, B. J.; Li, J. *Chem. Soc. Rev.,* **2014**, *43*, 5815—5840. (b) Heine, J.; Müller-Buschbaum, K. *Chem. Soc. Rev.*, **2013**, *42*, 9232—9242. (c) Allendorf M. D.;Bauer, C. A.; Bhakta, R. K.; Houk, R. J. T. *Chem. Soc. Rev.*, **2009**, *38*, 1330–1352.

154 Kreno, L. E.; Leong, K.; Farha, O. K.; Allendorf, M.; Van Duyne, R. P.; Hupp, J. T. *Chem. Rev.*, **2012**, *112*, 1105–1125.

155 O'Keeffe, M.; Peskov, M. A.; Ramsden, S. J.; Yaghi, O. M. *Acc. Chem. Res.* **2008**, *41*, 1782.

156 The three letter symbols, proposed by M. O'Keeffe, can be retrieved with examples and further information from the Reticular Chemistry Structure Resource database, http://rcsr.net/nets/.

157 Blatov, V. A.; O'Keeffe, M.; Proserpio, D. M. *CrystEngComm* **2010**, *12*, 44-48.

158 Carlucci, L. ; Ciani, G.; Proserpio, D. M.; Mitina, T. G.; Blatov, V. A. *Chem. Rev.*, **2014**, *114*, 7557.

159 (a) Proserpio, D. M. *Nature Chem.* 2, **2010**, 435; (b) Fang, L.; Olson, M. A.; Benítez, D.; Tkatchouk, E.; Goddard III, W. A.; Stoddart, J. F. *Chem. Soc. Rev.,* **2010,** *39,* 17; (c) Blatov, V. A. ; Carlucci, L.; Ciani, G.; Proserpio, D. M. *CrystEngComm,* **2004**, *6*, 377; (d) Xu, B.; Lin, Z.; Han, L.; Cao, R. *CrystEngComm,* **2011,** *13,* 440; (e) Habib, H. A.; Hoffmann, A.; Höppe, H. A.; Steinfeld, G.; Janiak, C. *Inorg. Chem.* **2009**, *48*, 2166-2180. (f) Brown, K. A.; Martin, D. P.; LaDuca, R. L. *CrystEngComm,* 2008, *10*, 1305; (g) Luo, F.; Yang, Y.-T.; Che, Y.-X.; Zheng, J.-M. *CrystEngComm,* **2008**, *10*, 981. (h) Wu, H.-P.; Janiak, C.; Uehlin, L.; Klüfers, P.; Mayer, P. *Chem. Commun.* **1998**, 2637-2638.

160 Boldog, I.; Rusanov, E. B.; Chernega, A. N.; Sieler, J.; Domasevitch, K. V. *J. Chem. Soc., Dalton Trans.* **2001**, 893-897.

161 He, C.-T.; Liao, P.-Q.; Zhou, D.-D.; Wang, B.-Y.; Zhang, W.-X.; Zhang, J.-P.; Chen, X.-M. *Chem. Sci.* **2014**, 5, 4755-4762.

[162] T. Zhao, L. Cuignet, M. M. Dîrtu, M. Wolff, V. Spasojevic, I. Boldog, A. Rotaru, Y. Garcia, C. Janiak, *J. Mater. Chem. C* **2015**, *3*, 7802-7812; A. Bhunia, I. Boldog, A. Möller, C. Janiak, *J. Mater. Chem. A* **2013**, *1*, 14990-14999.

[163] Bennett, T. D.; Fuchs, A. H.; Cheetham, A. K.; Coudert, F.-X. *Dalton Trans*. **2016**, *45*, 4058-4059. (Editorial to themed issue on "Flexibility and disorder in metal-organic frameworks")